UNIVERSITY OF BIRMINGHAM

NOVEL PROCESSING ROUTES FOR NEURAL INTERFACES

by

RICHARD BARRETT

A thesis submitted to

The University of Birmingham

for the degree of

DOCTOR OF PHILOSOPHY

School of Electrical, Electronics and Computer Engineering

College of Engineering and Physical Science

The University of Birmingham

April 2013

ABSTRACT

The thesis describes novel processing routes that have been developed to fabricate neural interfaces. A process has been investigated that uses microfabrication techniques to fabricate a multi-channel regenerative implant that can record nerve impulses in the peripheral nervous system (PNS), called the Spiral Peripheral Nerve Interface (SPNI). It is shown both theoretically and experimentally that the implant improves the ability to record signals in the PNS via micro-channels that act as axonal amplifiers. New processing routes are introduced to create robust interconnections from the SPNI to external electronics via 'Microflex' technology. To incorporate the new interconnection technology the SPNI had to be modified. During this modification the strain in the device was given specific consideration, for which a new bending model is presented. Modelling is used to show that electrochemical impedance spectroscopy can be used to assess the quality of the fabrication process. Electrochemical and mechanical tests show that the interconnection technology is suitable for a neural interfaces but the fabrication of perfectly sealed micro-channels was not evident. Thus, the SPNI was further improved by the introduction of a silicone sealing layer in the construction of the micro-channel array that was implemented using a novel adhesive bonding technique.

ACKNOWLEDGEMENTS

Many people have contributed to this work both directly and indirectly and I am grateful for their support. Firstly, to my supervisor Dr Edward Tarte; Thank you for granting me the opportunity to investigate many varied and interesting pursuits. Your sharp and critical intellect, and unassuming nature, helped greatly in this research and I feel our academic partnership can gather strength from here.

To my colleagues Samia Benmerah, who got the ball rolling with much of this work, and Andreas Frommhold who offered guidance in both the design and fabrication of microfabricated structures, your help has been invaluable. Also I would also like to acknowledge Donna Johnson, our technician, who maintains the clean room and lab facilities and Dr Mao Long and Dr Yingtao Tian who have offered their experience of cleanroom technologies.

I am grateful to Dr James Fitzgerald, who has offered his advice on the neural devices from a clinical perspective, as well as having significant input on the latest design of the neural interfaces. To Dr Liam Grover and his Ph.D student Parastoo Jamshidi, thank you for allowing us to use the Instron microtester and for the technical and operational guidance needed to perform the testing.

I would like to thank my family for their support throughout this work. You have all had a significant impact on the direction and evolution of my work and in the difficult moments your support and encouragement gave me renewed strength and determination. You are all very special to me. I hope I will get to spend a bit more time with you all now!

Finally, to Catrin, I couldn't have done without you, you are an amazing person. I love you.

CONTENTS

GLOSSARY OF TERMS

Miscellaneous Terms

Symbol/Abbreviation	Description
R	The universal gas constant, R = 8.31 $JK^{-}1mol^{-}1$
F	Faraday's constant, F = 9.64×10^{4} $Cmol^{-}1$
∇	Spatial Derivitive
T	Temperature
k_b	Boltzmann constant, $k_b = 1.38 \times 10^{-23}$ $m^{2}kgs^{-}2K^{-}1$
e	Charge of an electron, e=1.60 x 10^{-19}C
N_A	Avagadro's Number, $N_A = 6.02 \times 10^{23}$ $mol^{-}1$
ς	Capacitance

Biological and Electrophysiological Terms

Symbol/Abbreviation	Description
CNS	The central nervous system, comprising of the Brain and the Spinal Cord
PNS	The peripheral nervous system, comprising of nerves that extend from the spinal cord to control muscles and glands
Afferent/Efferent signals	Input/Output signals from the muscles, skin or organs to the brain, via the spinal cord
V_m	Transmembrane potential, potential difference between internal and external surface of cell membrane
φ_i, φ_e	Intracellular and Extracellular Potential of an axon respectively
$\vec{J}_{\text{diff},\kappa}$	Flux of κ ions that pass through a unit area of membrane per unit time (mole/m^2s)
C_κ	Concentration of κ ion (mol/l)
D_κ	Ficks Constant for κ ion (m^2s^-1)
μ_κ	Mobility of κ ions ($m^2V^-1s^-1$)
z_κ	Valency of κ ion
h	Width of membrane, metres
P_κ	Permeability of κ ion, m^2
G_κ	Conductance of current path of κ ion, S
I_κ	Current of κ ion, Amps
H-H	Hodgkin and Huxley
R_I, R_e	Resistance per unit length of intracellular and extracellular space respectively, in relation to the axon membrane
Wallerian degeneration/regeneration	Degeneration or regeneration of axons after injury
Myelin	Protective sheath that can wrap around nerve fibers
OHP	Outer Helmholtz plane respectively
ϵ_0,ϵ_r	The permittivity of free space (8.85×10^-12 F/m) and relative permittivity of a dielectric respectively

in-vitro/in-vivo	Experiments in biology that use cultured cells/whole biological systems
L_D	Debye Length of electrode interface, m
η	Charge overpotential of electrode interface, V
J_0	Exchange current density of an electrode interface [Am^{-}2]
R_t	Charge transfer resistance of electrode interface, Ω
σ	Conductivity of a solution, (S/m)

Technological Terms

Symbol/Abbreviation	Description
SPNI	Spiral Peripheral Nerve Interface
MEA	Multi-Electrode Array
BCI	Brain-Computer Interface
EEG	Electroencephalography, recording electrical signals from the surface of the skull
ECG	Electrocardiography, recording electrical signals from the heart
EMG	Electromyography, recording electrical signals from muscles
EcoG	Electrocorticography, recording electrical signals on the surface of the cortex
Photolithography	Chemical process that uses light to pattern objects
FES	Functional Electrical Stimulation
Handle/Carrier wafer, Wafer	(100) silicon wafer that has been pretreated with a 250 nm oxidised surface layer
IPA	Isopropyl achohol, Solvent used during fabrication of electrodes
Durimide 7020, 7505 (aka PSPI)	Two variaties of photosensitive polyimide used during fabrication
SPR-220-7, S1813	Two variaties of photoresists used to pattern the metal layers
MF-319, MF-26A	Chemical ancillaries used to develop photoresist
HTR-D2, RER600	Chemical ancillaries used to develop Durimide
PMMA	Poly-methyl-methacrylate, polymer used as sacrificial layer
PDMS	Silicone used for sealing layer, Sylgard 184
OPE	Oxygen plasma etching
PI-2611 aka Pyrallin	Polyimide (non-photosensitive)
MEMs	Micro-Electro-Mechanical structures
EIS	Electrochemical impedance spectroscopy
PCB	Printed Circuit Board
DIL socket	Dual-Inline Socket. A PCB input that has two parallel rows pins
DUT	Device under test

ZIF	Zero-Insertion Force connector
Microflex/MFI	Method of connecting flexible devices to PCB utilising riveting process
CMOS	Complementary-metal-oxide-semiconductor
TMAH	Tetramethylammonium hydroxide
NMP	N-methyl-2-pyrrolidone, solvent used in Durimide resin
MIBK	Methyl-Iso-Butyl-Ketone, Solvent used to strip PMMA
CPE	Constant Phase Element

LIST OF FIGURES

LIST OF TABLES

1. INTRODUCTION

The thesis discusses novel processing methods that have been developed to enhance the recording capabilities of a neural interface. In the following introduction the overall objectives and themes of the thesis are described, the specific fabrication methods that have been developed are briefly introduced, and the neural applications in which these novel processes can be used are outlined.

1.1 Motivation

One of the major challenges of modern science is to understand the fundamental principles and operation of the nervous system. Neural interfaces have been developed in the form of devices that are able to extract information from the nervous system as electrical signals that encode the activity of the brain, and other neural systems. The central and peripheral nervous system can be analysed via electrodes that record their electrical impulses, giving insight into their behaviour.

This kind of interface is important for basic neuro-physiological research and has enormous potential for clinical applications, where a 'neuro-prosthesis' is intended to restore or support paths of the neuromuscular or neurosensory system by stimulating muscle or neural tissue electrically. This idea has already been used in the development of cochlear and retinal prostheses [1] [2].

Similarly, the same neural interfaces can be used as recording devices to measure electrical activity from neural pathways. Experiments have shown that electrical activity recorded in a patient's motor cortex can be decoded to represent the movement of the patient's limbs [3] [4]. Most applications of this technology is aimed at people with severe impediments, helping them to achieve a better quality of life. As such, significant scientific investment has been made to develop a reliable and practical recording and stimulating interface to nerves. There are many excellent reviews that cover the basics of neural-prosthetics [5] and neural interfaces in general

[6] that are recommended when developing an interest in this field.

Neural interfaces are seen as realistic technology through which damaged functions of the nervous system could be replaced, by creating a bi-directional communication system with functioning neural tissue. A neural interface that is capable of replacing lost function completely has not yet been developed, but electronic devices for neural interfacing are advancing as new technology becomes available. The earliest neural interfaces were bare metal wires but they have since developed into complex microfabricated arrays that are capable of communicating with the nervous system through hundreds of 'active sites' [7]. Further advances in neural interfaces are driving them to have more active sites [8], with a better integration into the human body and to be robust for many years [6]. As such, new devices are under constant development, with better designs and fabrication processes being introduced to overcome the challenges outlined above.

This thesis introduces technology intended to improve the ability to record from small populations of axons in the peripheral nervous system and the fabrication routes investigated to increase the durability of that interface. Methods of predicting and testing the performance of these neural interfaces will also be outlined to assess the quality of the fabrication processes. Experimental work will show that the fundamental technology introduced in this thesis is sound but requires improvement.

1.1.1 Overview of the Thesis

To understand how neural interfaces work, the thesis introduces the anatomy of the nervous system first. In chapter two this is broken into two parts, where the central nervous system that includes the brain and the spinal cord is briefly introduced, followed by a description of the peripheral nervous system. The thesis discusses how these biological systems are arranged and how their electrical behaviour is propagated between neurons via action potentials, that derive from the physiology of the cell membrane of the nerves.

In extreme cases of neural degeneration caused by disease or injury a patient may have very little or no control of their skeletal muscles and so require significant technology to regain any independence. In the case of traumatic injury to the spinal cord, the motor control structures of the brain are largely intact and so may provide a rich source of relevant command signals that

could be reinterpreted to provide new function, via external devices. Similarly, in the case of an amputation, the relevant nerve signals are transmitted along the undamaged section of nerve, up to the point at which the amputation occurred. A neural interface can support a prosthesis by reinterpreting the nerve signals that are being transmitted into the peripheral nerve, that were originally intended to control muscles that have since been removed. The most famous neural interface is perhaps the 'Utah' array, which has been developed for use in many applications in the last 20 years and consists of around 100 densely packed electrode tips. Recently, an implanted Utah array has been shown to have some remaining functionality after 3 years post implantation, setting a new benchmark for chronic neural interfaces [9].

In chapter three the thesis will introduce the conventional methods that have been developed to measure electrical signals from the nervous system, including the Utah array, and the specific engineering considerations that should be applied to each method. A brief description is given of the physical mechanisms that underline the ability to record neural signals before recording interfaces that are designed for use in the peripheral nervous system are given specific consideration.

Chapter four is an introduction to the concept of axonal amplification, which is a mechanism that improves the ability to interface to regenerated nerves in the PNS by augmenting the extracellular resistance. By confining regenerated axons in a microfabricated channel the stimulus current required to excite the axons is reduced and the ability to record action potentials is improved. The thesis will describe how these mechanisms have been modelled analytically and computationally with specific consideration to the PNS.

In chapter five the thesis outlines all the methods that have been used to fabricate and test the neural interfaces in this thesis. This chapter is intended to be an accessible guide to microfabrication techniques, including spin coating, photolithography and methods of etching materials. The chapter will then describe the methods that are used to test the neural interfaces in vitro which focus on electrochemical impedance spectroscopy and tensile strength testing.

The concept of the spiral peripheral nerve interface (SPNI) will be introduced in chapter six, a novel neural interface that has been developed as a collaborative effort between the School of Electronic Electrical and Computational Engineering of the University of Birmingham, The department of Physiology in Kings College London, the Centre for Nanoscience, Department

of Material Science and the Brain Repair Centre all of the University of Cambridge [10]. The aim of the SPNI is to create a system of axonal amplifiers [11] to improve the signal quality recorded from 'sieve'-type neural implants. The design, fabrication and performance of this interface are described in detail.

The SPNI had a significant weakness that became evident during in vivo testing as the method of transmitting the recorded signals to external electronics was unreliable and needed to be improved. Chapter seven introduces fabrication processes that have been developed to improve the ability to connect the SPNI to external electronics, that are essential to perform signal processing and extract information from the signals that are recorded. Furthermore, the mechanical properties of the SPNI are discussed in detail and special consideration is given to the amount of strain that the device is subjected to during fabrication. It will be shown that previous attempts to model this strain were misguided and a new strain model is presented to correct this. Ultimately, the thesis shows that a micro-riveting technique called 'Microflex' [12] can be incorporated into the fabrication of the SPNI, when some design modification are imposed. Efforts to modify the thickness of the substrate of the SPNI will also be outlined to increase the range of designs that may be possible in the future. To make this work, materials had to be used in unfamiliar ways and severe design restrictions had to be overcome.

To assess the quality of the fabrication processes analytical models of the electrochemical performance of the SPNI will be introduced in chapter eight. The models are used to predict the electrochemical behaviour of gold electrodes in saline during in vitro testing, to provide a basis of comparison to experimental work. The analytical modelling shows the effect on the electrochemical behaviour of varying the geometry of the device to incorporate a micro-channel structure and how this is manifested in an impedance spectrum. It is shown that the electrochemical testing can be used to test both the quality of the electrode surface and the quality of the micro-channel fabrication.

The updated device was tested using the methods that are introduced in chapter five, and the results of these tests are shown in chapter nine. It will be shown that the updated SPNI device is at least as good as the previous studies, and the effect of altering the substrate thickness is discussed. The in vitro testing largely agrees with the behaviour that is described in the analytical modelling, but it was not possible to detect the perfect sealing of the micro-channel

structure in any of the electrodes tested. Comparing the modelled spectra to the measured results suggests that the electrodes of the SPNI have a dispersive capacitance and partially sealed micro-channels, suggesting that the sealing of the micro-channels needed to be addressed. Further to the electrochemical testing in this thesis, previous in vivo testing of the original device found that the SPNI required much larger stimulus currents than a similar silicone electrode array[13]. The silicone device completely enveloped any regenerated tissue that had grown into it, which increased its ability to act as an axonal amplifier[11] and it could not be guaranteed that the SPNI had achieved the same level of sealing. Sealing of the micro-channels could be improved through the inclusion of a sealing layer into the fabrication of the electrode array using a thin layer of silicone. How the sealing layer was incorporated into the fabrication of the SPNI is discussed in chapter ten of this thesis.

Chapter eleven will conclude the thesis, highlighting the significant achievements and the areas that should be improved in future research. The translation of the updated microfabrication techniques will be discussed, including the design and implementation of the latest neural interfaces that are being fabricated using the techniques introduced in this thesis.

2. NEURAL ANATOMY AND THE ELECTRODE TISSUE INTERFACE

2.1 Introduction

This chapter introduces the biology of the nervous system in order to understand a neural recording device. Neural devices are made to record from and stimulate neurons or populations of nervous tissue and so the biology of these is introduced first. It is desirable to model the signal propagation in simple terms via fundamental physics, this leads to the Nernst and Goldman equations, and ultimately to the Hodgkin-Huxley model of cell membranes. All of the information presented here is available in standard textbooks on the subject and has been compiled for this chapter from [14, 15], unless otherwise stated. Much of the style of the section on the membrane model is based on Struijk's introduction found in [14].

2.2 The Nervous System

Excitable tissue forms networks in the body that control motion, sensation, regulation, thought and emotion to enables us to perceive and interact with our environment. The mechanism that controls these bodily functions is called the nervous system and is made of nerve cells, labelled as neurons, that control function and 'communicate' via electrical signals. The nervous system has three main functions in the human body; The first is to communicate information from external and internal stimuli that is sensed, which is labelled as 'sensory' activity. Secondly, the information is interpreted and an appropriate response to the stimuli is determined, a function that is labelled as 'integration.' And thirdly, the nervous system causes the body to respond, which can be labelled as 'motor' output. The central nervous system takes in the input from the world, interprets the information and actuates a response, as is illustrated in Figure 2.1.

The nervous system is organised into the central nervous system (CNS), that consists of the brain and the spinal cord, and the peripheral nervous system (PNS) that incorporates everything

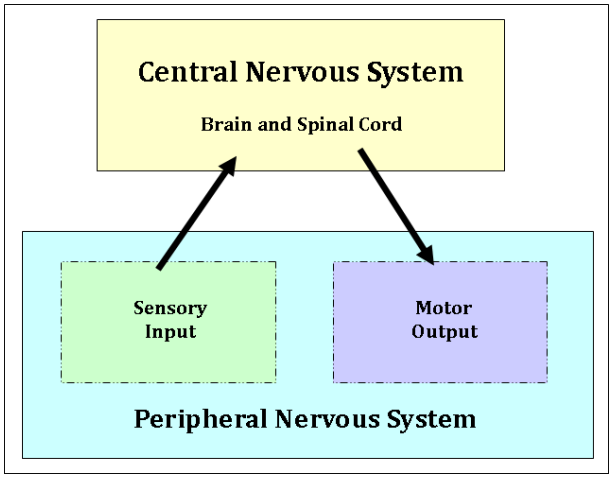

Fig. 2.1: Outline of the processes in the nervous system; The central nervous system processes sensory information and controls motor feedback responses. The peripheral nervous system translates the sensory information to the central nervous system and motor feedback to the appropriate muscle points.

[15]

else and extends into the muscles, the skin, the heart and the glands. Input signals (afferent) from the PNS to the CNS are processed and interpreted by highly organized architectures of neurons. The output signal (efferent) is transmitted along motor fibers to either, control effector organs, order glands to secrete or to contract muscles. Some movement of the human body is voluntary, such as moving your legs to walk, whereas some is involuntary (autonomic), such as the beating of the heart. Any technology that is designed to interface to a voluntary action may be influencing involuntary processes, so care is required. On the other hand, designing an electrode that works for one specific nerve is not necessary and there is a significant crossover between the applications that a neural interface may provide. The nerve fibers consist of neurons and support cells that are called neuroglia or glial cells. Neurons are the nerve cells that transmit the sensory input and the motor output between the CNS and the receptors or targeted muscle and the neuroglia provides the mechanical structure, physiological support and protect the neuron. The neuroglia can also wrap tightly around the neuron to form the myelin sheath.

2.2.1 Basic Neurophysiology

Neurons

The neurons are the basic building blocks for the complex functions of the nervous system. Each neuron can have direct contacts to over 1000 other neurons and their activity is highly organized

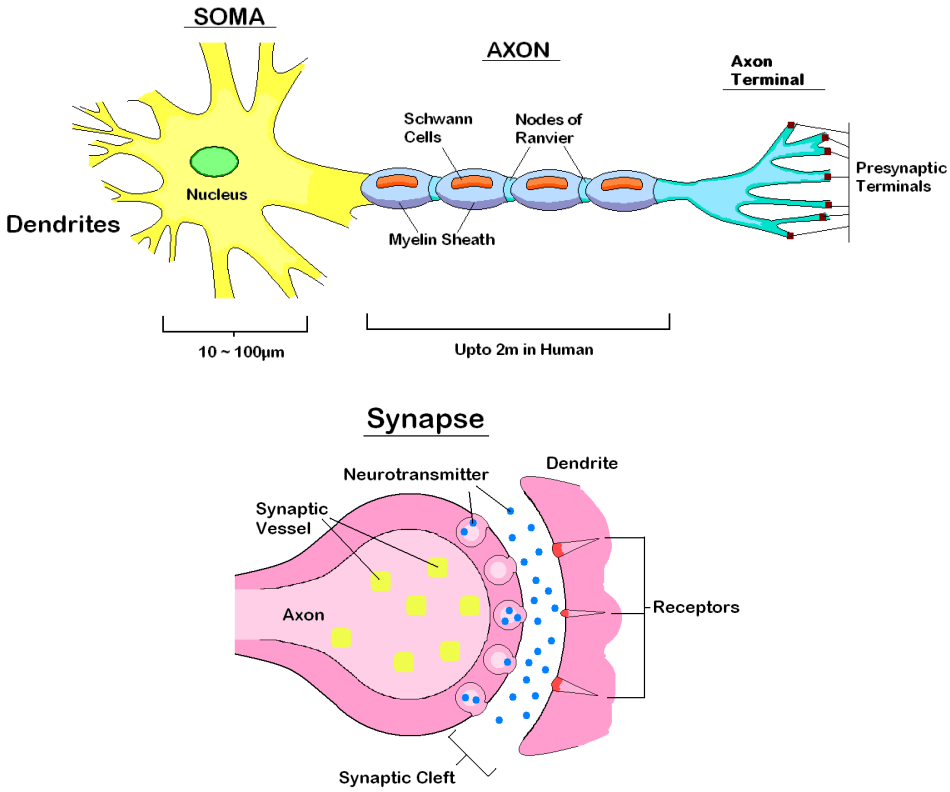

Fig. 2.2: Top: Illustration of the Neuron that contains the Soma, the Axons and the extending Dendrites. Bottom: Illustration of the synapse between two neurons.

and highly perceptive. A single neuron is illustrated in Figure 2.2. The neuron consists of a cell body (the *soma*) that contains the DNA for the cell, the proteins that maintain the cell and the neurotransmitters. Synaptic input and output of the neuron is transported through two types of extension from the soma that are called the *dendrites* and the *axon* respectively. Each neuron can have many dendrites that receive electrical inputs from other cells and relay the signal to the cell body. All neurons are limited to only one axon; a long, relatively thick fiber that extends from the cell body to carry electrical signals. At the ends of axon are the axon terminals that branch into the pre-synaptic terminals, the functions of these endings is to transmit the relayed signal to other neurons and cells via neurotransmitters that are released by electrical stimulation.

Signals are propagated between neurons via action potentials that derive from the physiology of the cell membrane, to be discussed later. Neurons connect to each other via synapses that are formed of the axon terminal, the dendrite of a neighbouring cell, and the accompanying glia. Between these components is the synaptic cleft, as in Figure.2.2. Axons can be wrapped by protective neuroglia (labelled as Schwann cells) to form the myelin sheath. Each myeli-

nated axon has many Schwann cells along its total length with gaps between the Scwhann cells that are called the nodes of Ranvier. The characteristics of the myelin sheath and the nodes of Ranvier allow for the propagation of electric signal along the fiber via saltatory conduction.

Bundles of axons in the peripheral system are called nerves and with the cell body in the spinal cord and the axon extending out to the fingers they can reach a significant length of $\approx$ 1m. Axons are grouped together into bundles called fascicles, encapsulated by the perineurium. The fascicles are not organised by any particular function and the axons are grouped in terms of their destination, over any other factor. In between the fascicles is the epineurium that provides mechanical durability and protection. Like all living tissue the PNS requires a constant blood supply to support its physiology, which is supplied by blood vessels that travel along the length of the fascicles. An illustration of the peripheral nerve is shown in Figure 2.3.

In the PNS the myelinated and unmyelinated axons conduct the nerve signal by different mechanisms. Whereas the unmyelinated axon is similar to a cable, the myelinated axon transports the signal via saltatory conduction. Unlike the brain the PNS is not protected by a layer of bone and it can be damaged by mechanical trauma. However, after it has become damaged the PNS has an ability to regenerate. After the peripheral nerve has been cut or crushed, it will enter a process called 'Wallerian degeneration/regeneration', where the axons that are separated from the neurons cell body will degenerate and the proximal part, still connected to the cell body, regenerates. This process generally starts after 24-36 hours post injury, and is characterised by the axonal skeleton disappearing followed by a breakdown of the axon membrane. Finally, for

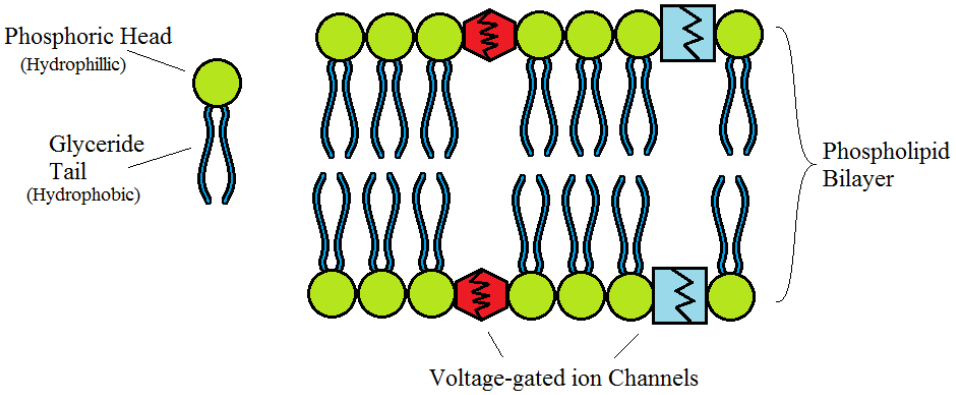

Fig. 2.4: Illustration of phospholipid bilayer, including ion channels for sodium and potassium [15]

myelinated axons, the sheath begins to break down and the resulting cellular debris is cleared up by macrophages. The degeneration will occur as far as the next node of Ranvier and, importantly, the degenerated nerve leaves behind hollow tubes that can guide any regeneration from the proximal nerve. Once inside the tube, growth factors encourage the regeneration and the proximal part can advance by around 1mm per day[17].

Cell Membrane

All excitable cells have common features that allow for a general description of their behaviour, the most prominent of which is the cell membrane. A neuron is able to transmit electrical signals due to the fact that its membrane is excitable and electrophysiology of neurons is the study of phenomena that result from ion movements across the membrane.

The membrane is formed of a bilayer of phospholipid molecules that is made of a phosphoric head (hydrophilic) and a glyceride tail (hydrophobic). The polarising nature of the phospholipids causes them to assemble into a bi-layer configuration, shown in Figure 2.4. In the cell membrane there are also ion channels that allow the transport of sodium, potassium and chlorine ions across the membrane. The ion channels are formed by ion-selective proteins, the permeability of which is controlled by the potential difference across the membrane. The combination of the bilayer with the voltage gated ion channels acts to maintain differential ion concentrations on the inside and the outside of the cell. The sum of these gradients is the voltage across the membrane and is called the trans-membrane potential, V_m and is defined as the difference in the potential of the inner surface of the membrane (φ_i) and the potential on the outer surface (φ_e),

such that $V_m = \varphi_i - \varphi_e$.

For humans, the trans-membrane potential has a resting value of around -65mV and the cell membrane maintains this by controlling the concentration gradients of the ion species between the extracellular and intracellular media: at rest there is more sodium outside the cell, and more potassium inside the cell. During an excitation the trans-membrane potential changes and, if the membrane potential reaches a threshold, an ion-pump acts to pump more sodium into the cell causing the intracellular medium to become more positive. This effect at the membrane is called the depolarization phase of the action potential. The pump will then return the cell to its resting potential by pumping out potassium. The rising and falling potential of the membrane represents a nerve pulse and is called an action potential. After the pulse, the cell enters the refractory period until the ions are returned to their original concentration, during which, the cell cannot fire again and so becomes insensitive to stimulation. An action potential is conducted along the membrane as a local membrane pulse where intracellular and extracellular currents perturb the potential of the membrane neighbouring the active regions, causing the signal to propagate. This will be discussed further later in this chapter.

2.3 To Model the Nerve

The simplest way to understand an excitable cell is to consider a closed volume of diffuse charged molecules, separated from a media of solvated ions by the cell membrane. The two driving forces that control the transfer of ions between the two media are diffusion, from the concentration gradient of ions, and migration as a result the electric field. For a net zero current these two driving phenomena must result in an active transport of ions through the membrane. A brief explanation of these phenomena for a single ion species, κ, is presented in the following section.

Ions move in response to a concentration gradient, where they will move from a region with a higher concentration of ions to a region of a lower concentration. This has been characterised through Fick's law, which describes the flux of ions for a particular concentration gradient($\vec{j}_{\text{diff},\kappa}$). Similarly, due to their charge ions will move in response to a potential gradient and there is an expression to describe the flux of ions driven by an electric field (potential

gradient)($\vec{j}_{\text{migr},\kappa}$).

$$\vec{j}_{\text{diff},\kappa} = -D_\kappa \nabla C_\kappa \tag{2.1}$$

$$\vec{j}_{\text{migr},\kappa} = -\mu_\kappa \frac{z_\kappa}{|z_\kappa|} C_\kappa \nabla \varphi \tag{2.2}$$

Where $\vec{j}_{\text{diff},\kappa}$ and $\vec{j}_{\text{migr},\kappa}$ is the number of κ ions that pass through a unit area of membrane per unit time (mole/m^{2}s) for both diffusion and migration respectively. For diffusion the expression is driven by the gradient of the concentration of κ ions is ∇C_κ (mole/m^3) and multiplied by Fick's constant, D_κ, which depends on the size of the ion and the viscosity of the solvent. For migration, the flux is driven by the electric field, $-\nabla\varphi$, and multiplied by mobility of the ions, μ_κ, the concentration and the sign of the charge of the κ ion, $z_\kappa/|z_\kappa|$, where z_κ is the valence of the κ ion. The expression requires that positive ions move from a higher to a lower potential as convention would suggest.

In 1905, Einstein showed that Fick's constant and the mobility of the ions species are proportional to each other, by

$$D_\kappa = \left(\frac{RT}{|z_\kappa|F}\right)\mu_\kappa \tag{2.3}$$

where R is the gas constant, F is Faraday's constant and T is the temperature in Kelvins.

2.3.1 Nernst Equation

From Einstein's proportionality, it possible to arrive at the Nernst equation by writing the total flux for the ion species caused by both diffusion and migration as;

$$\vec{j}_\kappa = \vec{j}_{\text{diff},\kappa} + \vec{j}_{\text{migr},\kappa} \tag{2.4}$$

$$= -D_\kappa \left(\nabla C_\kappa + \frac{F z_\kappa C_\kappa}{RT} \nabla \varphi\right) \tag{2.5}$$

And an expression for the current density from the flux density can be written as,

$$\vec{J}_\kappa = \vec{j}_\kappa F z_\kappa \tag{2.6}$$

where Fz_κ is the charge carried per mole of ions. To simplify the model the motion of the ions is restricted to the transverse direction only, where the flux of ions only occurs normal to membrane surface. The transverse direction is labelled as the x-direction. Thus, the Nernst equation becomes;

$$\vec{j}_\kappa(x) = -D_\kappa\left(\frac{d}{dx}C_\kappa(x) + \frac{Fz_\kappa C_\kappa}{RT}\frac{d}{dx}\varphi(x)\right) \tag{2.7}$$

For each ion species in the media there is a separate Nernst equation, however, all the ion species are influenced by the same potential $\varphi(x)$. This model ensures that there is no net flux of ions across the membrane; the concentration gradient is minimised due to diffusion of an ion from high to low concentration, whereas the trans-membrane potential will change in response to the migration of ions. However, like charges repel so the change in potential will act to force migration in the opposite direction of the diffusion. An equilibrium is reached when there is no net ion flux across the membrane which, for potassium ions for example, can be written as $\vec{j}_{K^+}(x) = 0$, and so;

$$\frac{d}{dx}[K^+](x) = -\frac{Fz_{K^+}[K^+](x)}{RT}\frac{d}{dx}\varphi(x) \tag{2.8}$$

The relationship between the trans-membrane potential and the concentration of potassium ions inside and outside the cell is the Nernst Equation for potassium, written as;

$$V_{K^+} = \varphi_i - \varphi_e \tag{2.9}$$

$$= \frac{RT}{Fz_{K^+}} ln\left[\frac{[K^+]_{\text{Ext}}}{[K^+]_{\text{Int}}}\right] \tag{2.10}$$

For biological tissue it is also necessary to consider the Nernst equations for Sodium (Na^+) ions and Chloride (Cl^-) ions, which can be written as;

$$V_{Na^+} = \frac{RT}{Fz_{Na^+}} ln \left[\frac{[Na^+]_{\text{Ext}}}{[Na^+]_{\text{Int}}} \right] \tag{2.11}$$

$$V_{Cl^-} = \frac{RT}{Fz_{Cl^-}} ln \left[\frac{[Cl^-]_{\text{Int}}}{[Cl^-]_{\text{Ext}}} \right] \tag{2.12}$$

2.3.2 Goldman Equation

If there are no fixed charges in the membrane and the influence of external surface charges is negligible the electric field, E_x generated by the diffusion of ions is constant across the membrane. If the electric field is constant, then it can be stated that the trans-membrane potential must vary linearly across the membrane, this is known as 'Goldman's Assumption'.

$$E_x = -\frac{d}{dx}\varphi(x) = -\frac{V_m}{h} \tag{2.13}$$

Where V_m is the trans-membrane potential and the h is the thickness of the membrane in the x-direction. Substituting the expression for the change in potential across the membrane into the Nernst Equation gives;

$$V_m = \frac{RT}{F} ln \left[\frac{P_K[K^+]_{\text{Ext}} + P_{Na}[Na^+]_{\text{Ext}} + P_{Cl}[Cl^-]_{\text{Int}}}{P_K[K^+]_{\text{Int}} + P_{Na}[Na^+]_{\text{Int}} + P_{Cl}[Cl^-]_{\text{Ext}}} \right] \tag{2.14}$$

Where P_K, P_{Na} and P_{Cl} are the permeability's of potassium, sodium and chlorine respectively. The 'Goldman' model for the trans-membrane potential completes the model by assuming that the total flux of all ions are zero, $\vec{j}_K(x) + \vec{j}_{Na}(x) + \vec{j}_{Cl}(x) = 0$. This is only applicable when the behaviour of the membrane is relatively static, where at rest the permeability of potassium is higher than that of sodium and chloride, ie. $P_K \gg P_{Na}$ and P_{Cl}. As a result, the trans-membrane potential tends towards the Nernst-potential for potassium. An action potential is a non-static case as a net current is flowing into and out of the cell, thus the Goldman Equation is not valid. At the peak of the action potential the net flow is minimised again, briefly, and the trans-membrane potential is approximately equal to the Nernst-potential for Sodium as $P_{Na} \gg P_K$.

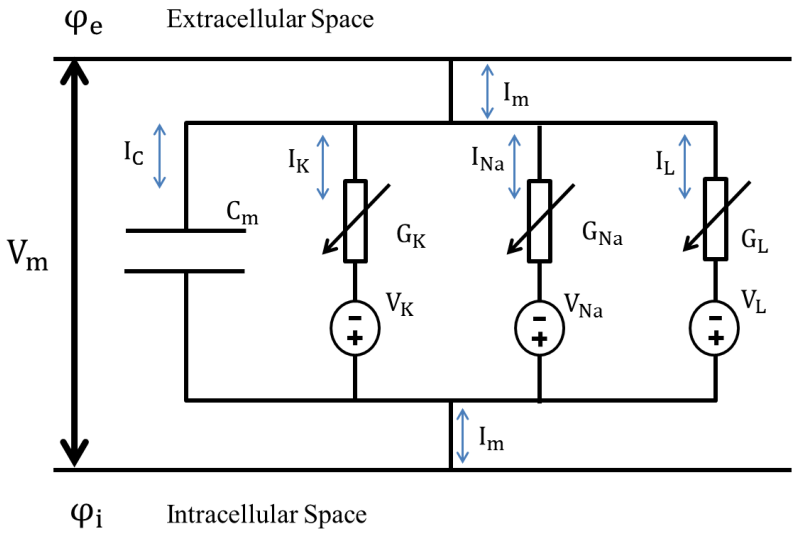

Fig. 2.5: Equivalent circuit model for a patch of membrane based on the Hodgkin-Huxley model [18]

2.3.3 Hodgkin-Huxley Model

To model the dynamic capabilities of the cell the behaviour of the ion membranes was investigated by A.L. Hodgkin and A.F. Huxley (H-H) in 1952. Their seminal experiments used a voltage clamp, where a step current is applied to force the membrane to adopt a constant voltage, to control the trans-membrane voltage externally. They selectively observed the corresponding ion flow at the fixed potential by chemically blocking (deactivating) the different ion-pumps in turn. Importantly, this model does not attempt to describe the membrane processes as whole, but provides a set of equations that can inform theoretical calculations of action potentials.

The work culminates in a model that describes separate ion-conducting branches called the parallel conductance model, where the four branches represent sodium, potassium, leakage current and a capacitive current from the separation of the charge carriers by the membrane. This is illustrated in Figure 2.5. The conductance of each branch is from the permeability of the membrane to each ion species;

$$G_{Na} = \frac{I_{Na}}{V_m - V_{Na}} \tag{2.15}$$

$$G_K = \frac{I_K}{V_m - V_K} \tag{2.16}$$

$$G_L = \frac{I_L}{V_m - V_L} \tag{2.17}$$

where the potential for each branch is the equivalent Nernst potential. For this illustration all currents and conductances are per unit area, as only a small patch of the membrane is being discussed. For this model, the total membrane current is the sum of the branch currents,

$$i_m = C_m \frac{dV_m}{dt} + (V_m - V_{Na})G_{Na} + (V_m - V_K)G_K + (V_m - V_L)G_L \tag{2.18}$$

To find the total membrane current Huxley and Hodgkin proposed a system of ion specific propagating charged particles that can pass through the membrane, but are not directly transporting the ions. Instead, they allow the permeability of each ion by arranging themselves into a specific configuration in the membrane, the rate of movement of these particles then directly effects the conductance of the ion species. This provides a method of gating the channels, where the probability of finding the transport particles in a certain configuration determines how open the ion-channel is for each species. As the transport particles are charged their motion is dependent on the electric field.

Using this methodology, H-H showed that for potassium the conductance varied according to a fourth-power relationship that changed with first-order kinetics. To model this, they chose a charged transport particle that controls the gating of the potassium channel, either open, closed or somewhere in between. This relationship of the potassium gate suggests that four transport particles need to be configured correctly (in the open state) to allow for propagation. The permeability of each species is independent, suggesting that the probability of the potassium ion channel being open as n^4, where n is the probability of finding the particle in the open state and $0 \leq n \leq 1$. Thus, the potassium conductance per unit area is the maximum possible conductance, for the state when all channels are open, scaled by the number of channels that are actually open.

$$G_K = G_{K,\max} \cdot n^4 \tag{2.19}$$

For sodium, H-H found that the rate conductivity change is best modelled by two transport particles, one activating particle that has activating probability of m (in the open state) and one inhibiting particle that has a probability of being in the non-activating (not inhibiting) state of h. Both particles follow first order kinetics. H-H suggested that the ion-channel was open

when three activating transport particles where in the correct configuration combined with one non-activating particle. This gives a sodium conductance of,

$$G_{Na} = G_{Na,\max} \cdot m^3 h \tag{2.20}$$

These gating particles have voltage and time dependent transfer rates that obey first order kinetics.

2.3.4 The Nerve Pulse

The voltage dependent gating particles allows for the generation of nerve pulses. At rest there is approximately 10 times more sodium ions in the extracellular space compared to inside the axon, whereas the concentration of the potassium ions is approximately 30 times higher in the intracellular space. H-H found that a depolarizing stimulus (that raises V_m from the resting potential) results in an exponential rise in m and a slower exponential decay in h. This behaviour initially increases the conductance of the sodium ion channel, allowing sodium to enter the cell (driven by V_m-V_{Na}) until the sodium conductance is reduced and eventually stopped by the decaying h.

Similarly, a depolarizing stimuli also increases potassium conductance via n, allowing potassium ions to flow from inside to outside the cell resulting in a trans-membrane current that is in the opposite direction to the Na ions. However, the potassium conductance increases over a much longer time period than the sodium conductance, so initially the sodium branch will dominate.

Eventually the decrease in sodium conductance and increase in potassium conductance causes the membrane potential to peak and begin to fall towards the resting value. Once the nerve pulse has been generated it propagates along the axon, which requires an axial component of the trans-membrane current, i_m.

The propagation of the Nerve Pulse

The nerve pulse propagates along the nerve via a local circuit current that arises from the activity of the cell membrane. For an unmyelinated axon, if a patch of membrane is stimulated beyond the excitation threshold (the patch is depolarized) then the membrane follows the H-H

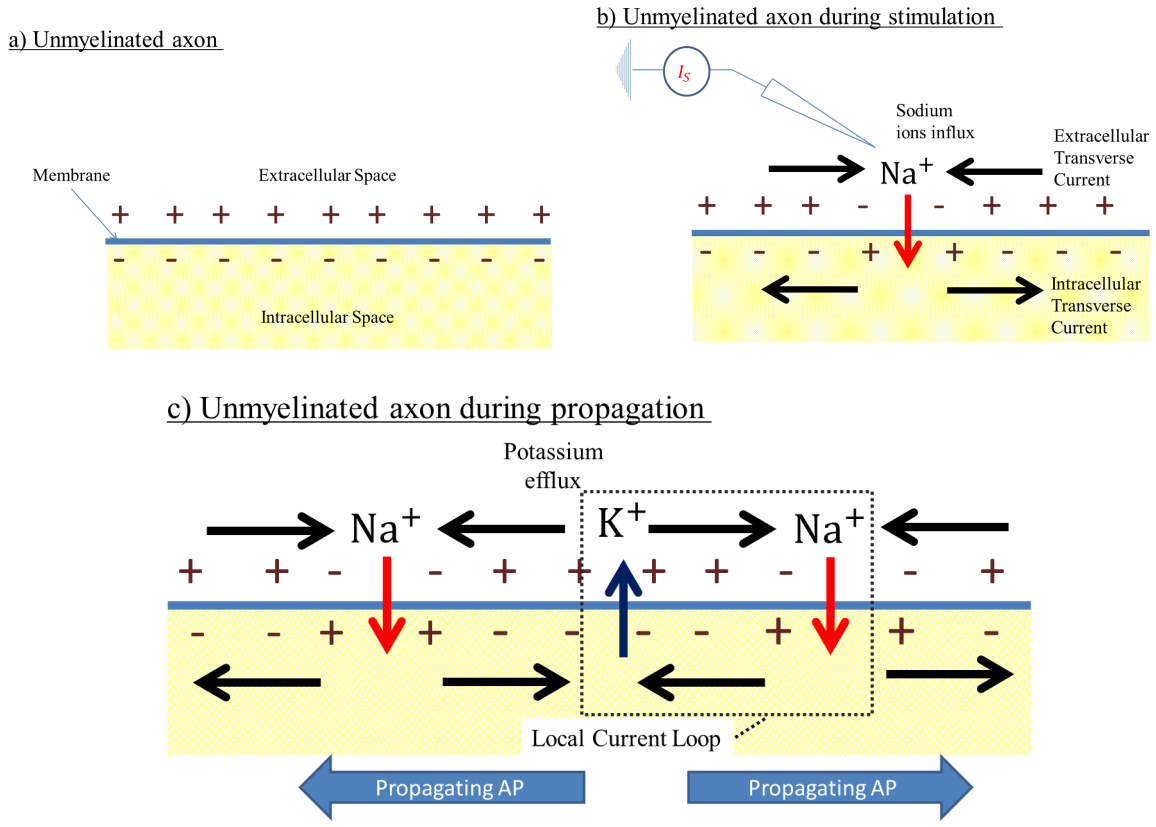

Fig. 2.6: Diagram to show how the local current loop develops for an unmyelinated axon. a) An axon at rest. b) An axon during stimulation, the red arrow represents the sodium influx. c) The propagation of the nerve pulse as the local circuit current.

model outlined above. Initially, there is an influx of sodium ions into the intracellular space that causes a dominant trans-membrane current into the axon. Once inside the axon the sodium ions move along their concentration gradient, diffusing into the neighbouring regions that have a lower concentration of sodium ions. This causes a transverse current, both proximal and distal to the stimulation, in the intracellular space. Similarly, in the extracellular space, sodium diffuses into the region of lower concentration where the cell membrane is open. There is also an extracellular transverse current in the opposite direction to the internal current from the movement of ions responding to the depolarizing wave. After a few milliseconds, at the peak of trans-membrane voltage in the excited region, the efflux of potassium ions dominates the sodium current and the membrane begins to repolarise. This process is depicted in Figure 2.6. The transverse current from the diffusion of sodium ions depolarizes the regions of membrane that neighbour the excited patch. During an action potential the neighbouring regions are depolarized beyond their threshold and the nerve pulse is generated again. This mechanism is

repeated along the membrane and the nerve pulse propagates along the axon unattenuated. Incorporating the H-H model this can be depicted as shown in Figure 2.7. The resistance per unit length of the inside and outside of the axon are R_i and R_e respectively, and the inner and outer surfaces are connected by the H-H model representing the voltage-dependent behaviour. For the myelinated axon the mechanism of propagation is the same, except that the voltage-gated ion channels are densely packed at the Nodes of Ranvier and there is no ion transfer through the membrane in the inter-nodal spacing. Thus the membrane can only be excited at the nodes and the local circuit current only flows through the membrane in the nodal regions. The transverse current propagates between the nodes in the same manner as before, where the ions follow their concentration gradients via diffusion. The equivalent diagram for the myelinated axon is shown in Figure 2.7.

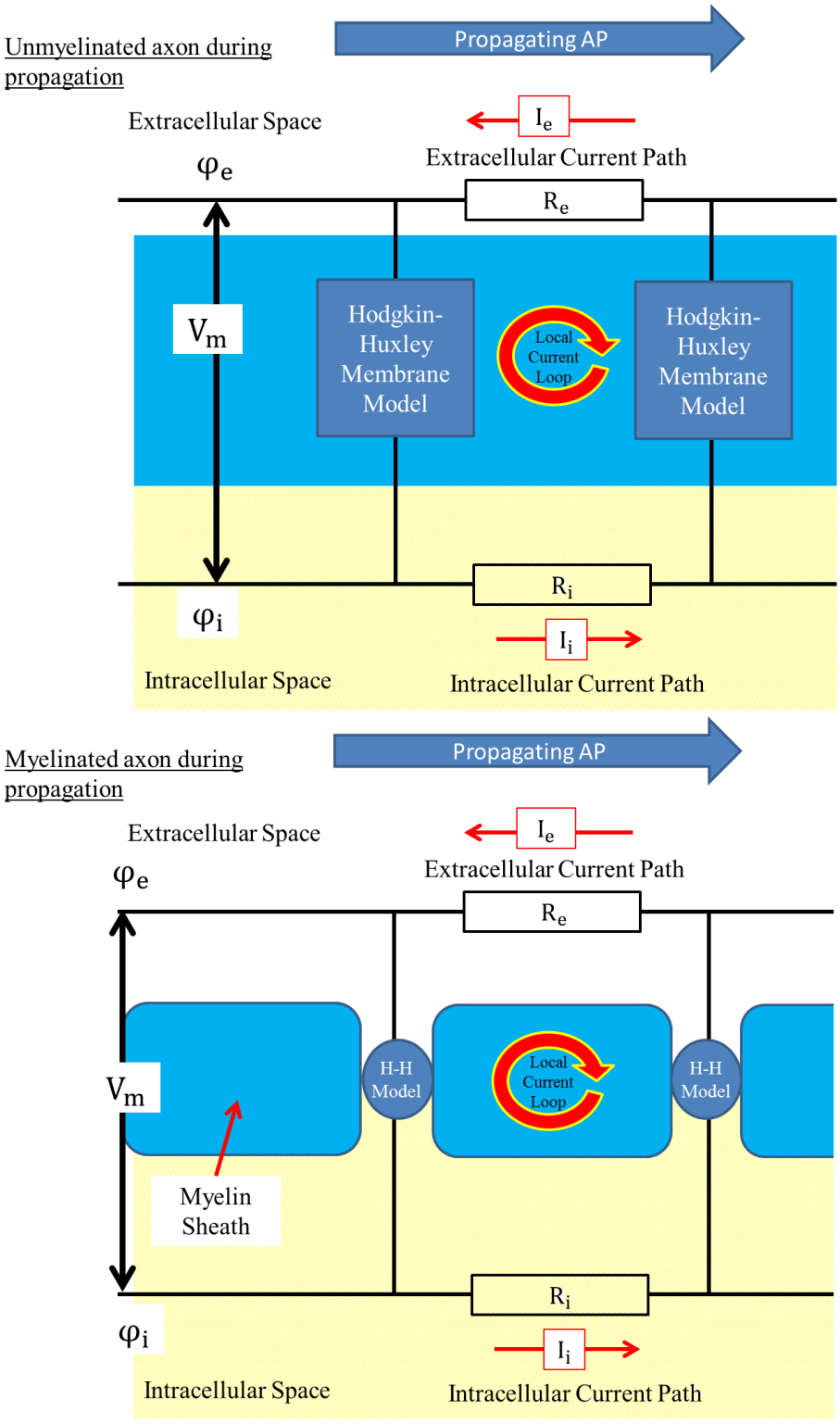

Fig. 2.7: Diagrams to show the circuit current loop for a propagating action potential of an unmyelinated axon (top) and a myelinated axon (bottom)

3. METHODS OF RECORDING ELECTRICAL SIGNALS FROM NEURAL TISSUE

This chapter will introduce the conventional technology that is used to record electrical activity from nerves, with specific interest for motor prostheses. Significant scientific investment has led to the ability to record biological events using metal electrodes and a few examples of these neural interfaces will be discussed. Firstly a brief description is given of the physics of the interface between the electrode and the biological medium. Secondly, the technology that has been implemented for PNS recording interfaces will be introduced. Specific consideration is given to cuff electrodes that offer advantages in terms of the amplitude of signals recorded, and regenerative implants that are similar to the technology researched in this thesis. All information presented here is compiled from four comprehensive texts on neural recording; These include the review of technology developed to record from the PNS by Navarro et al [19] and the review of PNS recording in general from [14], whereas the theory of the electrode interface is from Kovacs[20] and Fischer[21]. As such, much of the style is borrowed from these works as well as from [22].

3.1 Introduction

Traditionally, applications that require a high selectivity have usually been restricted to *in-vitro* applications using cultured cells. Intracellular recording of the trans-membrane potential can be made by inserting a micro-pipette through the cell membrane or alternatively a micro-pipette can be brought into contact with the cell membrane to record the trans-membrane potential, without compromising the internal structure of the cell. This requires a significant human interaction over long periods of time, significantly reducing the practicality and durability, especially for an in-vivo device.

To improve the practicality, significant scientific investment has been made to develop ways

of recording extracellular potentials with microfabricated electrodes. Via established microfabrication techniques it is possible to 'pattern' mechanical structures and deposit thin-film metal tracks and electrodes onto glass, polymer and other carrier materials to create devices to interface with neural tissue. Advances in microfabrication technology have allowed for devices that have decreased electrode size, increased amount of electrodes per unit area and the range of available materials.

3.1.1 Material used to Fabricate Neural Interfaces

The microfabricated electrical interfaces are generally made to a sandwich-type design where a layer of conductive material is mechanically supported and electrically insulated by a construction of substrate materials. There have been a huge variety in the configurations, but in general the carrier substrate has either been a silicon-based material, glass or a polymer, and the conductive material has been a metal deposited onto the carrier.

Each material is carefully chosen to match the requirement of the application; when signal processing is necessary at the interface electronic circuitry may have to be integrated into the design of the device and a silicon-based material will be preferable. This is necessary to allow for a monolithic fabrication process that incorporates the electronic components. However, for a long-term application it is more desirable to have a highly flexible and durable carrier material and in these applications the polymer generally forms the insulating medium as well as providing the mechanical structure.

Silicon and flexible polymers such as polyimide are the materials of choice for CNS and PNS implants respectively, as the dimensions of these materials can be precisely determined through a process of micro-machining, photo-lithography or etching. These concepts will be introduced in chapter five. This allows for the precise control over the size of the active sites and there position relative to each other. In general silicon has found most use for CNS probe type implants as it can be implanted into the cortex, however the brittleness of these probes make them less suitable for the PNS implantation through muscle or delicate, fibrous nerves.

Polyimide has gathered popularity as it offers a highly flexible and biocompatible substrate material, as well as being compatible with clean-room technologies. For microelectronics, polyimide has been mainly used as a passivation layer or as a dielectric between two layers, for ex-

ample in multi-chip modules, where successive layers can be spin coated relatively easily [23].

More recently photosensitive polyimides (PSPI) have reduced complex multi-step processing by allowing the definition of planar structures via photolithography. This gives access to large range of implant designs, with a less involved fabrication process. These microfabrication techniques and the use of polyimide as a substrate for neural interfaces will be discussed at length during this thesis.

Biocompatibilty

Although the engineering motivation is to record/stimulate biological activity in the tissue, the motivation of the body is to protect itself. To have a sustainable and durable interface the two competing motivations need to be optimised and so the biocompatibilty of the materials is a major factor to consider. The materials discussed above have generally been shown to be biocompatible such that they are not toxic or otherwise damaging to biological function. More recently, many materials used in neural prosthetics have been developed specifically to be biocompatible, and all material used in this endeavour have been summarised in ISO 10993.

In general, a material can be categorized in terms of both structural biocompatibilty and surface biocompatibilty [24]. To achieve structural biocompatibilty the devices material properties should mimic the properties of the biological environment that is being targeted. The surface biocompatibilty relates to the chemical/physical/biological/morphological properties that contact the biological environment directly, which of course should not be toxic or at least only release low-concentrations of toxic materials that do not induce the foreign body response. A mild inflammation is generally considered to be acceptable, but a strong foreign body response can lead to an encapsulation of the device in fibrous tissue that can ultimately lead to device failure. This is of greater concern for chronic implants, that have to provide stable and durable transducer properties throughout the lifetime of the implant. As such there is a degree to which a material needs to be biocompatible before it becomes suitable; for an acute study the biocompatibilty becomes less important than for a chronic implantation where a more diligent approach is necessary.

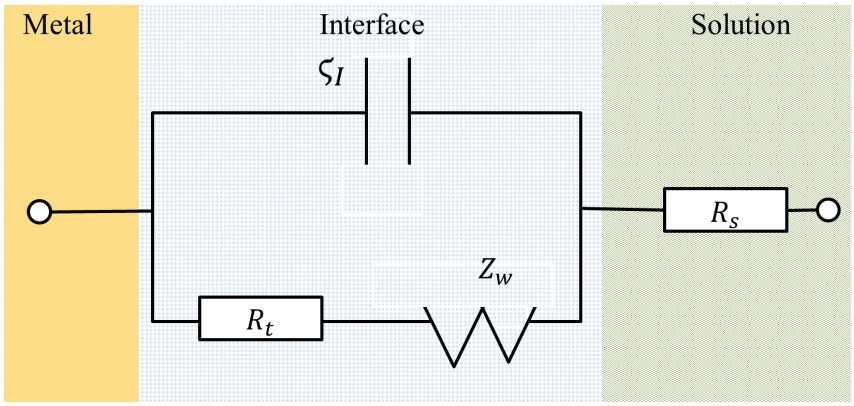

Fig. 3.1: Equivalent circuit model of electrode tissue interface including the interfacial capacitance, ς_I, the charge transfer resistance, R_t, the Warburg impedance Z_w and the solution resistance R_s. [18]

Use of Metal Electrodes

Nervous tissue conducts signals via an ionic transport mechanism, where ionic charge carriers move through the membrane from the electrolytes that surround the axon. Recording devices are however based on an electron conduction mechanism, as they are made of a conducting material such as metal. To record electrical activity in the tissue the signal has to interface between the metal electrode and the ionic electrolyte solution.

The interface can be simplified using an equivalent circuit model illustrated in Figure 3.1. The parallel branches of the circuit can be used to model phenomena at the interface including the interfacial capacitance (top branch) and the path of direct charge transfer (bottom) which is the transfer resistance and the Warburg impedance combined. The parallel branches are connected in series to the solution resistance.

Each of these phenomena will be briefly introduced here and a more thorough examination of the electrode interface is presented in Chapter eight of the thesis.

For a typical interface there is a capacitance between the metal and the electrode that can be described via the double layer theory. The capacitance arises due to an electrochemical difference between the metal and the ions in the solution and was first modelled using a hydration sheath that acts as a simple dielectric between the electrode and the solution. Models of this interfacial capacitance, ς_I, describe a linear potential drop between the electrode and a plane of water molecules at the electrode surface, followed by an exponential decay of potential out into the bulk solution.

The capacitance at the interface does not describe the entire electrochemical phenomena. If a DC potential is applied across the interface for neural stimulation an ohmic current may flow that is the net movement of charge from metal into the solution (or vice versa) which results in a shift of the potential of the electrode from the equilibrium. The resistance of this ohmic interfacial current is the charge transfer resistance, R_t.

The DC behaviour of the electrode is more relevant to stimulating electrodes: it is important to have stimulus current thresholds that do not adversely alter the chemical composition of the interface in a non-reversible way. If the stimulus current is small with regards to the exchange current density of the metal, J_0 then the electrode will not shift significantly from the equilibrium and will behave linearly. If the electrode has a very high exchange current density ($J_0 \rightarrow \infty$) the charge transfer resistance tends towards zero and even though a current is flowing across the interface no significant overpotential is being developed. This is labelled as a non-polarizable interface and can be considered to be the optimum material for neural stimulation as any potential across two non-polarizable electrodes in solution would vary the potential across the bulk of the medium rather than be localized at the interfaces. For the opposite conditions ($J_0 \rightarrow 0$) the interface behaves as a capacitor, where no current flows in the steady-state DC conditions, which is labelled as the ideally polarizable interface. In practice no interface is either ideally polarizable or unpolarizable and the important property to consider for any interface is the magnitude of the resulting current relative to exchange current density.

For most electrode/electrolyte interfaces the charge transfer resistance dominates the ohmic part of the electrode behaviour. If the charge transfer resistance is low the diffusion of reactants to the interface has a noticeable effect. However, for time-varying signals with higher frequencies it becomes more difficult for ions to follow the time-varying field, which dampens the effect of the spatial variation so that it reaches far less into the solution. For an ever increasing frequency the ions are not able to follow the field at all which leads to no diffusional impedance. In 1899, Warburg proposed a model for this frequency dependent diffusional impedance Z_W, which follows the frequency power law

$$|Z_W| \propto \frac{1}{\sqrt{f}} \tag{3.1}$$

where f is the excitation frequency.

As the current spreads out into the solution it also experiences a solution resistance, R_S that depends on the shape of the electrode and the conductivity of the solution. The conductivity is determined by the number of ions present and the temperature of the solution.

The recording electrodes are usually made from a thin-film metal such as gold, platinum, platinum-iridium, tungsten, and tantalum [25]. Gold was chosen for the neural interfaces that were fabricated in this thesis, as it has well known biocompatibility, does not form a surface oxide and has been used in many chronic recording interfaces. Furthermore, gold is ductile and flexible properties when used as a thin-film, which is advantageous for use in flexible electronics [26]. This flexibility is critical to the technology developed in this thesis. The behaviour of gold as a recording electrode will be discussed in detail in Chapter eight, which will be used to assess the quality of the fabrication processes developed in the thesis.

3.2 Neural Interface Technology

Having developed the basic theory of electrodes used for neural applications, some examples of interfaces that have been developed will now be outlined, starting with in-vitro devices. This thesis is intended to focus on recording from nervous tissue in-vivo and so the following sections are kept brief but are added to give a general picture of the development of neural recording interfaces.

3.2.1 In-Vitro Devices

In 1972, Thomas described the first extracellular recording of electrically active biological tissue cultured in-vitro. Since then, the use of multi-electrode arrays (MEA) to record extracellular activity has flourished, with practical applications in heart cells, spinal cord tissue, hippocampal slice cultures, cortical and retinal cells. The first MEAs were embedded micro-electrodes mechanically supported by a biocompatible carrier substrate. Electrode sites were typically arranged in an $m \star n$ matrix over a relatively large surface area, such that slices of biological tissue could be placed and recorded from on top of the substrate. These planar micro-electrodes generally consisted of a substrate of glass, silicon or polymer over which a metal conductor was deposited and patterned. Electrode sites were defined by the photolithographic patterning

Fig. 3.2: Micro-fabricated electrode arrays developed by Thomas et al for *in-vitro* recording [22]

of a passivation layer on top of the deposited metal conductor, an example of which is shown in Figure 3.2. Cells were cultured directly onto the array and contact the exposed electrode sites to allow for extracellular recording. Each electrode site was generally connected to a high-impedance, low-noise amplifier to enhance the recording of the small extracellular potentials.

Given a continual supply of nutrition, such a set up allowed for studies on toxicological and pharmacological agents on neurons as well as the general study of neural regeneration. These interfaces are not suitable for in-vivo recording, as they lack the flexibility and durability required. A whole range of interfaces have been created subsequently based on this earlier in-vitro work.

3.2.2 Interfacing to the CNS

To record activity of neural tissue in-vivo the type of devices that have been developed vary depending on the application and so it is necessary separate interfaces for the CNS and PNS respectively.

In extreme cases of neural degeneration caused by disease or loss of neural function through traumatic injury, a patient may have very little or no control of their skeletal muscles and require significant technology to regain any independence. In many cases the motor control structures of the brain are largely intact and can provide a rich source of relevant command signals that could be reinterpreted to provide new function via external devices. This is called a brain-computer interface (BCI).

Although signals can be recorded on the surface of the skull via Electroencephalography (EEG), or intracranially via Electrocorticography (ECoG), this generally only provides infor-

Fig. 3.3: Probe type micro-electrodes
[22]

mation about the relative activity of different regions of the brain and does not provide the required level of selectivity that a device recording directly from the motor cortex could offer. The design constraints of BCI require that the signals used contain specific information and convey it in a reliable fashion, which requires the need for penetrating electrodes that can operate with a long-term stability deep inside the brain tissue.

In general, two types of device have been designed to create this kind of interface; 'shaft-like' linear multi-electrodes and arrays of multiple electrodes that have many smaller probes each with an active site on the tip. The linear micro-electrodes are tissue-insertable and are often called 'probes'. They are typically several millimetres long, tens of micrometers wide and a few micrometers thick. On the shaft of the device is a one-dimensional array of electrodes, see Figure 3.3. Silicon probes have been produced since the 1960's and advanced photolithographic techniques have more recently allowed for precise control of electrode dimensions to provide multiple electrode sites on a relatively small substrate. Neural activity of cortical regions has also been recorded using 'needle-bed' electrodes, where silicon is etched to produce fine tip needles, each with a single electrode on the tip examples of which are shown in Figure 3.4. These types of arrays have been used in both chronic and acute applications and the most famous of these types of devices is the 'Utah' array, consisting of around 100 densely packed electrode tips. Recently, an implanted Utah array has been shown to have some remaining functionality 3 years post implantation setting a new benchmark for chronic neural interfaces, although only a small number of electrodes were still recording [9].

Fig. 3.4: Penetrating micro-electrodes for use in the CNS [22]

3.2.3 Interfacing to the PNS

The most obvious difference between CNS and PNS technology is flexibility; PNS devices have to work next to muscles and survive relatively vigorous activity, and so are not usually as rigid as CNS devices. Similarly, to conform to the geometry of peripheral nerves the design of PNS devices tends a be more tailored. Due to these considerations PNS implants that are fabricated using polymeric materials have been developed in parallel with the silicon technology since the early 1970's.

Conventional research has aimed to interface to the PNS to record sensory afferent and motor efferent information and/or selectively stimulate to any undamaged musculature. Different types of electrodes have been developed ranging from surface electrode on the skin to regenerating devices that are implanted directly onto sectioned nerves, the general properties of these technologies will be discussed in turn to highlight the advantages and disadvantages of their use. A major concern in the development of an interface for the PNS is the possible damage caused to the tissue surrounding the device. There is a balance between the ability to selectively record from small populations of axons to achieve fine muscle control and invasiveness to the surrounding tissue. This is illustrated in Figure 3.5. The number of electrodes in a device depends on the application, a low number of electrodes are used to create a robust interface with a reduced selectivity and functionality, whereas a high number of electrodes increases the spatial resolution of the signals captured but provides added complications in terms of durability and energy consumption. Increasing selectivity is often associated with increasing invasiveness, rather than increasing electrode number where regenerative implants are the most invasive devices that require months of intrusion to create the interface.

Fig. 3.5: Invasiveness of different types of electrodes in the PNS. [19]

Fig. 3.6: An example of a surface electrode, a 'Walkaid' stimulator [27]

Surface and Intramuscular Electrodes

The only non-invasive PNS devices are surface electrodes. These electrodes usually comprise of metal plates with an electrolytic gel to maintain contact to the skin. Electrodes with stainless steel, silver or silver chloride have been shown to have good impedance, durability and are relatively easy to use. Surface electrodes can be used for both recording and stimulation of nerves located directly beneath the pads and are often used as simple stimulating devices for FES systems such as WalkAid designed at the University of Alberta [27] and Odstock Dropped Foot Stimulator (ODFS) designed in the UK [28] in the early 90's, where surface electrodes aid posture and gait. A Walkaid stimulator is shown in Figure 3.6.

Surface electrodes are disadvantaged by the need to calibrate and reposition the pads after each application and movement of the muscles varying the electrode position during stimulation. As such, surface electrodes are generally considered to be easy to use but not highly advanced interface technology. To increase the effectiveness of the interface the next logical

Fig. 3.7: Eight channel stimulator with one Epimysial Electrode [19]

step is to place the electrodes closer to the targeted nerves by penetrating the skin. Two classes of electrodes have fallen into this category of interface, epimysial electrodes and intramuscular electrodes.

Epimysial electrodes are surgically fixed to the surface of the muscle, negating the problem of having to reposition the electrode between experiments. They have been made from platinum-iridium disks that are backed onto a 'silastic' carrier material that provides a flexible, biocompatible and mechanical support, keeping the stimulus signal directed into the muscle and not out into the cutaneous sensory fibres of the skin. Epimysial implants have a good signal-to-noise ratio due to their large surface area and have been used to provide muscle stimulation in paraplegics [29, 30, 31]. An example of an epimysial electrode is shown in Figure 3.7. The main drawback for epimysial electrodes is the high energy consumption required to activate muscle via the efferent nerves deep in the biological target. Furthermore, each muscle requires a separate epimysial device, and so to coordinate movement requires a very strategic approach. Finally, the implant has to accommodate the relative changes in shape of the muscle both before and during the stimulation in order to maintain a durable interface.

Intramuscular electrodes generally consist of single-strand, multi-filament, stainless steel wires insulated with Teflon. The tips of the wires are de-insulated to form electrode sites that are inserted into the muscle through the surface of the skin. This interface has been used for both recording and stimulation of motor nerves and have shown to be functional for at least 3

Fig. 3.8: An example of an epineurial implant
[19]

years post-implantation [32].

The intramuscular electrodes are not too complex and are relatively cheap to make, however high energy stimulation pulses are required to activate fibres that lie in the deep muscle which can cause pain to the patient. Similarly, each muscle requires a separate intramuscular electrode increasing the complexity of the interface.

The last kind of intramuscular electrode is the BION (BIOnic Neuron) implantable micro-processor that can be implanted within muscles[33]. The main difference between the BION and other intramuscular devices is that the BION operates wirelessly, via a radio frequency link to transfer the signals recorded. BIONs have been used in FES systems to correct foot drop.

Extraneural and Intraneural Electrodes

The next level of invasiveness is to penetrate through the surface of the muscle and to place electrodes directly onto the motor nerve. Epineurial electrodes are sutured directly onto the epineurium, the outermost boundary of the nerve fascicles. Helicoidal electrodes are more flexible and are wrapped around the nerve, conforming to the necessary contours and reducing the mechanical stress in the interface. Both implants are fabricated using an insulating substrate of biocompatible material with exposed metal electrodes on one surface. Epineurial electrodes have been used in FES systems to aid foot-drop and to relieve chronic pain, however as they are fixed to the nerve they are thought to be more susceptible to mechanical failure and nerve damage during motion, an example of which is shown in Figure 3.8.

Helicoidal electrodes require less invasive surgery as they are made of flexible platinum

Fig. 3.9: Examples of book electrodes. Left:Standard 3-channel book electrodes from Finetech-brindley, Right: Illustration of Advanced Book Electrode in situ
[35]

ribbon that naturally conforms to the shape of the nerve[34]. These devices are as easy to explant, without causing additional discomfort to the patient, however, this open structure does cause a reduction in the selectivity of the device when compared to the epineurial electrodes.

The 'Book electrode' has found widespread clinical use in the treatment of urinary bladder disorders by interfacing to the sacral nerve. The device consists of a block of silicone rubber with deep-trenches embedded within it, much like the pages of a book. An example of an Active Book electrode is shown in Figure 3.9. On each 'page' are platinum electrodes. Sacral nerves are surgically positioned between the pages and are fixed in place by a silicone flap the covers the openings, fixed with glue. These implants have been commercialised by Finetech and there has been a large amount of clinical experience with excellent results, however, the devices are still seen as being too large and a process of miniaturization is underway.

Another way of establishing an extraneural interface is to completely enclose a nerve in a tubular sheath, with exposed electrodes on the inside surface. Such interfaces are called cuff electrodes, and have found many applications in basic and clinical research. The most simplistic way of creating these interfaces is by utilising a 'split-cylinder' or 'spiral cuffs', as shown in Figure 3.10. Cuff electrodes have many advantages over less invasive interfaces; any stimulating current used is confined to the inner volume of the implant, avoiding the stimulation of un-targeted nerves, and the stimulation current required is one order of magnitude less than for other implants, due to increased proximity. Similarly, the cuff electrodes are relatively easy to implant.

Cuff electrodes have to be extremely flexible and self-sizing to survive chronic applications.

Fig. 3.10: Cuff electrodes from Fraunhofer IBMT
[19]

They are generally designed to have a slightly larger diameter than the targeted nerve to maintain reliable interface without constricting the nerve. Any constriction could modify the nerve shape, potentially harming larger nerves, that are most sensitive to compression.

Cuff electrodes have been proven to offer selective interfacing technology for recording and stimulation and have a range of electrode configurations that can be tailored for the application. The earlier models used a single electrode to allow for a robust interface. To improve selectivity of afferent activity bi-, tri-polar and screened tri-polar arrangements of electrodes have been developed [36, 37]. Tripolar arrangements have also been used for current steering during stimulation to improve the selectivity and applicability of the technology [38, 39, 40].

Cuffs also improve the interface due to the effect of restricting the extracellular space. This phenomena was theoretically outlined by Stein and Pearson in 1971 [41], and will be discussed in more detail in the next chapter. Briefly, the cuff increases the resistance of the extracellular return current path by restricting the extracellular space, so that during the propagation of action potentials along the axon the extracellular potential is increased. The physiology of the axons is not affected by the cuff, so this method is a less invasive way of improving the recording interface without directly penetrating nerves. Augmenting the extracellular resistance has been successfully demonstrated by many researchers and will form a central theme in the technology that is developed in this thesis [42, 43, 11, 13].

Intraneural and Regenerative Interfaces

The next step to increase the selectively is to place the electrode contacts inside the targeted nerve, thus increasing the signal-to-noise ratio and reducing the current necessary for stimulation due to increased proximity. Using intraneural electrodes, individual fascicles can be

Fig. 3.11: Schematic of LIFE electrode.
[19]

activated.

Longitudinally implanted intrafasicular electrodes (LIFE) are the most familiar of these interfaces, and are comprised of thin, insulated conducting wires made of platinum-Iridium or metallized Kevlar, that are implanted directly into the nerve. The active site is the de-insulated strip of wire which is generally 250-1500μm long. Stiffer wires are more likely to cause a foreign body response and flexible polymers have been introduced to reduce this, these implants are labelled tf-LIFE electrodes. An illustration of a LIFE implant can be found in Figure 3.11. LIFEs have been shown to have good selectivity and can record nerve activity associated with missing limb movements. However, the method of implantation is relatively involved and establishing a large numbers of LIFE interfaces in a single patient is surgically invasive.

When a peripheral nerve is severed the distal part will degenerate to the closest node, whilst the proximal part will regenerate in an attempt to regain connection. If the gap between the proximal and distal part is short then the best method of obtaining a functional recovery of the nerve is to directly suture the two ends together.

Alternatively, a sieve electrode is a flat device with an array holes that go completely through the device, that is placed at the end of a cut nerve and designed to allow the growth of tissue through it. Sieve electrodes have been fabricated from silicon and polyimide with electrodes around selected holes, strategically placed to allow for recording and stimulation of regenerated nerves. This method of recording is advantageous as it is easier to build a flat device rather than a complex 3D structure, and once the nerve has regenerated through the hole, the whole assembly is fixed in place to give consistent recordings over a prolonged period. Examples of sieve electrodes and illustrations of how they are intended to be used are shown in Figure 3.12

Fig. 3.12: Schematic of a sieve electrode application.
[19]

Fig. 3.13: Polyimide based sieve electrodes developed at IBMT

and 3.13.

The amplitude of the signals recorded from the extracellular potentials of individual axons is extremely small, and so a considerable enhancement of the signal-to-noise ratio is required for most clinical applications. This will be discussed further in the next chapter.

4. IMPLEMENTATION OF MICROCHANNELS AS AXONAL AMPLIFIERS

4.1 Introduction

A neuroelectric interface that relies on the peripheral nervous systems' natural ability to regenerate has been the subject of significant research, however there are numerous drawbacks with the technology that has so far been realised. The action potentials from individual axons within the PNS give rise to extremely small signals in the extracellular space ($\approx 10\mu$V) which are difficult to detect in the low resistive medium that surrounds the axons.

Furthermore, for myelinated axons the current flows into the extracellular space from the regularly inter-spaced 'nodes of Ranvier' and unless the electrode is positioned relatively close to a node the signal will be too small for allow for a meaningful recording[11].

Apart from stimulating devices for FES applications very few neuroelectric devices designed specifically for the PNS have reached clinical application. There has been limited success with the cuff electrodes, LIFE electrodes and sieve electrodes but these have drawbacks that restrict the final functionality; the cuff electrodes are positioned on the outside of the nerve where selectivity is restricted, LIFE implants offer good selectivity but only have a small number of electrodes and sieve electrodes have a limited capacity that is restricted by the balance between axon growth space and lead-out space.

The number of electrodes required for a PNS interface has not been determined, however the minimum number is related to the number of muscles replaced by the prosthesis, which for a lower arm device could be around 30 independent recording sites. This number is purely illustrative, but it represents a threshold that has not yet been reached by the conventional PNS interface technology. Furthermore, under the conventional regime an increasing number of electrodes may not translate to an increased functionality as many will fail to pick up a signal.

This is because all long-term in vivo implants must be able to reliably record extracellular

signals in the order of 10-500μV. Signals of this magnitude are difficult to detect due to thermal Johnson noise, which for extracellular recording devices determined by,

$$V_{\mathrm{RMS}} = \sqrt{4k_B T R \Delta f} \tag{4.1}$$

where T is the temperature in degrees Kelvin, R is the resistance, k_B is the Boltzmann constant and Δf is the bandwidth for which the electrode operates.

For a recording in the PNS a metal electrode typically operates within a frequency band of 10 kHz with an impedance of 1 MΩ translating to a thermal Johnson noise floor of around 13μV. Thus, for signal that is 10μV, it would be difficult to distinguish the real signals from electrical artefacts of the recording equipment. To make matters worse, in the low-resistive extracellular space any signal decays rapidly. Positioning a recording electrode next to the point at which the current originates is not realistic with the available technology.

To establish a successful interface to the PNS it is necessary to address these fundamental problems relying on solutions that are both achievable in an engineering sense and also do not compromise the physiology. In this chapter it will be shown that an effective solution could be reached if the extracellular medium could be made more resistive. Increasing the extracellular resistance increases the recorded signal due to the extracellular return current of the action potential being forced along a more resistive path. This concept will be introduced through the theoretical work of Stein and Pearson [41] and the modelling of Fitzgerald et al [11].

4.2 Axonal Amplification

Neurophysiologists have utilised the idea of increasing the resistance of the extracelullar space for many decades. Originally hook electrodes were used to suspend a section of nerve in the air or to immerse the nerve in oil, to increase the resistance of the extracellular medium and increase the amplitude of the recorded signals. The amplification is caused by the propagating signal having a higher resistance for the return current path, discussed in chapter two and shown in Figure 4.1. For the suspended nerve, the extracellular current cannot propagate in the oil/air and so is restricted to the material between the fibers. This raises the extracellular resistance when compared to a nerve suspended in saline, for example. Alternatively, reducing the volume

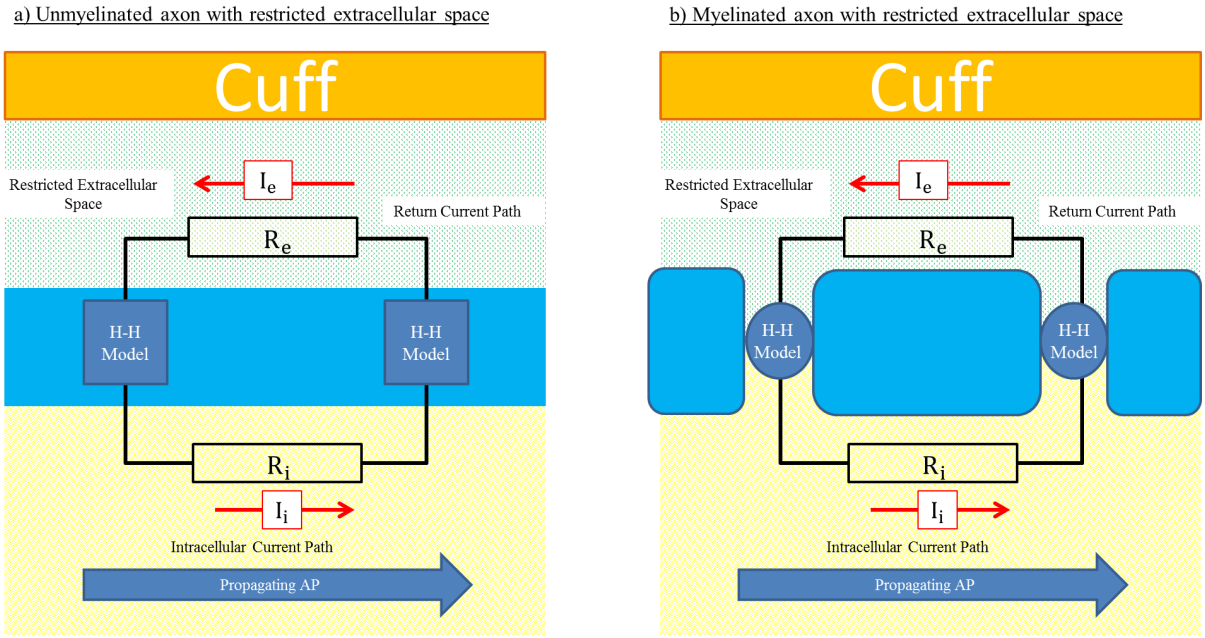

Fig. 4.1: Diagram to show restricted extracellular space and return current path of a propagating action potential of an a) unmyelined axon and b) myelinated axon inside a cuff

of the extracellular medium could augment the extracellular resistivity without changing the constituents of the extracellular medium. This idea was exploited by Huxley and Stämpli who demonstrated saltatory conduction in myelinated fibers by confining a nerve fiber in a perspex capillary of ≈50 micron diameter [42]. During the experiment the extracellular resistance was measured at ≈0.5 MΩ, compared with a resistivity of mΩ's for saline. This experiment focussed on restricting the extracellular space rather that suspending the individual axon in oil/air. This is because immersing an individual axon (with no extracellular tissue/fluid) would not allow for the propagation of action potentials as there be no ions in the extracellular space. Stein and Pearson showed that the extracellular medium could be made more resistive using a cuff electrode that envelops the nerve [41]. Their theoretical approach to explain the effect of augmented resistance is described next.

4.2.1 The Theory of Augmenting Extracellular Resistance to Increase the Signals from Axons

The theoretical model starts from a cylindrical axon in a restricted extracellular space as shown in Figure 4.2, where an unmyelinated axon of radius a is confined in a cuff of radius b that extends in the z-direction from 0 to *L*. The axon can be modelled as a leaky cable such that the

axonal membrane that separates the intracellular axonal fluid from the extracellular space is as combination of a distributed resistance, R_m (Ωm) in parallel with a capacitance per unit length ς_m, (F/m). The resistive current corresponds the ionic membrane currents that were described in the last chapter via the Nernst equations, and the capacitive current is a result of the membrane acting as a dielectric between the two conductors [40]. The system is defined as having axial symmetry such that potential is uniform in the transverse direction. The intracellular space has a resistance per unit length of R_i and an external resistance per unit length R_e [44], and so the total current inside the axon I_i and outside the axon I_e must be proportional to the potential gradients to satisfy Ohm's law. If the potential inside the axon is $\varphi_i(z,t)$ and the potential outside the axon is $\varphi_e(z,t)$ then this relationship is written as,

$$\frac{\partial \varphi_i}{\partial z} = -I_i R_i \tag{4.2}$$

$$\frac{\partial \varphi_e}{\partial z} = -I_e R_e \tag{4.3}$$

where the axon is defined to be extending in the z-direction [40, 45]. To satisfy Kirchhoff's law the current per unit length through the membrane is then,

$$i_m = \frac{\partial I_e}{\partial z} = -\frac{\partial I_i}{\partial z} \tag{4.4}$$

where the outward flowing current is positive. Intuitively it can be seen from Equation 4.3 for a longitudinal current I_e the resistivity of the extracellular medium effects the size of the extracellular potential. For the unrestricted case ($\varphi_e \rightarrow 0$) and remembering that the trans-membrane potential is defined as $V_m = \varphi_i - \varphi_e$, substituting Equation 4.2 into Equation 4.4 the current through the membrane can be written as,

$$i_m = \varsigma_m \frac{\partial \varphi_i}{\partial t} + \frac{\varphi_i}{R_m} = \frac{1}{R_i}\frac{\partial^2 \varphi_i}{\partial^2 z} \tag{4.5}$$

which relates the membrane current to the intra-axonal potential. Stein and Pearson showed that for a recording electrode positioned in the extracellular space at $z = z_{el}$, the longitudinal current I_e in the extracellular space (note there is also longitudinal current flowing outside of

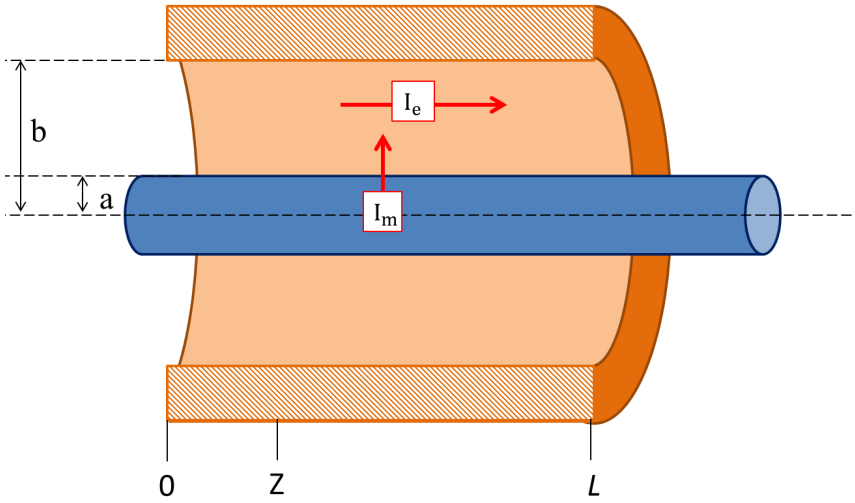

Fig. 4.2: Diagram to show an axon in the restricted extracellular space that extends from 0 to *L*. The space is restricted by a cuff of radius b.

[41]

the restriction) gives an extracellular voltage recorded at z_{el} of,

$$\varphi_e(z_{el}) = \varphi_e(0) - \frac{1}{G_e}\int_0^{z_{el}} I_e dz' \tag{4.6}$$

where G_e is the conductance of the extracellular medium that is directly proportional to the cross-sectional area and conductivity of the medium in the cuff σ_e, and is inversely proportional to the length of the cuff where,

$$G_e = \frac{\pi(b^2 - a^2)\sigma_e}{L} = R_e^{-1} \tag{4.7}$$

Again, Stein and Pearson assumed that the extracellular fluid can be modelled as a distributed resistance where radial voltage drops are neglected. This assumption was shown to be valid as long as the expression,

$$(b^2 - a^2) ln\left(\frac{b}{a}\right) \ll 2L^2 \tag{4.8}$$

is satisfied, assuring that the transverse conductance is much larger than the longitudinal conductance. Similarly, G_i is the conductance inside the axon ($G_i = \frac{\pi a^2 \sigma_i}{L} = R_i^{-1}$). Stein and Pearson argued that the extracellular current in the restricted space can be related to the trans-membrane

current by integrating Equation 4.4 over z.

$$I_e = \int i_m dz'' + \gamma \tag{4.9}$$

where γ is a constant of integration. By substituting equation 4.9 into equation 4.6 the trans-membrane current can be related to the extracellular potential at z. The constant of integration can be evaluated by applying equation 4.6 at the boundaries of the extracellular restriction and equilibrating, as the potential is the same at $z = 0$ and $z = L$. Thus, the extracellular potential in the cuff can be expressed as,

$$\varphi_e(z) = \frac{1}{G_e} \int_0^{z_e l} \left\{ \int i_m dz'' \right\} dz' + \frac{z}{LG_e} \int_0^{z_e l} \left\{ \int i_m dz'' \right\} dz' + \left(1 - \frac{z}{L}\right) \varphi_e(0) + \frac{z}{L} \varphi_e(L) \tag{4.10}$$

Finally, the membrane current can be written in terms of change in the trans-membrane potential and the potential in the extracellular space by substituting Equation 4.2 into Equation 4.4 to get,

$$i_m = -G_i \frac{\partial^2 \varphi_i}{\partial z^2} = -G_i \frac{\partial^2 (V_m + \varphi_e)}{\partial z^2} \tag{4.11}$$

Substituting this expression into Equation 4.10 yields the extracellular potential inside the cuff as a function of z as,

$$\varphi_e(z) = \frac{G_i}{G_e + G_i} \left[\left(1 - \frac{z}{L}\right) V_m(0) - V_m(z) + \frac{z}{L} V_m(L) \right] + \left(1 - \frac{z}{L}\right) \varphi_e(0) + \varphi_e L \tag{4.12}$$

If a recording electrode is placed at the mid-point of the local restriction ($z = \frac{L}{2}$=z_{el}) and measuring potential relative to a reference electrode placed in a fluid outside the cuff, φ_f, then the measured potential will be,

$$\varphi_{\text{REC}} = \varphi_e(z_e l) - \varphi_f = \frac{G_i}{G_e + G_i} \left[\frac{V_m(0) - 2V_m(\frac{L}{2}) + V_m(L)}{2} \right] + \frac{\varphi_e(0) + \varphi_e(L)}{2} - \varphi_f \tag{4.13}$$

Stein and Pearson argued that for experimental recording situations the voltages associated with the reference electrode and at the two positions at the each end off the cuff would be insignificant as they are in contact with a large volume of unrestricted medium. This cancels the last two

terms and the recorded potential can be written as,

$$\varphi_{\mathrm{REC}} = \frac{G_i}{G_e + G_i}\frac{\Delta^2 V_m}{2} \tag{4.14}$$

where $\Delta^2 V_m$ is the second difference of the membrane potential, which depends on the length of the cuff and the conduction velocity of the action potential inside the cuff, ν_c. For the recording set-up described, this can be expressed as,

$$\frac{\Delta^2 V_m}{2} = \frac{V_m\left(t + \frac{L}{2\nu_c}\right)}{2} - V_m(t) + \frac{V_m\left(t - \frac{L}{2\nu_c}\right)}{2} \tag{4.15}$$

Where,

$$\Delta V_m = \frac{V_m(z+k) - V_m(z)}{k} = \lim_{k \mapsto 0}\frac{\partial V_m}{\partial z} \tag{4.16}$$

and it is presumed that for a propagating action potential travelling in the positive z-direction with a velocity of ν_c the spatial and time derivatives depend on each other as,

$$\frac{\partial V_m}{\partial z} = -\frac{1}{\nu_c}\frac{\partial V_m}{\partial t} \tag{4.17}$$

as shown by Hodgkin and Huxley. From Equation 4.14 and 4.15 it can be seen that the amplitude of the recorded potential depends on two factors; Firstly, the relative cross-sectional areas and conductivities of the extracellular and intracellular media are accounted for by the $\frac{G_i}{G_e+G_i}$ term; Secondly, the second difference equation that depends on the length of the cuff and the conduction velocity as, $\frac{L}{\nu_c}$. If L is small then the recorded potential will closely resemble the derivative of the trans-membrane potential, as can be seen in equation 4.16. Stein and Pearson further showed for large values of L and for the condition that $a \ll b$ (both are true for most recording situations) the peak amplitude of the recorded signal becomes independent of L and is roughly equivalent to,

$$\varphi_{\mathrm{REC}} = \frac{3a^2\sigma_a|V_m|}{2b^2\sigma_e} \tag{4.18}$$

thus for large L and for the situation where the radius of the cuff is fixed, the peak amplitude varies as the square of the radius of the axon inside the channel. This expression shows that restricting the extracellular space amplifies the signal with a gain that is dependent on the geometry and relative resistivity's of the intracellular and extracellular spaces. This phenomenon is therefore referred to as axonal amplification.

Marks and Loeb applied the same theory to include myelinated axons [40] and they noted that when the length of the restrictive cuff is of the same size as the internodal distance ($\approx 300\mu m$ for a regenerated axon) the longitudinal position of the nodes effects the waveform of the potential recorded at the midpoint of the cuff. However, if the length of the cuff is at least four times longer than the internodal length then the waveform is unaffected. This should be regarded as minimum length of the extracellularly-resisted space and the axonal amplifier should be at least 1.2 mm long. The conductance's of the intracellular fluid and extracellular fluid can be estimated from the literature as σ_a =0.91 S/m [46] and σ_e =0.5 S/m [47] which substituted into Equation 4.18 gives,

$$\varphi_{\mathrm{REC}} \approx \frac{2.7a^2|V_m|}{b^2} \tag{4.19}$$

For an axon of 2μm-diameter in a channel of 36 μ-diameter (Area of channels$\approx$ 1000 μm^2), for a $|V_m|$ = 30 mV (peak amplitude) the corresponding recorded potential would be 250 μV, which would be well above the noise level of most recording electrodes.

4.2.2 Modelling of a Micro-Channel as Axonal Amplifier

To gain a fuller understanding of the benefits of axonal amplification a team from the Cambridge Centre for Brain repair used finite element analysis techniques to investigate the extracellular signals that can be recorded when altering the size of the axon and relative channel cross-sectional area for both myelinated and unmyelinated [11]. In order to supplement the theoretical approach from Stein and Pearson and Marks and Loeb the results of this study are also discussed briefly. The model used axisymmetric geometry shown in Figure 4.3 swept through 360° to give the structure of the axon in the channel. As can be seen, the channels and the axon inside it were both assumed to be isotropic cylinders of a controlled diameter.

The unmyelinated axon model consisted of an interior space inside the axon and extracellu-

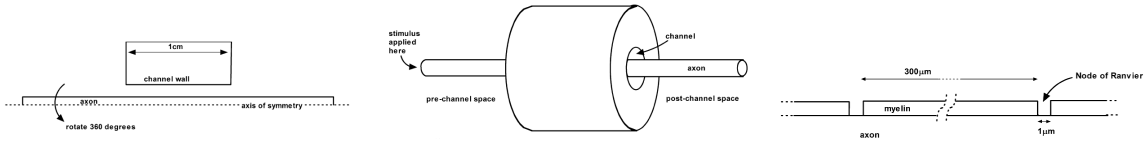

Fig. 4.3: Simulation geometry of FEM analysis by Fitzgerald in 2008. Top; 2D axisymmetric unmyelinated axon. Middle; In the analysis the 2D model is swept over 360° to give the 3D structure. Bottom; Myelin segments added to accommodate myelinated axons in the model

[11]

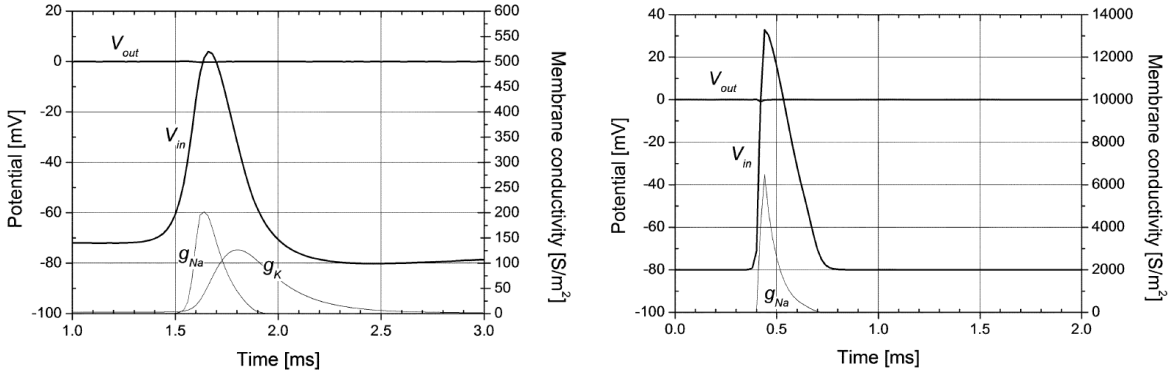

Fig. 4.4: Modelled AP for 2μm diameter unmyelinated axon (Left), and 10μm diameter myelinated axon (Right) in an unrestricted space.

[11]

lar space modelled as volume conductors with a resistivity of σ_a and σ_e (in the direction parallel to the membrane) respectively, separated by the axon membrane[11]. Unlike the Stein and Pearson model the current was not restricted to longitudinal paths and the extracellular space had a finite transverse resistivity that was approximately six times that of the longitudinal resistivity. For myelinated axons a different geometry was used to account for inter-nodal spacing.

The modelled action potentials for both myelinated and unmyelinated axons are shown in Figure 4.4, comprising of both the sodium and potassium conductances given below each voltage curve. It is clear to see that the external potential change is minuscule with respect to internal potential change for both unmyelinated and myelinated axon, as expected in the unrestricted extracellular space. This figure demonstrates the fundamental problem in trying to record from individual axons in the peripheral nervous system, as the potential on the extracellular surface changes little over the course of the ‘activity’.

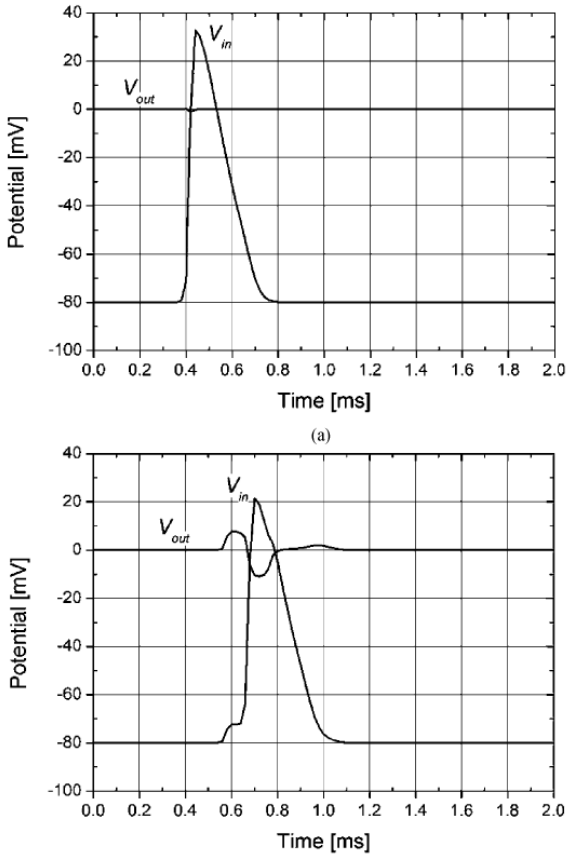

Fig. 4.5: Modelled AP for 10μm diameter myelinated axon as it approaches the channel (Top), and at the midway point of the 1000 μm^2 channel (Below).

Extracellular Amplification in the Channel

Figure 4.5 shows the AP of a 10 μm diameter myelinated axon as it approaches a 1000 μm^2 channel and at the mid-point of the channel. Again in the pre-channel space the potential on the exterior of the membrane is extremely small compared to the interior potential during the action potential. When the axon is confined, potential on the inside surface of the membrane falls from ≈35mV to ≈20mV and the exterior potential becomes triphasic, with a displacement from the horizontal of around 10mV in both the positive and negative peaks.

Figure 4.5 shows the benefit of confining the axon in a channel where the microchannels provides amplification to the extracellular potential and the signal has positive and negative maxima in the order of ±10mV for the myelinated axon.

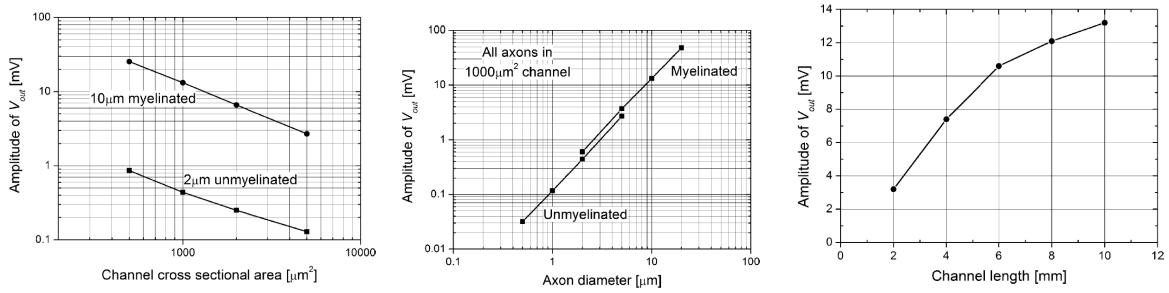

Fig. 4.6: The amplitude of V_{out} of a 10 μm myelinated axon versus the channel cross sectional area (left) for a 1 cm long channel, the axon diameter when confined in a 1 cm long channel (Middle) and the length of the channel when confined in a 1000 μm^2 channel (Right)
[11]

Varying Channel Length, Area and Axon Diameter

The study also investigated the effect of varying the channel area, the axon diameter and the variation of channel length on the ability to record extracellular potential and the results are briefly discussed below. Figure 4.6 shows the effect of varying the channel's cross-sectional area (channel length=1 cm) that encloses the axon to highlight the proportionality between increasing extracellular space and decreasing amplification. Varying the axon diameter with respect to a constant channel width (channel length=1 cm) produces the same effect. This suggests that for in vivo applications the recordings will be dominated by larger axons, as the amplification factor is not universal for all axons of varying thickness's.

Figure 4.6 also shows that increasing channel length (channel area=1000 μm) gives a similar increase in the ability to record action potentials. However, the curve appears to straighten out as the length of the channel begins to extend over 10 mm, suggesting that there may be a saturation point where the increasing the length of channel would not lead to a notable increase in the signal recorded.

This study reinforces the theoretical platform for the design of a regenerative implant by utilising insulating channels as axonal amplifiers. To create an optimal interface the channel should have a cross-sectional area that is similar to that of the axon that is being targeted and the channel should at least be 10 mm long. Anything >10 mm could provide an additional bonus up to the saturation point.

However, it is impractical for most regenerative applications to arbitrarily increase the distance through which the axon regenerates as the physiology of the axon changes. It has been

suggested that neurite regeneration cannot be supported over large distances (>2cm) in a polymeric interface without adding supporting growth factors such as Schwann cells[17][48]. No growth factors were used or considered in the evolution of the spiral peripheral nerve interface, and so the maximum length of the interface had to be reduced accordingly.

Comparing the work from Stein and Pearson with that of Fitzgerald shows much agreement. In Figure 4.6 Fitzgerald's modelling suggests that an unmyelinated axon of 2 μm diameter in a channel with a cross-sectional area of 1000 μm^2 gives an extracellular potential of $\approx$400 μV, compared to 250 μV from Stein and Pearson from the same geometry.

It may not be suitable to compare the studies directly as one is based on a finite element analysis that allows transverse currents to flow in the extracellular space, where the other is dependent on the axial symmetry of the uniform transverse potential to estimate the amplification. For the Fitzgerald model the transverse potential is not necessarily uniform in the extracellular space as the current is allowed to spread.

Despite these discrepancies, it has been well established in both studies that confining axons in micro-channels provides substantial amplification to the extracellular signal, increasing the ability to record from the PNS. In the following chapters of the thesis it will be shown how these theoretical models have directed the fabrication of a micro-channel array that can be implanted into the PNS to record extracellular signals.

5. METHODS OF FABRICATING AND TESTING POLYIMIDE DEVICES

This section of the thesis provides a brief outline of the processing methods that have been used to fabricate and test the neural interfaces presented in this thesis. For fabrication the chapter describes: the handling and cleaning methods, the fabrication of polyimide layers, the methods used to deposit thin metal films, the photolithographic procedures used to define the metallized layers, and the use of plasma etching to clean the samples. These methods are based on techniques that have been established in the fabrication of microtechnologies for decades and have become essential in the fabrication of the SPNI. For a fuller description of the fabrication processes that are outlined in this chapter there are several books on the subject, including [49, 50].

The final section of the chapter will focus on the methods that have been used to test the neural interfaces, including the use of an impedance analyser to characterise the electrode/electrolyte interface and an Instron Microtester, to determine the ability of the polyimide device to withstand longitudinal tensile loading.

5.1 Methods used to fabricate polyimide devices

5.1.1 The Silicon Wafer

All fabrication procedures discussed herein begin with a (100) silicon wafer that has been pretreated with a 250 nm oxidised surface layer, which is also known as the ‘handle’ or ‘carrier’ or simply ‘wafer’. Handle wafers are used in microfabrication processes as they offer good resistance to chemical processes and thermal stability during curing at elevated temperatures; the SPNI is fabricated on a 4” diameter handle wafer. The surface of the handle wafer is cleaned by rinsing the surface with acetone to remove any organic contaminants, before being further rinsed with isoproponol (IPA) to remove the contaminated acetone, which is then blown dry using N_2. The wafer is then dehydrated by elevating the temperature of the wafer using a hot-

plate to around 150°C. This evaporates any water molecules that have condensed onto the wafer surface from water vapour in the surrounding environment.

5.1.2 Spin Coating Polyimide Resins and photoresist

To fabricate thin, homogeneous layers of polyimide a resin is deposited onto the centre of the handle wafer and spun. The film thickness decreases as the inverse square root of the spin speed which can then be altered to define a certain range of film thickness that can be achieved. For low spin speeds or particularly thick layers (>60μm) the time required to achieve a final constant film thickness increases. The final film thickness is not only a function of viscosity and spin speed but also on the amount of resist that is dispensed onto the substrate. The polyimide is dissolved in a solvent to make the resin and during the first few seconds of spin coating the solvent concentration falls quickly and then saturates based on the value determined by the resist film thickness. The amount of solvent in the film can be further reduced at elevated temperatures during a 'softbake'. The relationship between the resulting film thickness and spin speed used is called the 'spin-profile', and is generally available from the suppliers of the material[51, 52, 53].

This process is also used for photoresist, a light sensitive material that is used to construct a patterned coating on a surface. The coating is usually added to the surface to protect certain parts of the films during chemical wet etching. The two photoresists used in the thesis are S1813 (Microposit, Shipley) and SPR-220-7 (Megaposit, Shipley).

The method of spinning does not always produce perfectly flat films, as areas that are slightly thicker than the desired thickness can form on the periphery of the wafer. These regions generally occur when applying thick layers of photoresist, and are referred to as 'edge-beads'. The formation of an edge-bead can be detrimental to the fabrication of the overall device, as it can reduce the resolution of the photolithographic process, as will be discussed later. Methods have been developed to remove edge-beads, including using acetone to strip the thicker area of the wafer, or having extra photolithographic steps that can eradicate them, but the most desirable method of avoiding edge-beads is to optimise the spin-coating methods, by increasing the amount of time that the wafer is spun or increasing the spin speed.

Methods to determine the film thickness

The thickness's of all films discussed in the following chapters, are measured using a Dektak surface profiler (Bruker Corp), unless otherwise stated. The system operates by dragging a low-force stylus across the surface of the sample, and reading off any variation in the step height. According to the operators manual the system can measure step-heights in the range of 200-655000Å[54], although surface abnormalities caused by the fabrication process, such as contaminants from a poorly developed substrate, and the shape of the stylus itself, would be expected to dominate for very thin films. As a result, any films that are less than 0.5μm, such as the metallization layers, are always stated as approximate. Similarly, the very thick polyimide layers used to make the insulating walls of the micro-channels could not be measured using the Dektak, as they are out of the measurement range. Instead a micrometer was used on these very thick films. It should be noted that any variation in the ambient conditions of the cleanroom, or the amount of resin/resist deposited onto the film prior to spinning may cause a variation in the film thickness. To minimise these conditions, the fabrication process was kept as consistent as possible.

Soft baking of Polyimide resins and photoresist

Soft baking is a process of hardening the spun resin by evaporating some of the solvent at elevated temperature to enable the photolithographic processes, by turning the liquid photoresist or polyimide into a semi-cured state that can be handled easily.

For both photosensitive and non-photosensitive polyimde the soft bake was performed on a hotplate using a slow temperature ramp of 20°C→90°C at 3°C per minute. The slow baking step was used so not to cause defects, via bubble formation. For the very thick polyimide layers, used to fabricate the micro-channel walls in chapters 6, 7 and 10, a softbake was performed by ramping between 0.5°C per minute between 30°C and 70°C, and then at 1°C per minute up to 100°C where it was held for 10 minutes.

For S1813, the thinner photoresist discussed in chapters 6 and 7 no soft bake ramp was used. Instead the sample was placed on a hotplate that had been preheated to 120°C and held for 6 minutes. For the thicker photoresist, SPR-220-7 discussed in chapters 7, a 'drop-down' softbake was used where the sample was placed on a hotplate at 90°C, and held for 2 minutes.

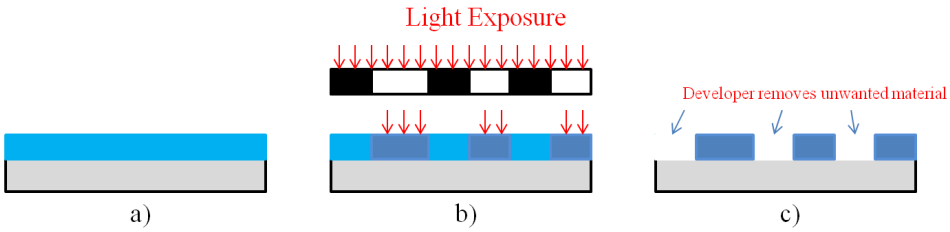

Fig. 5.1: Illustration of the photolithographic process, a) film is deposited onto wafer, b) areas of the film are exposed to light, whilst everything else remains unexposed, c) developer removes the unwanted material.

After this the sample was transferred onto a second hotplate at 120°C, and held for 6 minutes. The 'drop-down' procedure stops deformations in thick layer. After the softbake samples were left on the bench for at least 20 minutes to allow them to cool.

5.1.3 Photolithography

Photolithography is the process of changing the chemical structure of a material by exposing in to light. It is used to pattern the deposited film by changing the chemical structure of an exposed area, making it more or less soluble to chemical developers. Thereby, the regions that become more soluble will be etched away, or 'developed', by introducing the film to an appropriate developer. A 'photomask' is used to block the exposure of light to create a pattern which can then be defined in the developers. After development, only the desired regions remain, as illustrated in Figure 5.1. The illustration represents a negative photo-lithographic process, where the exposed region remains after the development. The photo-sensitive polyimides used in this thesis (Durimide 7505 and 7020, Fujifilm) are both 'negative' materials and the photo-mask has to be designed accordingly. The photoresists used in this thesis are 'positive'-photomaterials.

For the work presented in this thesis the PSPI and photoresist are both exposed using UV light in the wavelength range of 380-400 nm (i-line), using a Canon mask aligner. The PSPI is developed using the ancillaries HTR-D2 and RER-600, and specific method for development has been optimised, that will be discussed later. For the photoresists, either MF-319 or MF-26A from Shipley is used.

Fig. 5.2: Polaron Thermal Evaporator

5.1.4 Fabrication of Thin Metal Features

To fabricate the thin metal layers that eventually form the electrodes, tracks and connection pads of the neural interfaces, thermal evaporation is used. For this, the sample that is to be coated with the metal films is placed upside down in a vacuum chamber. The vacuum chamber is pumped down to <1x10^{-}5 mbar before the metal films can be evaporated. To evaporate the metal, a current is passed through a source containing the material causing it to heat up and sublime. As there is no air in the chamber the mean free path of the sublimed metal particles is high, allowing them to reach the surface of the sample. They cool on the surface to deposit a pure metal film the thickness of which depends on the amount of current that is passed through the source and the amount of time of evaporation; where higher currents and longer evaporations result in thicker films. For the metallization discussed in chapters 6 and 7 the thermal evaporation is performed in a Polaron thermal evaporator (Quorum Technologies, Discontinued), as shown in Figure 5.2. To fabricate the metal films for the neural devices, an adhesion layer of chrome is evaporated first followed by a gold layer. To evaporate the chrome, a current of 50A is passed through a tungsten rod that is coated with pure chrome, for 30 seconds. The adhesion layer is followed by the gold for which a current of 22A is passed through an alumina crucible, with pure gold pellets inside, for 1 minute. This results in metallized layers that are ≈80nm and ≈200nm of chrome and gold respectively. The adhesion layer is necessary as gold does not adhere to polyimide particularly well. Chrome is not biocompatible, so in future development of the neural interface this should perhaps be exchanged with titanium.

5.1.5 Etching and other surface treatments

To pattern the metallized layers chemical wet etching can be used where the metal layer is attacked by chemical that is introduced to the surface. To create a metallized pattern, some areas of the metal are protected by a layer of photoresist that has been defined into the desired pattern using photolithography. The unprotected areas are removed by the etchant whilst the protected areas remain. After this, the photoresist is stripped from the surface to reveal the metallized pattern.

For the neural interfaces developed in chapters 6 and 7 the metallization is coated in layer of either S1813 or SPR-220-7 photoresist that is defined into the electrodes, connection pads and tracks that connect the two. To etch the gold, the entire sample is immersed in a potassium iodide solution, typically for 40 seconds and then rinsed with deionised water. For the chrome layer, the sample is immersed for 15 seconds, to etch the unprotected chrome layer away, and again the sample is rinsed with deionised water.

Oxygen Plasma Etching and UVO Cleaning

Oxygen plasma etching (OPE) uses plasma of ionised particles to bombard the surface of the sample to etch away unwanted material. OPE is not directional and acts isotropically at the sample surface, in a similar way to a chemical etchant. To perform OPE, the sample is transferred into a vacuum chamber and pumped down to an appropriate pressure. After the chamber has been evacuated oxygen is allowed to flow into the chamber which is then ionised by applying a large potential between a cathode and an anode. The large potential causes any free electrons in the oxygen gas to accelerate towards the anode, which causes collisions to occur between the fast-moving 'hot' electrons and the slow moving 'cold' oxygen molecules. These collisions can ionize the oxygen molecules to cause a cascade effect to create the plasma.

OPE is used to clean the samples by removing organic matter in chapters 6 and 7 and OPE is also used to 'de-scum' any polyimide residue that is remaining on the electrode surfaces after processing. For this treatment, the sample is loaded into the barrel etcher and pumped down to a pressure of $\approx$1mbar(according to the manufacturer's manual[55], no attempt was made to measure the pressure inside the chamber), the sample was allowed to pump down for three minutes prior to the etching. The oxygen plasma was formed and allowed to etch the sample

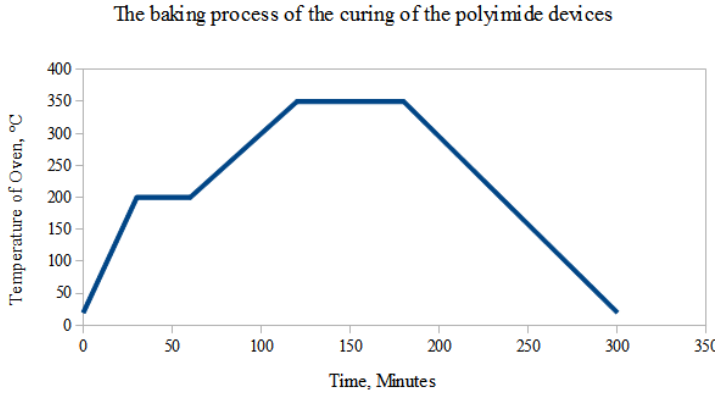

Fig. 5.3: An illustration of the curing temperatures used to hard-bake the polyimide devices.

for a period of 10 minutes. After the etching the barrel etcher was vented and the sample was removed. The oxygen plasma etcher was the Femto model from Diener Electronics.

Another method of cleaning the samples was employed in chapter 7, where a Jelight UVO cleaner was utilised. Again this system can be used to remove any organic surface contaminants such as oil or photoresists. The UVO cleaning method is a photosensitized oxidation process in which the organic contaminants are excited and/or dissociated by the absorption of short-wavelength, ultra-violet radiation. The resulting products of the excitation react with atomic oxygen, that is formed simultaneously through the absorption of UV, to form simpler molecules that can are readily removed from the surface. By combining these two surface treatments it was hoped that the electrodes would be free of any contaminants.

5.1.6 Curing of the polyimide structures

To cure the polyimide structures, a hardbake was performed in a convection oven, in an oxygen-free environment, according to diagram shown in Figure 5.3. The final baking step cured the PI-2611 at 350°C for 60 minutes. The dual-step baking was designed to give the convection oven enough time to achieve the oxygen-free environment, before the temperature rose above 200°C. If oxygen had been present above 200°C the PI-2611 layers would have burned, which seriously impacts on material properties, making it unsuitable for an implant. Baking the samples in this way drives of any remaining solvent in the polyimide layers and imidizes them into the final structures. Without performing the final cure, the polyimide structures are not as durable and are potentially more susceptible to up-take of water or other contaminants, which may be

Fig. 5.4: Laurier M9 Flip-Chip bonder
[56]

detrimental in the chronic performance of the implant.

5.1.7 Flip-Chip Bonding

A flip chip bonder is bonding tool that is designed to perform cold compression, thermal-compression, adhesive cures and reflows solder bonding of MEMs devices of various substrates. In chapter 10 a flip-chip bonder (Laurier-M9,BESI) is used to investigate the adhesive bonding of polyimide films. The bonder is able to apply a significant pressure (up to the equivalent of a 50 kg mass) over the entire surface of the wafer, and heat to a temperature of up-to 500°C, in a system that is programmable to optimise the curing and bonding pressure ramps. To partially cure the polyimide without burning the material in the atmosphere, the temperature of the plates was restricted to 200°C for these experiments. The flip-chip bonder is shown in Figure 5.4.

5.2 Methods used to test polyimide devices

5.2.1 Electrochemical Impedance spectroscopy

As discussed in a previous chapter, bioelectric potentials from axons are carried in an electrolytic media as ionic currents. For neural recording, the ionic currents are transduced into electronic signals at the electrode by a capacitive coupling and by a charge transfer reactions. Electrochemical impedance spectroscopy (EIS) has been used to characterize the elec-

trode/electrolyte interface for many micro-fabricated electrodes.

The impedance of the electrode determines the electrodes ability to record neural signals and EIS is performed by measuring the electrical impedance and phase angle obtained when the electrode is excited by a sinusoidal voltage or current. To find the impedance spectra, the impedance is measured over a broad frequency range that is typically between 10 Hz→1 MHz. Biological signals fall typically in the lower frequency range (< 10kHz) where as predominantly higher frequency phenomena includes leakage capacitance of the electronic components. For voltage excitation, the source is typically less than 50 mV [57].

Many, if not all, neural interfaces have been tested using some form EIS, and so it can serve as a useful comparison for the electrode/electrolyte characteristics of the neural interfaces developed in chapter 6 and 7. The samples were investigated using EIS to check that the fabrication process had been successful, and that the impedance of the electrodes was not too high to record/stimulate neural signals.

All EIS measurements were performed using a two-electrode set-up, connected to a network analyser (HP 9424, Hewlett Packard) in a saline solution that was designed to match the salty constituents of the human body, as shown in Figure 5.5. This salty solution was made by mixing 8.6 g of sodium chloride in one litre of deionised water. The first electrode was the micro-fabricated gold electrode of the neural interface and the second electrode was a platinum counter electrode, that had an electrode surface of 0.4 cm radius. A sinusoidal signal of 5 mV was applied between the electrode, and the impedance magnitude and the phase were measured for a frequency range between 40 Hz and 1 MHz, unless otherwise stated.

To perform the EIS the devices were glued to a conventional PCB (made in house) and wire bonded using 25 μm diameter aluminium wire, as shown in Figure 5.6. The sample was lowered into the saline solution and fixed in place using a crocodile clip. The section of the device that was being investigated was allowed to sit just below the surface of the saline, and it was ensured that the saline did not reach the connection pads of the SPNI. Each channel could be investigated by connecting to the terminal of the impedance analyser, via a DIL socket that was soldered to the conventional PCB, as shown in Figure 5.6. The counter electrode was very large compared to the micro-electrodes (actual areas were $3x10^4\mu m^2$ for the SPNI electrode and $\approx 5x10^7\mu m^2$ for the counter electrode), representing a negligible impedance compared to

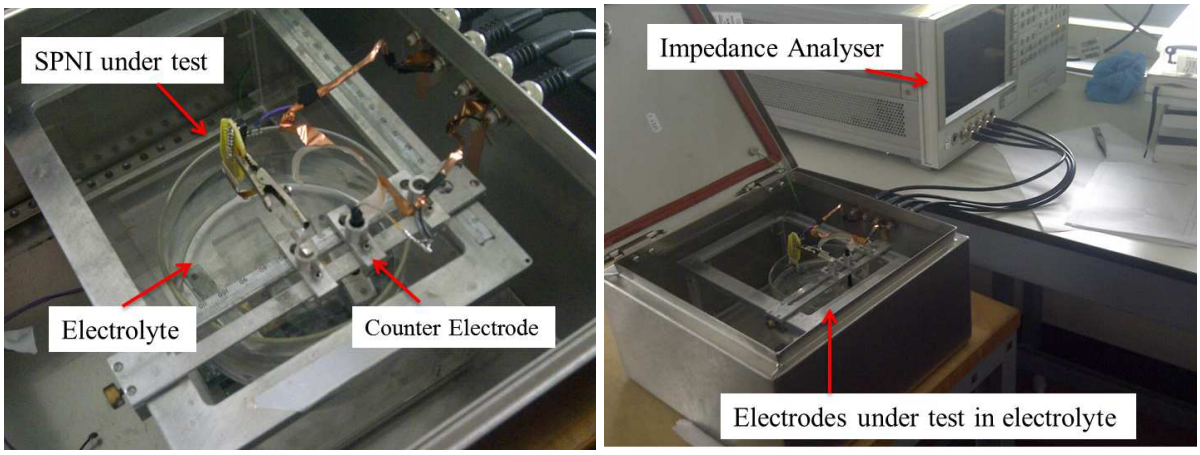

Fig. 5.5: Experimental set-up used to measure electrode characteristics; Top; Positioning of SPNI and counter electrode in electrolyte, Bottom; Electrodes under test connected to Network Analyser

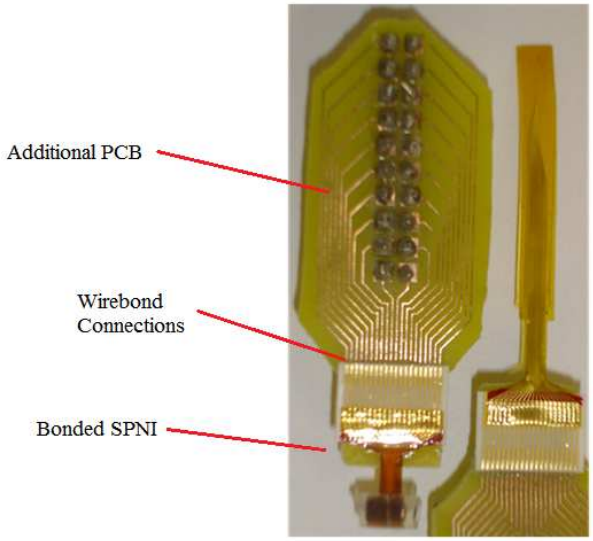

Fig. 5.6: The SPNI was bonded to an additional PCB, to perform the EIS

the electrode under test. The network analyser was software controlled by a custom-written LabView (National Instruments) program written by Andreas Frommhold, to allow for efficient data extraction.

Operation of Impedance Network Analyser

The impedance analyser operates through an auto-balancing bridge method which is illustrated in Figure 5.7. Put simply, the complex impedance of the device under test (DUT) can be measured using the voltmeter and ammeter (to measure magnitude and phase) in response to a signal generated at the signal source. In the auto balancing bridge method, the test signal current flowing though the DUT, I_x also flows through a 'range' resistor, R_r, to maintain a zero potential at

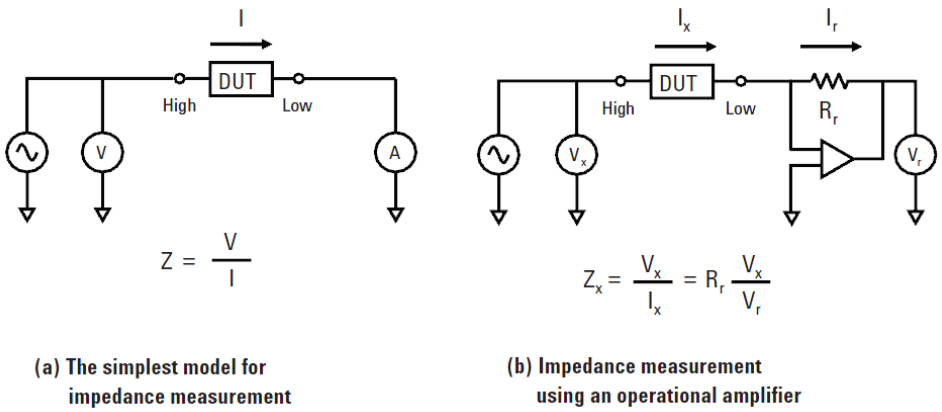

Fig. 5.7: Principle of Auto-Balancing bridge method-obtained from user manual of impedance analyser [58]

the 'low' terminal. The voltage at the low terminal is constantly monitored and balanced to zero by a feedback loop controlled through an IV converter amplifier. The impedance of the device is then determined via a measurement of the voltage at the high terminal through V_x and also at the range resistor through V_r, and then applying the equation,

$$Z_x = \frac{V_x}{I_x} = R_r \frac{V_x}{V_r} \tag{5.1}$$

as the value of the range resistor is known. This measurement system allows for a high accuracy (0.08% of measured impedance) impedance measurement over a large frequency range between 40-110MHz with an injected signal level of 5mv to 1 V_{rms}. The analyser can measure impedances in the range of 3mΩ and 500MΩ and the phase which will be between 0 and -90°[58].

5.2.2 Tensile Strength Testing

The mechanical durability of neural interfaces is an important consideration in the design and application, as the devices have to be capable of surviving handling, implantation and movement of the patient during its lifetime. Any mechanical weakness of the neural device during these phases would limit its ability to provide a stable recording/stimulation platform.

To test the overall mechanical strength of the device, a series of tensile tests were conducted using an Instron Environmental Mechanical Analyser (Instron 5848 MicroTester), that is able to measure mechanical properties, such as tensile and compressive strengths, under conditions

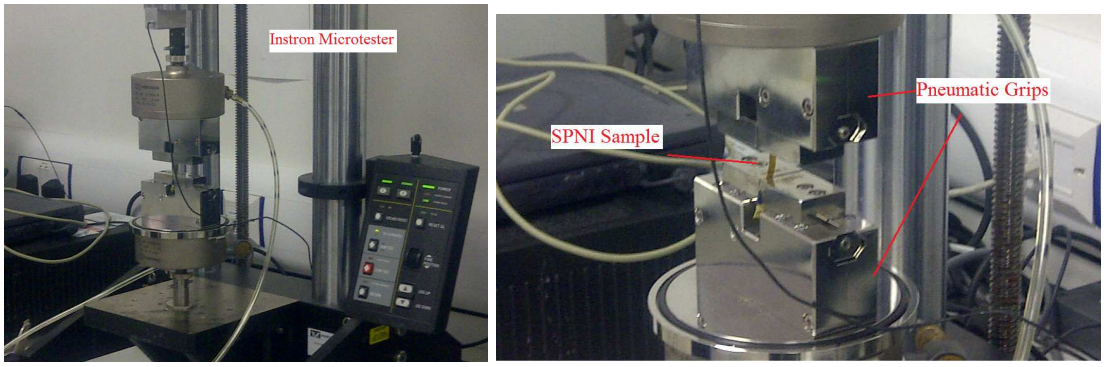

Fig. 5.8: The Instron Microtester.

of controlled temperature and humidity.

To test the polyimide interface, the two ends of the device were fixed onto the testing stage by the grips shown in Figure 5.8, and pulled apart at a rate of 0.1mm per second. The grip were either pneumatically operated, or fixed manually using screws. The test was ended automatically when the measured rate of extension was 40% larger for the same applied load, indicating a physical break of some sort. The tests were performed using a 100N load cell and 2kN stage and were designed to be illustrative of the devices overall ability to withstand longitudinal mechanical stress. To allow for data extraction the Instron tester is synchronised to software called ‘Bluehill 2’, that automatically calculated the load, strain, Young’s modulus and tensile extension of the sample, giving some in-putted initial conditions.

6. THE DEVELOPMENT OF THE SPIRAL PERIPHERAL NERVE INTERFACE

6.1 Introduction

The spiral peripheral nerve interface (SPNI) has been developed to record neural activity of regenerated axons whilst utilising micro-channels as axonal amplifiers, introduced in chapter four. The benefits of augmenting the extracellular interface have been outlined but it is necessary to consider the biological aspects of the constriction. To build a more complete model of the physiological environment Lacour et al investigated the optimal channel cross-section and density using in vitro cultures of the dorsal root ganglion of rats[59] and the results from this work will be introduced first.

The passive experiments of Lacour et al inspired an implantable device that is capable of providing a chronic recording array for use with technology designed to compensate for a loss of motor function. The latter parts of the chapter present the process through which the first recording micro-channel arrays was realised.

6.2 In Vitro study of axon outgrowth as a function of channel size, shape and transparency

The first study by Lacour used 2D channel arrays of polyimide(Pyrallin 2611(HD Microsystems) and Photosensitive Durimide 7020 and 7505) to test the effectiveness of ‘artificial’ mechanical guidance of axon growth through micro-channels; Dorsal root ganglions were seeded on a plating area and neurites were allowed to extend towards the channels as shown in Figure 6.1. From this study Lacour suggested that the best axonal growth would be achieved when the width of the channel and the spacing between channels has a ratio of 1:1. This allows for an efficient entry of axons into the channels and when the transparency of the device (the ratio

Fig. 6.1: Left; Dorsal Root Ganglions cultured onto polyimide arrays have an oblique approach, strait approach or turn away Right; Proportion of cultured neurites entering the 2D channels versus channel array transparency for a) neonatal rats and b) adult rats.
[59]

between the channel width and the channel pitch) was >50% the number of fibers entering the device was 80%, as shown in Figure 6.1.

6.2.1 3D Micro-channel structures

Polyimide micro-channels can support axon growth in the 2D plane but to achieve total encapsulation it is necessary to convert the planar micro-channels into a full 3D interface. Polyimide is a highly flexible material and can be rolled along the length of the channels as in Figure 6.2. This results in a mesh of parallel channels on concentric substrate layers that form a 'swiss roll' spiral-type structure as shown in Figure 6.3. Once rolled the polyimde devices can be inserted into silicone tubes, with an internal diameter of 1.5mm. The tube stops the polyimde from unravelling and also allows easier handling during the surgical process. Lacour et al [60] implanted this polyimide structure into the sciatic nerve of adult rats for 4 to 12 weeks and evaluated the axon regeneration, vasculation and the biocompatibility of the PI.

All the devices tested were passive, without the metallization, and so the fabrication process consisted of; Spinning a 25 μm thick layer PI substrate layer onto a silicon carrier wafer and curing to create a substrate before a further 40 μm thick layer of Photosensitive PI (Durimide 7020) was spun, defined into the 2D channel structure using photolithography and cured. After curing the devices were peeled from the wafer and cut into shape using scissors before being rolled and inserted into the silicone tube as described. The channel dimensions were 70 μm x 40 μm and each channel was separated by a wall of 40 μm tall PSPI that was 30 μm wide. The

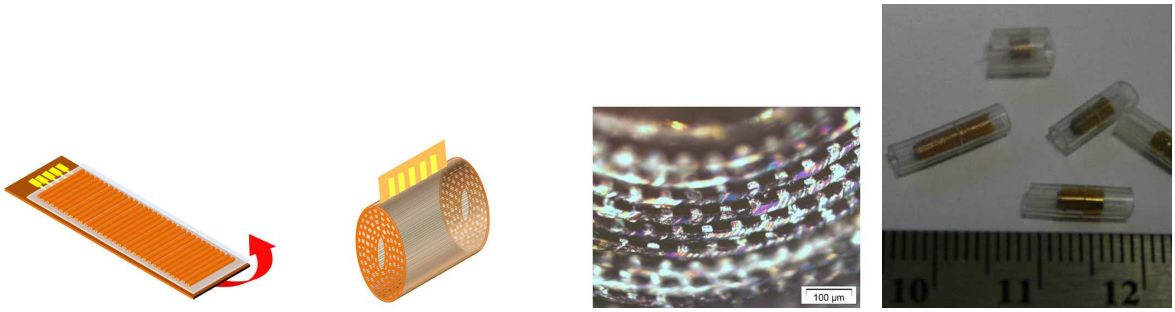

Fig. 6.2: The 2D channel array (Far Left) is rolled to give the 3D implant (Middle Left) which results in 'Swiss roll' micro-channel arrangement as pictured (Middle Right). Once the device have been rolled they are inserted into silicone tubing(Far Right)
[60]

channels were 6 mm long and the sciatic nerve was sutured to the silicone tubing at a distance of 3 mm from the channels. At four weeks and twelve weeks post-implantation the devices were ex-planted and any regenerated material in the device was investigated.

Unfortunately, axon regeneration through the polymeric device was low and in the devices that had been in the animal for twelve weeks mainly connective tissue and blood vessels had occupied the available space. It was suggested that the micro-channel cross-section and transparency may be too small to support regeneration. The transparency of the rolled device is lower than the 2D planar equivalent array due to the substrate that separates each concentric layer of channels; as the calculation of transparency includes all the walls that enclose the space. For channel width of 70 μm x 40 μm the transparency is 43%;

$$T = \frac{\text{Area of Channel}}{\text{Total Area of Device}} = \frac{wt}{(w+s)(t+x)}$$

$$T = \frac{2800\mu m^2}{(100\mu m)(65\mu m)} = \frac{2800}{6500}$$

$$T = 0.43$$

Where T is the transparency, w is the width of the channel, s is the width of the wall, t is the height of wall and x is the substrate thickness. At this transparency it would be expected that the maximum proportion of neurons to enter the channels is only 60-70% from Figure 6.1, which is not ideal for a regenerative application. Furthermore, the study also investigated silicone implants with channel dimension 100 μm x 100 μm (Transparency ≥0.49) that showed good axon regeneration and vasculation. All regenerated axons were surrounded by fibrous tissue that

in some cases filled up to half of the channel space, however it had been clearly demonstrated that the arrays of channels with a cross-section of 100 μm x 100 μm could support regenerating axons. Blood vessels were found to grow through channels up to 5 mm in length, vital to supply oxygen and nutrients to the regenerating tissue[60]. Thus this study showed that not only was the transparency important for neurites entering the channel but the diameter of the channel should be large enough to support regenerated fibers in the channel.

6.3 The Spiral Peripheral Nerve Interface

The passive devices had shown that polyimide channels could support nerve regeneration in vitro and in vivo. From the theoretical work it had been suggested that a micro-channel that is of a similar size to the regenerated axon would give the most amplification, and a micro-channel of up to 1 cm should be considered. The method of rolling the polyimide structure into the 3D polymeric micro-channel interface was a realistic method of achieving axonal amplification but, although regeneration is possible without growth factors, the polyimide implants that had a channel cross-section of 70 x 40 μm^2 showed relatively poor regeneration compared to a silicone implant that had a channel of 100 μm diameter.

Building on the theoretical predictions and the investigation of nerve regeneration in the micro-channel array, an implant has been designed with embedded electrodes that are capable of recording activity form the regenerated tissue. Samia Benmerah designed and fabricated the implant using computer assisted design software and processes that were discussed in Chapter 4.

6.3.1 Design

To improve the regeneration of the axons the micro-channel of the polyimide scaffold size was increased to 100 μm square channels, made from polyimide walls on top of a flexible polyimide substrate. Making the channels larger increases the transparency, allowing more regenerative media to enter the device. Once inside the SPNI, electrodes embedded into the channels can detect nerve signals from the regenerated tissue. The electrodes are coupled to connection pads via tracks that extend down the length of the device such that external connections could be made through a zero-insertion force connector, or by directly fixing external wiring with a

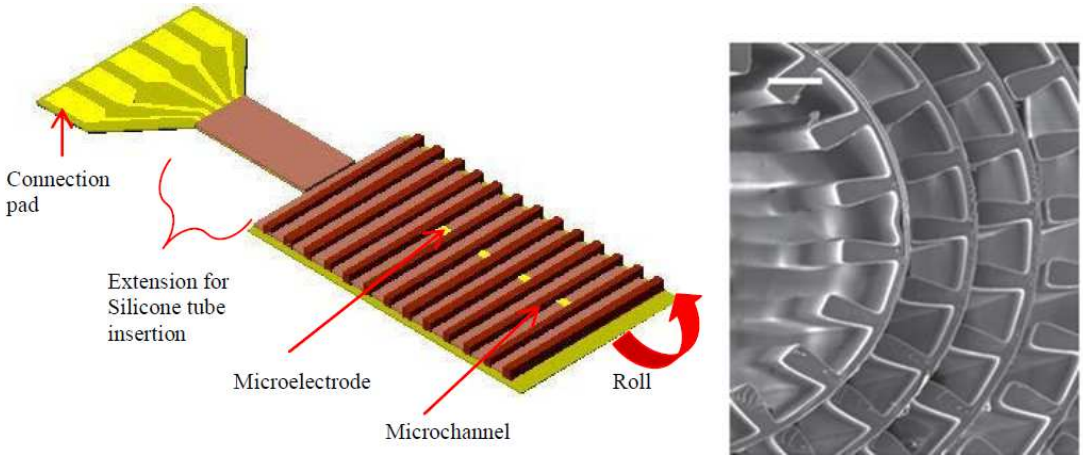

Fig. 6.3: Left; Schematic of Spiral Peripheral Nerve interface with recording capability, Right; Scanning Electron Microscope image of micro-channel array

conductive epoxy.

A channel of 100 x 100 μm has a cross-sectional area of 10000 μm, which is the equivalent of a circle with a radius of 56 μm. From the theory of Stein and Pearson (Equation 4.19) it can be suggested that an unmyelinated axon of 1 μm-radius in a channel of 56 μm-radius with a peak trans-membrane potential of 30 mV would be expected to give a recorded potential of 25 μV for an electrode placed at the mid-point of the channel. If the electrode has an impedance of 1 MΩ at 1000 Hz recording with a bandwidth of 10 kHz, Equation 4.1 suggests that this potential would be x2.5 above the noise floor and should be recordable. Thus a 100 x 100 μm channel should be suitable to provide an adequate amount of axonal amplification to record from the regenerated fibers.

Electrode Size and Placement

During the study of the passive devices it was found that the layers closer to the centre of the spiral supported more axon regeneration than the outer layers. The inner rolls of the device correspond to channels that are near to the end of the device before rolling and thus the electrodes were placed as close as possible to this region. As such, the electrodes were designed to be on the third roll of the device.

Each electrode was designed to be in the middle of its designated channel, with one electrode per channel, as the theoretical predictions indicated that the amplifying effects of the channels was maximised at the centre. To reduce the amount of cross-talk between the recording sites,

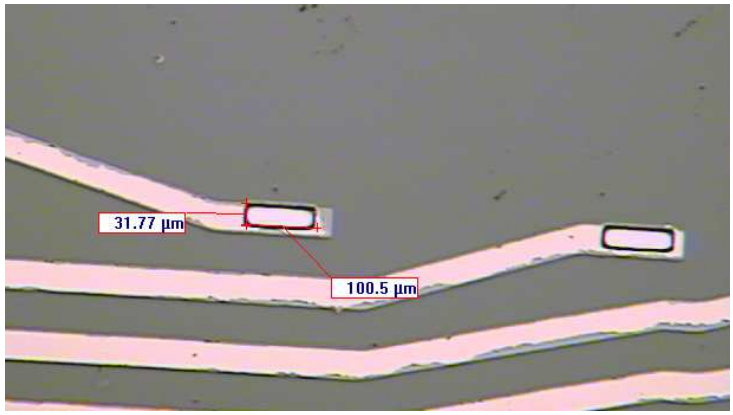

Fig. 6.4: Electrodes defined onto each gold track

the electrodes were not designed to be in neighbouring channels, and were instead designed to be situated in every 4th channel with a 600μm spacing between recording sites when the device is unrolled. The electrodes were designed to be 100 μm x 30 μm. Positioning the electrodes on the inside rolls of the spiral causes them to experience more strain than they would in the outer rolls, as the radius of curvature is smaller and so there is more bending in the thin-film metal layer. The strain is an important factor to consider in the performance of the device, as too much strain can cause fracture and failure of the metal layer. This will be discussed in detail in the next chapter, however it should be noted that very few devices have failed in the studies reported so far. Both Benmerah and Lacour calculated that the substrate needed to be around 25μm-thick to ensure that the stress on the wiring was minimised [10, 60]. It will be shown in the next chapter that this substrate thickness was calculated incorrectly.

6.3.2 Fabrication of SPNI

The SPNI was fabricated by Samia Benmerah according to the process flow as illustrated in Figure 6.5.

- a: A 4“ silicon wafer was cleaned with acetone and IPA and baked at 150°C for 5 mins .
- b-c: The substrate layer was formed by depositing a 12.5 μm of PI-2611, curing at 350°C in N_2 before depositing a second layer of 12.5 μm of PI-2611 and curing again. This gave a 25 μm substrate layer.
- d: 5 nm of chrome and 300 nm of gold were deposited by thermal evaporation. To define the metal layer into connection pads and the wiring that connects to the electrode, the

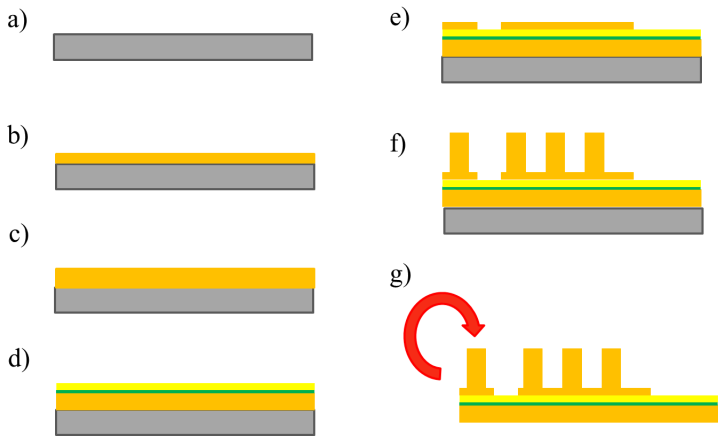

Fig. 6.5: The process of flow of SPNI fabrication [10]

metallization was patterned using a 2 μm layer of S1813 and a wet etch.

- e: To passivate the electrodes the patterned metal layer was encapsulated with a 5 μm layer of PSPI (Durimide 7505, Fujifilm), and defined using photolithography. The electrodes and the connection pads were left open to form a 30 μm x 100 μm electrode site and a 400 μm x 1 mm pad to allow for neural recording and connection, see Figure 6.4 and Figure 6.6.

- f: To make the channel layer, a 100μm PSPI layer was spun and baked at 0.5°C per minute between 20 °C and 90°C, and held for 30 minutes. This was defined using photolithography to give the channels shown in Figure 6.7

- After curing, the samples were removed from the carrier as a sheet, by peeling the substrate layers from the silicon wafer. The individual devices were cut out using scissors to form the connection region, the region that carries the channels, and a narrow 'neck' region that connects the two. The 'neck' of the device was chosen to be narrower that the other parts to allow for an easier insertion into the silicone tube.

- g: To roll the device into the spiral configuration, the end of the device was clamped into a pair of tweezers that were connected to a hand operated rotating mechanism. The tweezers were gently turned to form a tight spiral in the direction perpendicular to the channels and the rolled device was inserted into a silicone tube that leads the nerve stump into the micro-channel array. This is shown in Figure 6.8.

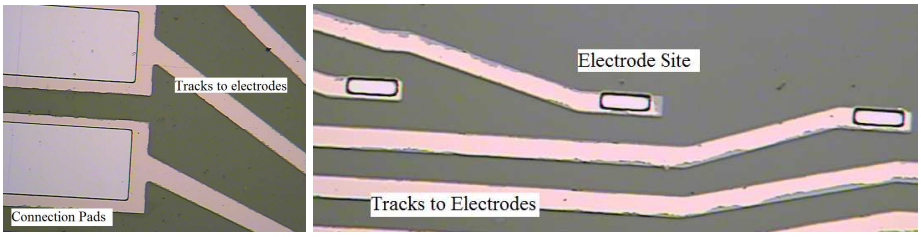

Fig. 6.6: Left: Connection pads surrounded by insulating Durimide 7505, the width of each pads is 400μm. Right: Electrode sites insulated by durimide 7505, the site are 100μm x 30μm

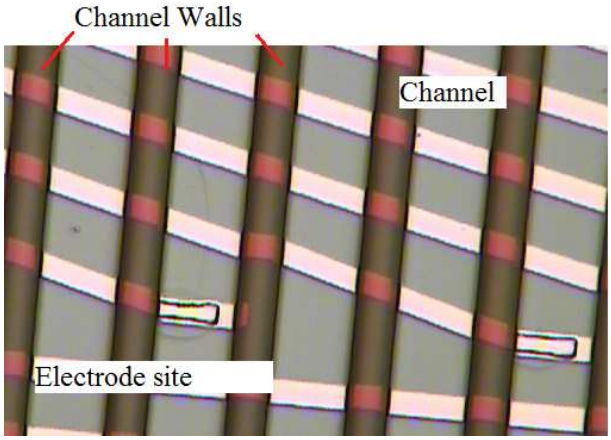

Fig. 6.7: Thick layer of PSPI defined into channels that are 100μm wide with 50μm wide insulating walls. Electrode sites are left open to allow the electrical coupling to the regenerated media

After rolling, the polyimide implants were 4 mm in length and the rolled micro-channels had a total diameter of 1.5 mm, which is determined by the inner diameter of the silicone tube. The SPNI contained ≈170 micro-channels in the array of which 20 micro-channels contained electrodes.

6.3.3 In Vivo Performance of Implants

To investigate the electrophysiology and the histology of the tissue that regenerated through the array, the SPNI device was implanted to the sectioned sciatic nerve of a rat [13]. Before implantation, the hole at the centre of the implant was blocked using a plastic plug to encourage the nerve to regenerate in the area of the electrodes rather than in the empty space. A total of 6 devices were implanted and left for 3 months. The study also investigated the use of a similar micro-channel array made of silicone (PDMS) that had 24 micro-channels of 130 μm diameter all contained within the same size 1.5 mm-diameter silicone tube. The performance of the silicone array serves as a useful comparison to the performance of the polyimide device.

To implant the devices the micro-channel arrays were filled with isotonic saline and the

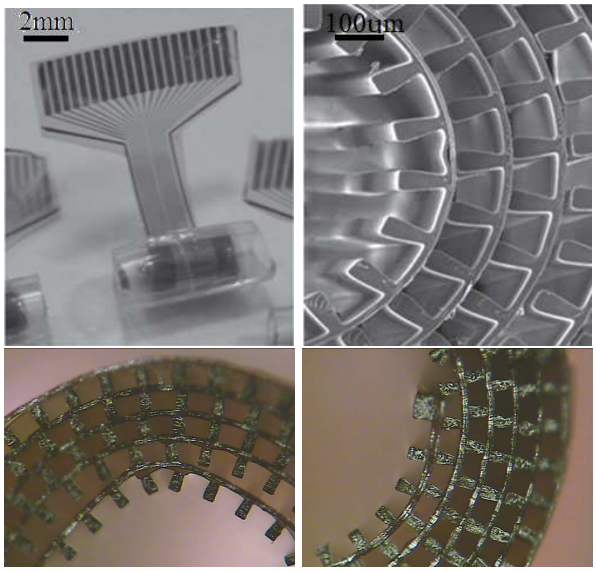

Fig. 6.8: The fabricated SPNI array, Top Left: Rolled SPNI in silicone tube, Top Right: SEM of the rolled channel, Bottom Left and Right: Microscopy of rolled channels, channels are 100μm square and separated by 50μm insulating walls. The sample has been evaporated with gold to allow for easier inspection. (Received through personal communication with Samia Benmerah) [13]

nerve stumps were fixed into the silicone tubing at either end of the implant with nylon sutures. The region containing the connection pads was led out through the muscular layer, and was positioned just beneath the surface of the skin. The wound was closed and the animals were allowed to recover.

After 3 months, animals were re-anaesthetised and the skin was opened to expose the connector pads of the SPNI. To make electrical connections the back of the pads were glued to a metal bar, positioned just above the wound. The bar gave mechanical support to the connector pads and electrical contact was made using a needle as shown in Figure 6.9. The reference electrode for the electrophysiology was a needle inserted into the hind-limb of the anaesthetized animal [13].

Impedance analysis of SPNI in vivo

To investigate the continuity of the thin-film gold on the rolled substrate and any degradation of the electrode sites, the impedance at 1 kHz of each of the 20 electrodes in each device was measured (total of 120 electrodes). At the end of the implantation four electrodes were open-circuit, suggesting that they had failed completely. The impedances of the 116 functioning electrodes at the end of the implantation are shown in Figure 6.10. Most of the electrodes

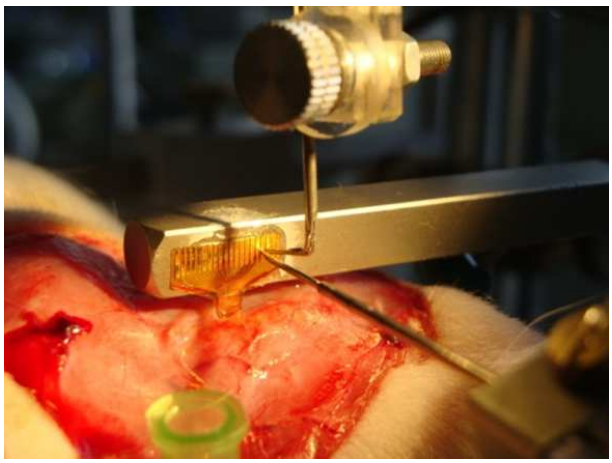

Fig. 6.9: Experimental set up used to couple the SPNI to external electronics[Received through personal communication with Dr J. Fitzgerald]

($\approx$ 75%) had an impedance up to 2.5 MΩ and within this group the impedances were normally distributed with a mean 1.24 MΩ [13]. The remaining electrodes had higher impedances that suggested electrode degradation and/or a microfabrication defects. Unfortunately no impedance spectra were presented for the samples before implantation The distribution reflects the ability of the SPNI to withstand the combined effects of the rolling process and subsequent three month exposure to the physiological environment. The distribution does not provide information about the variation of impedance for different electrodes within each device so it is not possible to evaluate how the impedance of electrodes varied relative to their position within the array.

Stimulation

To investigate the ability of the SPNI to stimulate EMG responses, current stimulus pulses were applied to each functioning electrode in each device. The EMG was simultaneously recorded in the tibialis anterior (t.a.) and at the gastrocenemius (gastroc.) using the set-up shown in Figure 6.11; the concentric electrodes were connected to a DC amplifier with filters set at 300 Hz (high pass) and 3 kHz (low pass).

Muscle activity was elicited in 5 out of 6 animals; EMG responses in the t.a. were seen in stimulation of 32% of functioning electrodes and more than one t.a. motor unit was activated in 28 of these channels; EMG responses in the gastroc. were activated by 41% of electrodes with multiple motor units being stimulated in 24 channels. Figure 6.11 shows EMG changes with increasing stimulus current in a channel which activated both t.a. and gastroc. motor units. For

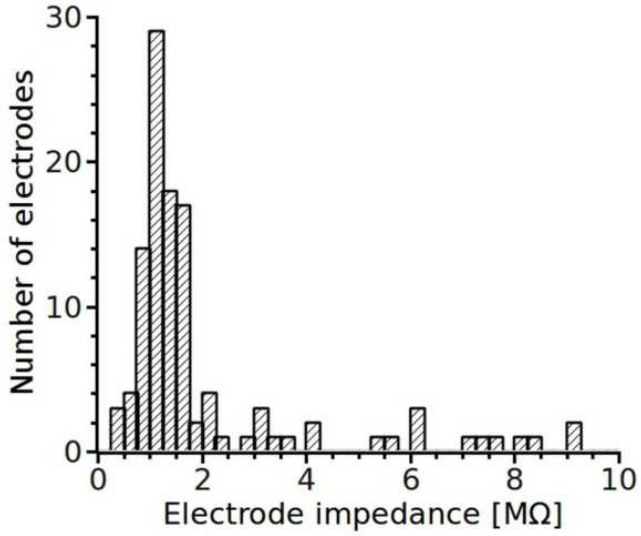

Fig. 6.10: Impedance of electrodes at 1 kHz, after being implanted for 3 months in the rat sciatic nerve. [13]

this study the firing of a motor unit is defined as the firing of a motor axon and all the muscle fibers that it activates. Different motor units can be distinguished by their patterns of activity in the EMG recordings.

The stimulus current required to activate an EMG response was relatively low. However, when compared to the silicone arrays the stimulus currents were several times larger. The mean stimulus current for the polyimide array was 26.2 μA, compared to 4.29 μA for the silicone device. The silicone devices had larger micro-channels suggesting that the stimulus current should be higher than the SPNI. However the silicone device had sealed micro-channels, which could not be guaranteed in the SPNI and the increase of the stimulation current could be due to imperfect sealing between layers of the roll. This can be seen in Figure 6.8, where there are visible gaps between the tops of the channels and the 'roof', which is the back of the substrate of the adjacent roll. The gaps can reduce axonal amplification by allowing stimulation current to spill out of the channel.

The study also showed that the imperfect sealing of the channels was great enough to generate cross-talk between electrodes. The investigation suggested that the same EMG response could be generated from adjacent channels.

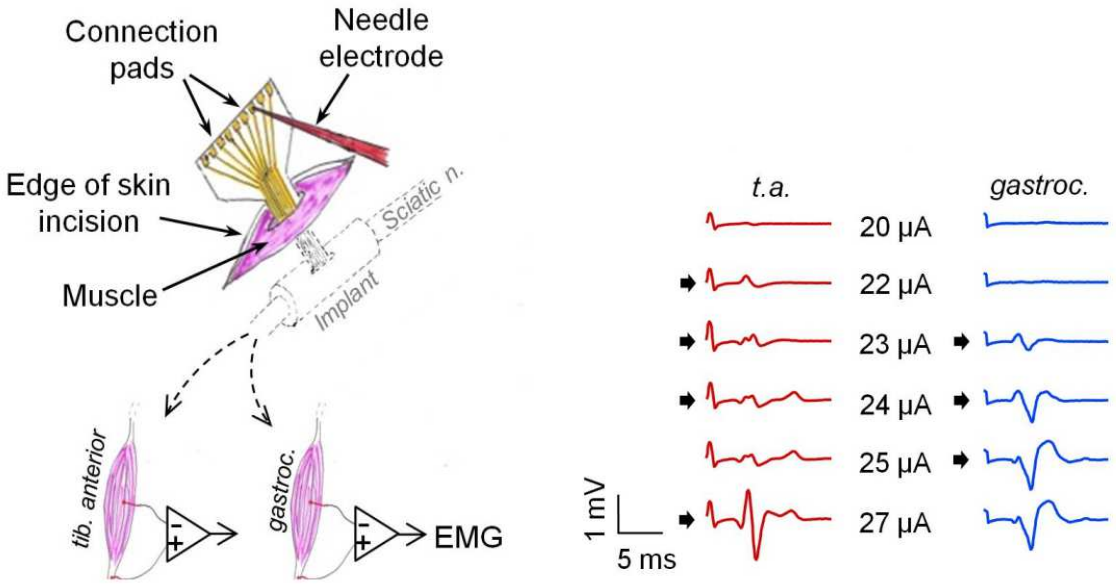

Fig. 6.11: Left: Experimental set-up used to investigate the EMG response from stimulation through the SPNI implant, Right: The EMG response evoked in the gastroc and the t. a through the stimulation of one innervated channel, arrow represents onset of stimulus.

[13]

Recording in the SPNI

To investigate the ability of the SPNI to record from the regenerated tissue inside the channel action potentials were generated in the foot of the rat by applying signal current pulses of 1-10 mA through needle electrodes. The stimulating electrodes were applied to nerves distal to the implant, while recording from the electrode in the channel. The study focused on channels that had generated clear EMG responses which were likely to contain regenerated tissue. The study recorded potentials in 8 channels, demonstrating that the implant could interface to axons that were connected to distal sensory nerves.

A typical example is shown in Figure 6.12, which shows an early large compound action potential between the arrows, followed several milliseconds later by a smaller signal at the block star. Fitzgerald et al argued that by computing the distance from the stimulating electrodes to the SPNI implant, and the time from onset of stimulus to recording the signals, the conduction velocities of the recorded APs could be estimated. In general the conduction velocity of an axon is proportional to fiber diameter and from this relationship the study suggested that the largest fibers in the implant had a diameter of around 1.9 μm. Myelinated axons have a faster conduction velocity than unmyelinated axons, so it was suggested that the recorded EMG may

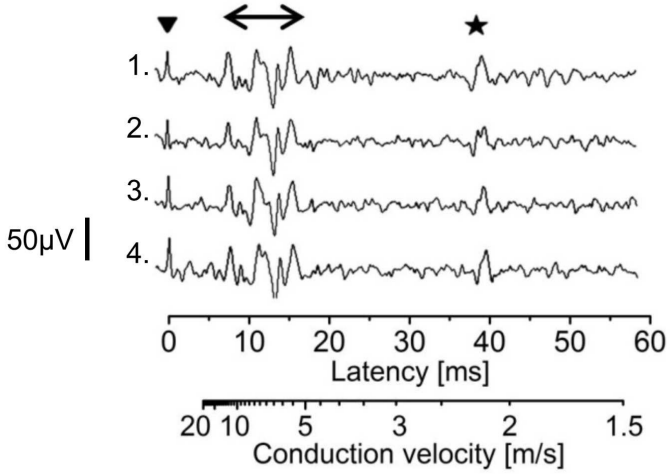

Fig. 6.12: Detection of evoked signals from axons that had been stimulated distally to the implant. The recording shows that afferent action potentials can be recorded from the regenerated tissue inside the SPNI.
[13]

be suggesting that both types of axon had regenerated into the implant where the larger, faster signal is a myelinated axon and the smaller, slower signal is an unmyelinated axon. This analysis may be flawed however as Stein and Pearson showed that the conduction velocity of the axon inside an axonal amplifier is reduced, when compared to activity in an unrestricted space. Instead, Stein and Pearson argued that a better estimate of the fiber diameter could be made by relating the size of recorded signal to the geometry of the restriction and the conductivities of the extracellular and intracellular regions [41]. Using Equation 4.19 it may be suggested that for a 50 μV recording the maximum fiber diameter is instead $\approx$5 μm. However, this estimate is based on a perfectly sealed channel, which cannot be guaranteed for this study.

Alternatively, the response indicated by a black star may be related to a reflex action that is triggered by the compound action potential, but this was not discussed in the original study. At this stage Figure 6.12 can only be used to highlight that the SPNI is capable of recording activity from regenerated axons and more work is required to relate this activity to specific axons/functions.

Histology of Regenerated Tissue

A histological investigation of tissue was not possible inside the implant as it could not be sectioned without damaging its contents. However, the study was able to investigate the nerve

that emerged immediately distal to the array which contained groups of myelinated axons that were separated by connective tissue [13], which is shown in Figure 6.13. The total number of regenerated myelinated axons in the distal nerve had a range of 1317 to 9380 with a mean of 6244. The silicone-type micro-channel array had far less regenerated axons (range of 1517 to 2734 with a mean 2059) when compared to the SPNI, despite the SPNI having smaller, longer channels. The improved regeneration of the SPNI's larger channels may be explained in terms of device transparency, as discussed previously. For the silicone implant ≈85% contained regenerated axons with a mean of 99 axons per channel.

$$\text{Transparency of SPNI} = \frac{170 \cdot (100\mu m)^2}{\pi(750\mu m)^2} \approx 96\% \tag{6.1}$$

$$\text{Transparency of Silicone Device} = \frac{24 \cdot \pi(130\mu m)^2}{\pi(750\mu m)^2} \approx 70\% \tag{6.2}$$

The above calculations show the relative transparency of the SPNI and silicone devices respectively. The SPNI has a densely packed array of channels that fills all of the available space in the tube (inserting the device into the tube causes the tube to swell slightly to accommodate the array.) The SPNI was designed in this way to try to guarantee that the micro-channels were tightly sealed. The slight swelling can be observed in Figure 6.13, where the radius of the structure after implantation is clearly greater than 750 μm (the radius of the tube). This image was taken after implantation, so there may be some discrepancy between this and the radius of the structure before implantation. The transparency depends hugely on the radius of the tube, if the radius of the tube increases by 50 μm due to swelling, Equation 6.1 suggests that the transparency of the SPNI interface goes down to ≈84%.

The histology of the tissue was investigated further using micro-computed tomography. In the study, whole SPNI implants containing regenerated tissue were treated with osmium tetroxide, making myelin-containing tissue radio-dense, see Figure 6.13. In the resulting image the regenerated nerve tissue is dark, the channel walls and the centre of the implant is grey, and the empty channels are white. Blood vessels appear as small white dots within the dark regenerated tissue in several of the channels, although the resolution of this imaging technique was not high enough to see individual axons [13]. This technique suggested that ≈ 70% of the SPNI channels contained myelinated regenerated tissue, which corresponds to ≈ 50 axons per channel.

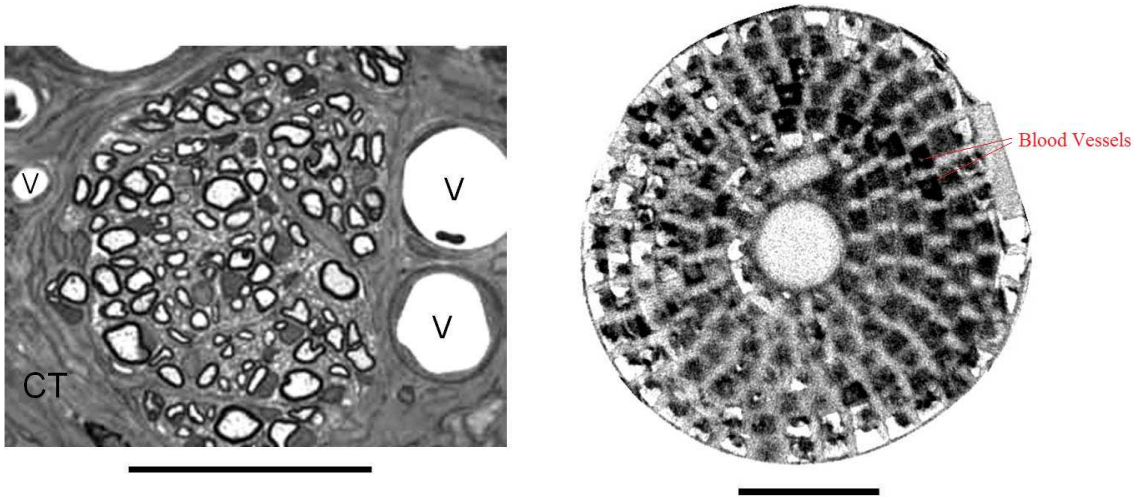

Fig. 6.13: Left: Bundles of axons, connective tissue(CT) and blood vessels(V) that have regenerated through the SPNI (bar=50μm) Right: Micro-comuted tomography of SPNI to show vasculation through the array (bar = 500μm).
[13]

6.4 Summary of this Chapter

This work provided a useful benchmark in the development of the SPNI, proving that;

- The array supported regenerated axons and the vasculation needed to sustain them.
- The array was able to record action potentials from the regenerated media.
- The SPNI was able stimulate activity in the t.a. and the gastroc.

Stimulation of the proximal sciatic nerve generated EMGs distally in the SPNI, demonstrating that regenerated axons inside the array had interfaced to muscle units. Action potentials were recorded inside the channels in the SPNI by stimulating the sciatic nerve distally, recordings of robust action potentials of various sizes and latencies were taken, indicating that the micro-channels provide sufficient amplification to allow extracellular recording from a range of axon diameters. The study estimated that the recorded signals had originated from a myelinated axon of 1.9 μm

The histology showed that the SPNI had more regenerated axons than the silicone implant, and the 100μm square channel supported axon regeneration well when compared to the earlier passive experiments. The sections of nerve just distal to the micro-channel array showed groups of axons fusing into a single nerve and micro-computed tomography suggested regenerated

neural tissue within the channel. This technology is still under development and will be of more use in assessing tissue within future generations of implant.

The silicone devices showed a mean stimulus threshold of 4.29 μA, however for the SPNI stimulus current requirements were significantly higher, and a minority of motor fibers were activated by current injected into more than one channel, probably due to imperfections in channel sealing.

The SPNI showed good durability, with 97% of the electrodes surviving the manufacturing process and remained functional after 3 months implantation. Although only 3% failed, a further 20% of channels exhibited impedances suggesting a significant degradation. The origin of this degradation is not known, however it may be related to the biocompatibility of the array. As discussed, the SPNI devices used were not optimised for biocompatibility, as they contained the chrome adhesion layer for the electrodes. However, despite this lack of optimisation the nerves appeared to be physiologically robust.

This work suggested that the SPNI was a good first model from which an interface could be developed. it was encouraging that significant regeneration could be supported through the micro-channel, from which axonal signal could be recorded. This architecture could offer the means to develop a peripheral nerve interface capable of providing sufficient resolution for the most complex applications. However, the method of integrating the device to the external electronics required to perform signal processing was highly unsatisfactory. The integration needs to supply a durable and stable coupling to each electrode simultaneously, which could not be achieved with the current device.

Before the study, it was suggested that a zero-insertion force(ZIF) connector could be used to make the connections. The ZIF connector works through a clasping mechanism where the connection area of the SPNI is inserted into the mouth of the ZIF, which is then closed to form a connection to the SPNI via pins on the inside surface. The clasp locks shut so that the SPNI should be fixed in place. However, once this technology had been tested it was determined that it was not suitable for the requirements of the implants as the clasping mechanism wasn't stable enough for chronic applications; The SPNI was too thin and would slip out during movement. By glueing the back of the SPNI to a piece of silicon wafer it may be possible to create a manifold onto which the ZIF connector could clasp correctly. Some earlier work suggested that this

may provide a workable solution, but this has been usurped by a more durable interconnection technology called ‘Microflex’. This new method of integrating the SPNI is the focus of the next chapter of the thesis.

Finally, to achieve the same level of performance as the silicone implant, the SPNI needs to have completely sealed channels. As discussed, the roof of the micro-channel array needs to be closed via an appropriate fabrication step, in addition to the previous steps of the device. This sealing of the channel layer is dealt with in the scope of this thesis.

7. IMPROVEMENT OF THE CONNECTION OF THE SPIRAL PERIPHERAL NERVE INTERFACE

7.1 Introduction

Establishing a durable and practical connection to external electronics has been a long term concern in the development of the SPNI. Many standard interconnection methods such as the use of solder, silver epoxy and ultrasonic bonding are not suitable for applications inside the human body due to biocompatibility problems and degradation of the coupling as a result of biological fluids in the PNS [61, 12]. This section of the thesis presents an updated fabrication process of the SPNI allowing for an easier integration to external electronics via ball-bonding to printed circuit boards. This 'Microflex' technology [62] creates electrical coupling by the thermosonic bonding of a gold ball (or 'bump') through the substrate of the implant to a gold surface underneath. The gold-gold bond is biocompatible and durable in the physiological environment and has been successfully incorporated into other nerve interfaces [63, 64].

During the development of the latest SPNI design it was found that to achieve a reliable ball bond the photosensitive polyimide (PSPI) substrate layer should be no thicker than 20μm. On the other hand, the gold layer should be on the neutral plane of the structure during rolling, to avoid stress on the thin film. Earlier studies of the SPNI incorrectly suggested that to achieve a neutral plane at the gold-layer a substrate of 25μm-thick should be used. However, by utilising the elastic theory of bending this calculation will be revised in this chapter.

To investigate the ability to vary the substrate thickness with the interconnection technology the new SPNI was designed to have a 20μm-thick, first substrate layer that would support the connecting area. On top of this a 18μm thick layer was defined that did not cover the connecting area. This creates a 18μm-high step that the gold tracks must cross before they enter the rolled section of the device. It was found that it was possible to maintain the electrical continuity in the thermally evaporated gold tracks.

Finally, whilst it is necessary to use PSPI as a substrate to efficiently make connection holes for ball bonding and define the overall footprint of the SPNI, PSPI adheres very well to the silicon carrier wafer, so it was not possible to peel the devices mechanically. Thus a suitable sacrificial material needed to be chosen that was compatible with other fabrication processes of original SPNI design. Poly-methyl-methacrylate (PMMA) was found to be suitable as it has been demonstrated to be a compatible sacrificial material with polyimide and it can be used with standard clean-room processes [65], with some special considerations. The updated design of the SPNI that include the Microflex interconnections is shown in Figure 7.7.

7.2 Interconnection techniques for neural implants

The interconnection technique used for the in vivo investigation of the SPNI was not satisfactory and an alternative interconnection technique is needed if the device is to be developed into a long-term neural interface, with reliable and durable function. The increasing miniaturization of biomedical devices has led to interest in interconnection techniques for micro-fabricated devices with stringent conditions imposed; all materials need to be biocompatible, lightweight to avoid stress on the delicate tissues, flexible enough to withstand prolonged implantation, and have small dimensions for successful implantation.

Due to the size restrictions faced when aiming for an integration to chip sized packages (or bare die), the interconnection techniques tend to focus on ultrasonic bonding (referred to as 'wedge/wire-bonding)', flip-chip technology or related methods. It is difficult to create repeatable, consistent bonds on this scale without resorting to these technologies. Ultrasonic wedge bonding is less desirable due to the possibility of the wires touching each other after implantation and the lack of a durable bonding technique to polymer materials. These problems can be reduced if the package is hermetically sealed to create a barrier to the physiological environment. However, the choice of material for the sealing is non-trivial as silicone, for example, can create small defects that cause mechanical stress on wire-bonds during curing, potentially causing failure [66].

As an alternative to these methods a new assembling technique was invented specifically for integration of flexible interconnections to microelectronic chips called Microflex interconnection technology (MFI). This technology has been successfully implemented in many devices

Fig. 7.1: Process flow to create flexible polyimide devices that are compatible with MFI technology [62]

similar to the SPNI.

7.2.1 Microflex Interconnection Technology (MFI)

In 1998 Beutal, Stieglitz, and Meyer developed Microflex technology to create a long-term, biocompatible coupling between a flexible neuroelectric interface and electronics for communication to the external world [67]. The fabrication of a 15μm-thick flexible polyimide ribbon cable, shown in Figure 7.1, was described that could be coupled to a CMOS package or other external electronics via MFI. Briefly, a 4" silicon wafer was coated with a 7μm-thick layer of polyimide (PI-2611) and cured on top of which metal layers were deposited to create interconnection tracks and connection pads, which are then insulated with a further layer of PI. Via holes were made through the PI layers by reactive ion etching and the devices were mechanically removed from the support wafer before MFI was performed. To couple the flexible cable to external electronics the MFI technology was adapted from traditional wire-bonding where a metal ball is thermosonically bonded to a pad made of suitable material, and then coupled to another pad via a wedge bond and loop of connected wire. Several combinations of ball and pad material are possible and the only determinants on which metals can be chosen are the ability of the two materials to form a welded bond for electrically reliable interconnections. Reference [68] is a review of wirebonding technology.

The standard ball-wedge bonding using gold wire is performed in the following steps;

- The gold ball is formed on the end of the gold wire by a 'flame-off' electrode
- The first 'ball bond' is made on the desired connection pads (source pad) by pressing the gold ball into the pad with pressure and thermosonic force

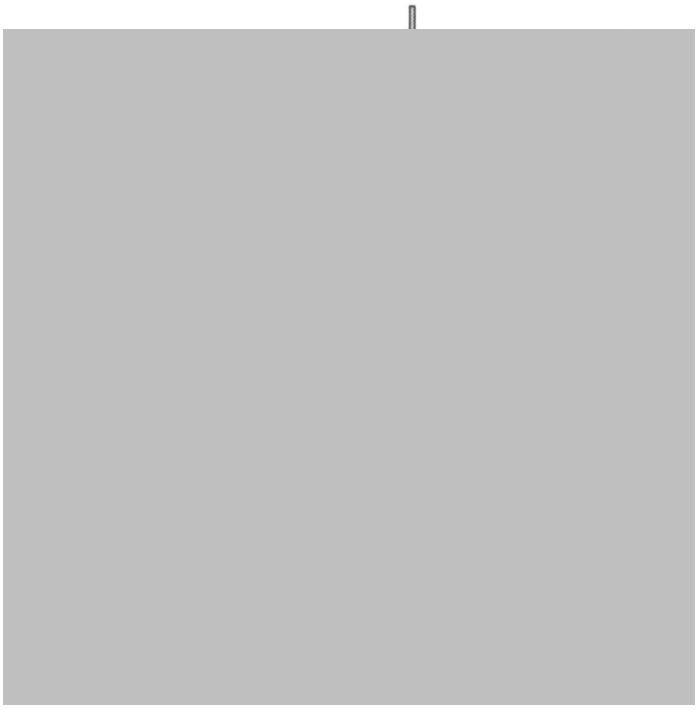

Fig. 7.2: Illustration of the MFI technique to connect a flexible ribbon to a substrate material [62]

- The second bond connects to a destination pad
- The bonding-tool is lifted and the wire is separated from wedge bond

Stieglitz et al adopted the traditional technology by bonding a 25μm-diameter gold wire, threaded through a small neck bonding-tool, through the PI substrate to make connections to aluminium bond pads [12]. This eliminated the second (wedge) bond, and used the first gold ball bond as a 'micro-rivet' between the two components that need to be connected, illustrated in Figure 7.2. In general, one component is the IC and the other component is the flexible device that has a via hole though which to rivet. After the gold ball bond is performed, the wire is broken to leave a rivet that connects the two components as seen in Figure 7.2.

The MFI technology was incorporated into the fabrication of polyimide-based neural interfaces of different designs (a sieve electrode and a cuff electrode) [69], fabricated using thin PI as the substrate material and are shown in Figure 7.4. The technique for making a single bond is illustrated Figure 7.3 where via-holes were designed to be slightly smaller than the ball bond to fix polyimide substrate after bonding, however making it too small causes the ball-bond to fail [62]. To make the connection in [62] the via hole had been riveted with a 35μm-diameter gold ball, made using 25μm gold wire. For these studies the substrate thickness varies between

Fig. 7.3: Overview of the ball bonding MFI technique and an SEM of a misaligned gold ball bond on a ribbon cable interconnection pad
[62]

Fig. 7.4: Flexible neural devices fabricated in PI and integrated with MFI technology
[69]

10-15μm. The via holes of the PI were aligned to 30μm wide CMOS bond pads that were separated by 70μm, suggesting that very fine pitches are possible with this technology. By measuring the contact resistance before and after thermal and mechanical stress [62][67] it was shown that MFI technology is robust, after stressing the connection no bond failures were observed. These devices showed that MFI was a suitable connection technique for neural devices fabricated using PI and more recently this technology has been incorporated into laser patterned electrode arrays of silicone and platinum foil, bonded to alumina substrates [70] [64]. Ceramic was chosen as a carrier material as it can be used as a platform for electronics and wireless data transfer systems [71]..

Fig. 7.5: Laser patterned electrode arrays incorporating MFI technology, Left: Long term micro-EcoG electrode bonded to alumina, Right: Laser printed electrodes bonded to ceramic PCB [64, 63]

Fig. 7.6: Comparison of the relative strengths of interconnection technologies for neural implants. Left; Examples of bending techniques used to conduct the tensile experiments, Right; Results of the tensile experiment. [70]

It has been reported that the maximum stress that the bonds could withstand is less than gap welding and soldering, as shown in Figure 7.6, however it should be noted that MFI was not the main source for failure as the stress concentration on the substrate material around the hole caused fatigue. By increasing the ratio of substrate material area to area of the via hole this problem could be reduced. Similarly, increasing the number of bonds reduces the amount of stress that each hole is subjected to. This lead to a connection scheme as illustrated in Figure 7.5. Microflex has also been shown to work in a long-term in vivo study with subdurally implanted Micro-EcoG electrodes [64], incorporating the MFI technology bonded to ceramic PCBs. The connected region was encapsulated with silicone to protect the bonds and provide strain relief, which was necessary as the device was implanted into a freely moving animal. Because of the silicone the MFI connections were not expected to degrade during the implantation, which was

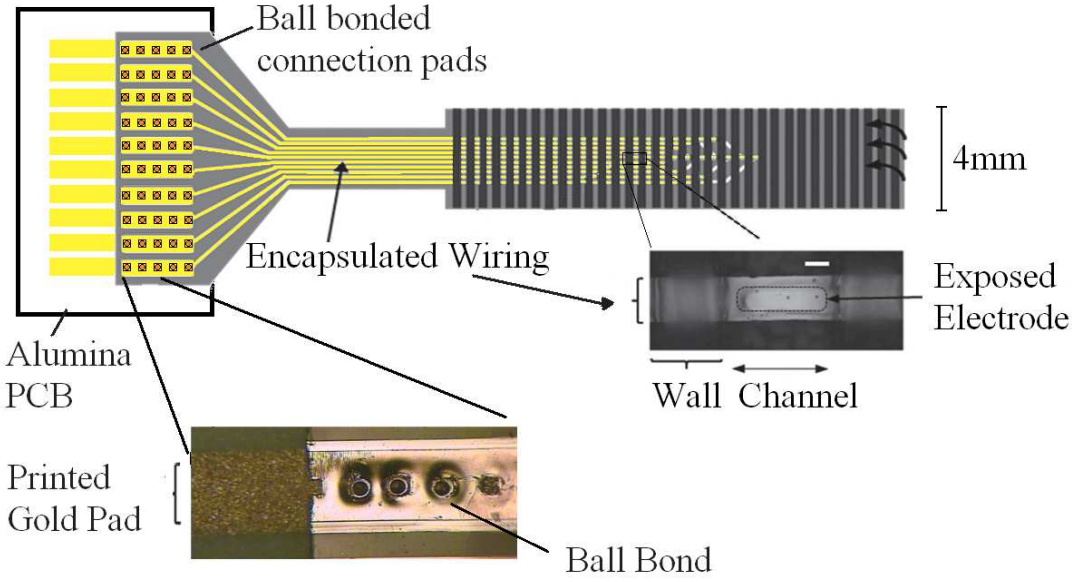

Fig. 7.7: Updated design of the SPNI including a connection region that is compatible with Microflex technology.

confirmed by performing impedance spectroscopy pre-, during and post-implantation. After 18 weeks there was no systematic degradation as the impedance of electrode interface remained constant.

7.3 Integration of MFI into SPNI fabrication process

To incorporate the Microflex technology into the SPNI it was decided to fabricate the substrate layer using the PSPI (Durimide 7020, Fujifilm), previously used for the 100μm-thick channel layer. By doing so, via-holes for the micro-rivets could be fabricated using the photolithographic techniques, negating the need for the reactive-ion etching process that was used by Steiglitz et al. The remainder of this chapter describes how this aim was achieved.

7.3.1 The Sacrificial Layer

The SPNI is fabricated onto a silicon wafer as it is inert to the fabrication process and easy to use with the clean room technology. Unfortunately, PSPI adheres very well to the silicon wafer due to the inclusion of an adhesion promoter (a methacrylate monomer) in the polyimide precursor, and so the previous method of releasing the SPNI (peeling) at the end of the process can no longer be used. A sacrificial layer must be used to ensure safe release of the processed

devices.

The ability to release micro-fabricated structures has been addressed widely in the recent literature as it is a common problem in micro-machining applications and the main methods to remove a sacrificial material are heating, chemical wet etching, dissolution and or dry etching. As such, a wide variety of sacrificial materials are available including metals, semiconductors and insulators. The most commonly used processes are wet etching and dissolution in an appropriate solvent, which are heavily diffusion dependent; Structures that have a larger surface area to surface boundary ratio will take a longer amount of time to release, as the solvent/chemical etches away the sacrificial material from the edges first.

7.3.2 Use of PMMA Sacrificial Layer

Kim et al [65], have used PMMA as sacrificial material with PI in the fabrication of flexible biosensors using a ≈1.2 μm layer of PMMA to support a 1.5 μm polyimide layer. Thus the PMMA process is compatible with the polyimide in general, but this study does not relate to the use of photosensitive polyimide, which has subsequent development stages using specific ancillaries.

Poly-methyl-methacrylate is a high resolution, organic photoresist that is used as a sacrificial material in many micro-fabrication applications to produce low-stress, thin layers via standard clean room processes [72]. The organic structure of PMMA is shown in Figure 7.8. Specifically,

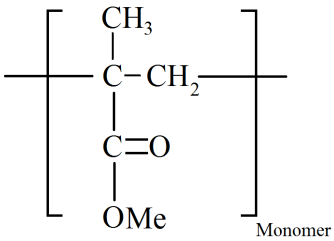

Fig. 7.8: Chemical structure of Methyl Methacrylate monomer, which is polymerised into PMMA

PMMA has found use as a sacrificial material in the production of suspended MEMS structures where sub-micron layers are fabricated onto Si wafers, photo-lithographically developed, and etched away using a dry etch process with an oxygen plasma. For a review of the possible uses of PMMA the reference [73] is recommended.

Johnstone, Foulds and Parameswaran also describe a method of using PMMA as a self-sacrificial layer for micro-machining and highlight important characteristics that need to be considered for the successful integration into the SPNI process [74].

Firstly, UV exposed PMMA is porous, which makes it good for development as it increases the etch rate, but could be potentially problematic during curing steps of the SPNI. At room temperature the exposed PMMA will shrink over time, a process which is accelerated for higher temperatures. This can cause cracks in sacrificial layer that may harm any further fabrication. To counteract this affect, the PMMA should not be baked at elevated temperatures, in excess of 150°C during the fabrication of the SPNI.

Secondly, the PMMA can produce volatile gasses during UV exposure which, when trapped under a barrier such as a PSPI layer, can cause blistering defects to form. This process is dependent on the total UV exposure and temperature history of the sample but a there is not a complete understanding yet. The study suggests that any baking steps performed after the initial bake of the PMMA should be stepped to reduce the effect of the blistering, which fits well with the fabrication of the SPNI.

Lastly, the study reported that most failures occurred as a loss of adhesion between the PMMA layer and the carrier material, most likely caused by absorption of IPA, water or both. The absorption can cause swelling which leads to stress between the layer interfaces. To reduce the risk of absorption the amount of IPA and water used during the development of the SPNI should be reduced, and acetone should be avoided altogether as this can etch PMMA. To avoid the use of acetone alternative cleaning methods have been employed including the combination of short oxygen plasma and UVO surface treatment.

Most of the reported studies use very thin (<1μm) sacrificial layers of PMMA which can be etched very quickly using the described techniques. To make the sacrificial layer of the SPNI more resilient a thicker layer of PMMA was required. Thus, a layer of 3μm thick PMMA was used in all investigations.

Investigation of PMMA

PMMA (PMMA-A9, MicroChem) was spun on wafers at 1500 rpm and baked at 180°C for 10 minutes. Different thicknesses of PSPI, ranging from 5 to 50 microns, were spun, developed

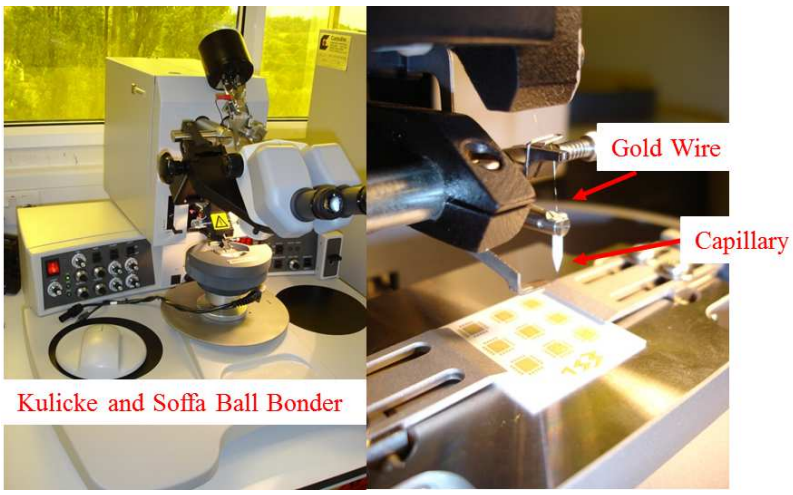

Fig. 7.9: The Kulicke and Soffa gold ball bonder in the EECE clean room

using photolithographic techniques and cured on the PMMA layer. The PMMA sacrificial layer was found to perform well during the development procedures, and did not cause any defect in the usual PSPI structures.

After curing, the PSPI had curled slightly around the edges, suggesting a de-lamination from the PMMA (possibly caused by the shrinking of the porous PMMA at elevated temperatures, discussed earlier), but overall the structure appeared to have cured normally. To release the samples, the wafer was immersed in a mixture of MIBK and IPA at a ratio of 3:1, and left for at least 24 hours. The samples were then carefully peeled from the carrier wafers using blunt tweezers and a razor blade, whilst wetting the samples with IPA.

This release mechanism produced well defined PSPI structures of different thickness and it was decided that 3μm sacrificial layers of PMMA were suitable for further use. As the method to produce photosensitive substrate layers was established it was then possible to start investigating the use of Microflex with the SPNI.

7.3.3 Initial tests of Microflex

Varying the Thickness of the SPNI

The original studies of MFI reported that it was possible to make reliable connections using a 10-15μm thick layer of Polyimide[62]. As photosensitive polyimide may produce different results it was necessary to investigate which thickness of PSPI could be reliably bonded.

PSPI of varying thickness were spun and defined as before. The samples were cured and

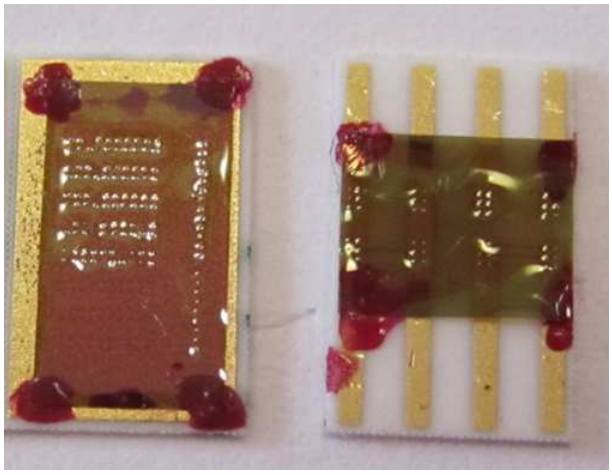

Fig. 7.10: Bonded samples used to test the hole width and substrate thickness. Each alumina piece is 0.5cm wide

then released, before being bonded to the alumina. Micro-rivet bonds were made according to the process flow in Figure 7.2, as previously discussed, using 25μm gold wire and a bonded through the polyimide to the alumina PCB underneath using a ball bonder shown in Figure 7.9 (Kulicke and Soffa, Model 4522). The size of the balls could be varied using the machine, but for consistency the ball was kept at ≈60μm-diameter at the base, as was recommend by the supplier of the wire bonder. It would have been possible to use a smaller diameter of bond, to mimic the earlier studies, however the shape of the bonding capillary may not have been appropriate to fabricate reproducible bonds using the smaller diameter bond (again from consultations with the supplier of the machine).

It was found that for PSPI layers thicker than 20μm it was very difficult to make reliable ball bonds as the ball could not reach the alumina underneath through the connection hole. PSPI layers thinner than 20μm could be bonded to the alumina without much difficulty, although the overall size of the connection hole did affect the reliability of the bonding process. This is consistent with the earlier studies of MFI technology. Examples of samples bonded using the Microflex technology in these initial investigations are shown in Figure 7.10.

Size of the via holes that are compatible with MFI

Once the reliable thickness of the PSPI had been realised the mask was used to investigate the effect of varying the size of the hole for the ball bonding. Holes ranging from 30μm to 70μm were defined into the PSPI layer and each hole was bonded using the same bonding force,

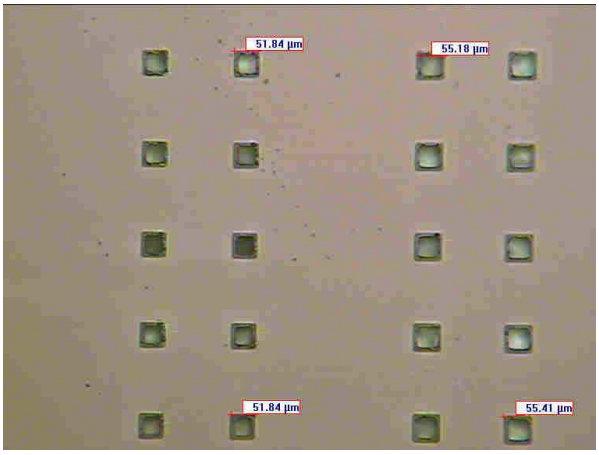

Fig. 7.11: Different sized holes used to test the Microflex technology

bonding time and size of ball. The size of the ball was determined by microscopy, shown in Figure 7.28. It was found that holes smaller than 35μm square were more difficult to develop, as the solvent used cannot etch out the material effectively. This can be seen as the darker areas inside the squares in the Figure 7.11, where the darker are is undeveloped PSPI. If there is undeveloped PSPI in the connection hole it will make it more difficult to bond, and for this reason it was found that holes greater than 50μm square, in general, gave the most reliable bonds, with the fewest bonds failing during the riveting process. This is possibly also due to the size of the ball bond used, which was kept at $\approx$ 60μm-diameter. To successfully incorporate the Microflex technology into the SPNI fabrication the PSPI substrate should be no thicker than 20μm with micro rivet holes between 50-70μm, and the PSPI layer should be fully cured before it is coupled to the alumina board.

Testing that the Microflex connections were Electrically Conductive

A strip of photosensitive polyimide was fabricated, on top of which a single band of metallization comprising of thermally evaporated chrome and gold was defined. This gold strip, on top of the PSPI, acted as a bridge in order to test that the Microflex interconnections were conductive. Connectivity through the Microflex connection via the gold strip was tested using a multimeter with probes in contact with the gold on the alumina. Several samples were tested using this method and all samples proved to have successful coupling though the Microflex connections. No attempts were made to measure the resistivity of the Microflex connection, as this was not the main objective of the project and this data has been reported elsewhere [12].

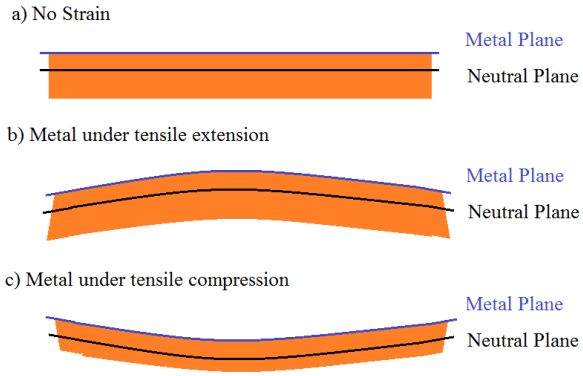

Fig. 7.12: Illustration of effect of bending the polyimide substrate on the metal layer, a) No strain, b) Tensile Extension of the metallization, c) tensile compression of the metallization

7.4 Stress in the Metal Layer due to Bending

It has been demonstrated that MFI could be successfully implemented for cured PSPI substrates thinner than 20μm. The range of substrate thickness that is compatible with SPNI is limited as the metallization is required to be on the neutral plane of the structure; during the rolling of the device into the micro-channel array the gold tracks experience either tension or compression, relative to the neutral plane of the device, as shown in Figure 7.12. If the wiring experiences tension/compression beyond its fracture limit then it will break. The gold tracks need to be durable enough to survive the rolling into the micro-channel array without diminishing the ability to record neural signals.

To reduce the strain on the wiring plane the gold layer should be designed to be on, or as close as possible to, the neutral plane of the device so that the metal layer experiences a minimal amount of stress.

To calculate the amount of strain on the gold layer due to rolling the elastic theory of bending is applied, for which several assumptions about the polyimide structure have to be made;

- The SPNI has constant, prismatic cross-section that is homogeneously flexible in the direction of bending
- It has a constant modulus of elasticity for compression and tension
- It is linearly elastic within the range of stresses being exerted

Clearly, these assumptions do not reflect true bending in the composite polyimide structure,

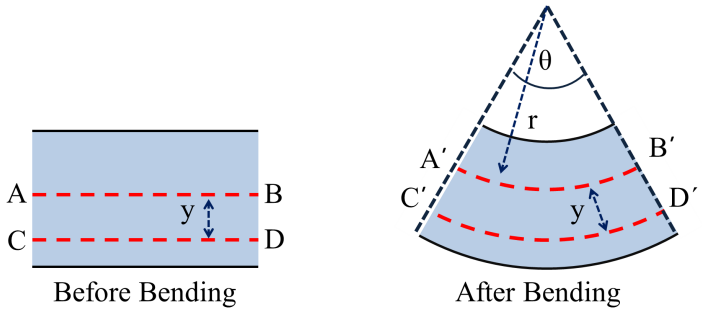

Fig. 7.13: Rectangular cross-section before and after bending, AB is the neutral plane, CD is a plane extending through the cross-section at a distance y from neutral plane. A′B′ and C′D′ are the planes through the section after bending, where θ is angle that characterises the length of the arc.

however, to build a theoretical prediction and to better understand the mechanics of the micro-channel array these assumptions are necessary.

For a rectangular section (shown in Figure 7.13) the neutral plane (AB) passes through the centroid where both the top and bottom surface of the section are equidistant. As the structure bends, a curve develops and the line $C'D'$ is elongated by a distance of $C'D' - CD$. As by definition the neutral plane is not deformed $A'B' - AB = 0$.

A transverse load on the rectangular object causes bending as shown in Figure 7.13, where the curve acts to distribute the load evenly across the structure and the length of the neutral axis can be related to its radius of curvature by,

$$AB = A'B' = r\theta \tag{7.1}$$

Where r, represents that radial distance to the neutral axis from the centre of the circle that includes the arc from A' to B'. The layer that extends from C to D is a distance y from the neutral axis, thus the radius of curvature for the arc from C' to D' is given by $r + y$. The length of the arc can be written as,

$$C'D' = (r + y)\theta \tag{7.2}$$

The arc from C' to D' is longer than the neutral axis by $y\theta$. This extra length causes strain (ϵ)

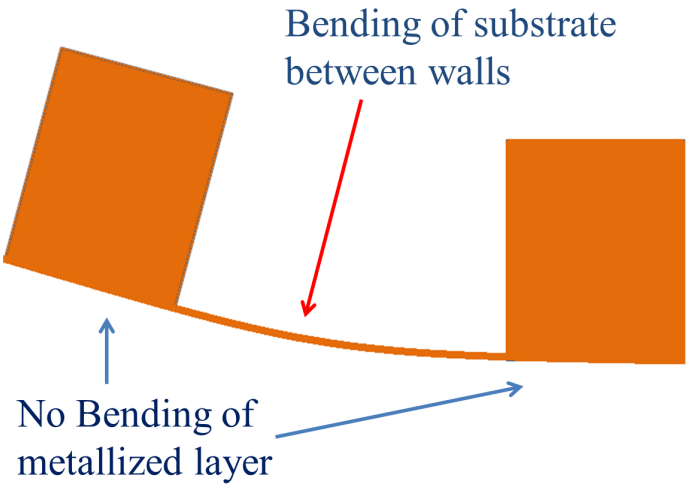

Fig. 7.14: Diagram of an alternative model of bending, only metallization in the regions between the walls is bent.

which can be written as,

$$\epsilon = \frac{C'D' - CD}{CD} = \frac{C'D' - AB}{AB} = \frac{(r+y)\theta - r\theta}{r\theta} = \frac{y}{r} \tag{7.3}$$

Thus the magnitude of the strain is proportional to the distance from the neutral plane (y).

7.4.1 The Neutral Plane of the SPNI

It is logical to assume that the micro-channel structure is having a direct impact on the distribution of the bending forces throughout the SPNI. If it is assumed that the regions of substrate carrying the thick channel walls do not bend then the only region that is under strain is between the walls. This is illustrated in Figure 7.14. This assumption is valid as the very thick polyimide regions are much more rigid than the flexible thin regions, and so the thin regions are expected to bend. To calculate the neutral axis of the composite structure the parallel axis method is used, where the centroid of each area, N_i, is calculated relative to the reference axis and multiplied by its area, A_i, as illustrated in Figure 7.15. The distance of the neutral axis from the reference axis is then found by summing the contribution of each section and dividing by the total area of the structure [75];

$$NP = \frac{\sum N_i A_i}{\sum A_i} \tag{7.4}$$

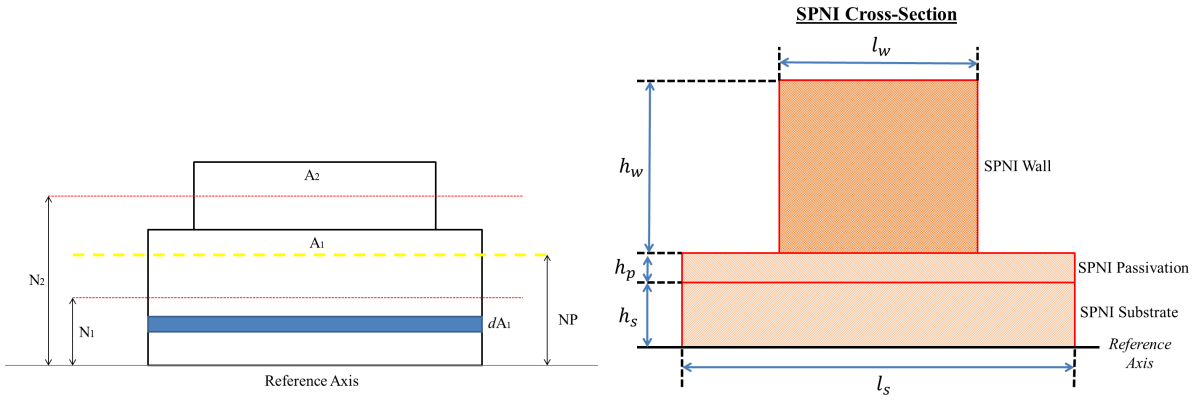

Fig. 7.15: Left: Illustration of the parallel axis method to calculate neutral plane of composite structure, Right: Diagram of the cross-section of a region of the SPNI micro-channel array with relevant notations (Not to Scale)

Calculating the relative position of the centroid of each rectangle is easy, as it falls at the mid-point that bisects each area. Similarly, the area of each rectangle can be calculated by multiplying its length by its height. If the metallization is only bent between the walls of the device then the position of the neutral axis depends on the thickness of the substrate and passivation only. Applying Equation 7.4 to the SPNI shown in Figure 7.15 shows that neutral plane is at,

$$\textbf{Neutral Plane} = \frac{(\frac{h_s}{2})(h_s \cdot L) + (h_s + \frac{h_p}{2})(h_p \cdot L)}{(h_s + h_p) \cdot L} = \frac{h_s + h_p}{2} \tag{7.5}$$

where h_s and h_p are the height of the substrate and the passivation layer respectively and L is length of the section between the channel walls, $L = l_s - l_w$. The metal layer itself is not included in the calculation as it is at least one order of magnitude thinner than the polyimide layers and thus is not expected to influence the position of the neutral plane. This assumption is used in other similar models [76]. For the SPNI samples used in the in vivo study this would equate to a neutral plane of $\frac{25\mu m+5\mu m}{2} = 15\mu m$, resulting in the metallization layer being 10μm away from the optimal distance. Importantly though, as the SPNI was rolled with the channels on the inside, the metallization layer was above the neutral plane with respect to the direction of bending to give tensile compression.

To calculate the equivalent strain that would be expected in the rolled structure for varying substrate thickness Equation 7.3 can be used, where the radius of curvature of the deformation is determined by the position of the film within the roll. Using a radius of curvature of 750μm,

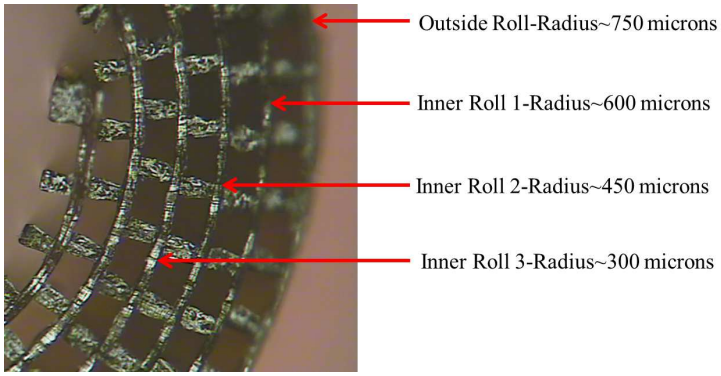

Fig. 7.16: Distribution of rolls within the SPNI, radial distances used as radius of curvature for strain calculations, each roll is assumed to be 150 microns apart

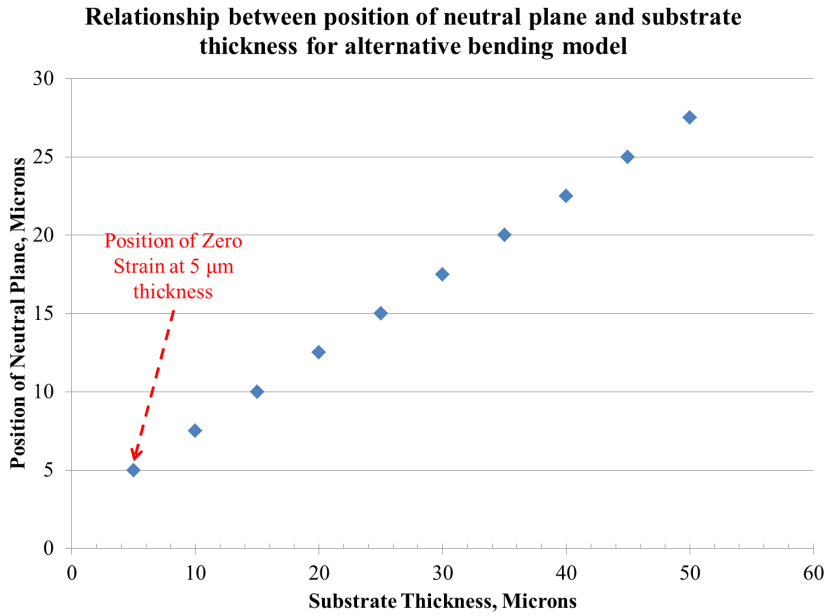

Fig. 7.17: Position of neutral plane against substrate thickness. Zero strain is at the point were the substrate thickness equals the passivation thickness (which is fixed at 5μm-thick), as indicated by the red arrow.

600μm, 450μm and 300μm for the outer roll and inside rolls respectively, as illustrated in Figure 7.16. The rolls on the very inside of the device have no metallization and can be neglected from the study. Equation 7.3 shows that the strain in any plane is equal to the distance to the neutral plane divided by the radius of curvature and so the relationship between the strain for each roll of the SPNI and the substrate thickness can be calculated. The effect of varying the substrate thickness on the position of the neutral plane and the equivalent strain in the structure are both plotted in Figure 7.17 and Figure 7.18 respectively. As a 5 μm passivation layer is usually used with the SPNI and this value has been fixed for the two plots. The figures suggest that the metallization is under no strain when the substrate thickness is equal to the thickness

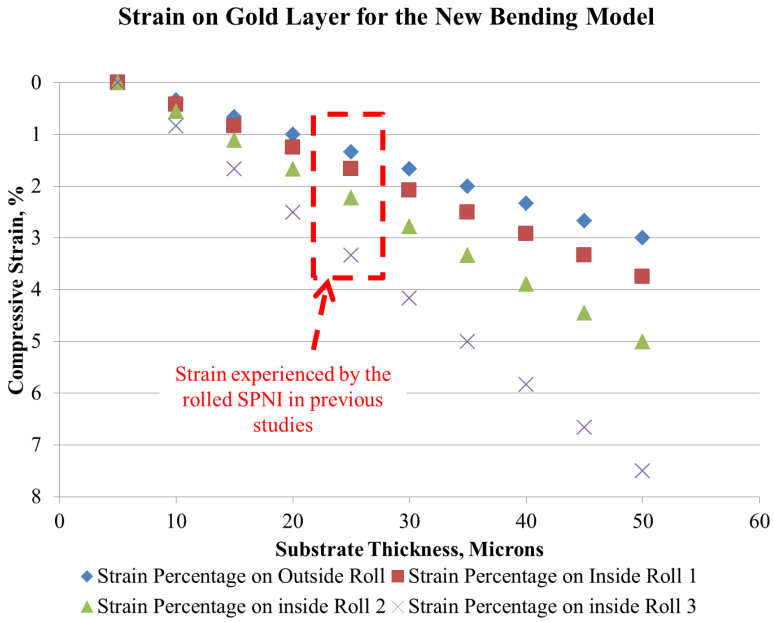

Fig. 7.18: Compressive strain in the SPNI for different substrate thickness for the new model of bending, where the passivation layer is fixed at 5 μm. The strain experienced by the SPNI samples in previous studies is highlighted in the red box.

of the passivation layer, as would be expected, and for the original SPNI the strain experienced was between 1-4%. Again, the gold layer was under tensile compression rather than tensile extension. The plots suggest that increasing the substrate thickness increases the amount of compression the gold film is subjected to during rolling. Currently there is no known limit for the substrate thickness, and for that reason any thickness that is greater than or equal to the passivation layer thickness should be expected to perform well. A substrate thickness that is less than the passivation layer thickness would result in tensile extension, which is envisaged to be more problematic. A thicker substrate may make the SPNI more mechanically robust, but this requires further investigation. Furthermore, the model assumes that the substrate is much more flexible than the channel walls, but as the substrate thickness is increased this assumption becomes less valid, suggesting that the bending model should be revised for very thick substrates. As this thesis focuses on relatively thin substrates the bending model presented is adequate.

7.4.2 The Bending Model of Lacour and Benmerah

In an attempt to calculate the position of the neutral plane the original studies of Benmerah and Lacour misapplied beam theory to the SPNI by assuming that it could be modelled as a 'T-beam' structure and then calculating the neutral plane for the wrong axis of bending. In these

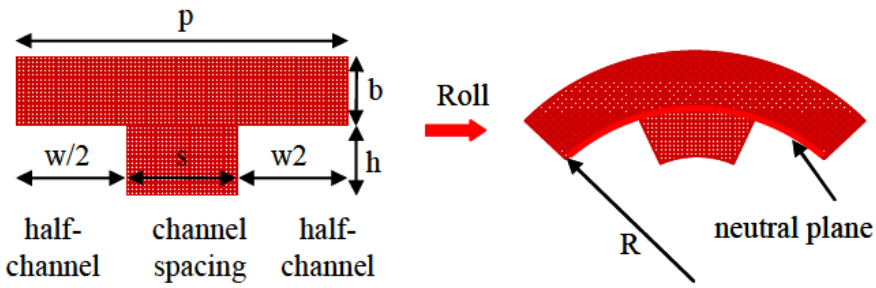

Fig. 7.19: Illustration of SPNI used by Benmerah to incorrectly calculate the neutral plane of the device. [10]

studies both Lacour and Benmerah state that for the gold tracks to be on the neutral plane the substrate thickness should be 25μm thick; derived from a formula to calculate the neutral plane that is quoted as,

$$Y_{\text{neutral}} = \frac{pbh + 0.5pb^2 + 0.5sb^2}{pb + sh} \tag{7.6}$$

to calculate the necessary substrate thickness; where p, b, h and s represent the length of the cross section, the height of the substrate, the height of the insulating channel wall, and the width of the wall respectively. This calculation is based on their diagram shown in Figure 7.19. It appears that Benmerah and Lacour both misunderstood the bending theory as, although it is true that the neutral-axis of a T-beam like that shown in Figure 7.19 can be calculated by Equation 7.4, the bending axis is not the one that is shown on the right in their diagram. The diagram on the right of Figure 7.19 suggests that the bending axis is perpendicular to the page, however for Equation 7.4 to be applicable on a T-beam structure the correct bending axis is perpendicular to the beam, which could be drawn as a line that is horizontal and parallel to the page. Furthermore, if the parallel axis method(Equation 7.4) is applied to Figure 7.19 the neutral plane of the T-beam structure is calculated as;

$$Y_{\text{neutral}} = \frac{\sum N_i A_i}{\sum A_i} = \frac{pb(h + 0.5b) + sh(0.5h)}{pb + sh} = \frac{pbh + 0.5pb^2 + 0.5sh^2}{pb + sh} \tag{7.7}$$

This result is different to Equation 7.6, which is quoted directly from Benmerah and Lacour's work [77, 10], as the last term in the numerator is $0.5sh^2$ rather than $0.5sb^2$. This further

suggests that Benmerah and Lacour's original work was flawed.

7.4.3 Failure Rates in Previous Studies

Despite these previously undiscovered problems with the original modelling two reports have suggested that at least 80%[77] and 97%[13] of SPNI's that have previously been fabricated survived rolling. No failures of gold tracks have been reported due to rolling directly. This suggests that the SPNI gold layer that is under tensile compression is durable although the mechanisms that allow the gold tracks to endure tensile compression are not yet understood. This may impact design decisions in the evolution of the array as for gold layers thicker than 100 nm it has been reported that the maximum applied extensive strain before a failure is as low as ≈1%[78]. This study is not totally analogous to the SPNI as the elastomers used were not as stiff as the polyimide and the films under stress were not encapsulated in any way.

7.4.4 The Fabrication of a Dual-Substrate

In the development of the SPNI it was decided to investigate the strain on the wiring and to increase the range of possible designs by tailoring the substrate thickness. A thicker substrate may allow for a more durable interface, for example. As has been discussed, the maximum thickness of the SPNI substrate that is compatible with the Microflex technology is 20μm.

However, a total substrate thickness greater than 20μm could be fabricated using a dual substrate. If the first Durimide layer (<20 μm) is treated as a base, a second Durimide layer can be spun directly onto the base and defined so that it does not cover the connection region and only extends through the regions that needs to be rolled. This creates a step over which the thin gold tracks must be electrically conductive, which is illustrated in Figure 7.24.

It was found that a ≈20μm step between the two regions could be fabricated that was relatively gently sloped, see Figure 7.20, suggesting that it could be effectively covered with the thin-gold film during the evaporation process. Although thermal evaporation of thin metal films can generally be thought of as a 'line of sight' process, it is possible to thermally evaporate onto steps given the right conditions. Step coverage is a poorly understood phenomena in microfabrication, especially for thin film evaporation, but it has been suggested that for a vertical sidewall, the thickness of the thin-film on the side will be ≈50% of the thickness on the bottom

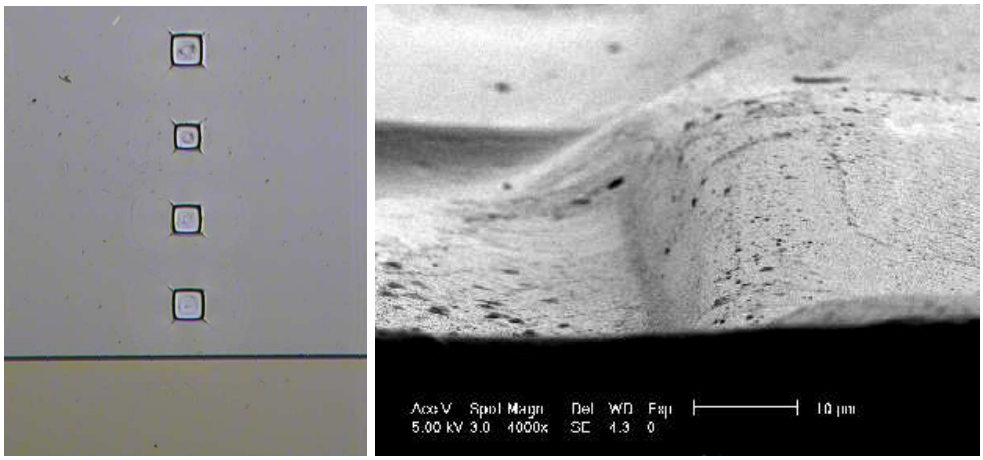

Fig. 7.20: Left: Step between the connection area and the wiring area of the device, Right: SEM to show that the step is sloped (Black spots on the SEM image are dirt).

surface [50].

As the step is sloped it is reasonable to suspect that this ratio will be improved so that the thickness of the thin-films will be more equal, but it was not possible to verify this assumption. Indeed, after evaporation it could be seen that there was no 'shadowing' at the step using a microscope; the layer appeared homogeneous without any uncovered regions of the substrate.

Although a step of $\approx 20\mu$m is possible, steps thicker than this have not been investigated. As will be outlined, it was decided that the fabrication of the SPNI would not be possible with a step $>20\mu$m.

Patterning the step

To pattern the thin-gold film the previous chapter described the use of a thin layer of S1813 positive photo-resist. It was found that S1813 photo-resist was too thin to coat both substrate layers with a homogeneous layer. This was because the S1813 would pool at the bottom of the step during spin-coating causing short-circuits across the gold tracks that extended over the stepped region, as seen in Figure 7.21. It was found that this pooling could not be eliminated by varying the exposure time, spinning profile or the baking ramp.

Megaposit SPR-220-7 is a much thicker photo-resist that is used in fabrication processes that require prolonged exposure to reactive ion etching. It is possible to spin and develop photo-resist layers up-to 30μm, with good uniformity in a single coating [79].

Thicker photoresist can cause contact with the photomask, especially with the topology

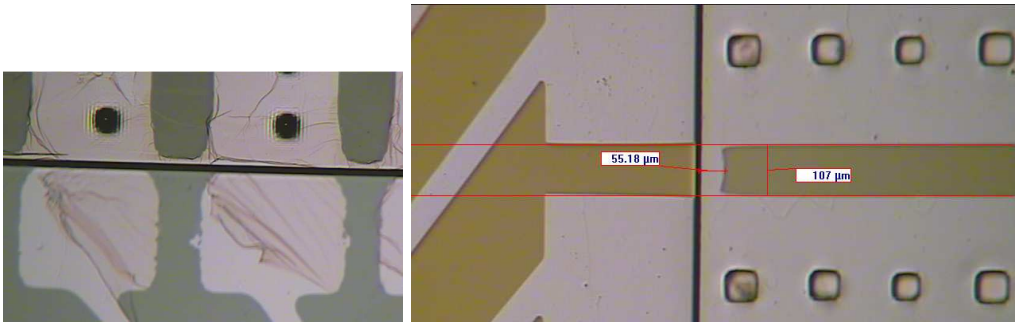

Fig. 7.21: Failed S1813 patterning of step, Top: S1813 failed during the wet etch process, Bottom: Pooled S1813 causes a short across the pads.

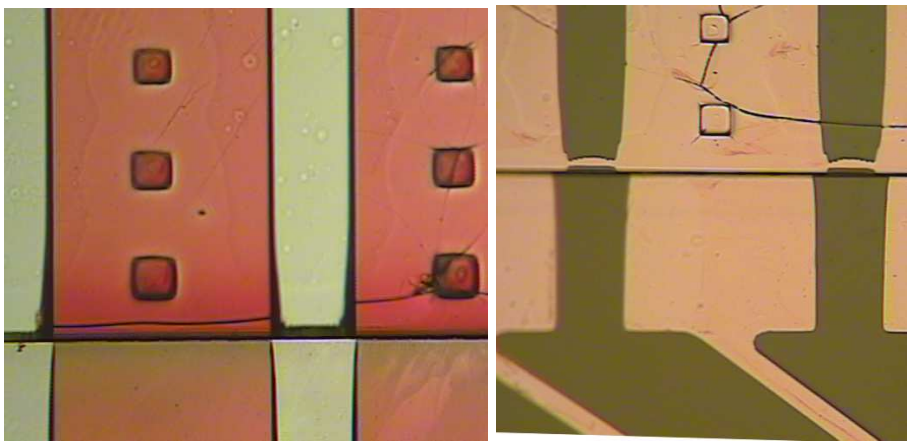

Fig. 7.22: Thicker SPR-220-7 could not be developed satisfactorily, due to the reduction in photo-lithographic resolution caused by the step height.

of steps, causing the UV exposure to be non-uniform. This can reduce the reproducibility of well-defined features and for the SPNI this was problematic, leading to thinner tracks after development and short circuit being developed over the step region, examples of these phenomena are shown in Figure 7.22 and 7.23. For the examples shown a thicker layer of SPR-220-7 photo-resist was used, which led to the problems shown.

It was found that if the SPR-220-7 photo-resist was too thick it would be very difficult to develop and some pooling was noticed as with the S1813. Similarly, if SPR-220-7 was too thin it would not adequately cover the step.

[t]

An alternative approach to the fabrication of the step was investigated which involved spinning the stress-relief layer first, on top of which the 20μm is deposited which could then be defined into the connection region, see Figure 7.24. This could offer benefits in the ability to pattern the step as the cavity in the corner would be reduced and the thin metal film would be

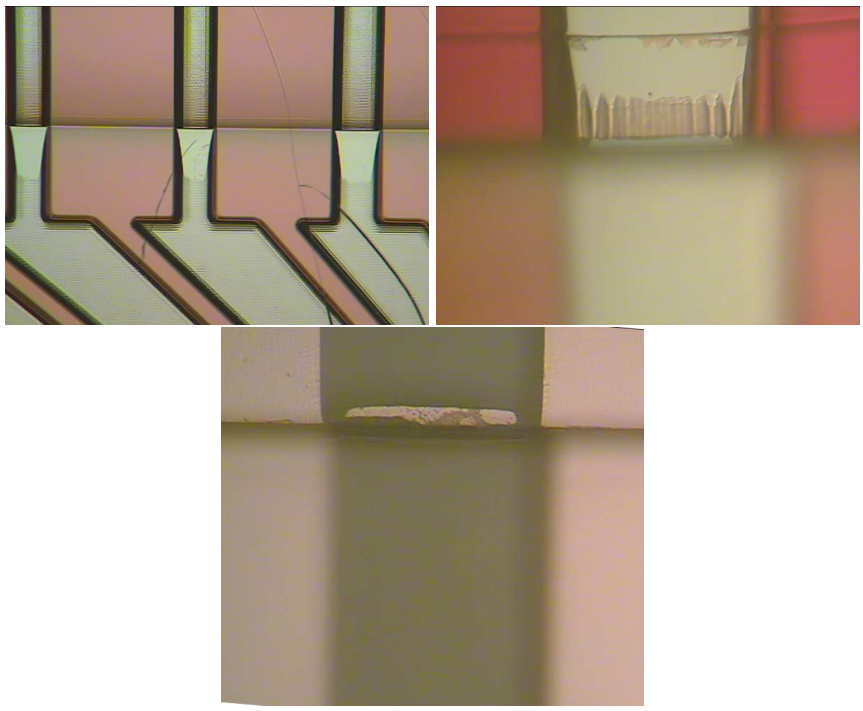

Fig. 7.23: Problems caused by the gap between the photomask and photoresist; Top Right and Top Left; Undeveloped photoresist at the step, Bottom Middle; Possible short circuit after wet etching, the connection pads are 400μm wide with a spacing of 100μm.

deposited over a continuous layer. However, this method seriously affected the ability to define the holes for the micro-rivet, as the gap scattered the UV exposure, causing the holes to be blocked after development. Some samples were made using this alternative setup, but all were abandoned due to a blocking of the holes for connection.

By adjusting the fabrication processes and using the correct thickness of SPR-220 the problem with first process, spinning the layer for MFI first, were overcome. An example of a fully developed step with the continuous gold tracks is shown in Figure 7.25. At 10-15μm-thick, the photoresist layer could be spun and developed over the device, without difficulty. To speed up the development procedure, and to avoid prolonged exposure to the SPR-220-7 developer, the photoresist was developed using a spray technique were the surface was continuously washed with the developer, through a thin nozzle. This stopped the PMMA sacrificial layer from being severely etched during the development process.

To the author's knowledge, this is a unique application of SPR-220-7 photo-resist as the ability to pattern non-isotropic surfaces in this way has not been reported. Although the processing conditions to develop the step need to be carefully tailored, this represents a breakthrough in the development of the SPNI.

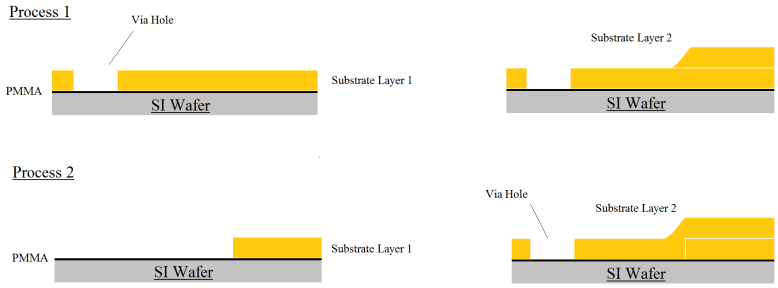

Fig. 7.24: Two possible processes to create the step, Process 1: The first substrate is the 20μm PSPI layer for MFI technology, followed by an 18μm layer to support the wiring during rolling. Process 2: The first substrate is the 18μm PSPI layer, followed by the 20μm layer. It may be expected that the second process gives a continuous step, as shown

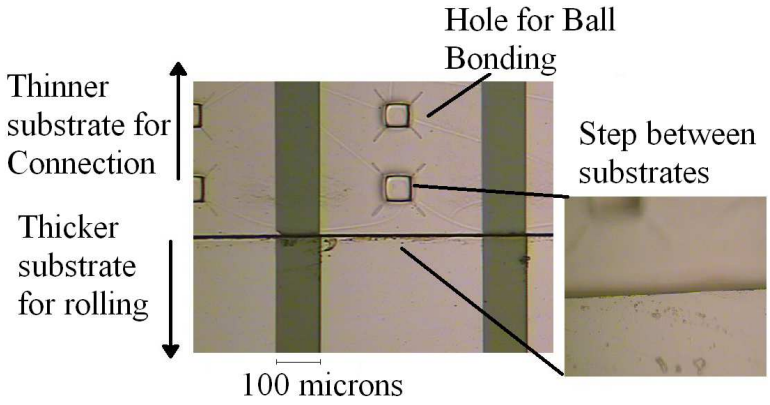

Fig. 7.25: Fully developed connection region that covers the step.

7.5 Updated Fabrication Process

Given these considerations, the device was fabricated according to the process flow illustrated in Figure 7.26.

a-b: A 4” silicon wafer was cleaned using Acetone and IPA and dehydrated at 150°C for 5 minutes, before a 3μm-thick layer of PMMA was spun and baked at 180°C for 10 minutes.

c: A layer of PSPI (Durimide 7020, Fujifilm) was then spun, exposed and developed to define the overall footprint of the device and the via holes for the ball-bonded connections. To prevent a premature release, the amount of developer used was reduced by using a spray technique, through a thin nozzle.

d: The region that supports the tracks is the second PSPI layer. For the dual-layer devices presented in this thesis a second layer of 18μm is used. The substrate layers were placed

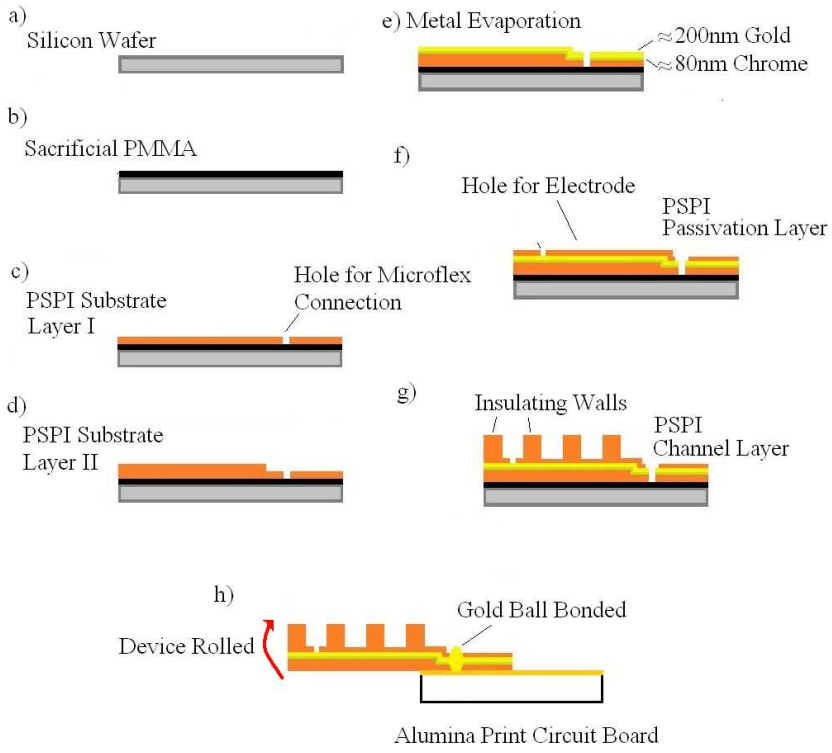

Fig. 7.26: The updated fabrication process of the SPNI

in the oxygen plasma barrel etcher for 10 minutes to 'de-scum' any remaining PSPI from the connection windows and to activate the surface of the substrate to aid adhesion to the subsequent metal layers.

e: A thin Chrome adhesion layer (≈80nm) was thermally evaporated onto the substrate followed by a layer of Gold (≈200nm) to provide the metal for the integrated electronics of the recording interface. The gold was structured into connection pads, electrode sites and the wiring that connects the two via the photolithographic, wet etch process, as described.

f: Electrode tracks were encapsulated with a 5μm layer of PSPI (Durimide 7505, Fujifilm), baked and exposed in the same way as the other PSPI layers. Electrode opening were 30μm x 100μm, and the connection pads were 400μm x 1mm. The passivation layer was then de-scummed for 10 minutes and also cleaned in the UVO cleaner to remove any organic matter from the electrode surfaces.

g: A 100μm PSPI layer was spun and baked and the layer was allowed to cool for atleast 30 minutes before exposure. After the final layer had been developed the wafer was again

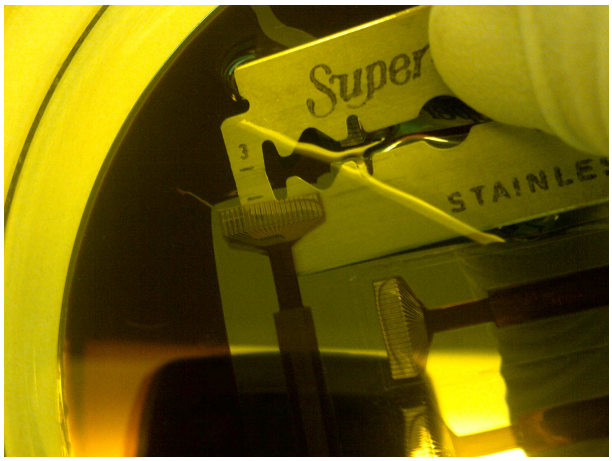

Fig. 7.27: Method of releasing the SPNI samples, after immersion in MIBK and IPA

de-scummed and UVO cleaned. The processed wafer was cured in N_2 at 350°C for 1 hour in a convection oven and is left for atleast 5 hours to cool to room temperature before the sample could be released from the carrier wafer.

h: To release the device the samples were submerged in MIBK(Methyl-iso-butyl Ketone):IPA at a ratio of 3:1 and left for at least 24 hours. Using IPA and a razor blade, see Figure 7.27 the samples are peeled from the wafer and cleaned using acetone and IPA. The device was then rolled into the spiral configuration. The end of the device was clamped into a pair of tweezers that were connected to a hand operated rotating mechanism. The tweezers were gently turned to form a tight spiral in the direction perpendicular to the channels and the rolled device was inserted into a silicone tube. To make external connections to the electrodes the samples were ball bonded through the hole on the connection pads to alumina printed circuit boards underneath (ESL Europe) using 25 micron gold wire and a manual ball bonder (Kulicke and Soffa, Model 4522).

7.5.1 Problems during Curing

Most applications of polyimide in neural interfaces employ a curing step before the metallization layer is introduced to the structure [62, 80, 22]. Although the reason for this curing step is not discussed in detail it is most likely necessary to reduce stress and stop the devices from wrinkling after release from the carrier. Unfortunately, due to the PMMA sacrificial layer it was not possible to perform this curing step until the end of the process after the metallization had

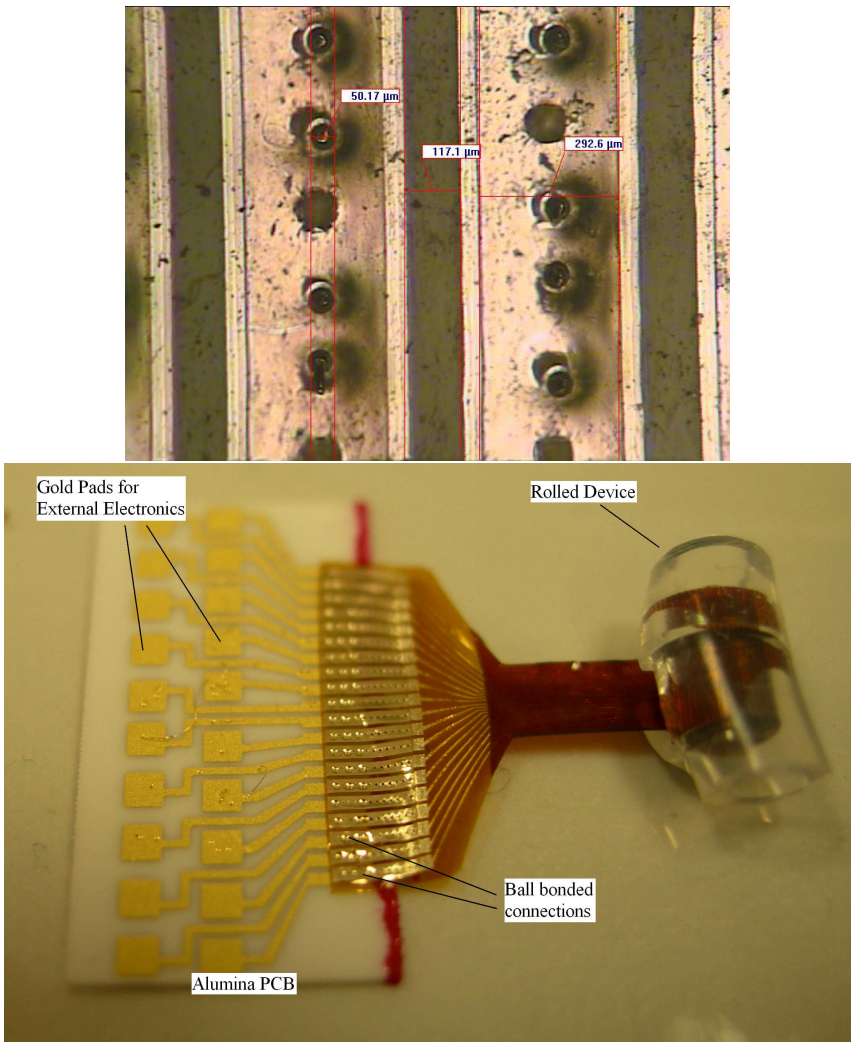

Fig. 7.28: Fully bonded SPNI device; Top, Microscopy of ball bond, Bottom, Fully bonded device

already been defined.

Unfortunately, carrying out the curing step at this stage did cause problems with the SPNI that need to be addressed in the future development of the neural interface. The polyimide is cured at a temperature above the glass transition of PMMA ($\approx$ 180°), which means that during curing the polyimide can de-laminate. Then, due to the shrinking of the polyimide layers during the curing (solvent is outgassed and the polyimide imidizes), the connection pads become significantly narrower than they were designed to be. Furthermore, at the step, the gold layer can be cracked and fractured by the shrinking, as shown in Figure 7.29.

This effect does not occur uniformly across the wafer as devices in the centre of the wafer showed less or no damage after curing than those on the outside of the device. Furthermore, this shrinking during the curing caused the outside regions of each device to be misaligned

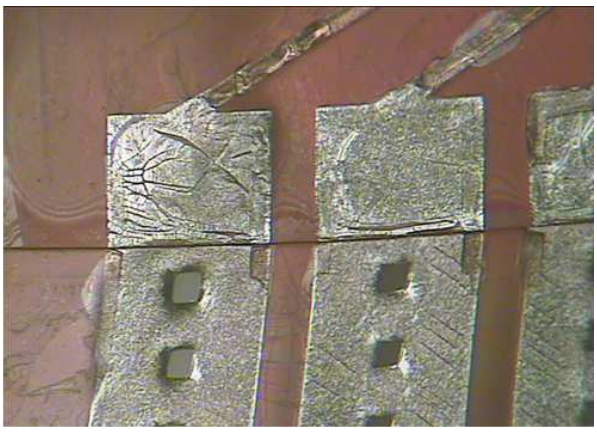

Fig. 7.29: Problems caused during curing

for ball bonding, making it difficult to characterize these devices electrically. These problems significantly reduced the yield of the SPNI as out of 8 samples that could be fabricated on a single wafer, in general only four devices would survive the curing process. Furthermore, in each 'successful' sample only ≈10 of the available electrodes could be coupled to via MFI ball bonding. If a thicker second substrate layer had been used it is possible that this could have caused more failures.

Single layer samples

As a result, it was decided to fabricate some SPNI samples that had a single layer substrate, to determine whether these problems of alignment and gold failure during curing would be repeated, and to also determine whether the thin-gold film could survive the compression associated with rolling.

To fabricate these samples, the PMMA was spun and baked, as before, followed by a 20μm substrate layer of PSPI, that was exposed and developed as before. The second substrate layer was omitted and the rest of the fabrication process was kept the same. After curing, the single layer samples did show some signs of misalignment, due to shrinking, but there were no obvious fractures in the gold layers.

For both types of samples, each electrode pad that could be aligned, was connected using at least 6 bonds to provide both an electrical coupling and a mechanical support for the device, see Figure 7.28.

7.6 Summary of this Chapter

To implement the novel interconnection technique required a significant amount of work. It is possible to fabricate SPNI devices that are compatible with MFI using the fabrication methods that have been discussed.

The use of PMMA is a novel application of a sacrificial technique, and although care is needed to ensure that the samples do not delaminate, it represents a reliable method to fabricate photosensitive polyimide as a substrate for neural interfaces. Again, this needs careful consideration in terms of design, as the polyimide cannot be fully cured until the final step, meaning that shrinking of the polyimide layers may cause failures, especially in the thin film gold layer.

It was found that a substrate thickness below 20μm could be bonded without difficulty, with a via hole between 60-70μm. The substrate thickness influences the strain on the thin metal film during rolling. Using the elastic theory of bending a bending model has been described that accounts for the geometry of the SPNI and suggests that the metallization of the original SPNI was under tensile compression during rolling, which may have allowed it to be bent without causing a fracture. To minimise the strain the new model predicts that a substrate thickness that is an equal thickness to the passivation layer is required. It has further been shown that the original model of bending in the SPNI was flawed as the neutral axis was incorrectly calculated for the wrong axis of bending.

In order to be compatible with MFI there is a limited range of substrate thickness that is possible for the SPNI, and so methods of fabrication have been investigated to increase this range by incorporating a dual substrate design. Implementing this design represented a significant challenge using the photolithographic techniques as it required the ability to pattern a step with continuous wiring. This was overcome using a thicker photoresist layer. The dual substrate layer, although possible, suffered significant problems during curing. The yield of the process was reduced by mechanical problems caused by shrinking of the polyimide structures, which caused misalignment and fracturing of the metallization of the step. Roughly half of the samples survived the curing. For the single layer samples these problems were reduced, where no samples showing any fracturing despite some misalignment.

The performance of the SPNI depends on the quality of the fabrication processes that have been presented, however until now no attempts have been made to predict the performance that

should be expected from these electrodes. The next chapter presents a theoretical model to predict the electrochemical performance of the devices that can be used to evaluate the in vitro testing.

8. THEORETICAL MODELLING OF THE ELECTROCHEMISTRY OF THE SPNI ELECTRODE FOR IMPEDANCE SPECTROSCOPY

This chapter develops a theoretical model of the electrode interface that can be used to assess of the quality of SPNI fabrication and to evaluate the impedance spectra presented in the next chapter. This modelling is based on a widely accepted interpretation of the thin-film metal electrode/saline interface that was described by Kovacs in 1994 [20]. This chapter will show how the interface can be modelled as resistive and capacitive phenomena, working in parallel, whose behaviour can be modelled for a range of frequencies of applied potential, using Microsoft Excel. This model can then be used to show what the expected impedance and phase spectra of the SPNI should be. These results significantly improve the ability to assess the quality of the SPNI fabrication process, and give insight into whether some of the processing steps needs to be reviewed.

8.1 Modelling The Electrode/Saline Interface

As stated earlier in chapter three, to record electrical activity in the body requires an interface between the metal electrode and the ionic electrolyte that surrounds the neural tissue. The interface between these the metal and the electrolyte is electrochemical. This is also true for impedance spectroscopy, so to predict the performance of the SPNI electrode requires an understanding of this electrochemical interface. The electrodes discussed in this thesis have gold active sites and as a result this chapter will discuss this electrochemical interface between a thin-film gold electrode and saline.

The electrochemical phenomena that dictate the impedance spectra of the electrode interface can be depicted as a parallel circuit known as Randle's model, this is shown in Figure 8.1. The model consists of; the interfacial capacitance Σ_I, the charge transfer resistance R_t, the Warburg impedance Z_w and the solution resistance R_s. By computing the effect of each component across

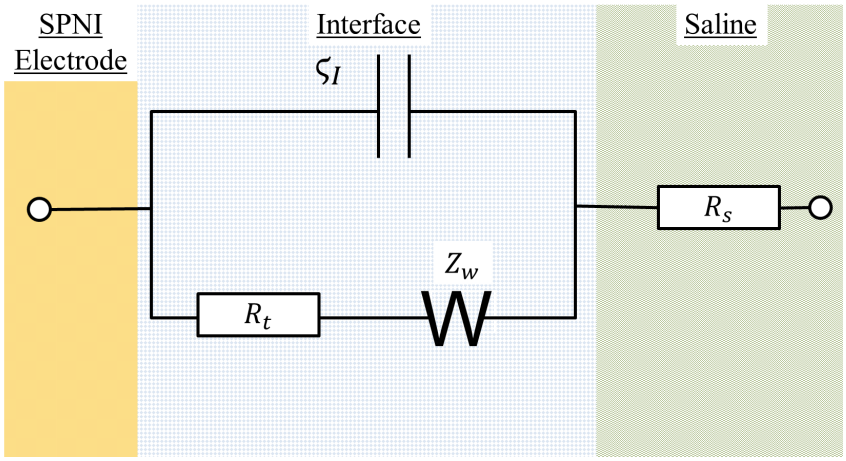

Fig. 8.1: Diagram to show electrical components that make the gold-solution interface [20]

a broad frequency range, the total impedance spectra of the interface can be predicted.

8.1.1 Interfacial Capacitance

Before the metal electrode is placed in the ionic electrolyte solution, the metal and the solution are electro-neutral. When the metal is in the solution free electrons are attracted to the positive ions in the solution and thus travel to the electrode surface. The electric field generated by surface charges of the metal then begins to impact the electrolyte where disassociated ions in the solution are attracted to the surface charges, varying the ion concentration from a maximum at the electrode surface to a bulk concentration in the rest of the solution. As a result of the charged metal surface, polar water dipoles orient themselves and determine the closest approach of the charged ions in the solution at a distance which is known as the outer Helmholtz plane (OHP) as illustrated in Figure 8.2.

For a typical interface the outer Helmholtz plane has a thickness of around a few angstroms, and so the potential difference between ions and the metal surface drop over a very small distance. Helmholtz developed an initial theory to describe the spatial charge distribution at the interface as a simple capacitor by assuming that the charged ions are confined at the OHP, with an equal and opposite effect in the metal. The space in between acts as a dielectric and the capacitance ς_H per unit area is then determined by the dielectric permittivity of the space between the water molecules and the electrode, ϵ_r and the distance of the OHP from the metal electrode, d_{OHP} in the parallel plate capacitor formula,

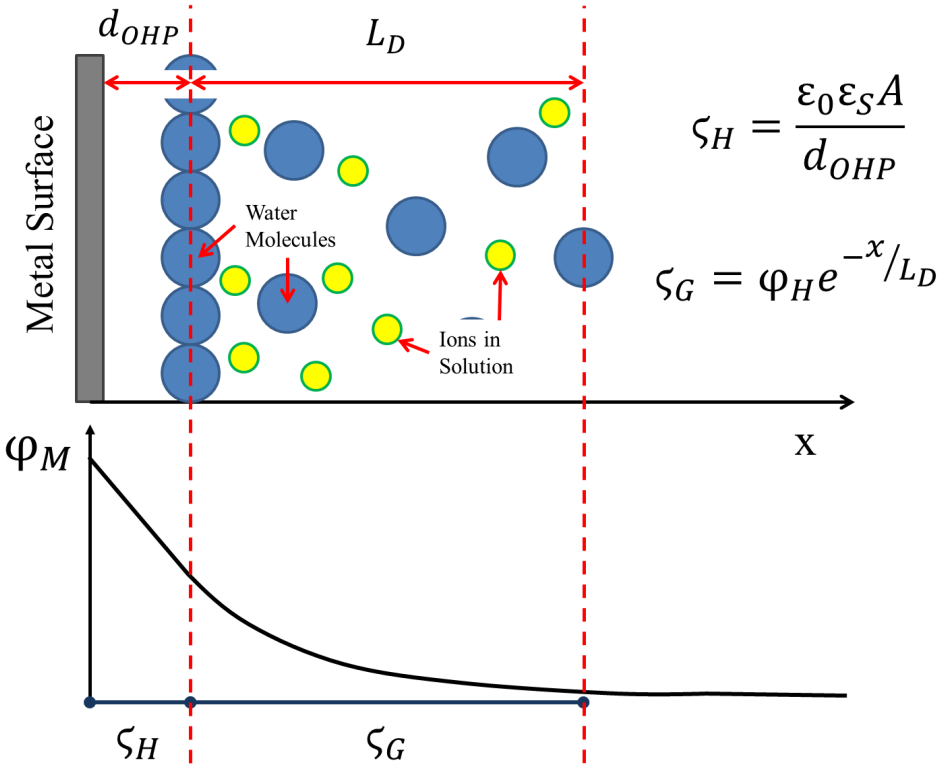

Fig. 8.2: Illustration of the interfacial capacitance between the metal surface and the ions in solution. [21]

$$\varsigma_H = \frac{\epsilon_0 \epsilon_r}{d_{OHP}} \tag{8.1}$$

Multiplying the above expression by the area of the electrode gives the total Helmholtz capacitance for the interface. A value for the Helmholtz capacitance can be calculated by taking the dielectric constant of water as 79.4 and an Outer Helmholtz plane distance of 5Å(which were both chosen to represent physiological saline at 25°C)[20]. These approximates yield a Helmholtz capacitance of per unit surface area of 1.41 F/m^2, which is often useful as a design guide, although both the relative permittivity and d_{OHP} can change this approximate considerably, which will be discussed further as model is made more complex.

The Helmholtz model was flawed as it neglected the role of potential on capacitance and negated the movement of ions in the solution, where mobile ions ensure that charge is not concentrated entirely at the OHP but instead diffuses into the solution, thus lowering the actual capacitance of the interface. In 1910 to 1913, Gouy and Chapman changed the simplified model

to account for mobile ions at the interface that are dependent on thermal factors as well as the electrical forces already described.

The result of this updated model, labelled as the G-C model herein, is an ion cloud near the interface where thermal and electrical effects are equilibrated in a time-averaged ionic distribution. Thus the total charge is maintained by extending the charge layer into the bulk electrolyte so that the potential distribution can be considered to be an exponential decay of the form;

$$\varphi(x) = \varphi_0 exp\left(-\frac{x}{L_D}\right) \tag{8.2}$$

$$L_D = \sqrt{\frac{\epsilon_0 \epsilon_r k_b T}{2 N_0 e^2}} \tag{8.3}$$

Where φ_0 is the potential at the electrode, x is the distance from the electrode, and L_D is the Debye length (measured in meters). The Debye length characterizes the spatial decay of potential and can be viewed as the characteristic thickness of the diffuse layer. Also included is the Boltzmann constant k_b, the temperature T, the charge of the electron e, the bulk concentration of the solution N_0, which is given by the concentration of the ions (mol/l) multiplied by Avagadro's number (N_A). For the saline solution $N_0 = N_A \cdot [NaCl] = 6.02 \times 10^{23} \cdot 0.147 = 8.9 \times 10^{22}$. Alternatively, for saline the Debye length can be calculated using,

$$L_D = 0.304 \times 10^{-9} \cdot [NaCl]^{-\frac{1}{2}} \tag{8.4}$$

which gives a value of 7.92×10^{-10} m [81, 82]. Thus the G-C capacitance spreads ≈ x1.5 further into the solution than the Helmholtz hydration sheath, due to the mobile ions.

The differential capacitance per unit area (F/m^2) can be calculated by using Gauss's law on the region near the electrode to give;

$$\varsigma_G = \frac{\epsilon_0 \epsilon_r}{L_D} cosh\left(\frac{ze\varphi_0}{2k_b T}\right) \tag{8.5}$$

Where the coefficient ($\frac{\epsilon_0 \epsilon_r}{L_D}$) is the capacitance per unit area of two plates separated by a distance L_D and the effects of mobile charges are represented as the hyperbolic cosine.

For a potential at the electrode of 5 mV (used in the experimental investigations shown

later) the G-C capacitance at the electrode is 0.89 F/m^2, which is approximately two thirds of the Helmholtz capacitance.

However, the G-C model does not give a finite plateau for capacitance with increasing potential, as observed in real systems due to the presence of the OHP acting as a dielectric. Thus, the Stern model is used to combine the G-C model with that of Helmholtz to rectify this problem. This gives a layer of bound ions at the OHP with a diffuse ion cloud beyond it. For this case, the total interfacial capacitance is a series combination of both models;

$$\frac{1}{\varsigma_I} = \frac{1}{\varsigma_H} + \frac{1}{\varsigma_G} \tag{8.6}$$

Where ς_I is the interfacial capacitance per unit area, ς_H is the Helmholtz capacitance and ς_G is the G-C capacitance due to the diffuse cloud as described earlier. This model describes a linear potential drop between the electrode and the OHP, followed by a near exponential decay from the OHP out into the diffuse solution.

This interfacial capacitance per unit area can be written as,

$$\varsigma_I = \left(\frac{1}{1.41} + \frac{1}{0.89}\right)^{-1} \tag{8.7}$$

which gives a value of 0.54 F/m^2. A 1 micron square patch of electrode (Area=1×10^{-12} m) will therefore have a capacitance of 0.54 pF.

8.1.2 Overpotential and Charge-Transfer Resistance

The capacitance at the interface does not describe the entire electrical picture as in general, when a metal is added to an electrolyte spontaneous Faradaic reactions can occur where electrons are transferred across the boundary. These reactions eventually reach equilibrium whereby the currents due to electron transfer flowing to and from the metal are equal, resulting in no net current flow across the interface. For the SPNI electrode these spontaneous reactions are more likely to be caused by impurities as it is highly unlikely that Faradaic reactions occur at the gold surface. This is because in most electrolytes gold possesses very weak chemical adsorbing properties and is often thought not to allow Faradaic behaviour, for this reason it isseen as the

ideal metal for the investigation of solid electrode behaviour [83, 84].

A DC potential applied across the SPNI interface may allow a Faradaic current to flow, however, given the right conditions. Thus it is necessary to consider the resistive path in parallel to the capacitive path for the interface, which is highly non-linear with the applied potential. The flow of current through the metal-electrolyte interface requires the net movement of charge in the response to an electric field, which can be considered as the difficulty to place or remove a charge from the electrode. An applied voltage pushes the interface away from the equilibrium (φ_0) and the potential difference that results is called the overpotential;

$$\eta = \varphi - \varphi_0 \tag{8.8}$$

The overpotential is thought to be a sum of three processes; η_t represents charge transfer across the double layer; η_d represents diffusion of reactants to and from the electrode; η_r represents chemical reactions at the electrode surface.

$$\eta = \eta_t + \eta_d + \eta_r \tag{8.9}$$

Thus, a potential in excess of the equilibrium will drive charge transfer, diffusion and chemical reactions. In general, for the operation of an electrode near the equilibrium position the charge transfer overpotential tends to dominate the overall current and as the applied potential is pushed further from equilibrium the diffusion of reactants would become a more limiting factor. In biological applications the overpotentials associated with chemical reactions are negligible and for noble electrodes it would not be expected to reach a diffusion limited case as there would be relatively few charge transfers. Thus, for the modelling work only the overpotential associated with direct charge transfer is considered.

The exchange current density J_0 of the interface is used to quantify this behaviour and depends on the material of the electrode and the composition of the solution. J_0 is often experimentally assessed by measuring the charge transfer resistance around the equilibrium potential of the electrode in the electrolyte of interest.

If the current is small with regards to J_0 then the electrode will not shift significantly from the equilibrium and will behave linearly but as the current becomes a similar magnitude or above J_0,

non-linearities become more prevalent and the charge transfer resistance falls off exponentially with applied voltage. If the potential is close to the equilibrium then the Butler-Volmer equation can be used to calculate the resulting current density J (in Acm^2):

$$J = J_0 \left[exp\left\{ \frac{(1-\beta)ze\eta_t}{kT} \right\} - exp\left\{ \frac{-\beta ze\eta_t}{kT} \right\} \right] \tag{8.10}$$

Where J_0 is the exchange current density as described, z is the valence of the ion involved in the charge transfer, and β symmetry term that accounts for the energy barrier difference associated with oxidation and reduction reactions. The Butler-Volmer equation describes an exchange current that has a fraction that assists ionization ($\beta\eta_t$) and a fraction that retards discharge ((1-$\beta\eta_t$)) [85]. Therefore β determines the symmetry in the I-V characteristics; when both reactions proceed at the same rate β is 0.5. From Equation 8.10 it can be seen that any small change in η_t can have a large impact in the current density J and the electrode material has a significant impact on the amount of current that flows in response to an applied potential due to the effect of the exchange current density. At high voltages electrochemical reactions at the interface are more likely, thus it is desirable to limit the experimental analysis to as close to the equilibrium as possible. For stimulation, an electrode with a higher exchange current density is desirable.

To determine a theoretical value for the resistance that appears in parallel to the capacitance at the interface, it is useful to examine the $J - \eta_t$ relationship via a small-signal analysis where a low-field approximation is taken to represent a neural recording. The charge transfer resistance, R_t under low-field conditions and with non-rectifying system ($\beta = 0.5$) can be calculated by first rewriting the current density in hyperbolic form, taking the derivative with respect to η_t and finding the inverse. This gives,

$$R_t = \frac{\partial \eta_t}{\partial J} = \frac{k_b T}{J_0 ze} \left[cosh\left(\frac{ze\eta_t}{2k_b T} \right) \right]^{-1} \tag{8.11}$$

in Ωcm^2. For the approximate the charge transfer resistance can be written in a linear form as:

$$R_t = \frac{k_b T}{J_0 ze} \tag{8.12}$$

and the resulting current is satisfying ohm's law,

$$J = \frac{\eta_t}{R_t} = \frac{J_0 ze\eta_t}{k_b T} \tag{8.13}$$

The limit for this approximation to be valid is assumed to be,

$$\frac{ze\eta_t}{2k_b T} < \frac{1}{5} \tag{8.14}$$

to keep the error due to approximation below 1%[18]. This corresponds to an overpotential of around 50mV, up to which one can assume linearity. This range of validity is suitable for neural recording as spike amplitudes are normally below this threshold. This also complies with impedance spectroscopy where all evaluations are performed at 5 mV.

In 1975 Wise and Angell experimentally assessed the exchange current density of drawn-wire, metal electrodes in saline, held at a fixed dc potential relative to a saturated calomel electrode, and the results of their experimental analysis are shown in Figure 8.3 [85]. It can be seen that gold had the smallest exchange current out of all the metals investigated, reflecting the fact that gold is the noblest metal. For gold it can be seen that the exchange current density was determined to be $\approx 2\times10^{-9}$ A/cm^2 in the experimentally relevant potential range ($|V| < 50mV$). This gives a charge transfer resistance for gold of 1.29×10^7 Ω/cm^2. From this result Wise and Angell suggested that noble metals operating at a low voltage should not be expected to pass an appreciable current [85].

This value determined by Wise and Angell is largely in agreement with the experimental work of Frommhold, who performed impedance analysis on gold electrodes in saline using the same methods described in chapter 5. Frommhold found that the charge transfer resistance of a thermally-evaporated gold microelectrode of 0.283 cm^2 area was 0.8×10^6 Ω [18]. Thus, from these two studies, a 1 micron squared patch of electrode can be expected to have a charge transfer resistance of $\approx 1 \times 10^{15}$ Ω, which is very large, again reflecting the fact that gold is a noble metal [85, 86, 83, 84].

The experimental work of Wise and Angell, and later Frommhold, did not attempt to assign the chemical processes that resulted in the measured exchange currents to any specific reactions, for example no attempt was made to classify the amount of dissolved oxygen in the saline nor

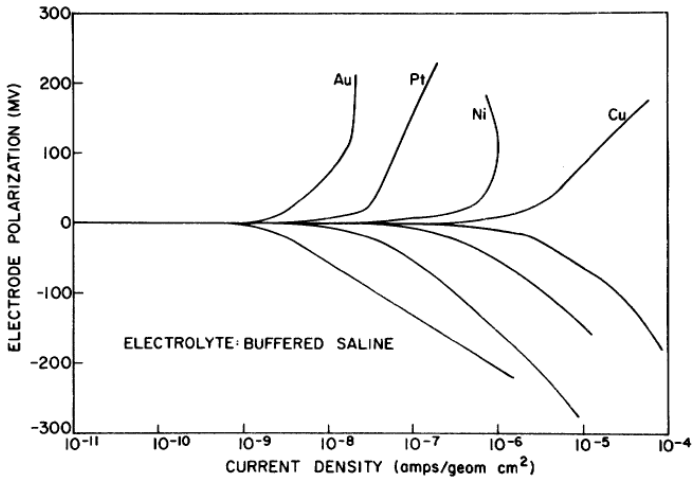

Fig. 8.3: DC behaviour of metal electrodes in saline. The electrodes were in the form of drawn wires and were referenced to a saturated calomel electrode.
[85]

to investigate what affect the amount of dissolved oxygen has on the exchange current. The experimental results presented above should therefore be seen as representative of a gold electrode operating in relevant experimental conditions. Cyclic voltammetry could allow detailed investigation of the Faradaic reactions at the gold-saline interface under d.c. conditions, but this has not been investigated in this study.

8.1.3 Warburg Impedance

For most electrode/electrolyte interfaces the charge transfer resistance dominates the resistive branch of the electrode impedance. However, this situation changes when the current density (AC or DC) is so large that the reactants cannot diffuse from the bulk material and the increased chemical reaction rate depletes the local reactants causing a concentration gradient from the electrode to the bulk solution. As a result the current density is limited by the diffusion rate of reactants to the interface, which results in a diffusion overpotential.

For time-varying signals with higher frequencies it is worth considering the case of a sinusoid forcing function acting on the ions at the interface. A sinusoidal, spatial variation of ions develops rather than a linear gradation, with a higher concentration of ions at the OHP and falling off into the solution. As the frequency of the excitation is increased it becomes more difficult for ions to follow the field, dampening the effect of the spatial variation. The effects of the diffuse ion cloud become less significant and for an ever increasing frequency the ions are

not able to follow the field at all. This leads to no diffusional impedance and in 1899 Warburg proposed a model for this frequency dependent diffusional impedance for a unit area ($\Omega \cdot m^2$) that is made a resistive (R_w) and capacitive term (Σ_w) that can be written as,

$$R_w = K_w \cdot \frac{1}{\sqrt{f}} \tag{8.15}$$

$$\varsigma_w = \frac{1}{\omega R_w} \tag{8.16}$$

that act in parallel to each other and in series with the charge transfer resistance. K_w is the Warburg constant that can be written as,

$$K_w = 10^{-7} \cdot \frac{kT}{q^2 N_0 \sqrt{\pi D}} \tag{8.17}$$

where D is the diffusion constant for the ions in the solution (1.49×10^{-9} m/s^2). For a 1 micron patch of electrode operating a 1 Hz, the Warburg impedance is then $2.74 \times 10^3 \Omega$. As stated, the Warburg impedance is traditionally represented as a combination of a parallel capacitance and resistance, however it has more recently been shown that the two circuit elements are better represented by a single circuit element with a constant phase of -45° [20].

It has been shown above that the Warburg impedance is much smaller that the charge transfer resistance, and so the measured impedance of an SPNI gold electrode is not expected to be affected by the Warburg impedance, as the impedance of the Faradaic current branch will be dominated by the charge transfer resistance. However, the Warburg impedance has been included in the model for completeness.

8.1.4 The Solution Resistance

For a flat electrode, as the current spreads out into the solution it experiences a solution resistance that depends on the shape of the electrode and the resistivity of the solution. The resistivity is determined by the number of ions present and the temperature of the solution. For a rectangular electrode, the solution resistance is given by,

$$R_s = \rho \frac{ln\frac{4l}{w}}{\pi l} \tag{8.18}$$

where ρ is the resistivity of saline which at 25° =0.7 Ωm[26] and l and w are the length and width of the electrode respectively.

8.2 Calculating the Resulting Impedance and Phase spectra

The impedance of a resistor (Z_R) and a capacitor (Z_ς) can be written as,

$$Z_R = R \qquad Z_\varsigma = \frac{1}{j\omega\varsigma} \tag{8.19}$$

where R and ς are the resistance and the capacitance of the components and j and ω are the imaginary unit ($j = \sqrt{-1}$) and the angular frequency of the ac impulse respectively. It is then possible to calculate the total impedance of the interface by calculating the resulting impedance of each component and working through whether the components are in parallel or in series.

Following this methodology the impedance of the capacitive current branch can be written as,

$$Z_{\varsigma I} = \frac{1}{j\omega\varsigma_I} \tag{8.20}$$

and the impedance of the Faradaic current branch (Z_F) can be written as an addition of the charge transfer and the Warburg impedance,

$$Z_F = R_t + R_w \tag{8.21}$$

Adding these current branches in parallel gives an impedance of the electrode interface, Z_E as

$$Z_E = \left(\frac{1}{Z_{\varsigma I}} + \frac{1}{Z_F}\right)^{-1} \tag{8.22}$$

and substituting the components of the interface that have previously been outlined into the above expression gives,

$$Z_E = \frac{[(R_w + R_t)(1-\gamma) + (R_t)(1+\tau+\gamma)] + j\,[(R_t)(1-\gamma) - (R_t + R_w)(1+\tau+\gamma)]}{(1-\gamma)^2 + (1+\tau+\gamma)^2} \tag{8.23}$$

where $\tau = \omega R_w \varsigma_I$ and $\gamma = \omega R_t \varsigma_I$. For the above equations, ς_I is the capacitance of the double layer, R_t is the charge transfer resistance of the interface, R_w is the Warburg resistance and ω is the angular frequency of the potential impulse. Finally, adding the solution resistance (R_s) in series with the interfacial impedance gives a total impedance of,

$$Z = Z_E + R_s \tag{8.24}$$

and again substituting the components of the interface gives,

$$Z = \frac{[(R_w + R_t)(1-\gamma) + (R_t)(1+\tau+\gamma)] + j\,[(R_t)(1-\gamma) - (R_t + R_w)(1+\tau+\gamma)]}{(1-\gamma)^2 + (1+\tau+\gamma)^2} + R_s \tag{8.25}$$

The magnitude and phase of the impedance can be calculated analytically if the equation is separated into the real and imaginary parts,

$$\Re\,[Z] = \frac{[(R_w + R_t)(1-\gamma) + (R_t)(1+\tau+\gamma)]}{(1-\gamma)^2 + (1+\tau+\gamma)^2} + R_s \tag{8.26}$$

$$\Im\,[Z] = \frac{[(R_t)(1-\gamma) - (R_t + R_w)(1+\tau+\gamma)]}{(1-\gamma)^2 + (1+\tau+\gamma)^2} \tag{8.27}$$

and magnitude and phase can be evaluated as,

$$|Z| = \sqrt{\Re\,[Z]^2 + \Im\,[Z]^2} \tag{8.28}$$

$$Arg\,[Z] = \arctan\left(\frac{\Im\,[Z]}{\Re\,[Z]}\right) \tag{8.29}$$

Once the real and imaginary parts have been separated, it is easy to evaluate these functions for a frequency spectrum. Using a spreadsheet program like Excel impedance and phase spectra can be plotted that serve as a theoretical prediction of the experimental results.

For a gold electrodes in saline the values for the constants used to build the models are outlined in Table 8.1. After computing these values, the corresponding impedance and phase spectra can be calculated by applying different values of frequency. The experimental testing is restricted to measuring the electrochemical behaviour of the interface between 40 Hz - 1 MHz and as a result the modelling work presented is restricted to this range.

The modelled impedance and phase spectra of a planar gold electrode of the equivalent size

Property, Units	Value	Reference
Exchange Current Density of Gold, A/m^2	2×10^{-5}	[86]
Ionic Strength of Saline, mol/L	0.0815	-
Signal Strength (φ_0), V	5×10^{-3}	-
Temperature of Experiment, K	298	-
Dielectric Constant of Solution	79.4	-
Electron Charge, C	1.6×10^{-19}	-
Valence of NaCl (z)	1	
Boltzmann Constant, JK$^-$1	1.38×10^{-23}	-
Concentration of NaCl, mol/l	0.147	-
Permittivity of Free Space, F/m	8.85×10^{-12}	-
Resistivity of Saline at 25°, Ωm	0.72	[26]

Tab. 8.1: Values and units for the Physical phenomena used to build the model of a gold electrochemistry in saline.

of the SPNI, a 1 μm^2 electrode and a 1×10^6 μm^2 electrode are shown in Figure 8.4. As can be seen, the relationship between the area of the electrode and the corresponding impedance is inversely proportional and for all areas the capacitive phenomena of the interface dominates. As the frequency is increased the total impedance falls until the interface is dominated by the solution resistance. Larger electrode reach the solution resistance at a lower frequency. For an electrode of the equivalent size of the SPNI, the magnitude of the impedance ranges between 5 MΩ and 1000 Ω between 40 Hz and 1 MHz. The impedance spectrum begins to plateau at around 100 kHz, which corresponds to the frequency at which the solution resistance starts to become dominant. This is also seen in the phase spectra as the phase goes towards 0° for increasing frequency above 100 kHz.

8.2.1 Interfacial Capacitance Modelled using Constant Phase Element

In general, the interfacial impedance of electrodes (impedance of the top current branch in Figure 8.1) cannot be modelled with a pure capacitor, even in the absence of the resistive branch current [87]. Instead, the interfacial capacitance of the electrode has a ‘dispersive’ nature that is frequency dependent and can best be modelled using a constant phase element (CPE). By using the CPE to model the dispersive capacitance of the double layer, the interfacial impedance can be written as,

$$Z_{CPE}(\omega) = \frac{1}{\varsigma_I (j\omega)^n} \tag{8.30}$$

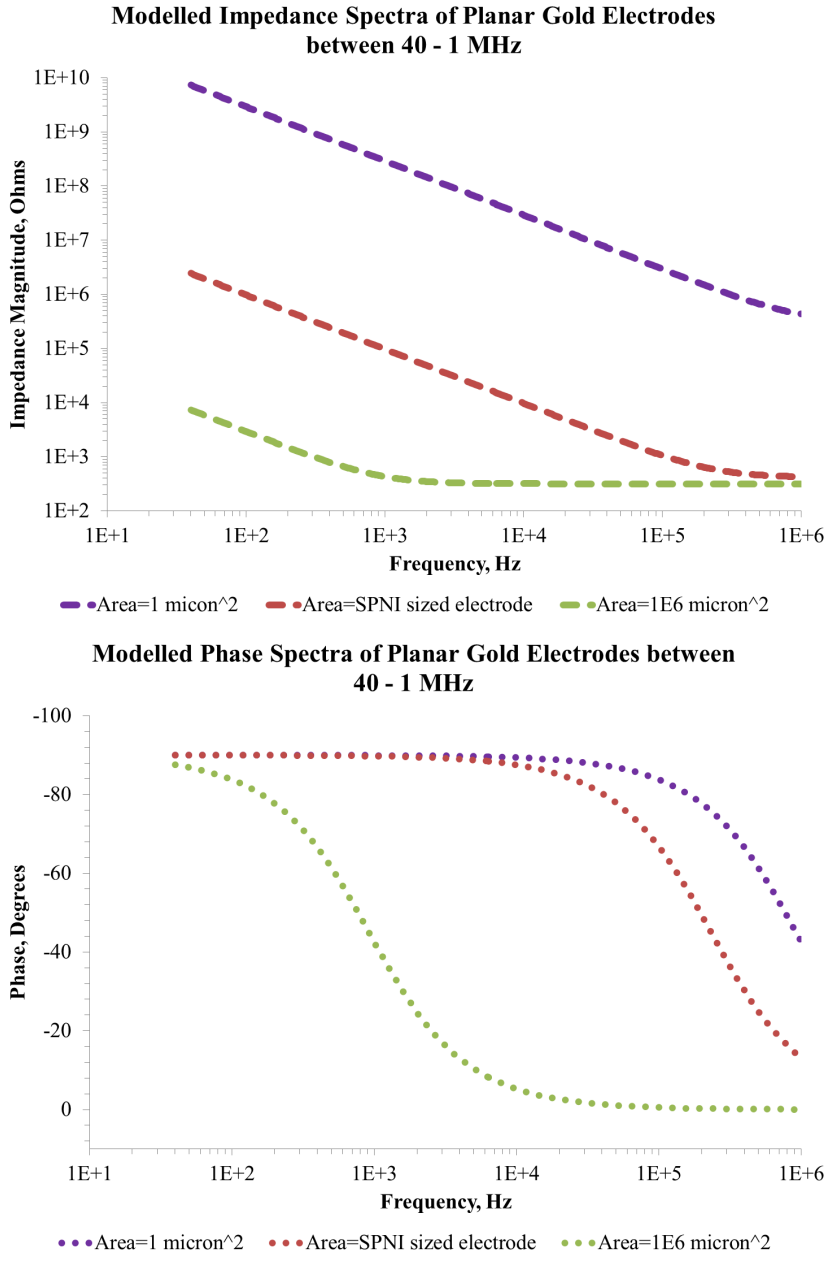

Fig. 8.4: The modelled Impedance and Phase spectra of a planar gold electrode for three surface areas; 1 μm^2, the area of an SPNI electrode (3000 μm^2) and 1×10^6 μm^2.

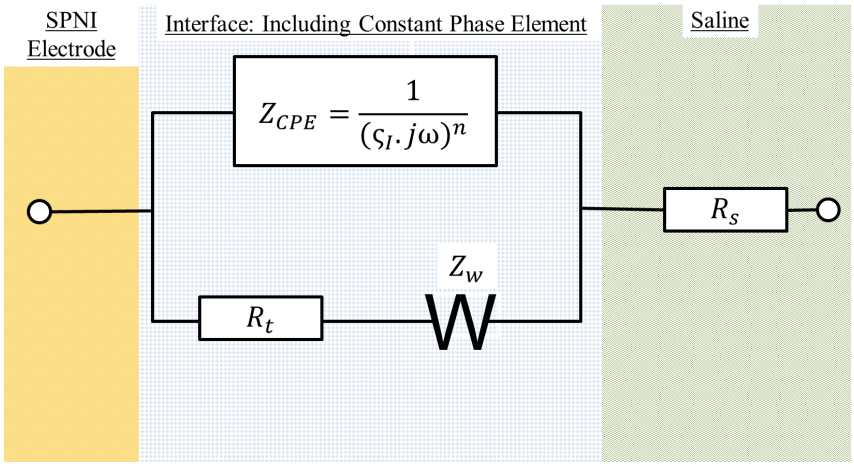

Fig. 8.5: Diagram to show electrical components that make the gold-solution interface including the constant phase element

[20]

and *n* is a constant between 1 and 0 that determines the 'idealness' of the interface (*n* = 1=pure capacitor)[18]. A model of the gold-saline interface that includes the dispersive interfacial capacitance is shown in Figure 8.5.

The dispersive capacitance is thought to model slow processes that involves; the formation of chemical bonds of some species to the electrode surface(adsorption) or the rearrangement of atomic structures on the electrodes surfaces. Capacitive dispersion has been shown to be related to surface roughness and as a planar electrode can never be made perfectly smooth in the microscopic range (describing features from 10 nm to 100 μm) it is important to consider it for the impedance spectroscopy model [87].

By using the expressions,

$$(j)^n = exp\left\{\frac{n\pi}{2}\right\} \tag{8.31}$$

$$exp\left\{\frac{n\pi}{2}\right\} = \left[\cos\left(\frac{n\pi}{2}\right) + j\sin\left(\frac{n\pi}{2}\right)\right] \tag{8.32}$$

the impedance of the constant phase element can be written as,

$$Z_{CPE}(\omega) = \frac{1}{\varsigma_I(\omega)^n\left[\cos\left(\frac{n\pi}{2}\right) + j\sin\left(\frac{n\pi}{2}\right)\right]} \tag{8.33}$$

Which can be used to model the impedance of the interface depicted in Figure 8.5 as,

$$Z = \frac{(R_t + R_w)\left[1 + (R_t + R_w)\,\omega^n \varsigma_I \left(\cos\left(\frac{n\pi}{2}\right) - j\sin\left(\frac{n\pi}{2}\right)\right)\right]}{\left(\varsigma_I \omega^n (R_t + R_w)\cos\left(\frac{n\pi}{2}\right) + 1\right)^2 + \left(\varsigma_I \omega^n (R_t + R_w)\sin\left(\frac{n\pi}{2}\right)\right)^2} + R_s \tag{8.34}$$

where, ς_I is the capacitance of the double layer, R_t is the charge transfer resistance of the interface, R_w is the Warburg resistance, ω is the angular frequency of the potential impulse and n is the dispersion factor. The real and imaginary parts can be separated out as,

$$\Re[Z] = \frac{(R_w + R_t)\left(1 + (R_w + R_t)\varsigma_I \omega^n \cos\left(\frac{n\pi}{2}\right)\right)}{\left(\varsigma_I \omega^n (R_t + R_w)\cos\left(\frac{n\pi}{2}\right) + 1\right)^2 + \left(\varsigma_I \omega^n (R_t + R_w)\sin\left(\frac{n\pi}{2}\right)\right)^2} + R_s \tag{8.35}$$

$$\Im[Z] = \frac{-(R_w + R_t)^2 \varsigma_I \omega^n \sin\left(\frac{n\pi}{2}\right)}{\left(\varsigma_I \omega^n (R_t + R_w)\cos\left(\frac{n\pi}{2}\right) + 1\right)^2 + \left(\varsigma_I \omega^n (R_t + R_w)\sin\left(\frac{n\pi}{2}\right)\right)^2} \tag{8.36}$$

It should be noted that when n=1 the original expression for the impedance of the electrode interface is returned (Equation 8.25), which is expected as this represents the purely capacitive double layer. Adding the dispersive capacitance gives the corresponding impedance and phase spectra for a gold electrode of the size of the SPNI shown in Figure 8.6. As can be seen, the dispersive capacitance increases the impedance of the electrode interface and results in a more gradual decrease in impedance for increasing frequency. At 1000 Hz the impedance of the electrode for n=1, 0.9, 0.8 and 0.7 are 97 kΩ, 235 kΩ, 561 kΩ and 1340 kΩ respectively. In the phase plot, for n<1 the behaviour shows a constant phase spectra that is independent of the applied frequency. As n decreases the value of the constant phase line increases accordingly. Finally, the impedance and phase spectra for the dispersive SPNI electrodes (n<1) do not indicate that the impedance becomes dominated by the solution resistance.

Estimating the relative Dielectric Constant, ϵ_r

One constant that does not get discussed in detail in the modelling work of Kovacs and others is the effect of varying the dielectric constant, which effects the capacitance of the double layer. Figure 8.7 shows the effect of changing the magnitude of ϵ_r (between values of 79.4, 40, 20, 10 and 5) on the relationship between the total impedance and the area of the electrode at 1 kHz. As can be seen, decreasing the value of the dielectric constant increases the total impedance.

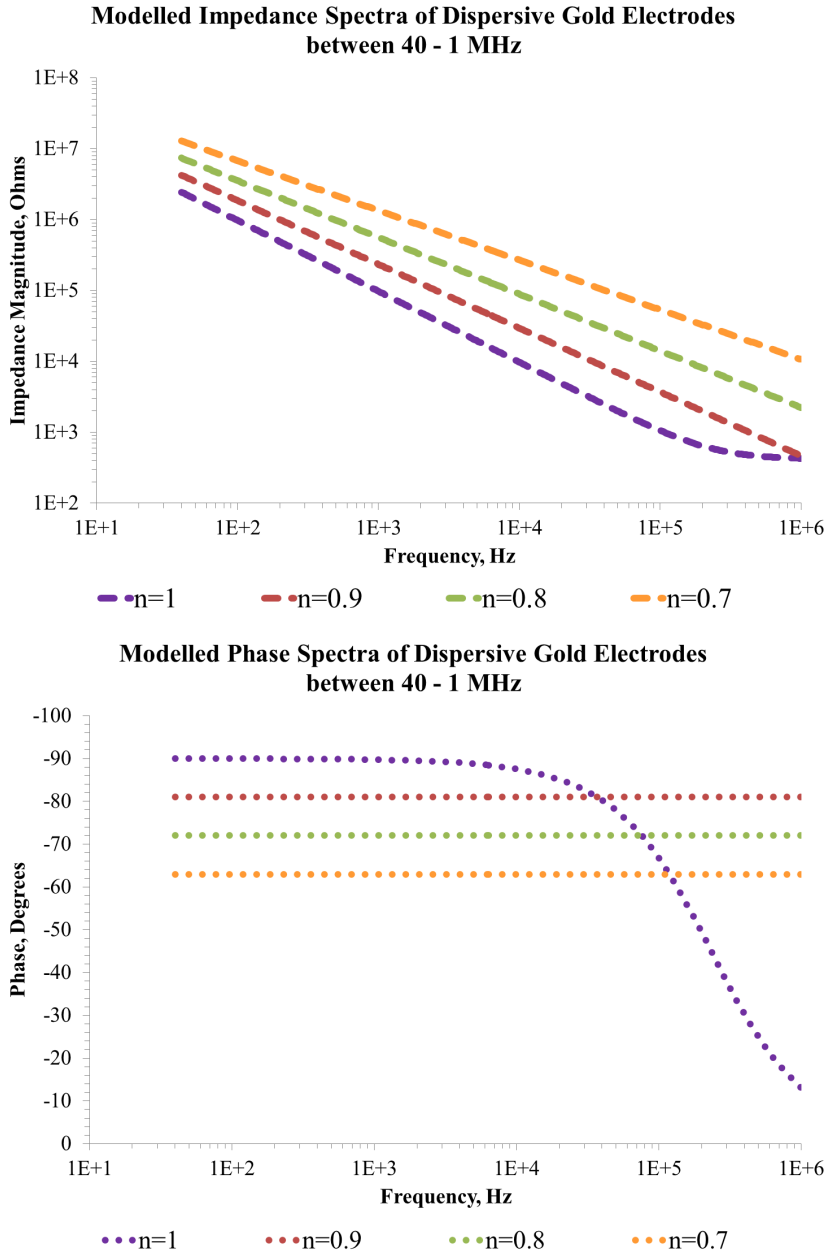

Fig. 8.6: The modelled Impedance and Phase spectra of an SPNI electrode with dispersive capacitance of varying 'idealness'

The dielectric constant of water is 79.4 at 25°, but in the interface the electric field is varying over such short distances (Angstroms) it is hard to justify that the potential field would be linear and so the true value of the dielectric constant is hard to determine. In the interface Kovacs suggests that the dielectric constant could be as low as 6 [20].

By comparing the modelled impedance with values reported in the literature, as collated by Fung et al in 2010 [88], it appears as though a dielectric constant of 79.4 may be most closely matching the reported values. As shown in Fig 8.5, the gold electrodes have an impedance around 0.5×10^7 Ω for an area of 1 μm^2 and an impedance of around 10^4 Ω for an area of $1x10^4$ μm^2, which is consistent with a dielectric constant of 79.4. However, the modelled data here is only considering a pure capacitor and the reported values may be influenced by surface inhomogeneities. Also the collated data highlights the variation of measured impedance between research groups, which makes it difficult to draw concrete conclusions. As a result the dielectric constant for this modelling work is kept at 79.4, as this gives the right order of magnitude for the general relationship between increasing area and impedance.

Varying the Charge Transfer Resistance

The model so far does not account for the possible effect of contaminants at the interface on the charge transfer resistance, or the effect of varying the oxygen partial pressure that could change the rate of oxygen reduction/oxidation. In the literature it suggests that the exchange reaction of a noble metal with an electrolyte may be effected by impurities of an unstated origin [85, 84]. If these impurities increase the exchange current density of the electrode material then the impedance of the interface may be affected, whereas a decrease in the exchange current density would not affect the impedance. To demonstrate this, the impedance and phase spectra of three modelled electrodes that have different charge transfer resistance are shown in Figure 8.8. This figure therefore models a reduction in the charge transfer resistance (caused by an increase in the exchange current density). As can be seen, reducing the charge transfer resistance by 10^3 Ω does not effect on the impedance spectra, as it is still extensively dominated by capacitive phenomena. However, reducing the charge transfer resistance by 10^6 Ω does lead to a plateau in the lower frequency behaviour as well as an increase in the phase behaviour of the interface. However, it is hard to justify what would cause such a large change in the charge transfer

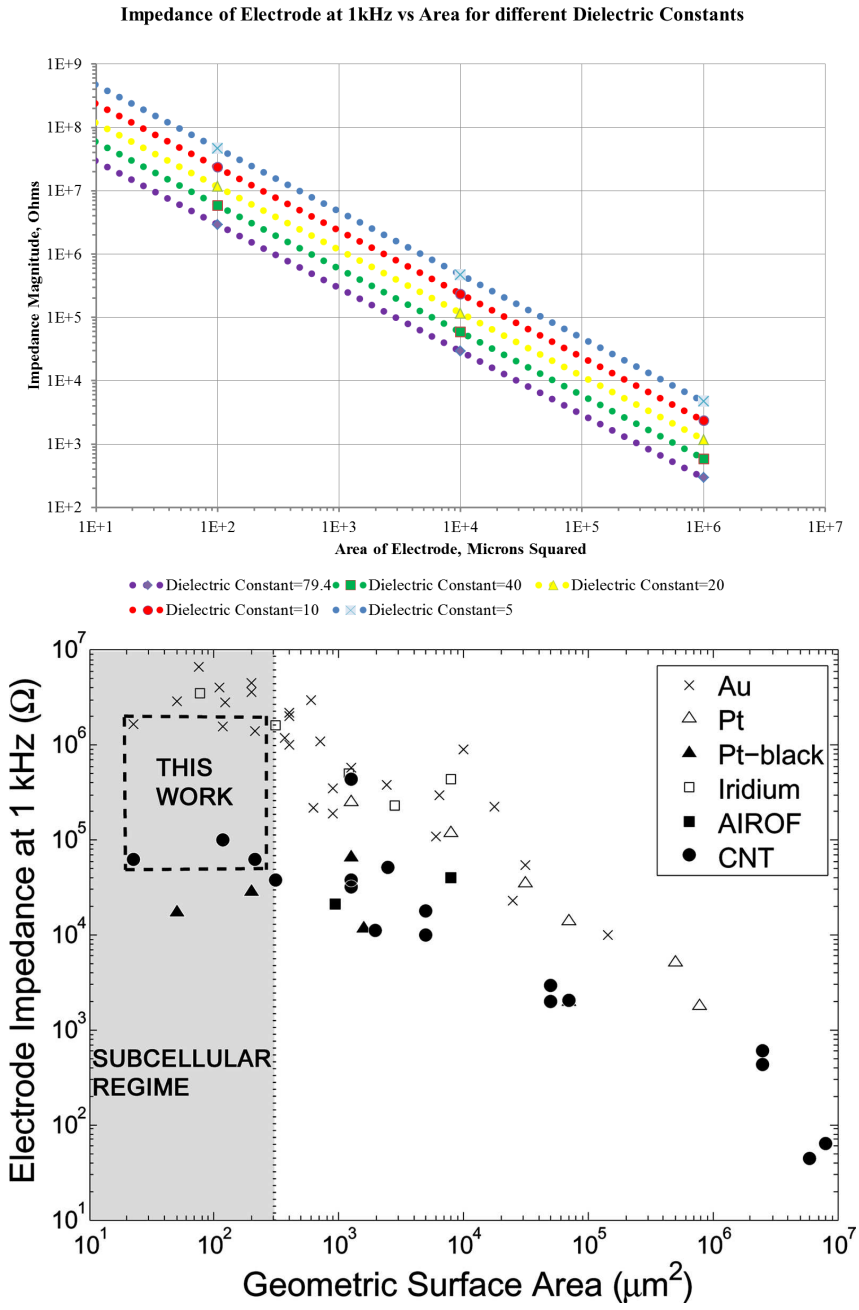

Fig. 8.7: The modelled Impedance magnitude at 1 kHz versus Area of gold electrode for different dielectric constants of the solution, The top graph shows the modelled impedance with respect to surface area and the bottom graph shows the impedance of other interfaces from the literature (gold electrodes are marked by crosses, all annotations are the original authors and do not relate to this thesis)

[88]

resistance. Thus it is fair to assume that the charge transfer resistance would have a minimal impact on the measured impedance of the SPNI electrode.

The geometry of SPNI

So far the model has been for a planar electrode with no other geometric considerations, however the SPNI is a complex micro-fabricated structure for which each micro-channel has walls and a roof. If the channel is completely sealed it may be expected that the current between the two electrodes in the impedance spectroscopy would be forced to travel through the length of the sealed channel which would have a corresponding resistance,

$$R = \rho \frac{L_{\mu-c}}{A_{\mu-c}} \tag{8.37}$$

where $L_{\mu-c}$ and $A_{\mu-c}$ are the length and area of the section micro-channel through which the current must travel and ρ is the resistivity of the solution. For the SPNI, the electrode is 2 mm from the edge of the device and the micro-channel is 100 x 100 μm. This gives a corresponding resistance of 1.4×10^5 Ω. As both ends of the device are open the current can travel through either opening, this give a solution resistance of $R_s = 1.4\times10^5/2 = 7\times10^4$ Ω. This resistance would be expected to dominate the higher frequency behaviour of the device and give much higher impedance than the solution resistance of the flat SPNI electrode.

If the sealing is incomplete, however, this resistance will be reduced and the impedance at higher frequency would be expected to plateau at a value closer to solution resistance of the planar electrode, shown earlier in Figure 8.4, as the current would not be confined to the micro-channel and would be able to follow a more direct path.

The effect of including the solution resistance of the sealed micro-channel on the impedance and phase spectra is shown in figure 8.9 and 8.10, for both the ideal and dispersive interface respectively. As expected, the impedance plateaus at the solution resistance at a lower frequency than in the previous, flat models. In Figure 8.9 the 1 μm^2 electrode begins to plateau at very high frequency, reflecting the need to measure impedance over a large frequency range to include all the electrochemical phenomena. This behaviour should be extremely noticeable when analysing the experimental data taken from the fabricated samples and may serve a useful indication as to whether the channels have been sealed effectively. Thus, the experimental testing

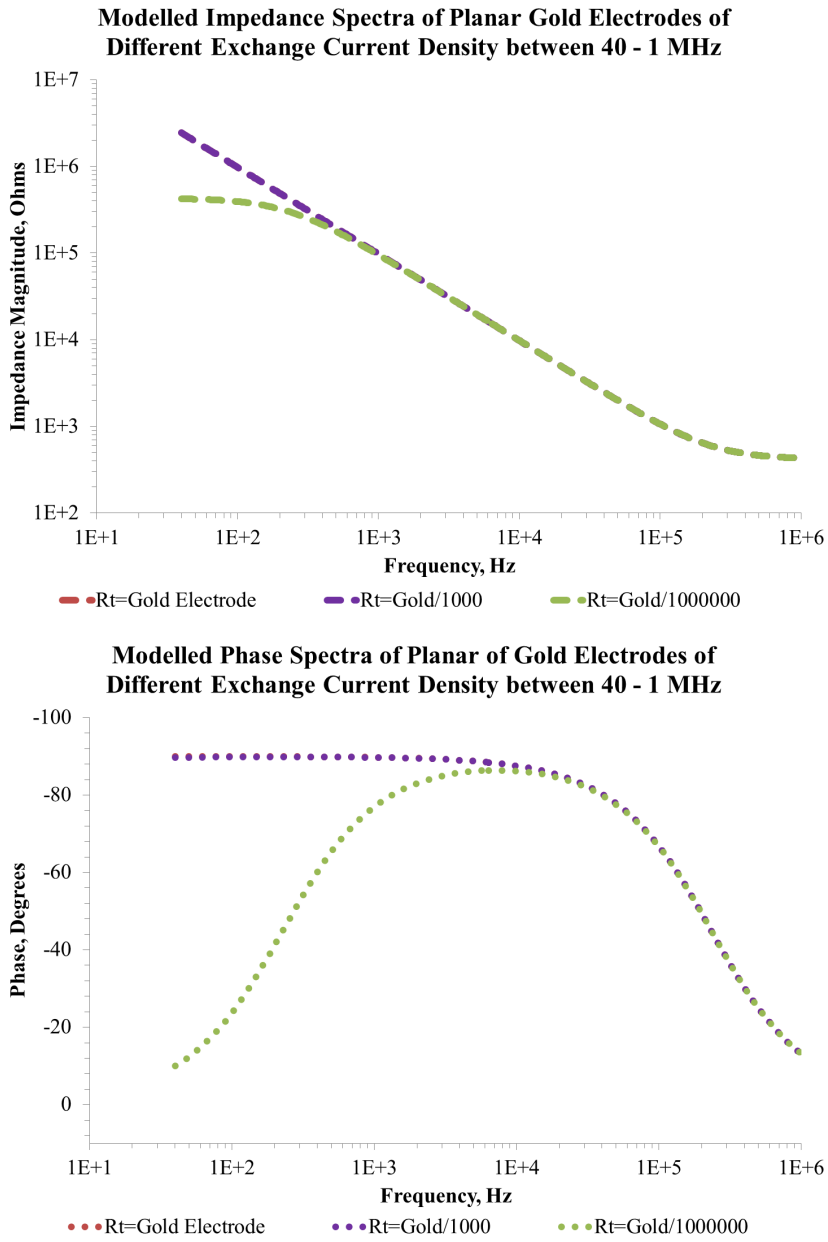

Fig. 8.8: The modelled Impedance and Phase spectra of a SPNI sized gold electrode for varying charge transfer resistance. A large reduction in charge transfer resistance reduces the lower frequency impedance of the electrode.

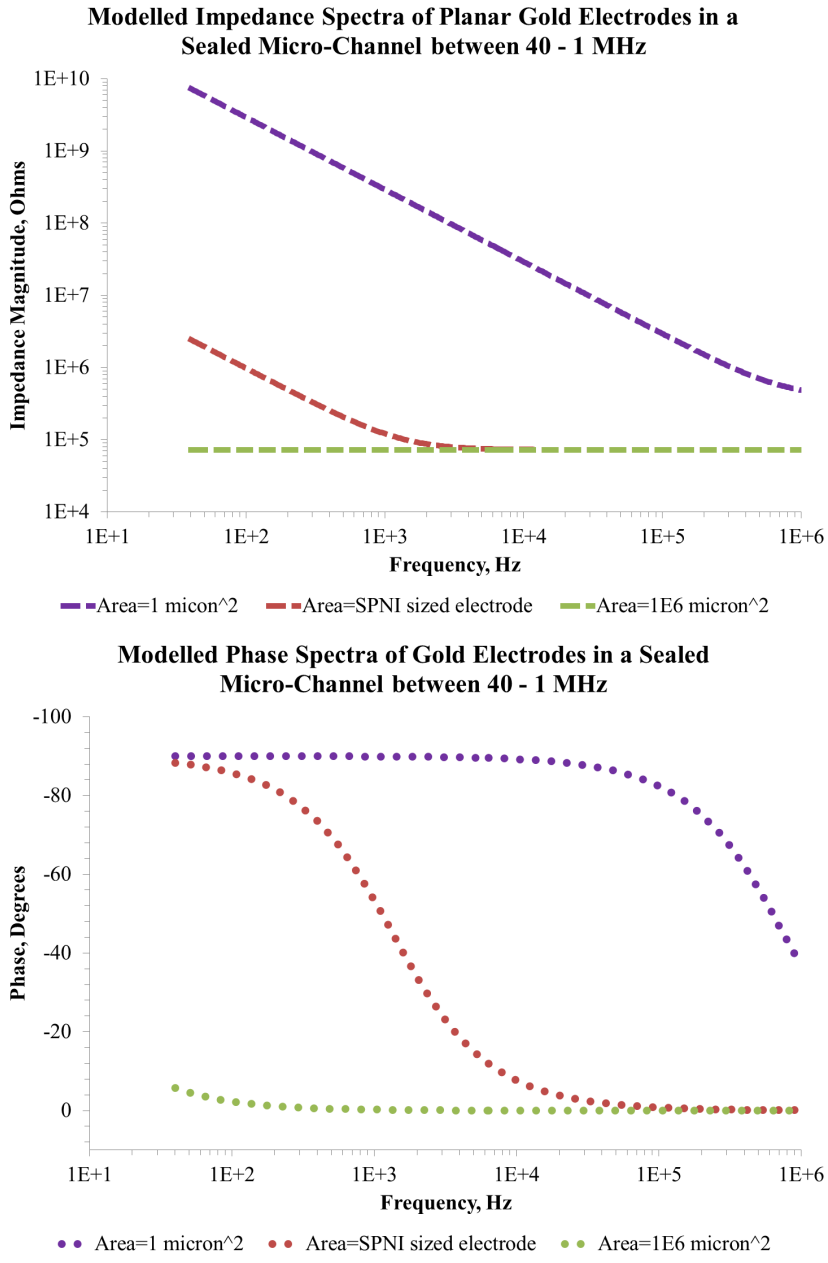

Fig. 8.9: The modelled Impedance and phase spectra of a pure electrode of different surface areas including the added geometry of a sealed micro-channel. The SPNI electrode is modelled by the brown dashed line.

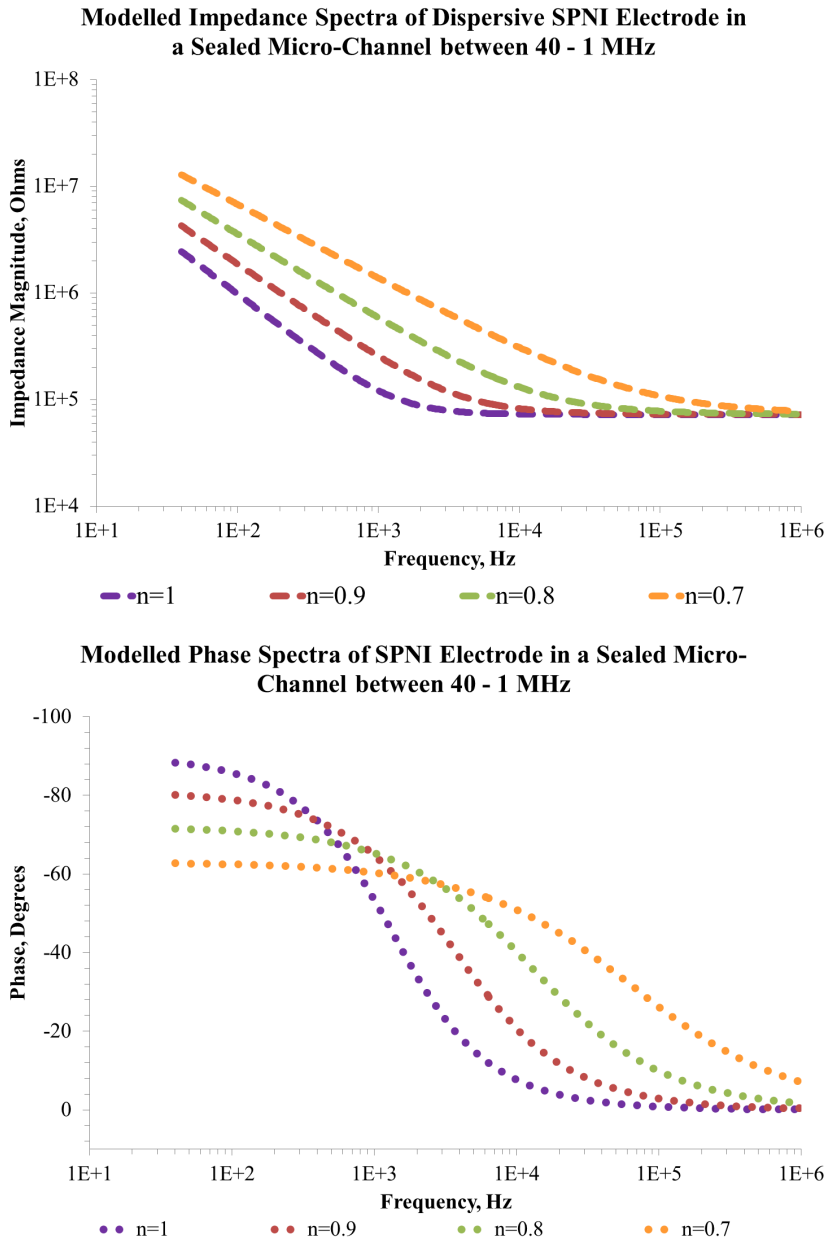

Fig. 8.10: The modelled Impedance and phase spectra of dispersive gold electrode (Surface Area=SPNI-sized) for varying 'idealness' factor, n, including the added geometry of a sealed micro-channel.

should be able to detect if the channels are leaking.

This result completes the modelling of the SPNI electrode for impedance spectroscopy. The next chapter presents the experimental results of the in-vitro testing to determine both the impedance of the SPNI electrode and it's mechanical durability during tensile testing.

9. ELECTRICAL AND MECHANICAL TESTING OF THE MODIFIED SPNI

9.1 Electrochemical Impedance Spectroscopy (EIS)

As a result of the problems that have been discussed so far, in particular the problems during the final curing of the PSPI, the amount of in-vitro testing that could be conducted on the SPNI was limited. However, it was possible to perform electrochemical impedance spectroscopy on a small number of samples to assess the quality of the electrodes that had survived the fabrication process and determine whether the MFI had been successfully incorporated into the SPNI. The results presented are intended to validate some fabrication processes that have been discussed, whilst highlighting areas that need further investigation.

The methods of obtaining impedance spectra and the reasons why such tests are important in the development of a neural interface is introduced in chapter five. To analyse the results obtained from performing these tests a model of the electrode interface has been presented in the previous chapter that can be used as a guide. The effects of varying the capacitive and resistive elements of the interface and the area of the electrode on the impedance and phase spectra have been outlined. Furthermore, the effect of introducing sealed micro-channels has also been introduced. Thus, these modelled impedance spectra can be used to assess the quality of the SPNI fabrication process.

9.1.1 Incorporation of the Microflex Technology into the SPNI

Typical impedance spectra for electrodes in a dual substrate, rolled SPNI is shown in Fig.9.1. The electrodes measured correspond to connection pads in the middle of the device, as these were the only pads that could be aligned correctly for MFI. The plot shows the typical impedance of the electrodes measured as well as the spectra from the highest and lowest impedance measured. The mean impedance at 1000 Hz for 10 electrodes of the rolled SPNI was 747 kΩ with a

range of 280 kΩ to 1.2 MΩ, as shown. From the modelling work it can be said that this amount of impedance is higher than what would be expected for a pure, planar gold electrode that had a corresponding impedance of ≈100 kΩ at 1000 Hz (as in Figure 8.4). Thus the impedance is approximately seven times larger that would be expected for the ideal case. Similarly the phase spectra varies greatly than what would be expected in the ideal case, as the measured phase at lower frequency (between 40→1000 Hz) is ≈-60°, whereas the modelling work suggested that the lower frequency response would be dominated by the capacitive coupling with a phase closer to -90°. It has been well reported that electrodes cannot behave as ideal capacitors due to slow chemical processes that evolve at the interface. Instead, a dispersive capacitance can be used to represent the double layer of the electrode. This will be discussed further later in this chapter. For the higher impedance measurement there is a large amount of scattering at low frequency whereas for the typical electrode, whose behaviour is reflective of the majority of electrodes and close to the mean impedance measured, there is less scattering at low frequency. For the lowest impedance measured, there is much less scattering. The origin of the scatter is unknown, but seems to be more prevalent for higher impedance electrodes. This requires further investigation.

The three impedance spectra appear to be similar up to 10^4 Hz, before deviating in the higher frequency range. The lowest impedance electrode appears to plateau at around 10^5 Hz with an impedance of 40 kΩ, which may correspond to a solution resistance. However, the typical electrode does not show an obvious plateau with increasing frequency, and has an impedance of ≈10^4 Ω at 10^6 Hz. This behaviour is repeated in the higher impedance electrode.

Looking at the phase spectra at higher frequency the three spectra show very different behaviour. The lowest impedance electrode shows a gradual increase and peaks at -28° at ≈200 kΩ before showing more capacitive behaviour at higher frequency. Both the typical electrodes and the higher impedance electrode are relatively flat for frequencies up to 10^4 Hz, before showing a tendency to a more resistive impedance by slowly rising up to 10^5 Hz. Above 10^5 Hz the highest impedance electrode shows more capacitive behaviour by decreasing to towards -70°.

The behaviour of the lowest and highest impedance electrode may suggest that there are other phenomena that are affecting the impedance spectroscopy that were not represented in the earlier modelling. The behaviour shown would be consistent with a leakage capacitance

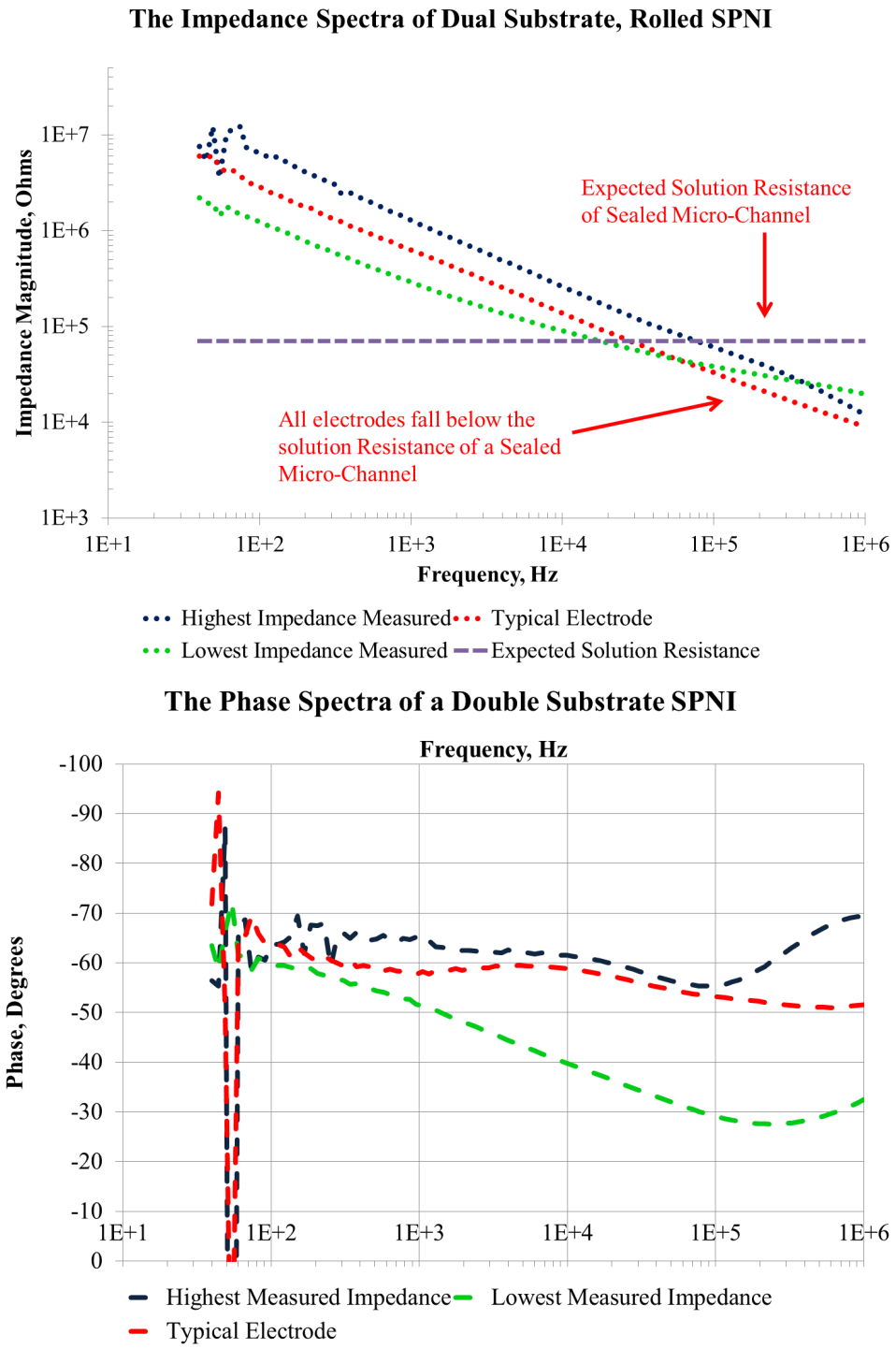

Fig. 9.1: Impedance and Phase spectra of dual substrate, rolled SPNI sample including the spectra of highest and lowest impedance measured and a typical electrode. The horizontal line represents the expected solution resistance of a sealed channel. Top; Impedance Spectra, Bottom; Phase Spectra

that starts to dominate at higher frequency, leading to a more capacitive phase. This leakage capacitance could arise from the capacitive coupling between the wires that connect the DUT to the impedance analyser or from the passivated tracks of the SPNI, but this requires further investigation.

Also included on the graph is a line to show the value of impedance at which the impedance spectra would be expected to plateau if the micro-channel was perfectly sealed. This value was calculated in the previous chapter and as can be seen none of the electrodes plateau at that line. This result suggests that the micro-channels have not been perfectly sealed.

Single layer SPNI

Single layer samples were also fabricated to assess whether there was any difference for the impedance or phase spectra, as discussed in the previous chapter. As the fabrication processes associated with adding the step are specifically challenging, if it can be shown that single layer samples offer as good an electrochemical interface as the dual substrate samples that would argue against the use of the dual-layer substrates in further development of the SPNI.

It should be noted that single layer samples were easier to fabricate than the dual layer substrates, without many of the significant problems associated with the shrinking of the polyimide layers during the curing step. Some misalignment was seen with the single layer sample, as had been observed with the dual-layer samples, but the gold layer was not obviously degraded after the final curing step. The impedance and phase spectra of a rolled, single layer sample are shown in Figure 9.2.

It was found that the mean impedance for the single layer SPNI electrodes was 687 kΩ, with a range of 380 kΩ to 1.1 MΩ (N=14), which were the only electrodes that could be aligned onto the connection pads. No electrodes had failed as a result of the rolling. It should be noted that the measured impedance is again higher than what would be expected for this electrode, based on the modelling of a pure electrode, however, it is largely in agreement with the earlier in vitro and in vivo studies.

The impedance curves again follow roughly the same behaviour, where the typical electrode and the highest impedance electrode both show lower frequency scatter. The lowest impedance electrode for this sample again showed less scatter at lower frequency and a plateau at 10^5

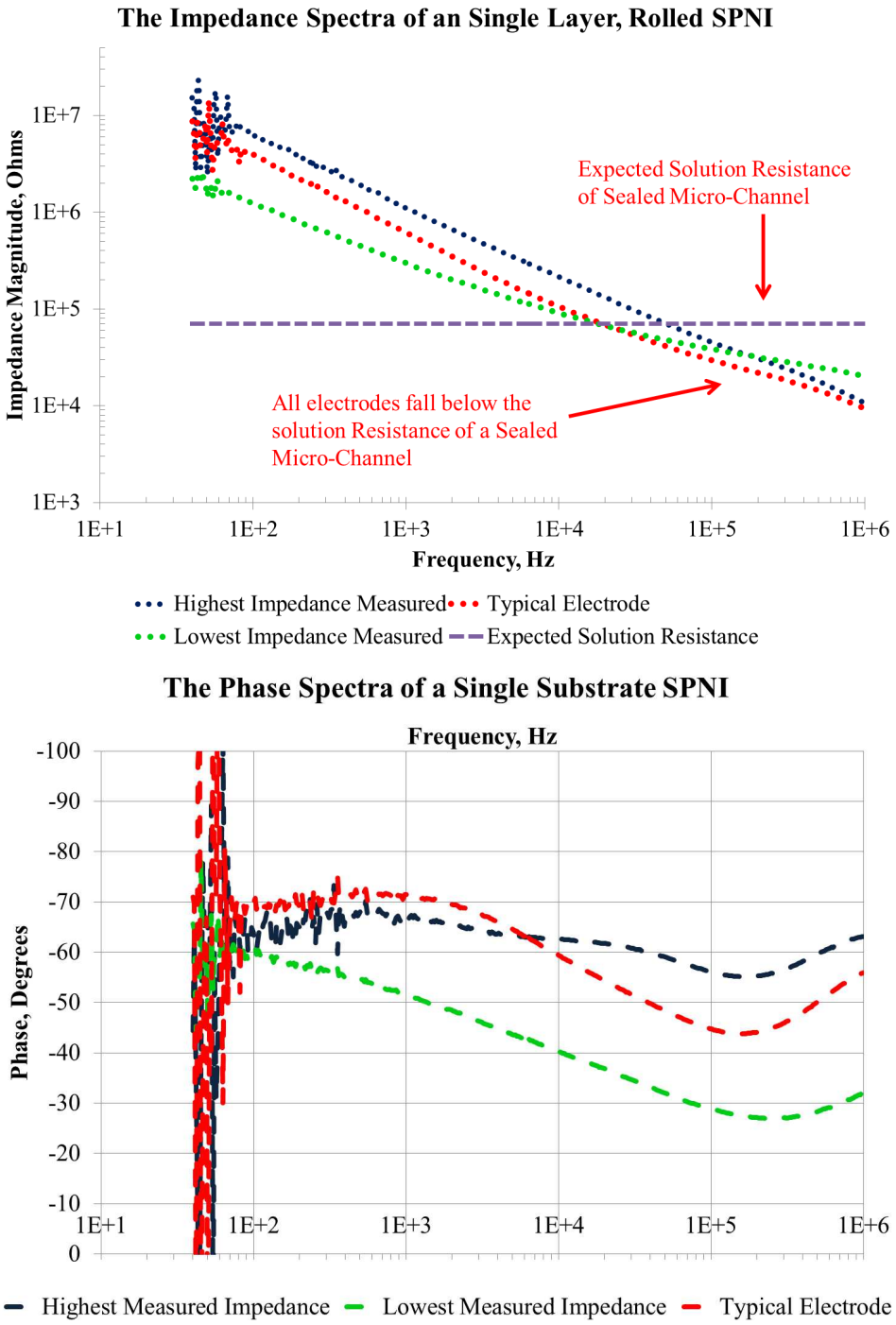

Fig. 9.2: Impedance and phase spectra of a Single substrate, rolled SPNI sample. The horizontal line represents the expected solution resistance of a sealed channel. Top; Magnitude of Impedance, Bottom; Phase Spectra

Hz. The phase plots are perhaps most revealing, with all three samples appearing to have their most resistive impedance at around 10^5 Hz, suggesting that the more dominant current at this frequency is ohmic and may be related to the solution resistance. After this dip, the three curves show more capacitive behaviour that again may be related to a leakage capacitance. This, along with the other important features of the impedance spectra, will be discussed in the conclusion to this chapter.

Again the effect of sealing resistance would be expected to cause the impedance spectra to plateau at the line shown on the graph, and the experimental behaviour of the sample suggests that the micro-channels have not been sealed perfectly.

Comparison of Experimental Result to Theoretical Models

Comparing the impedance spectroscopy to the theoretical modelling presented in the previous chapter suggests that the typical electrodes for both the single and double layer sample have a dispersive capacitance with an 'idealness' of $n \approx 0.8$, as shown in Figure 9.3. Included in the figure are the spectra of the typical electrode of both the single and double layer SPNI, as well as the modelled impedance and phase spectra of a dispersive SPNI electrode. It can be seen that in the lower frequency range the impedance spectra match the theoretical model with all the spectra following the same curve. For the model of the dispersive electrode in the sealed channel the impedance spectra begins to plateau at 10^4 Hz, whereas the other three curves continue to decrease. As the frequency increases the experimental results deviate from the modelled impedance of the electrode without sealing (labelled as planar in the previous chapter) and show a higher impedance than would be expected of a unsealed channel. Again, at lower frequency the phase spectra of the modelled and experimental results are well matched, all beginning at around 70°. As the frequency increases the modelled phase of the sealed electrode shows a dominant solution resistance with a phase of 0° above 10^5 Hz, whereas the planar electrode stays at a constant phase across the frequency range. Both the single layer and double layer spectra show high frequency behaviour that is roughly between these two extremes. The phase spectra of the single layer sample shows a similar shape to the modelled spectra of the sealed channel shifted along the frequency axis (before some capacitive phenomenom begins to dominate for frequency $>10^5$ Hz).

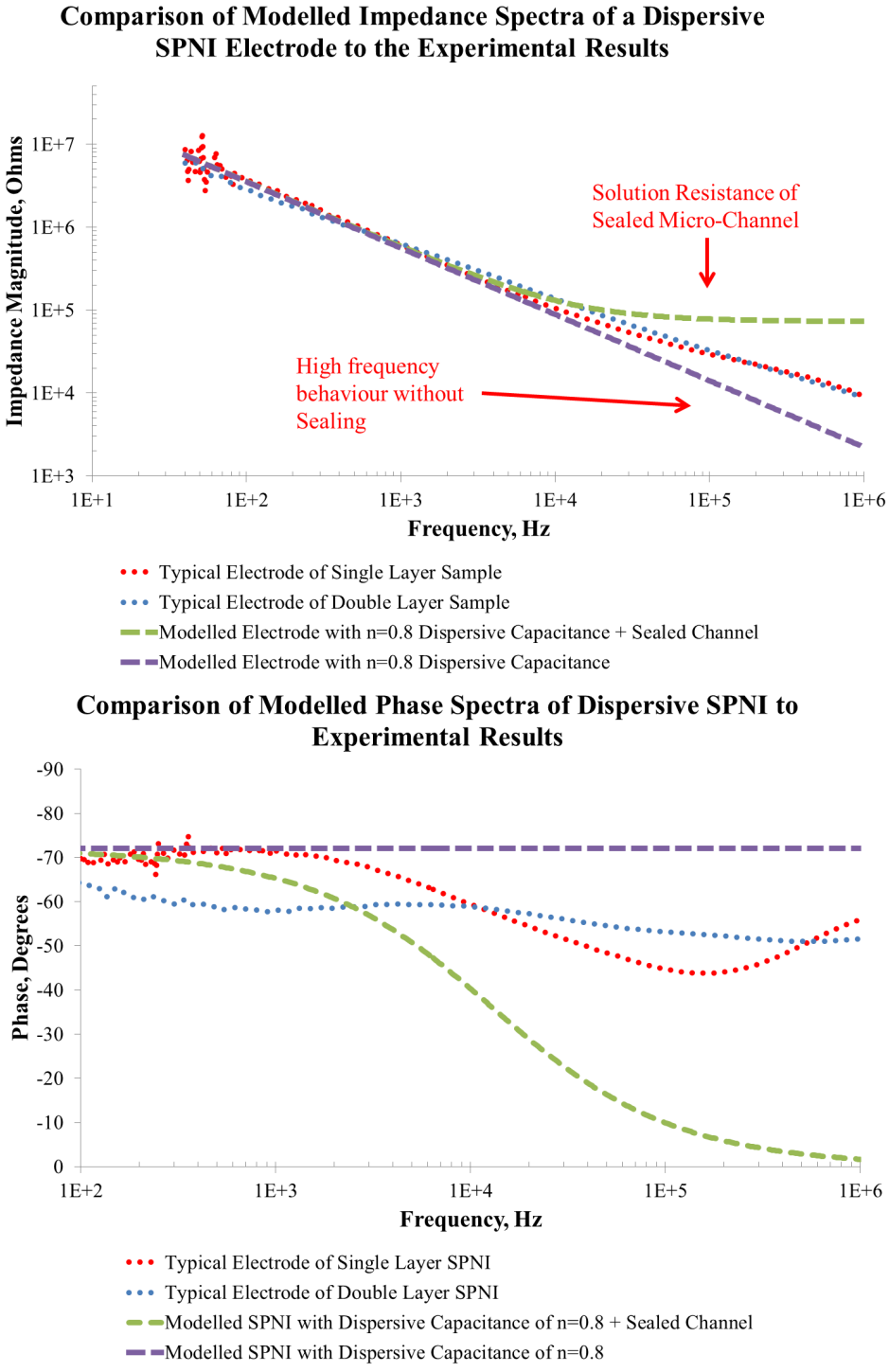

Fig. 9.3: Comparison of Impedance and Phase Spectra of SPNI with Theoretical Modelling. Both the typical electrodes for the single layer and double layer samples are included with the modelled spectra of an SPNI electrode with a Dispersive capacitance of n=0.8. Also included is the dispersive SPNI electrode (n=0.8) in a sealed micro-channel with the corresponding solution resistance.

These results may suggest that the micro-channels of the SPNI are only partially sealed, where the measured impedance and phase spectra for higher frequency show behaviour that is neither indicative of perfect sealing nor a totally planar electrode. From these spectra it would be hoped that improving the sealing of the device would make the behaviour more like that of the green dashed lines in Figure 9.3. These results suggests that there should be further investigation into methods of sealing the micro-channel.

Impedance of SPNI with Failed Gold Layer

To serve as a comparison to the 'successful' impedance spectra presented, also included is the impedance and phase spectra measured for a failed electrode, shown in Figure 9.4. This result was taken from an electrode that had obvious failure in the step region caused by shrinking during curing, similar to the failed step shown in the previous chapter. To serve as a comparison, and to gain more insight into the possible origin of the leakage capacitance shown in Figure 9.1 and 9.2 it is interesting to consider what the impedance measurement on a device with fractured tracks looks like.

The results are potentially interesting as, although for frequency less than 1000kHz the measured impedance is highly variable, it appears to show that the failed metal layer begins to show capacitive behaviour at higher frequencies, with a very high corresponding impedance ($\approx 10^8\Omega$ for frequency >1000Hz). This is also hinted at in the phase spectra, where the measured phase begins to settle around -90° at higher frequency, which is the phase of an ideal capacitor.

The break in the metal layer may act as a capacitor to give measurable impedance at higher frequencies. However, the measured impedance is at the limit of the dynamic range of the network analyser (500MΩ), so this data should be treated with caution.

Estimating the Impedance of a Fracture

In the design of microstrip transmission lines for microwave resonators and transmissions the capacitance between two coplanar conductors has been modelled. It is possible to use this work to estimate the corresponding impedance of a fracture in the thin metal film.

As shown in Figure 9.5, the fracture is modelled as a break in the wire that has a gap spacing of S, combined width of the wires of W and the length of the gap L. For this model the

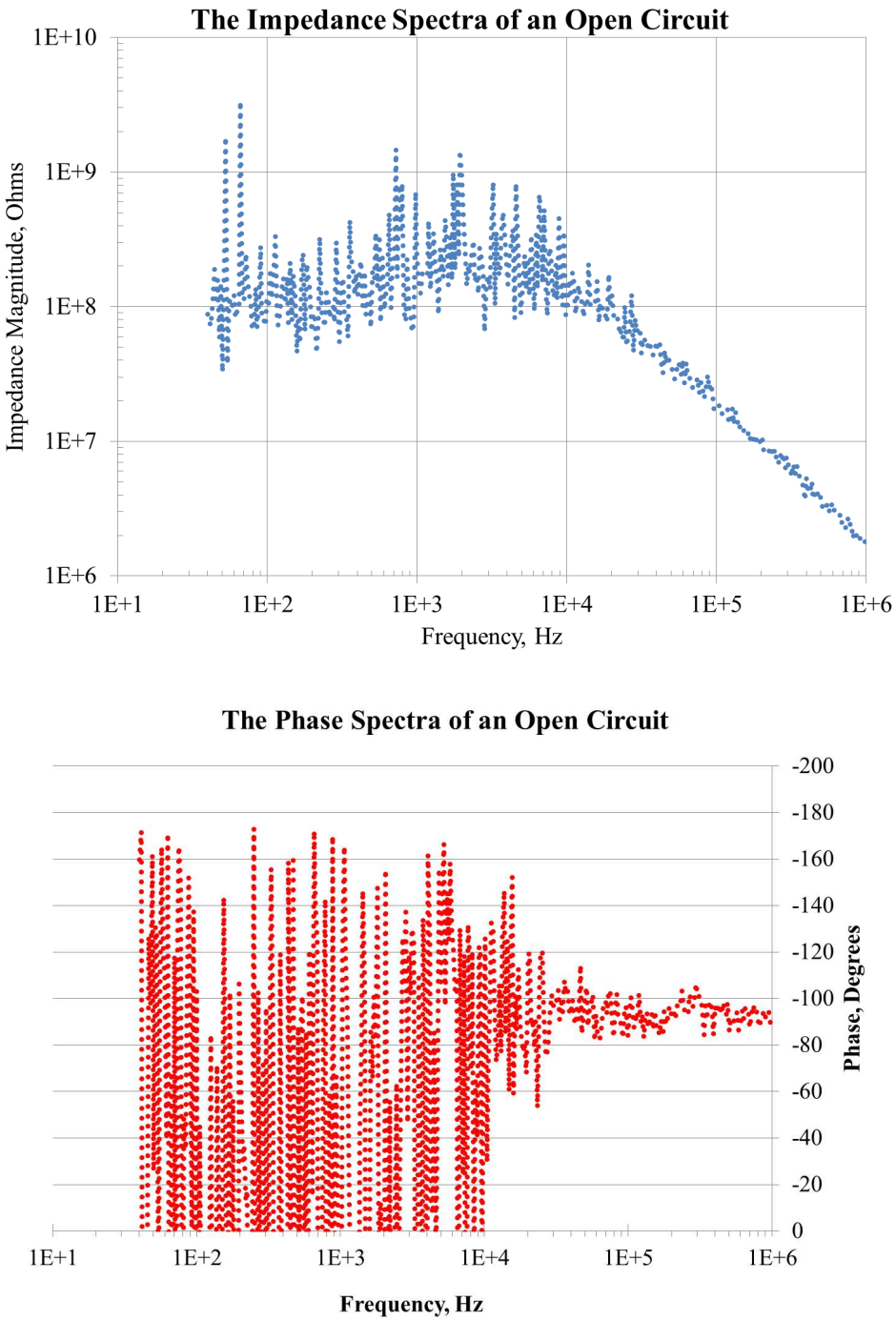

Fig. 9.4: Impedance and Phase spectra of failed electrode

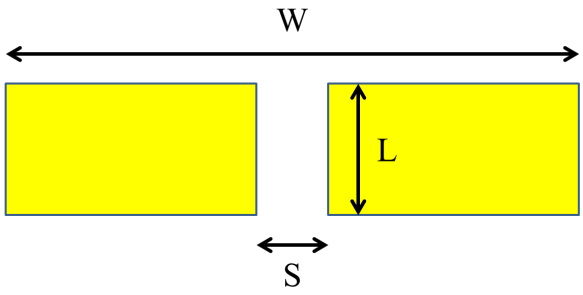

Fig. 9.5: Illustration of a fracture in the metallization of the SPNI

capacitance per unit length between the transmission lines, ς' can then be written as,

$$\varsigma' = \left(\frac{\xi_r + 1}{2}\right)\xi_0 \left[\frac{K(k)}{K(k')}\right]^{-1} \tag{9.1}$$

where k and k′ is the variable that relates the gap spacing and the combined width and can be written as

$$k = \frac{S}{S + 2W} \tag{9.2}$$

$$k' = \sqrt{1 - k^2} \tag{9.3}$$

The $\frac{K(k)}{K(k')}$ term is the ratio of the elliptical integrals that is used to characterise the gap and ξ_r and ξ_0 are the relative dielectric constant of substrate, which for Durimide 7020 is 3.3, and the permittivity of free space respectively. To calculate the complete elliptic integrals requires significant endeavour, using a computational algorithm or otherwise. However, from the reference [89] the ratio between the integrals can be estimated as,

$$\frac{K(k)}{K(k')} = \frac{\pi}{ln\left[2(1 + \sqrt{k'})(1 - \sqrt{k'})\right]} \quad \text{for} \quad 0 \leq k \leq 0.707 \tag{9.4}$$

$$\frac{K(k)}{K(k')} = \frac{ln\left[2(1 + \sqrt{k})(1 - \sqrt{k})\right]}{\pi} \quad \text{for} \quad 0.707 \leq k \leq 1 \tag{9.5}$$

Once the capacitance per unit length has been found it is possible to find the total impedance of the gap for different frequencies by multiplying by the length of the gap, L and using the

Tab. 9.1: Impedance of different sized fractures in a gold track (L=30 microns) at 1 and 10kHz

S(μm)	k	Impedance of fracture at 1Hz (Ω)	Impedance of fracture at 10kHz (Ω)
0.1	$5x10^{-6}$	$3x10^{13}$	$3x10^{9}$
1	$5x10^{-5}$	$4x10^{13}$	$4x10^{9}$
10	$5x10^{-4}$	$5x10^{13}$	$5x10^{9}$
100	$5x10^{-3}$	$6x10^{13}$	$6x10^{9}$

Tab. 9.2: Impedance of different sized fractures at the step L=400 microns at 1 and 10kHz

S(μm)	k	Impedance of fracture at 1Hz (Ω)	Impedance of fracture at 10kHz (Ω)
0.1	$5x10^{-}6$	$2x10^{12}$	$2x10^{8}$
1	$5x10^{-}5$	$3x10^{12}$	$3x10^{8}$
10	$5x10^{-}4$	$4x10^{12}$	$4x10^{8}$
100	$5x10^{-}3$	$5x10^{12}$	$5x10^{8}$

expression,

$$|Z| = \frac{1}{\omega\varsigma} \tag{9.6}$$

where ω is the angular frequency, $\omega = 2\pi f$. The impedance has been calculated for a gap thickness of S=0.1, 1, 10 and 100 microns respectively, for a fracture in the tracks where the combined metallization has a length of W=1 cm and the results are tabulated in Tab.9.1. These results suggest that the corresponding impedance of a fracture in a track is out of the dynamic range of the impedance analyser across the frequency range in Figure 9.4. The impedances of a fracture at the step of the device, where L=400 microns, is tabulated in Tab.9.2. These results suggest that the impedance of the fractures between 0.1-100 microns at the step may be measurable for frequencies >10 kHz, but possibly not at lower frequency. This suggests that the impedance spectrum presented in Figure 9.4 may be a measurement of the impedance a fracture at the step between 0.1 and 100 microns wide. It can be seen that none of the fractures would be measurable at 1000Hz, as the impedance would be 10 times larger.

This is consistent with the impedance spectra presented, however these calculations are only estimations of the impedance across the step and the measured impedance may also be affected by artefacts of the experimental apparatus, caused by the cables to the analyser or other phenomena and as the impedances estimated are at the limit of what is measurable caution is advised. Without further investigation it can only be assumed that very high impedances are only evidence of a fracture and not a characterisation of the spacing between the wires.

Furthermore, the result in Figure 9.4 suggests that a leakage capacitance from the apparatus is not effecting the higher frequency impedance spectra of the successful samples presented in Fig 9.1 and 9.2. All tests were performed over the same frequency range using the same experimental conditions, so any leakage capacitance from the apparatus should have been present in all the results. As the open circuit and successful samples show different higher frequency behaviour, it may be suggested that higher frequency phenomena are not driven by instrumental artefacts. Again this requires further testing.

9.2 In Vitro Tensile Strength Testing

To ensure that the Microflex technology had not decreased the mechanical strength of the SPNI device a series of tensile tests were conducted using an Instron Environmental Mechanical Analyser (Instron 5848 MicroTester), that is able to measure mechanical properties such as tensile and compressive strengths.

Similar tests have been performed on the Microflex connection in the past and have suggested that a Microflex connection is not as strong as a traditional solder join[70]. As such it was necessary to perform a small amount of tests to determine whether this caused a noticeable decrease in the durability of the ball bond connections.

During the initial testing, using the scheme outlined in chapter four, it was difficult to obtain any satisfactory results. The pull tester can be operated with or without pneumatic gripping tools to hold the sample during the test, but both methods were problematic. If the pneumatic tools were not used, where the grip tools were manually locked in position on the stage using adjustable screws, it was found that the SPNI sample would slip through the grips during the test. An example of slipping is shown in Figure 9.6. In the example illustrated, it appears that there is some loading on the sample (‘specimen 1’) before the slipping occurs, and in ‘specimen 2’ no result could be inferred. Alternatively, if the pneumatic grips were used, the SPNI and the alumina were significantly damaged by the crushing force that the grips provide, ensuring that the mechanical test could not be completed. Twelve samples were tested and all showed some signs of slipping or damage caused from the grips.

A workable solution was found by gluing the alumina PCB to a piece of sand paper using super-glue, to provide a manifold onto which the Instron pneumatic grips could hold. A further

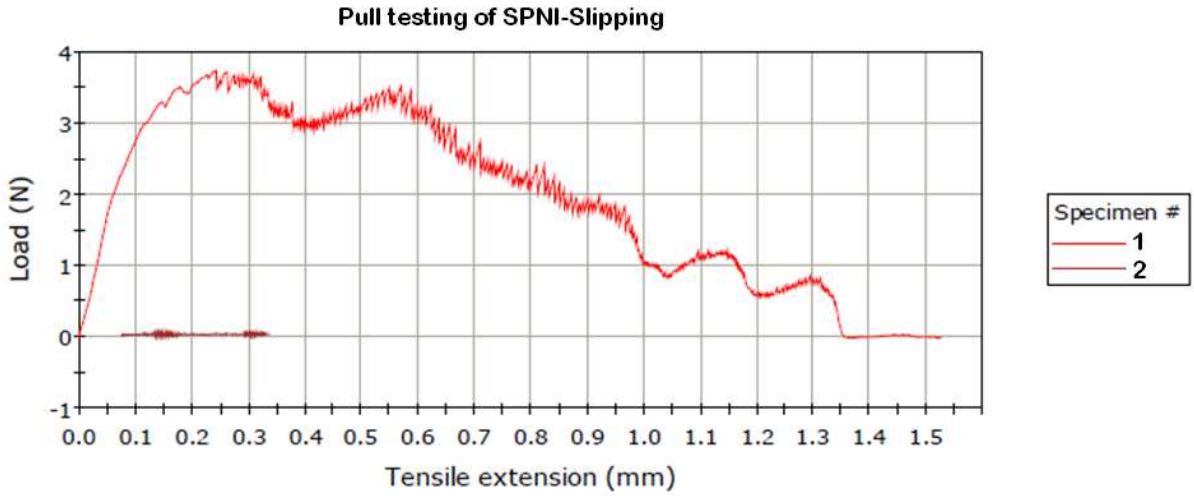

Fig. 9.6: An example of the result obtained from the pull tester as the sample was slipping through the grips

piece of sand-paper was glued to the front of the PCB (not touching the connected ball-bonds) and the two pieces of sand-paper were glued together. Two further pieces of sandpaper were glued just below the neck of the SPNI.

To test the SPNI devices four unrolled, cured, single-layer samples were ball-bonded to the alumina PCB, glued to the sand-paper in the method that has been described before the Instron machine was used to pull the two ends of the device apart, providing both a shear force at the Microflex interface and a longitudinal force through the body of the SPNI. The test was designed to see which part of the device was stronger, and to test whether the Microflex connections had added weakness to the SPNI.

At the beginning of the test the 'Bluehill program' required an input of the sample length to give an accurate readout of the extension of the tested specimen. This was kept constant value of 1cm for samples 1, 2 and 4 and 0.5cm for sample 3. As such the software was calibrated to accurately give the total strain required to break the SPNI as well as demonstrating whether the SPNI broke before the MFI interconnection could be stripped from the board. The results are shown in Figure 9.7. None of the device failed as a result of the Microflex technology, and all samples failed at some point around the neck of the device, as shown in Figure 9.8. This point coincides with the point at which the connection pads taper into the thinner connection region and the point at which the thicker Durimide layer begins. The measured strain and force applied at the break as determined by the Bluehill software are shown in Tab.9.3. The strain at which

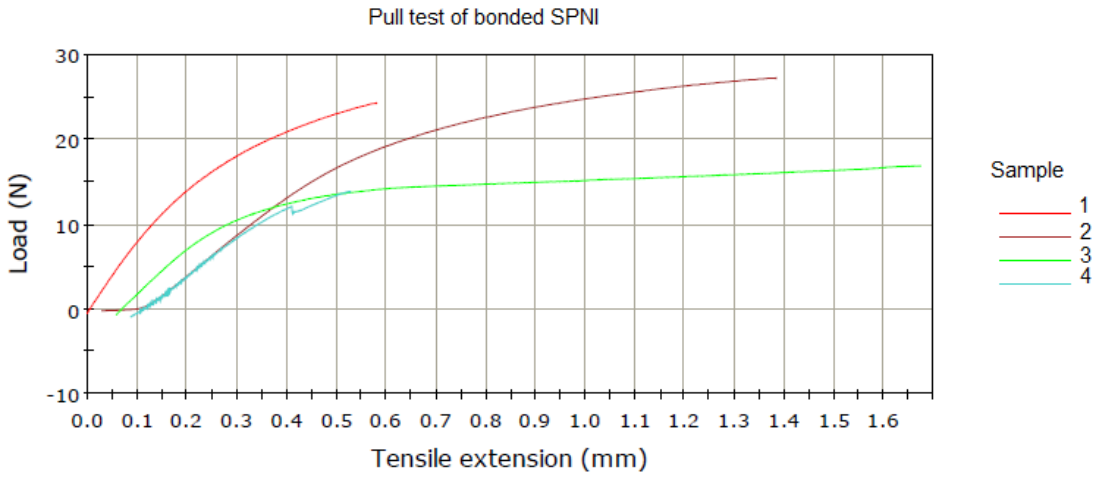

Fig. 9.7: Results of the pull testing on the bonded SPNI sample

Tab. 9.3: Measured Stain and Force applied at break, from Bluehill Software

Sample	Strain at Failure %	Force applied at break(N)
1	6	27
2	13	24
3	32	16
4	6	12

the samples broke is much less than the stated ability of the Durimide, which is 73% [51]. Sample 3 was tested over a shorter distance and only included the ball bonded connection pads, the tapered section of the device and around 2-3mm of the thin neck. This sample performed better than the other samples, and had a higher strain at the breaking point.

9.3 Summary of this Chapter

This work has suggested that the Microflex technique is a suitable connection scheme for the SPNI device. The first thing to note is the impedance could be measured successfully. The maximum number of electrodes that could be aligned in a dual layer sample was around 10, but this is still a larger number of electrodes than could be achieved with some more established electrode interfaces to the PNS. This suggests that the Microflex interconnections are compatible with the SPNI array.

The maximum and minimum impedances measured are included to highlight the variation in electrode impedance that was measured in an individual sample. There was no systematic variation of the impedance corresponding to the position of the electrode on the device. The variation

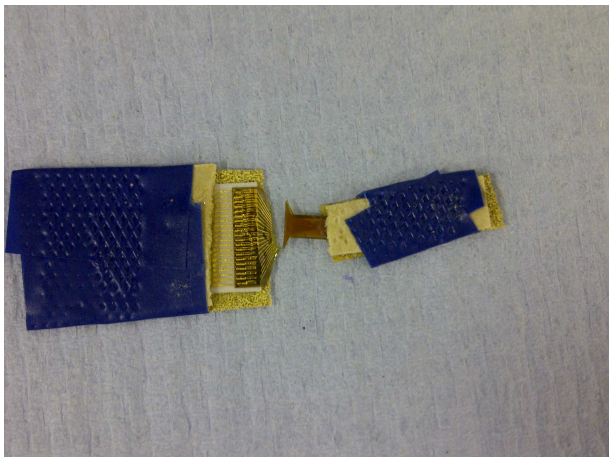

Fig. 9.8: An example of an SPNI sample that has been pull tested to destruction.

between electrodes is not ideal, as it suggests unpredictability in the ability to record/stimulate for each electrode.

Comparing the impedance spectra to the modelling work, it can be suggested that the impedance of the SPNI electrode may be higher that would be predicted for a planar, pure gold electrode of that size. There may be some contamination on the surface of the electrodes or a surface roughness that leads to a dispersive capacitance that is causing this. Indeed, the measured spectra seem to match the modelled spectra of a dispersive electrode with an idealness factor of n≈0.8. For a completely sealed micro-channel the solution resistance is expected to be $\approx 7\times10^4$, but all the electrodes measured achieved impedance lower than this value. For the single layer sample all three phase curves presented have a maxima in the phase spectra around 10^5 Hz, suggesting that this may be the point at which the solution resistance is most dominant, corresponding to an impedance of $\approx1.5\times10^4$ Ω. This may further suggest that the electrodes have not been completely sealed, as discussed in the previous chapter. However, the higher frequency behaviour also suggests that there is some leakage capacitance that is effecting the spectra for frequencies $>10^5$. At this time the origin of this leakage capacitance is unknown, however it may be ruled out that is from the apparatus as the impedance and phase spectra of a failed electrode did not show the same high frequency behaviour as the successful electrodes. Alternatively, the leakage capacitance could be from the passivated gold tracks that run along the length of the device. As the frequency increases it may be expected that capacitive coupling across the polyimide insulation between the gold layer and the solution may be effecting the results as capacitive current is able to flow from the gold into the solution (and vice versa) from

areas other than the exposed electrode surface. This capacitance should be investigated in future work.

If it is assumed that the electrode is not behaving as a perfect capacitor then it may be suggested that the dispersive capacitance has a constant around $n \approx 0.8$ as shown by the comparison between the modelled and experimental work that are well matched for lower frequencies. This suggests that there is some surface roughness that is affecting the interface, and may explain why the measured impedance is higher than would be expected for a perfect gold electrode of the equivalent size. This is also backed up in the phase spectra that have a higher value than would be expected across all electrodes.

For electrodes that have higher impedances, the results show that there is generally more scattering and a lower phase at lower frequency. The scattering is not ideal, and perhaps suggests a difficulty of the testing set up to accurately measure the impedance and the phase at lower frequency. The modelling work predicted that for a pure gold electrode there would be very little direct charge transfer with a phase of -90° for lower frequencies, which is not present in the experimental data. A dispersive capacitance, caused by surface roughness or contamination may be influencing the spectra.

The result of the single layer SPNI were also interesting as they suggested that the samples that included the step did not perform any differently than the single layer samples. This is consistent with the updated bending model, as both types of SPNI are expected to be under tensile compression. Having estimated the capacitance and corresponding impedance of a fracture in the thin metal film, it may be possible to rule out that any of the electrodes tested had failed. Adding these findings to that of SPNI fabricated on a 25μm substrate layer, which suggested that 80% of electrodes survived the rolling for one study[77], and 97% for another[13], leads to the conclusion that the fabrication method is suitable.

The 2010 study [77] compared the measured impedance for both rolled and unrolled devices, which were remarkably similar, as shown in Figure 9.9, suggested that the strain on the metal layer did not affect the impedance. The impedance values presented in both the 2010 study and this thesis are consistent, suggesting that the updated fabrication process is at least as good as previous ones. Furthermore, the previous studies did not show an increased solution resistance for the rolled samples, although the spectra only went up to 10^5 Hz.

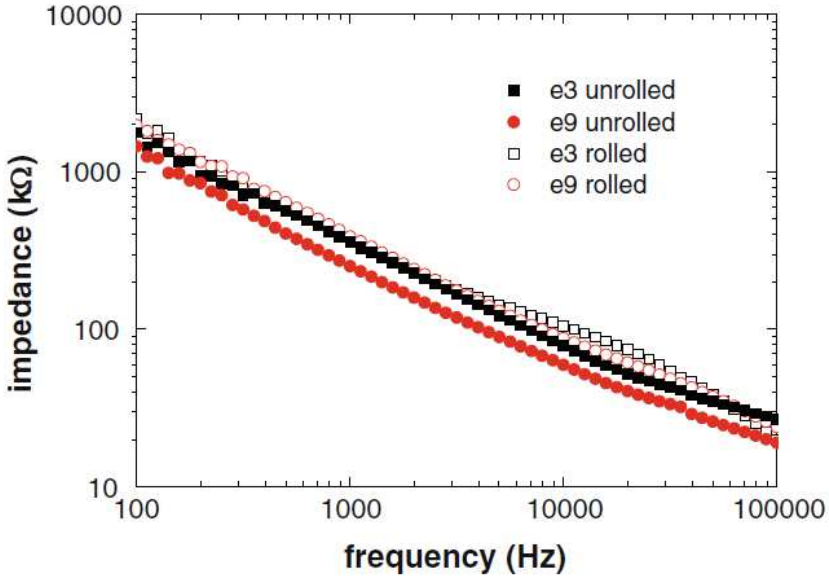

Fig. 9.9: The impedance spectra of both rolled and unrolled device on a 25μm substrate

The variation seen across the samples could be a result of a combination of factors, including variations of the completeness of the sealing of the SPNI micro-channel, an encapsulating film that has developed on the electrodes or the effects of surface roughness by the dispersive capacitance. If any of the electrodes had not been developed completely, so that the PSPI that was used for the insulation or channel layer is partially occluding the contact window, the total electrode area is reduced which would increase the impedance.

To try to alleviate these effects, each SPNI goes through a consistent fabrication process and several 'descums' to ensure that the electrodes are open, but it cannot be guaranteed at this stage that no contamination was present. The impedance spectroscopy suggests that the updated SPNI device is at least as good as the previously tested samples, although further work is required to refine the process and to make perfectly sealed micro-channels. This should be a priority in any future evaluation of the SPNI, as the reliability and functionality of the interface should not be compromised by any technological aspects.

The pull tests have demonstrated that the Microflex interconnects are at least as strong as the SPNI substrate layer. The force required to 'break' the sample was around 30N, with a corresponding strain between 6 – 30%. This is not within the strain that should be achievable with PSPI substrate. This suggests that there is an underlying cause of failure that needs further investigation.

In the previous SPNI experiments the neck of the device provided a significant point of

weakness causing the polyimide layer to fracture [discovered through personal communication with Dr E. Tarte]. It was initially proposed that the this weakness was due to the SPNI being cut out manually using scissors from a full sheet of PI, as discussed in a previous chapter. It was thought that if the edges are not defined perfectly, stress can concentrate at the weak points, causing a mechanical failure.

These tests suggest that the overall shape of the device may be having a more fundamental role in the ability to endure mechanical loading, as the weakness of the substrate layer seems to be present in the photosensitive substrate layer that should have no defects associated with the manual shaping.

The mechanical durability of neural interfaces is an important consideration in the design as the devices have to be capable of surviving handling, implantation and movement of the patient during its lifetime. If there is any mechanical weakness it cannot be guaranteed to provide a stable recording/stimulation platform. Any interface to the PNS would be expected to survive mechanical stress from many directions, especially during the handling and implantation phase, where the surgeon may have to manipulate the device onto a nerve for cuff electrodes, or in between fascicles. Similarly, for the SPNI implants the nerve has to be carefully inserted into the silicone tube which may cause a small amount of force acting transversely to the neck of the device. Because of these considerations any future testing of the SPNI should include fatigue testing to determine the durability.

The MFI technology is a well-established method of connecting neural interfaces to external electronics, and as a result it was not expected to introduce any significant problems in terms of reliability and ease of implementation. These tests have shown that MFI is at least compatible with the SPNI array, but further investigation should be conducted to establish failure rates and to determine the cause of the variations seen across the impedance spectra of the SPNI.

The next chapter introduces fabrication processes that have been developed to seal the micro-channel structures.

10. IMPROVEMENT IN THE CHANNEL SEALING OF THE SPIRAL PERIPHERAL NERVE INTERFACE

After it was found that Microflex technology could be successfully incorporated into the SPNI process, it was necessary to tackle unreliable sealing of the micro-channels as demonstrated by the experimental data shown in the previous chapter, as well as in [13]. The next chapter describes how this problem was addressed and outlines the use of a thin layer of PDMS to 'seal' the channels.

10.1 Introduction

One major flaw discovered in the SPNI design during the in vivo study was that the micro-channels were 'open'. This stops the channel from completely encapsulating the regenerating nerves reducing the local extracellular resistance, discussed in chapter four. During the rolling of the SPNI the top of the channels should be pressed against the substrate of the next spiral layer. However, in vivo measurements in reference [13] as well as experimental evidence presented earlier suggest that this was not entirely successful. The imperfect sealing is likely have caused the stimulation current for the SPNI device to be considerably higher ($\approx$20 μA) than a completely sealed device made of PDMS ($\approx$4 μA) despite the PDMS channel having a larger volume.

It is reasonable to suggest that this increase in stimulus current may also reduce the ability to record from the regenerated material and it was found that there was significant 'cross-talk' between neighbouring channels in the device. If a single electrode is able to activate both a muscle and its antagonist then the ability to provide useful technological assistance is diminished. To reduce this, each electrode should interface to the regenerated tissue inside a specific channel. If the stimulating current is able to spill out of the channel to activate axons in neighbouring channels, the selectivity provided by the interface is reduced.

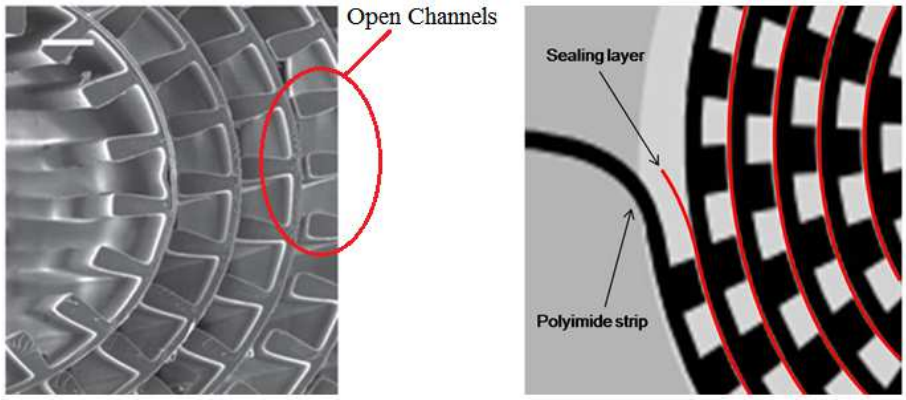

Fig. 10.1: Schematic of how the sealing layer will work for the SPNI micro-channels.

Thus it was desirable to investigate methods of sealing the channels that were compatible with the other fabrication processes associated with the SPNI. Both sealing layers of polyimide and PDMS were investigated during this work, and in the end it was found that PDMS gave the best results.

10.1.1 Methods of Sealing Micro-Channel Structures

Most inspiration for this type of work can be found in the field of microfluidics where micro-fabricated structures are designed to handle small quantities of fluids for drug delivery or for biological analysis. There has been a recent drive toward drug-delivery systems and complex chemical analysis of small quantities of fluids, using microfluidic devices [90].

For the interest of this thesis only the ability to make sealed micro-channels using polyimide and PDMS is considered as it is possible to integrate these flexible polymers into the microfabrication of the SPNI, which needs to be highly flexible to be compatible with the rolling. For this, it was envisaged that the simplest way to generate sealed micro-channels was to bond an additional layer of the insulating material onto the top of the open channel structure, by an appropriate procedure, and rolling the channels as before. This idea is illustrated in Fig. 10.1.

The bonding procedures that have been developed in MEMs fabrication are very different for each material used, and have been carefully tailored to produce the best results for each application. Bonding in this way can generally be split into three categories that are most common, they are;

1. The ‘Direct Bonding’ of two materials, typically Silicon, Pyrex and Quartz, that are brought into contact, without any significant external pressure, and are annealed together

using a curing step that is typically between 600 and 1200°C [91].

2. Alternatively, 'Anodic Bonding' is based on the joining of a material that contains electron conductors and a material that has ion conductivity, the materials are heated and voltage is applied to pull the surfaces together where they fuse. This technique is generally useful for bonding samples that have intermittent layers of glass or polycrystalline silicon [92].

3. Finally, 'Adhesion Bonding' is performed via an adhesion material flowing or deforming at the interface to make a bond. After the bonding has taken place, the materials should be sufficiently hardened to maintain the bond, and is typically performed using organic polymers.

For a review of the different bonding processes used in MEMs fabrication, that potentially have a direct translation into the sealing of the SPNI channel structures, the references [93, 94] are useful. And for adhesive bonding in particular, that most applies to the adopted processing mechanism for the sealed SPNI, there is a review from Niklaus et al [95].

The methods of bonding that were investigated for use in the SPNI are adhesive related, bonding two polymeric materials together to provide a seal on the micro-channel structures. For this, the basic principle is that once the two materials are bought into a sufficiently close contact, they will adhere. This adhesion is caused by the deformation of at least one of the material surfaces, which can happen via a process of 'wetting' of the surface, plastic or elastic deformation or diffusion of a solid material [95].

Most of the studies on adhesive bonding have focused on the bonding of two wafers with an intermediate adhesive layer. In the case where a polymer is used, the polymer adhesive deforms to fit the surfaces to be bonded via a liquid (or semi-liquid) phase that is able to flow to match the surface profile. This is the process of 'wetting', and is seen as being crucial for successful adhesive bonding using polymers [95]. The more the adhesive polymer material is able to flow the better the resulting bond quality will be as any unfilled space on the surface can allow for the migration of water molecules or gas bubbles between the bonded surfaces, potentially causing areas of weakness. Thus, it is reasonable to suggest that the polymer adhesive must exist in a liquid or semi-liquid state during the bonding process, and then must transform from this state into a more solid state to achieve a lasting bond [95].

Fig. 10.2: Process flow of sealing of polyimide channels developed by Metz [22]

For polyimide, this semi-liquid state is when the material has not been fully cured and so it is feasible to suggest that polyimide could be used in an adhesive bonding process. However, in contrast to other bonding methods, the polyimide channels serve as both the bonding interface and the structural support of the device. For this type of bonding, polyimide lamination has already been investigated by Stefan Metz [22], see Figure 10.1.1. In this lamination process, 5-20 μm-thick layers of PSPI were spin coated onto silicon wafers, with a chrome/aluminium sacrificial layer, and channels were fabricated using photolithographic techniques. After the structures had been shaped, the samples were cured at 300°C and submerged in N-methyl-2-pyrrolidone (NMP) to cause the polymide to swell (the necessity of this step was not discussed in the original work but it most likely to be to improve adhesion of the sealing layer, as discussed later in this chapter). A second layer of polyimide (5-30 μm-thick) was spun onto Mylar foil^{TM}, that had been attached to a silicon carrier wafer with vacuum grease, and soft-baked to 150°C. After the soft-bake, the wafer was flipped over and bought into contact with the swollen polyimide channels and laminated. The second carrier wafer and the Mylar foil were removed and the top layer of polyimide could be photolithographically structured. After this step, the final assembly was cured again at 300°C and the polyimide devices were removed from the carrier wafer by anodic dissolution of the sacrificial aluminium layer.

10.2 Methods developed to seal channels

10.2.1 Flip Chip Bonding of PI

To mimic this fabrication method, layers of polyimide (PI-2611) and PSPI (Durimide 7020) were spin coated onto silicon wafers, soft-baked and bonded together using a flip-chip bonder (Laurier M9 ultra high precision bonder, BESI). The thickness of each polyimide layer, both PSPI and PI, was kept at 20 μm as polyimide is flexible and durable at this thickness.

Several problem were discovered when attempting to utilise this procedure. Although possible with some work it was difficult to align the two wafers before the bonding was performed. Thus, it was decided to bond the two sheets of PI without alignment, only ensuring that the two wafers weren't overlapping, which could be achieved by monitoring the bonding process by eye. Using this set-up, it was found that during the curing of the polyimide sheets, out-gassing solvent can create 'voids'. The solvent out-gas caused large areas of the polyimide surfaces not to be bonded, which ultimately caused the bonds to fail. This voiding has been reported in other adhesive bonding processes, and can significantly weaken the bond [96].

This could be prevented by defining 'venting' tracks in the polyimide layers that would allow the out-gassing to happen in a controlled manner, avoiding the voids. However this would require significant investigation and the necessity to align the two wafers.

To reduce the effect of the voiding, it was decided to investigate ability to bond fully cured PI to a partially cured sheet of PI. This may have led to a weaker bond, due to only one of the adhesive surfaces having the 'wetting' properties, discussed earlier, but may also have reduced the voiding. However, for this set-up it was found that the bonding forces required to create durable bonds were very high, at the maximum operating pressure of the bonder. Very high bonding pressures were undesirable as these could potentially damage the final SPNI devices, although this was not tested.

This is perhaps why Metz et al [22], first submerged the cured polyimide structures in NMP to cause them to swell. The bonding pressure is not described in Metz's work, but it is assumed that it would not be too great to damage the underlying polyimide structures. Since NMP can be used to strip uncured polyimide, it was felt that it would be likely to cause delamination in the multi-layered SPNI. For these reasons the use of the polyimide lamination technology,

developed by Metz, was not pursued in favour of a different approach.

10.3 Use of PDMS to seal the channels

An alternative to the lamination bonding procedure was discovered by spin-coating a thin PDMS layer onto a carrier wafer that could then be released and laminated onto the polyimide channels. The bonding method has been developed that utilises the fact that PDMS swells in contact with IPA [97] [98], which can be applied between the two bonding surfaces. As the IPA evaporates, the two surfaces are bought into contact and the PDMS shrinks, due to the out-gassing of the IPA. An adhesive bond is formed between the two surfaces that is durable enough to survive the rolling into the spiral configuration and the subsequent insertion into the silicone tube. After the SPNI has been inserted into the tube it was possible to confirm that the PDMS layer has sealed the channels visually using a microscope. Unfortunately, it was not possible to test whether the channels had been sealed 'electrically', using impedance spectroscopy or otherwise.

10.3.1 Fabrication of thin PDMS layers

To achieve a reliable sealing of the channels between the rolls of the SPNI it was decided that a 10-20 μm-thick layer of PDMS would be appropriate, as this was expected to offer the mechanical durability required. To fabricate an isotropic layer of this thickness it was necessary to use a spin coating method. To find which spinning protocol would give the desired thickness of PDMS, several spin speeds were used during the fabrication process, and the subsequent thickness of the layers generated was measured using the Dektak surface profiler.

It is well known that uncured PDMS adheres very well to silicon and glass wafers during the curing process thus, as was the case with PSPI, a suitable sacrificial material was needed to ensure a safe release of the thin PDMS layer. For this, PMMA was again the sacrificial material of choice, as it could be spin coated into flat layers and dissolved at the end of the fabrication. The mechanism for releasing the PDMS is slightly different than the PSPI, and a lot faster, as in contact with IPA and MIBK solvent mixture, the PDMS swells causing a de-lamination, and the release is made permanent by dissolution of the PMMA underneath. This process takes a few minutes, and the PDMS is released as a large flat sheet that can be safely manipulated with

blunt tweezers.

To make the thin, flat PDMS layers;

1. A 3 μm sacrificial layer of PMMA was deposited and baked on a 4" silicon wafer as before

2. To make the PDMS, (Sylgard-184, DOW Chemicals) was mixed with a curing agent (Dimethyl, methylhydrogen siloxane) in a ratio 10:1 by weight. The mixture was continuously stirred for 3 minutes and allowed to stand for a further 5 minutes

3. The PDMS was applied to the centre of each wafer and allowed to spread out so that it covered at least 20% of the wafer surface. The PDMS was spun at 500rpm for 30 seconds before ramping up to the final spin speed, which for the initial investigations was between 1000→2400rpm, and held for 1 minute.

4. After spinning, the wafer was placed on a hot plate at 20°C and ramped up to 100°C at 16°C per minute. The wafer was further ramped to 150°C at 25°C per minute and held at 150°C for 10 minutes. The wafer was removed from the hotplate and allowed to cool for 20 minutes before being released.

5. To release the sample, the wafer was placed in a mixture of MIBK and IPA at a ratio of 3:1, where the PDMS could be seen to wrinkle as it swelled and de-laminated from the carrier.

6. After 5 minutes the PDMS was removed from the solvent mixture and placed on a clean silicon wafer where it was allowed to dry. As the PDMS was fully cured at this point, the thin layer did not permanently adhere to the silicon wafer.

To measure the thickness of the PDMS layers generated, sections of the PDMS were carefully cleaved using a scalpel and placed on a glass slide. The Dektak was used to measures the distance between the top of PDMS and the glass slide underneath, to give the step height. The PDMS spin-coat profile is shown in Figure 10.3. The profile suggests that to achieve a thickness of 10-20 μm a spin speed of approximately 1800-2500rpm should be used. At 1000rpm the sample was approximately 60 μm thick, however this was at the maximum of the dynamic range of the Dektak surface profiler, so this result should be treated with caution.

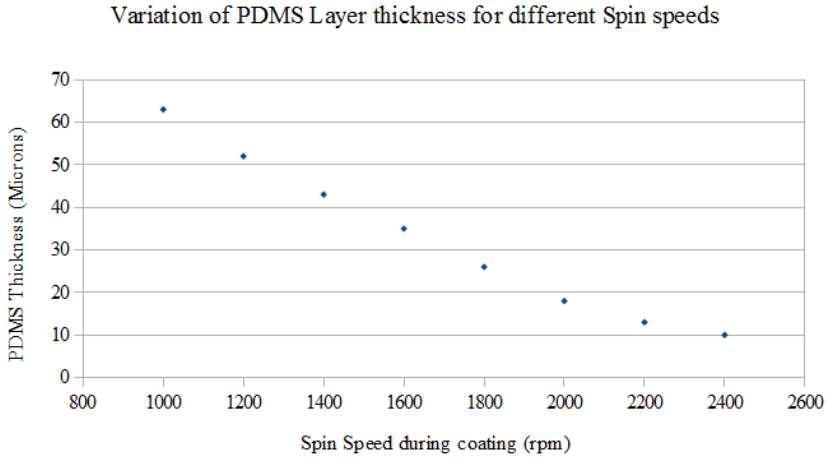

Fig. 10.3: Variation of PDMS thickness for different spin coating speeds

10.3.2 Bonding to Polyimide

After it was confirmed that it was possible to make and release flat, thin PDMS layers the next step in developing an appropriate sealing layer was developing the adhesive bonding. It was found that a bond could be made between the PDMS and cured polyimide channels by implementing IPA as a bonding intermediate. As mentioned before, the PDMS swells as it exposed to IPA with an approximate 5% weight gain reported for a PDMS sample soaked in IPA for 10 minutes [97]. As the IPA evaporates, the swelling reverses with a −5% weight change after the solvent has been driven off using a hotplate in reference [97]. It was theorized that this swelling and contracting of the PDMS could lead to adhesion between the two polymers, as a result of the surface of the PDMS being made temporarily wet-able by the IPA. This is similar to the process outlined in Kim et al's paper on the use of PDMS as 'Micro-contact Mould' for patterning three-dimensional structures [99]. This paper discusses the wetting of a PDMS mould with a solvent and describes the liquid solvent as being able to fill the recessed regions of the PDMS mould in order to minimize the liquid/vapour interface area and maximise the solid/liquid interface. Kim et al suggest that as the elastomer is compliant it adheres to surface of the polymer that they are moulding, forcing out the excess solvent. In their study the mould was allowed to remain on the surface of the 'printed polymer' for 5 minutes to allow the solvent to dissipate, and then the stamp was peeled away.

The process developed for the sealing of the SPNI mimics this procedure, only omitting the final peeling step. A small amount of IPA is applied to the polyimide channels using a pipette.

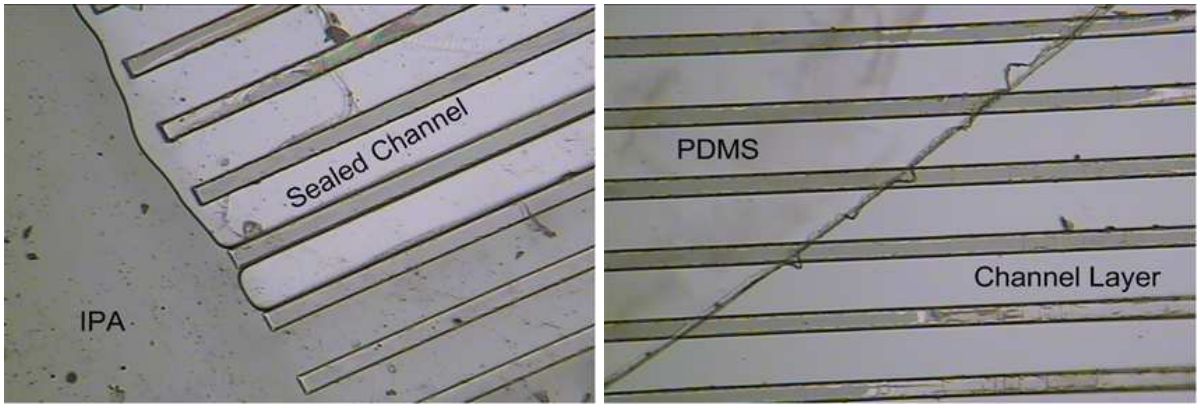

Fig. 10.4: Left; Microscopy of the liquid IPA in the adhesion bonding process, Right; A PDMS sealing layer that has been cleaved. For both images, the channel walls are 50 μm wide and the channels are 100 μ across.

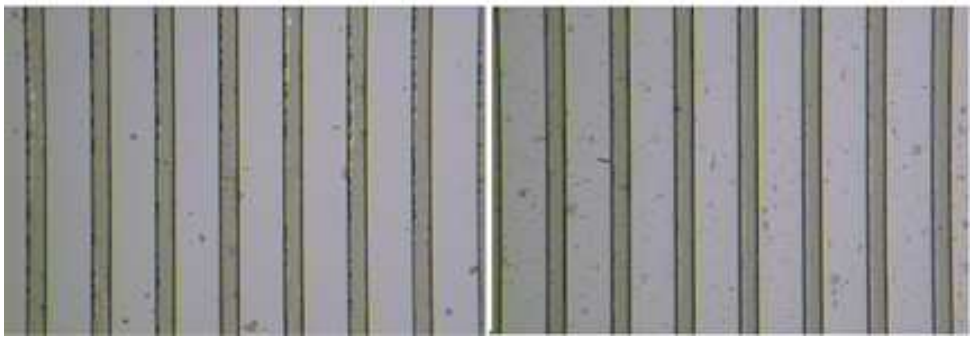

Fig. 10.5: Comparison of channels sealed with PDMS(right) and unsealed channels (left). For both images the channel walls are 50 μm wide and the channels are 100 μm across.

Once the IPA has been applied, the PDMS can be placed on top and spread out into a flat layer using tweezers. Once the solvent has evaporated, the PDMS adheres to polyimide as desired. To test this, 100 μm-thick polyimide channels were fabricated onto a silicon wafer using the photolithographic techniques and cured.

PDMS was made spun onto a silicon wafer with an intermediate sacrificial layer of PMMA. 10 μm thick layers were spin coated and the PDMS was baked and released using the described methods. After the release the PDMS film was placed onto the SPNI channels that had been soaked with a small amount of IPA, flattened using tweezers and left to bond for 5 minutes. Fig.10.4 shows the distribution of the IPA during the bonding process, as the IPA evaporates it exits the channels leaving them bonded. Fig.10.5 suggests that the channels are unaffected by the bonding process, as there is no noticeable difference. It was found that it is easier if the PDMS is applied on top of the channels as a large, flat sheet. For this procedure, many SPNI devices were arranged on a silicon wafer, or in a Petri dish, and IPA was spread out over the

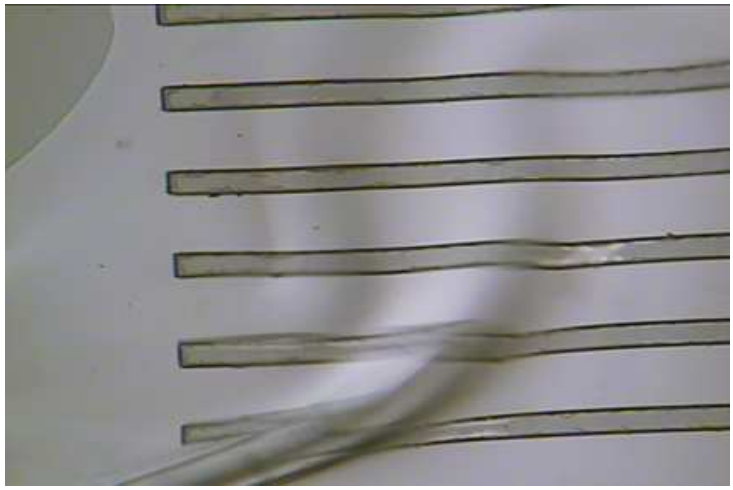

Fig. 10.6: A crease formed in the PDMS during bonding.

entire wafer. The PDMS was removed from the MIBK:IPA solvent in which it had been released and applied directly onto the SPNI channels. As the solvent does not evaporate instantly, it is possible to arrange the PDMS layer as necessary, ensuring that it is flat and there are no creases, before it is allowed to bond for at least 30 minutes. After 30 minutes the PDMS can be shaped using a scalpel, and the sample can be rolled into the spiral configuration using the same method as before. During these experiments, it was found that 10μm-thick PDMS layers were hard to manipulate, and some regions of the channels were not sealed, where creases had formed in the PDMS, an example of which is shown in Fig.10.6. For this reason, it was decided that 20 μm-thick PDMS layers were used in further investigations. One disadvantage of the thicker layer is the increase in overall diameter of the spiral configuration. In the conventional SPNI, before sealing, the rolled section was inserted into a silicone tube that had an internal diameter of 1.5mm. With a thick sealing layer, a larger diameter tube is necessary. For a sealing layer of 20 μm-thick PDMS, it was found that a silicone tube of an internal diameter of 2mm was adequate to give a tightly wound spiral, with good sealing of the layers. To test the ability to bond and roll the 20 μm-thick PDMS layer, the fabrication process was repeated with the new spin-profile (based on Figure 10.3) to produce the layer shown Figure 10.7. The PDMS was removed from the solvent and flattened out over passive SPNI samples, that were fabricated without electrodes and had been immersed with IPA. The passive SPNIs had been laid out on an upturned petri-dish, as shown in Figure 10.7. The PDMS was left to bond, and the final outline of the sealing layer was shaped using a scalpel.

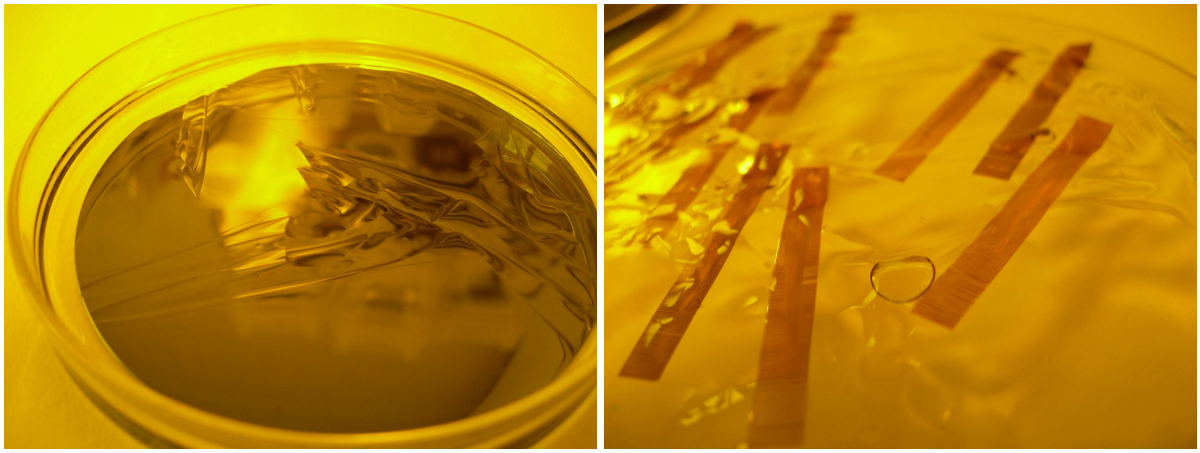

Fig. 10.7: Release and bonding of the PDMS layer, Left: Release of PDMS in MIBK:IPA, Right: Sealing of passive SPNI samples

The sample was carefully placed in the tweezers and rolled using the hand operated mechanism. The rolled sample was inserted into a silicone tube of an internal diameter of 2mm. This gave tightly spiralled channels, with a sealing layer, as shown in Figure 10.8.

It is logical to assume that the direction of rolling is important for a successful sealing of the SPNI channels. In the previous procedure for producing the spiral, the SPNI was rolled so that the channels were facing the inside of the device, as can be seen in Figure 10.1 and Figure 10.2. This configuration results in the top of the channels being slightly closer together than the bottom of the channels, which may cause the PDMS to sag into the channel possibly occluding it for any regeneration. As the channel needs to be as clear as possible, rolling the devices the other way, with the channels facing outwards, makes the tops of the channels slightly further apart than the bottom of the channels. This stretches the PDMS, avoiding any sagging, as shown in Figure 10.10. In can also be seen that the PDMS has sealed the polyimide channel by noting how the PDMS appears to be pressed against the roll of substrate that envelops it. The PDMS appears to be compressed between the top of the channel and the substrate of the channels on the adjacent roll. At this point, this sealing layer has not been incorporated into a full SPNI device. To implement the sealing layer the main body of the SPNI, including the substrate, channel structures and gold electrodes and interconnections, could be fabricated in the same method as used previously. After curing and release from the silicon carrier wafer the SPNIs could be placed on the surface of an upturned Petri dish, as shown. The regions that are designed to be connected to could be left on the outside of the dish, so that the PDMS layer could be deposited

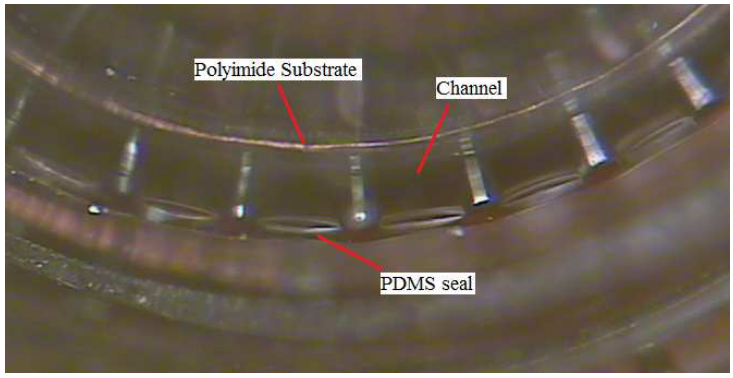

Fig. 10.8: Sealing of the passive SPNIs, the PDMS layer can be seen to be sealing across the top of the channel structure.

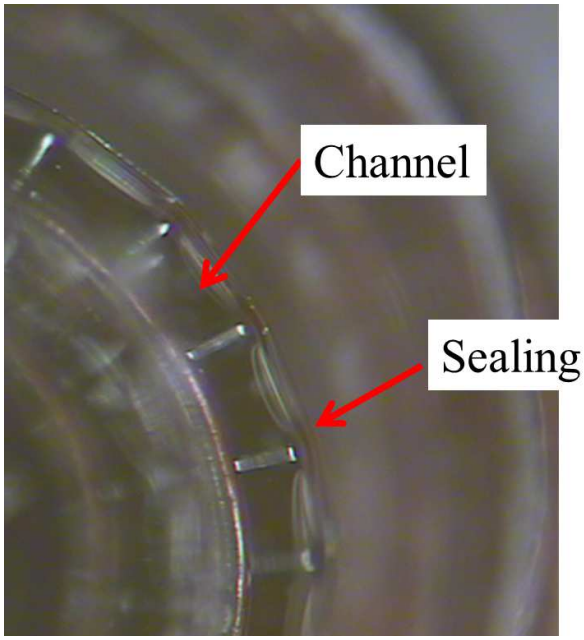

Fig. 10.9: Sealing of the passive SPNI

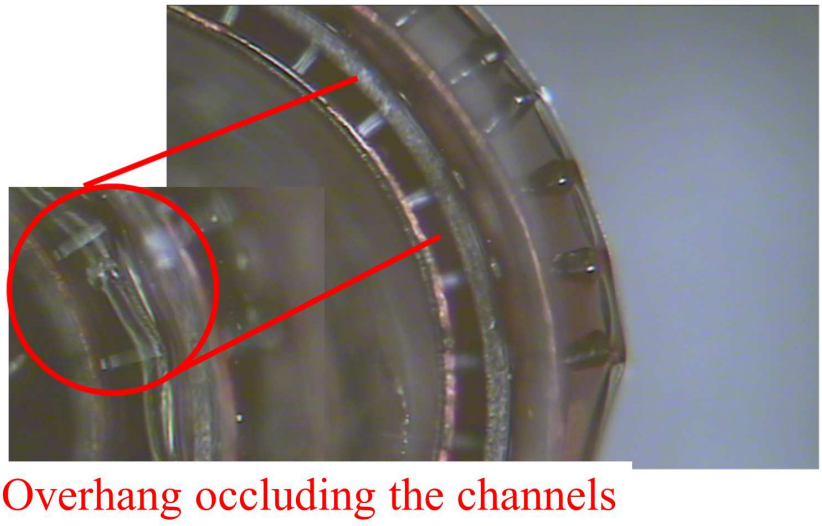

Fig. 10.10: Extra PDMS can overhang and block the channels. This is most likely caused by the manual shaping of the PDMS layer.

into the middle of the dish, flattened and left to form the adhesive bond without covering the area for the micro-rivets. The PDMS layer could then be cut to shape, as described earlier.

Once the PDMS has bonded to the SPNI, the channel layer could then be rolled, with the channels facing the outside, and inserted into the silicone tube. The SPNI is then bonded to an alumina PCB using the Microflex technique described in chapter seven.

10.4 Problems with this Fabrication Process

Although the images presented suggest a good sealing for the SPNI implant there are some problems that need to be addressed if this fabrication method is to be developed further. As the PDMS layer is structured by hand there is a lack of control over the final dimensions of the sealing layer and the excess PDMS can overhang and partially block the micro-channel, as shown in Figure 10.10. To prevent this from happening, photolithography could be used to define the sealing layer prior to, or post, bonding to the channels. However, it would be difficult to spin-coat photoresist onto the uneven PDMS layer after bonding, as the photo-resist would tend to pool in the troughs of the surface, leading to errors during the exposure. Also, the photoresist layer would be difficult to soft-bake on a hotplate, although it would be possible to bake the layer in a convection oven. Thus it would be desirable to define the PDMS layer first, before aligning over the channels. If the PDMS is made slightly narrower than the SPNI

channels the risk of an overhang would be reduced.

Alternatively, the sealing layer could be shaped prior to bonding using a mould. PDMS is conventionally moulded, even with very thin layers, as Thangawng et al [100] have reported the fabrication of both ultra-thin (>1nm) and relatively thick (≈100 μm) PDMS layers onto a prepatterned mould of Teflon or photoresist via spin-coating. After the spin coating, the photoresist could be washed away using acetone to leave the PDMS structures. If the mould and the PDMS, were fabricated onto a sacrificial layer of PMMA, the PDMS could then be released. Similarly, it has been reported that PDMS could be fabricated using moulds made of SU-8 [101]were it is possible to peel the moulded PDMS structure away from the substrate.

Another consideration of this application is the stress caused to the channel structures after rolling. Although no major defects have been found so far, one sample shown in Fig.10.10 seems to suggest that the channel may be collapsing due to the PDMS layer. In general PDMS is more flexible than polyimide, however some stress may be effecting the stability of the channel in the sample shown. This would need to be tested by fabricating and rolling more sealed samples. If the PDMS layer is causing weakness in the channels, perhaps a thinner layer could be used.

Finally, rolling the channels in the other direction will change the relative position of the metallized layer to the neutral plane of the SPNI. In the previous studies it is thought that the gold film was under tensile compression relative to the neutral plane, whereas in the updated design the wiring will be under tensile extension. This may influence the ability of the device to transfer the signals detected at the electrodes to the external electronics as the gold tracks may fracture. All of these factors require further investigation before it can be stated with confidence that the PDMS sealing layer is an improvement for the SPNI device.

11. CONCLUSIONS AND AREAS FOR FUTURE WORK

The main achievements presented in this thesis are the novel processing routes that have been discovered for neural interfaces. These include; the ability to spin-coat layers of PMMA as a suitable sacrificial material for photosensitive polyimide and thin layers of PDMS, the ability to utilise photosensitive polyimide as a substrate layer for neural interfaces, the ability to incorporate Microflex interconnections with the photosensitive polyimide substrate, the ability to pattern inhomogeneous surfaces (steps) using photolithography and the ability to seal a micro-channel array with a thin layer of PDMS.

These fabrication processes have been optimised to fabricate a regenerative implant with the intention of providing a chronic neural interface in the PNS of a nerve injured patient. The thesis presents the processing routes that have been investigated and shows which materials are compatible and which fabrication processes are most suitable.

The use of PMMA as a sacrificial material allowed the ability to create neural interfaces out of photosensitive polyimide in an efficient manner. Although PMMA has been used for non-photosensitive polyimide it has not previously been demonstrated to be compatible with photosensitive polyimide before this study. Although care is required and the amount of solvent that can be used in the fabrication process is limited, this represents a novel application of PMMA.

After discovering that PMMA could be used to fabricate photosensitive polyimide structures, it was possible to investigate the incorporation of Microflex technology into the fabrication of the regenerative implant. The thickness of the polyimide and the size of the hole that is compatible with this technology has been optimised, such that the thickness of the polyimide layer should not exceed 20 μm and the via hole should be a square with sides of length 50-70 μm.

It was discovered that previous attempt to calculate the position of the neutral plane of the SPNI had been incorrect, and so it was necessary to apply the elastic theory of bending

to estimate the strain on the thin gold film. An updated model has been described for the bending of the SPNI structure for which the SPNI substrate is only allowed to bend between the rigid channel walls. This new model predicts that the original SPNI was experiencing 1-4% of compressive strain. The effects of compressive strain on the flexible electronics is not yet known and further investigation is required.

Both single and dual-substrate samples were fabricated that incorporated Microflex interconnection technology and it was shown that the added substrate thickness was not necessarily changing the electrode characteristics, as no noticeable difference between the impedance and phase spectra could be observed. This is further evidence that tensile compression is less problematic, as for the bending model described the electrode tracks on the thinner substrate are subjected to 1-2.5% compressive strain in the roll, compares to 2-6% compressive strain for the thicker substrate, from Figure 7.18. This suggests that the mechanism that allows for the gold tracks to withstand 1% compressive strain allow further compressive strain up to 6%, and the limit of compressive strain has not yet been reached.

The amount of data presented for both types of SPNI is limited. As the complexity of the fabrication process reduced the yield of the dual-substrate due to failure of the metallized layer during curing. This difficulty in curing the SPNI leads to the suggestion that the maximum thickness of the dual substrate is $\approx 40\mu$m, which limits future development of the SPNI using this process.

A theoretical model of the electrochemical behaviour of gold electrodes in saline was presented so that the impedance spectroscopy could be used to assess the quality of the fabrication processes. This model was created by breaking down the physical phenomena of the electrode interface into mathematical expressions that depend on the geometry of the electrode, the potential and frequency of the signal and the ionic strength of the solution (amongst other thermodynamic factors). These physical phenomena were then calculated using values from the literature and applied to generate impedance and phase spectra over a large frequency range. The theoretical model predicted that a planar, gold electrode of the equivalent size of the SPNI should have an impedance of $\approx$ 100 kΩ at 1000 Hz. The model also suggested that for a completely sealed micro-channel the solution resistance should be in the region of $\approx 7\times10^4$ Ω, compared to a solution resistance of $\approx 1\times10^3$ Ω for the non-sealed case. Thus, it was suggested that the impedance

spectroscopy could be used to test whether the micro-channels had been sealed. Based on this prediction, it can be said that none of the electrodes demonstrated impedance spectra that would be consistent with perfectly sealed micro-channels.

When comparing the measured impedance of the electrode to the modelled spectra of a dispersive interface (n=0.8) there was much agreement in the lower frequency range. However, as the frequency increased the measured impedance showed behaviour that was consistent with neither a perfectly sealed channel nor a planar electrode. This suggests that the micro-channel may have been partially sealed, although this sealing has not yet been quantified. Furthermore, the higher frequency behaviour may have been effected by a leakage capacitance, the origin of which has not yet been determined.

The impedance spectra of a 'failed' electrode is also included to highlight both the ability of the impedance spectroscopy to detect fractures in the metal layer and to show that there was no instrumental artefacts in the measured impedance at higher frequency for the successful samples.

One failure of the experimental work is not to include impedance measurements of the same sample both before and after rolling. This would perhaps be the most illuminating test as it may be possible to show direct changes between the solution resistance's of sealed and unsealed channels. Unfortunately, due to the complexity of the fabrication process this was not possible for this study, but should be included in further investigations.

Nevertheless, experimental work presented in this thesis suggests that the fabrication process was flawed and needed revising in order to seal the channels. This was addressed by introducing a laminating layer of PDMS into the fabrication that seals the top of the channels. This technique has not yet been tested electrically, but visually the initial results were promising. However, in order to stop the PDMS layer from blocking the micro-channels the SPNI had to be rolled in the opposite direction from previous studies. Using the new model of bending it is suggested that this will cause the metal layer to experience tension (the magnitude of which depends on the substrate thickness). This potentially problematic in future designs of the SPNI and should be investigated further.

Similarly, the lamination of the PDMS was not perfect as occasionally the PDMS was able to overhang the micro-channels which would block regeneration. New fabrication models should

be investigated to accurately shape the PDMS layer before it is laminated on the SPNI channels. This may be possible using micro-moulding.

Mechanical testing was conducted to determine whether the Microflex interconnections were at least as strong as the substrate layer. Although the Microflex interconnection survived the mechanical loading, the testing highlighted a possible weakness in the SPNI design. The narrow neck of the device was a common point of failure in the earlier SPNI, the updated device did not survive more than 30% strain as would be expected for polyimide. The testing only loaded the SPNI in the longitudinal direction, whereas the final neural interface would be expected to survive multiple modes of stress in many directions. Thus it is advisable to investigate methods of reducing the strain at the neck of the device, or to remove the neck completely, in the updated SPNI design. Further fatigue testing should be performed to test the durability of the SPNI.

11.1 Future Experimental Testing

11.1.1 Assesing the Bending Model

To determine the effect of bending on the metallization and to determine a mechanical limit of the strain that the gold can endure more SPNI samples should be made of varying thickness and rolled in each direction. Electrochemical impedance spectroscopy of each electrode would then show whether the SPNI was viable for the given thickness and rolling orientation. This data could then be used to determine whether the SPNI with the added sealing would survive the fabrication, and what adjustments need to be made.

A simpler test could be performed by changing the design of the gold layer so that each electrode is shorted together, as shown in Figure 11.1. The continuity of the gold layer could then be assessed by testing for short circuits (using a multimeter) between electrodes connected in series, and any open circuits would suggest that the gold layer had failed. By doing so it may be possible to isolate which electrodes had failed and relate this to the amount to the strain relative to its position within the array. Thus it may not be necessary to create a range of SPNI with different substrate thickness in order to test different levels of strain. Similarly, the new model predicts that if the substrate is of an equal thickness to the passivation layer the strain

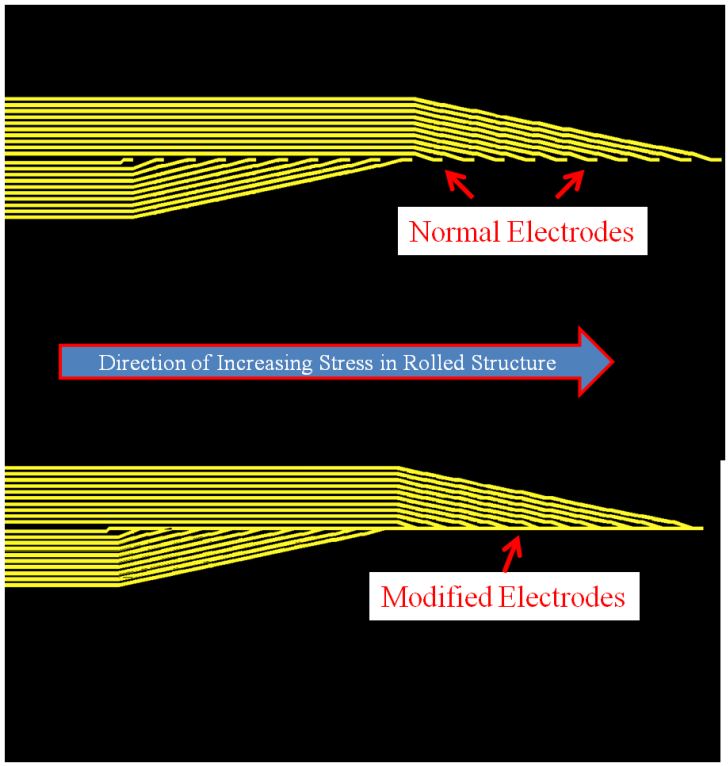

Fig. 11.1: Diagram of modified gold layer that could be used to test each bending model

on the metallization is minimised. By creating a batch of SPNIs that satisfy this condition this hypothesis can be tested. If it can be shown that the electrical behaviour does not change when the direction of rolling is reversed then this will be an important result.

Assessing the Durability of the Interface

To assess the ability of the SPNI to withstand the physiological environment fatigue tests should be performed. By submerging a sample in a salty environment held at a fixed temperature (physiological conditions ≈40°) and monitoring the impedance of the electrodes over an extended period of time it may be possible to show whether there is any degradation in the interface. As the materials used can uptake water, swelling in the interface may cause problems in the channel sealing that should be investigated. By using careful controls, including testing samples that have not been exposed to the physiological conditions) it should be possible to conclude whether or not the SPNI has a reliable functionality over an extended period of time. This could be done on samples that both include the PDMS lamination and don't, to see if there is any difference.

Other research groups also subject their implants to accelerated fatigue by submerging them

in a salty environment held at a very high temp (>80°) and monitoring their progress. By repeating this type of approach the durability of the SPNI can be tested for extreme conditions. This type of testing will be imperative if the SPNI is ever going to reach a clinical application.

11.1.2 Assessing the Sealing of the SPNI

It is desirable to test the sealing of the channels beyond the visual inspections that have been presented so far. It may be possible to perform a T-Peel test to compare the adhesion of the PDMS to the top of the channel to other adhesive bonding techniques. Ultimately however, as long as the adhesion is durable enough to survive the rolling into the spiral, this method of testing may be inappropriate. Instead, work should be done to test whether the sealing layer has improved the electrical performance of the device. As has been demonstrated in the theoretical modelling, a perfectly sealed channel should have a very large ($\gtrsim 7 \times 10^4\ \Omega$) solution resistance. Using the same protocol as has already been demonstrated it should be possible to detect whether the micro-channels have been sealed effectively.

To test the amount of crosstalk that exists between electrodes of the sealed and unsealed SPNI, impedance spectroscopy could be performed between neighbouring electrodes of both sealed and unsealed implants. If there was a noticeable change in the impedance spectra between neighbouring channels it suggest that the channels had been sealed.

In this case the spectroscopy would be performed using a two-electrode set up connected to the network analyser in a saline solution, where the first electrode would be one electrode of the SPNI and the second would be a neighbouring electrode. As there is no reference electrode and the micro-fabricated electrodes are of similar areas this measured impedance would not be considered as an accurate measurement of the impedance of the micro-fabricated electrodes, as the result will be a combination of both impedances.

Using the two-electrode set-up in the sealed case, the current path would be forced to travel along the length of one micro-channel, out of the micro-channel array and into the channel that contains the second electrode under test. This would lead to a solution resistance that is approximately double that of a single micro-channel. If there was no sealing the current path would not be blocked in this way and the resultant solution resistance would be much lower.

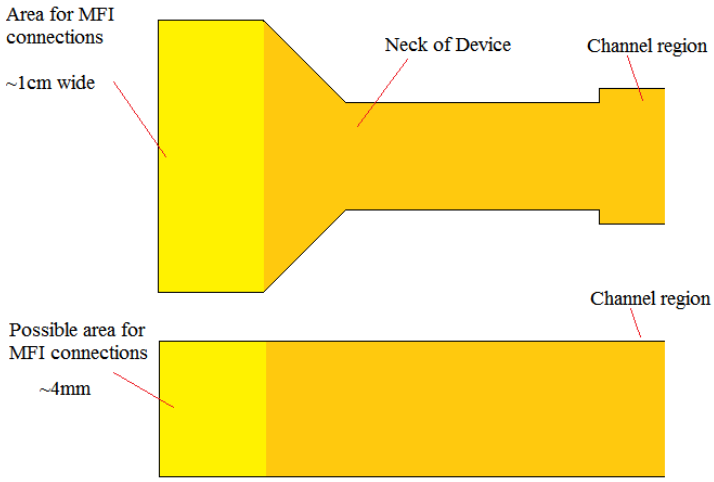

Fig. 11.2: Possible reduction in the width of the SPNI though incorporation of MFI

11.1.3 Translation of Fabrication Techniques into New Technology

A project has started that aims to translate these novel processing routes into an updated SPNI device that will be integrated with signal processing inside the biological target. The miniaturization offered by the improvement in the connection regime, via the Microflex technology, has lead to the ability to construct an implant that will; capture the neural activity from the regenerated tissue, employ differential amplification to extract the important features of the signals and perform analog multiplexing to provide a way extracting the information through a single cable. The use of MFI can offer a significant improvement in future designs of the SPNI as the connection pads can be reduced in size and have a much finer pitch, increasing the amount of connection pads that can be included in a given area. Before the implementation of the MFI technology, the connection pads of the SPNI were 400 μm wide with a pitch of 500 μm, which resulted in 20 electrode pads occupying a width of 1 cm. Using MFI, it is envisaged that these proportions can be brought down to an electrode pad that is $\approx$150 μm, to incorporate a 70 μm via hole with $\approx$40 μm of PSPI either side, to give a pitch of $\approx$200 μm. These values are illustrative, and have not yet been tested for the SPNI, but similar connection regimes have previously been reported[70]. This suggests that the connection area can be reduced down to a total width of 4 mm, which would remove the need for a neck, which has been a point of significant weakness in the progression of the SPNI. This is illustrated in Figure 11.2.

Once the adjustments had been made to the SPNI it should be relatively easy to couple the devices to the alumina PCB via MFI, which offers the ability to include signal processing at

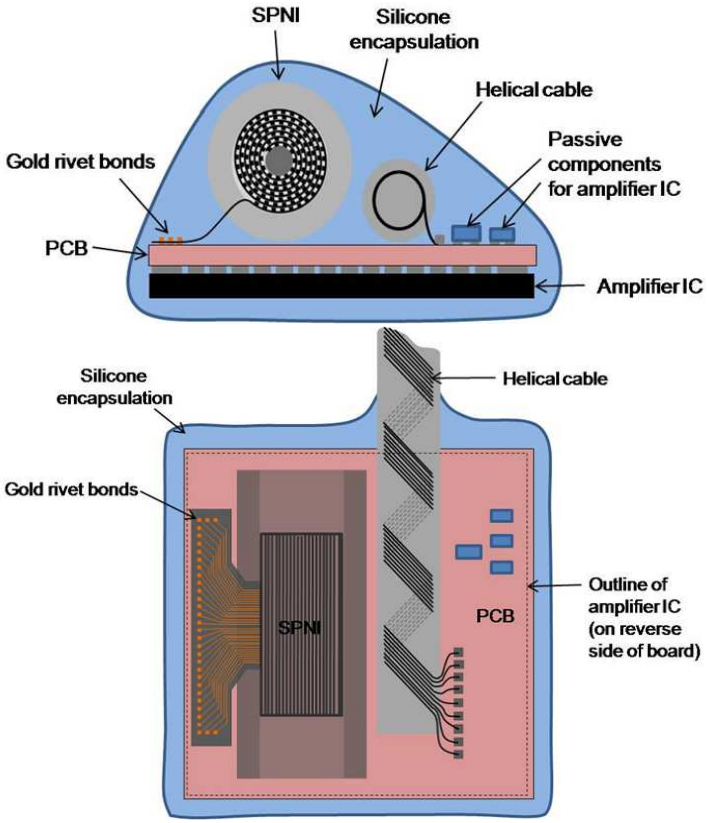

Fig. 11.3: Schematic of updated SPNI that is integrated to chip that is able to perform signal processing signal

the interface. To perform the signal processing, the SPNI device will be mounted onto a chip (RHA2216, Intan Technologies) via the alumina PCB. The chip and the PCB will be integrated so that a single home-made helical cable can be used to carry all the input to control the chip, and carry out the processed information from the device. The SPNI will have 16 electrodes that are coupled to the alumina PCB via Microflex technology. An illustration of the design is shown in Figure 11.3.

All the components of the interface, including the SPNI, electrical components, and helical cable are designed to be integrated onto a PCB that is mounted onto the surface of the chip. The surface area of the chip is 8 x 8 mm square, and the PCB is 5.5 x 5.5 mm square so that it can be mounted onto the chip without covering the connection pads. A schematic diagram of the chip is shown in Figure 11.4.

The surface area of the PCB determines the maximum size of connection area that can is available for the SPNI. For this project, the connection area fits in a space that is 2600μm square (total surface area = 676000μm^2), to allow for all the other components that are necessary for

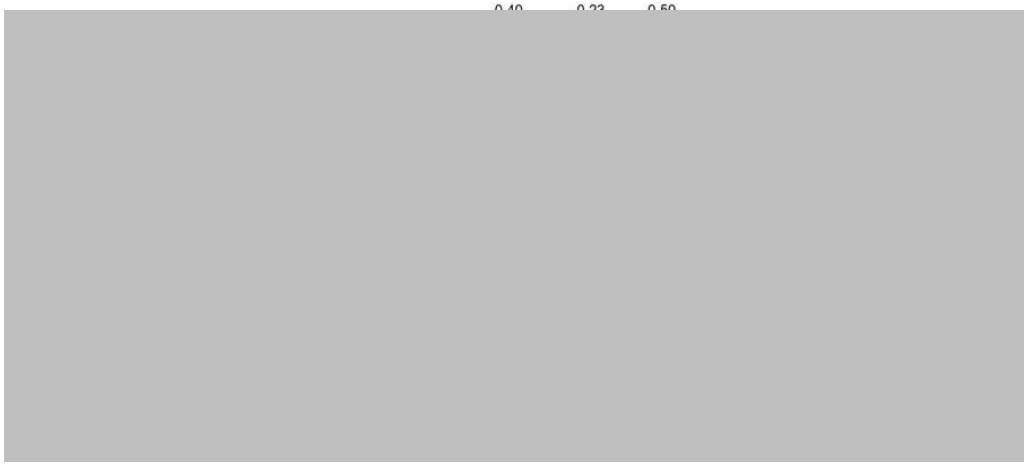

Fig. 11.4: Schematic of the Intan RHA2216 chip, obtained from the company brochure [102]

the chip and to allow space to incorporate the helical cable. The area of the connection region on the original SPNI device was 1cm x 5 mm, which gives a total surface area of 5×10^7 μm^2. This kind of miniaturization can only be achieved using the fabrication methods that have been developed in the thesis, and highlights the necessity of developing the Microflex technology for the SPNI. The latest SPNI design, and how it will bonded onto the chip is shown in Figure 11.5. The rolled tube is not shown, only a schematic of the connections is presented. The latest SPNI, as well as the supporting electronics, will be encapsulated in silicone before implantation. This will reduce the strain at the neck of the device to remove a possible mode of failure as well as protect the Microflex interconnection from corrosion and short circuits..

The fabrication processes developed in this thesis are also being used to develop technology to record electrical activity form the surface of a rat's brain (EcoG) and to record elecrocardiographs from zebrafish embryos for use in chemical-compound screening, examples of which are shown in Figure 11.6. These applications show how the novel processing routes presented in this thesis have value across a range of electrophysiological studies. The adaptability of the photolithographic processes allow for a range of deigns that can be utilised in many different applications. The devices shown comprise of thin-substrates of Durimide that were fabricated on a sacrificial layer of PMMA, with thermally evaporated metallization and thin passivation layers. Figure 11.6 shows how the EcoG electrodes are connected to a PCB via Microflex interconnections, that would not have been possible before this study was conducted. This allows for a high number of electrodes in a small area without difficulty.

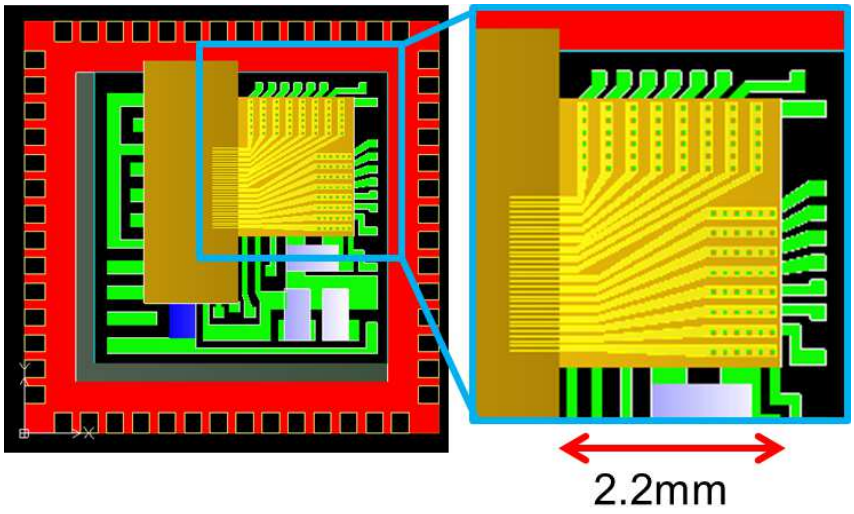

Fig. 11.5: The updated connection of the SPNIs onto the Intan chip, the other features are the passive components (the three white block are resistors and the blue block is a decoupling capacitor) the green sections are screen printed gold. The red section is the chip, with the grey ground plane. The black sections in the edges are the connection pads of the chip.

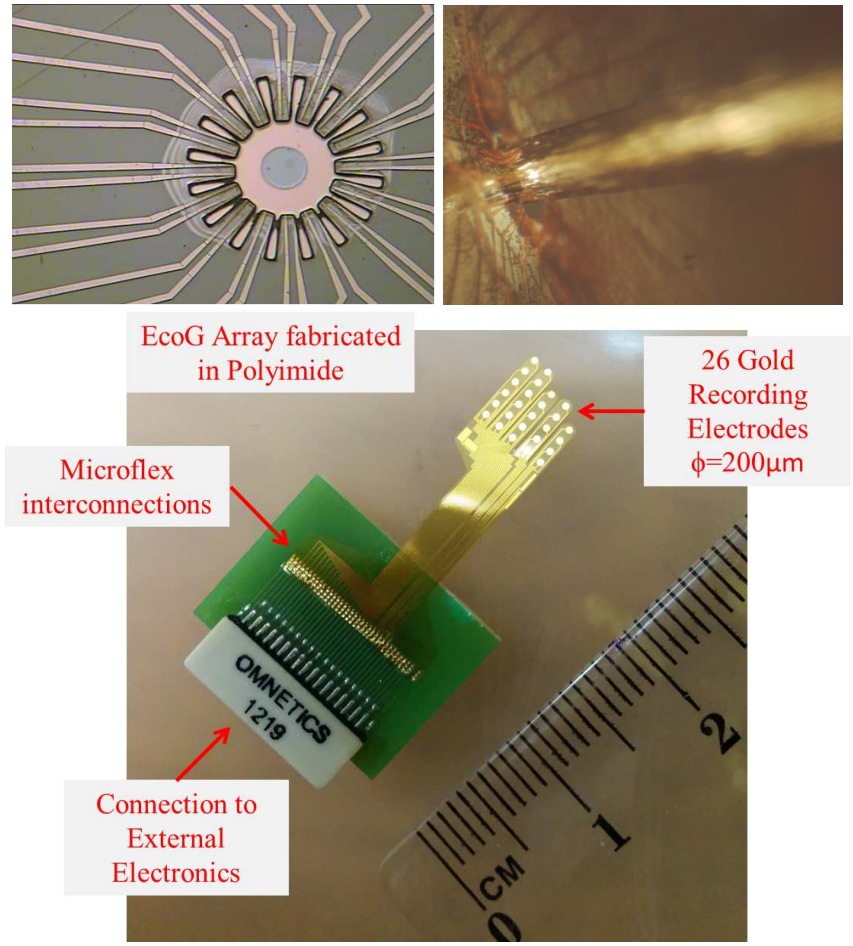

Fig. 11.6: Technology that has directly led from the novel processing routes discussed in this thesis. The top two images are microscopy of an array of electrodes that are designed to fit around a zebrafish embryo in order to record electrophysiological activity from the surface of the skin. The top right picture shows how the array is able to bend which is important as the arrays have fingers that are designed to conform to the surface of the embryo. The bottom image shows an electrode array that has been designed to record from the surface of a rat's brain.

APPENDIX

A. PHOTO-LITHOGRAPHY MASK DESIGNS

A.1 SPNI Devices 1: Used in Earlier In Vivo Studies

- Width at connection Pads: 1 cm
- SPNI Length: 4 cm
- SPNI width at channels: 4 mm
- SPNI channel Width: 100μm
- Electrode Wiring Width: 30 μm
- Electrode Dimension: 30 μm x 100 μm
- Connection pad: 400 μm x 1000 μm

A.2 SPNI: Incorporating Microflex Technology

- Width at connection Pads: 1 cm
- SPNI Length: 4 cm
- SPNI width at channels: 4 mm
- SPNI channel Width: 100μm
- Electrode Wiring Width: 30 μm
- Electrode Dimension: 30 μm x 100 μm
- Connection pad: 400 μm x 1000 μm
- Via hole for microflex interconnection: range from 35-70μm square

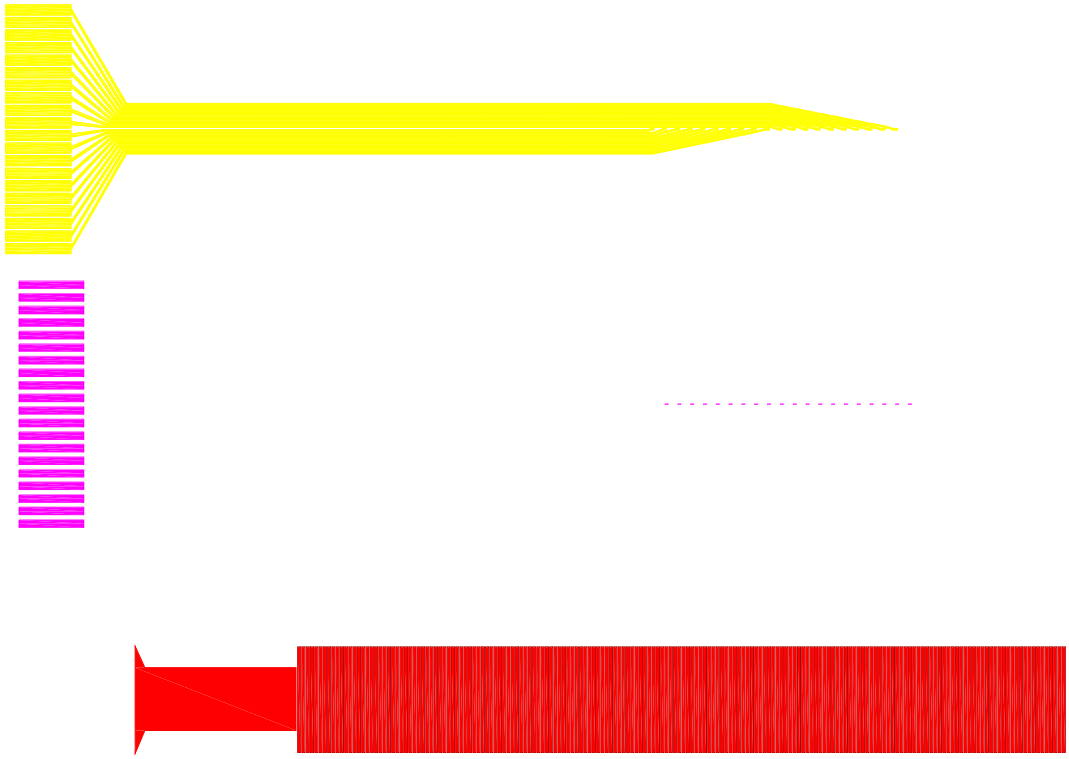

Fig. A.1: Photomasks for the original SPNI device, Designed by Edward Tarte and Samia Benmerah. Yellow section used to pattern photoresist for electrodes, Pink used to pattern passivation layer, Red used to pattern channel layer

A.3 SPNI: Latest Design

- Width at connection Pads: 2.7 mm
- SPNI Length: 4 cm
- SPNI width at channels: 4 mm
- SPNI channel Width: 100μm
- Electrode Wiring Width: 30 μm
- Electrode Dimension: 30 μm x 100 μm
- Via hole for microflex interconnection: 50μm square
- Connection pad: 150 μm x 1000 μm

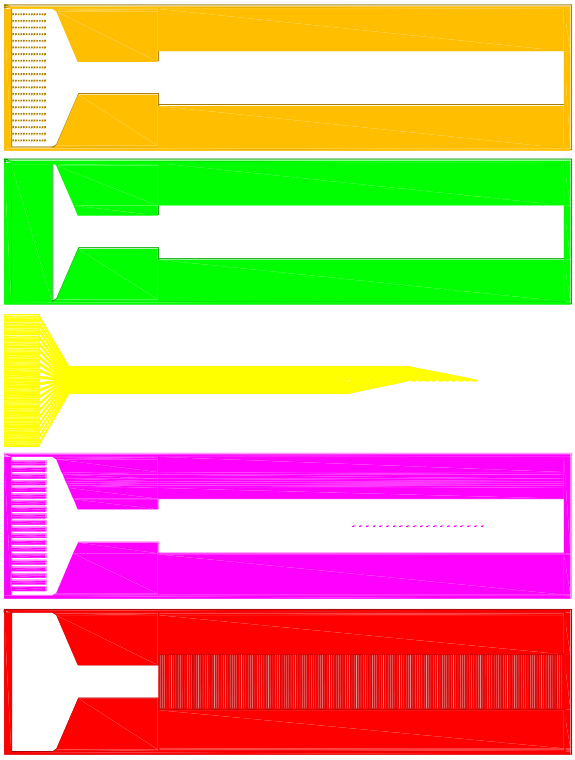

Fig. A.2: Photomasks for the updated SPNI device incorporating MFI, Designed with help from Samia Benmerah. Brown used to pattern first substrate layer, green used to pattern second substrate layer, yellow section used to pattern photoresist for electrodes, pink used to pattern passivation layer, red used to pattern channel layer

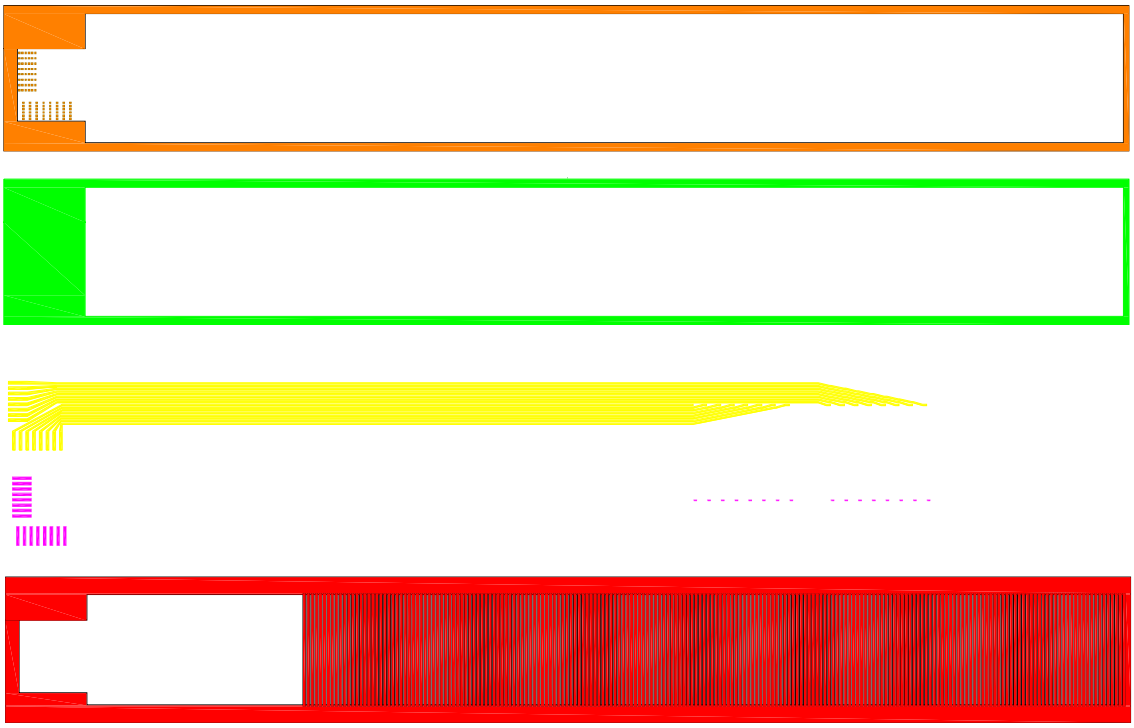

Fig. A.3: Photomasks for the latest SPNI design, Brown used to pattern first substrate layer, green used to pattern second substrate layer, yellow section used to pattern photoresist for electrodes, pink used to pattern passivation layer, red used to pattern channel layer

B. PUBLICATION PLAN

- Publised: Richard Barrett, Samia Benmerah, Andreas Frommhold and Edward Tarte; "Spiral Peripheral Nerve Interface: Updated fabrication process of the regenerative implant", 35th Annual Int. Conf. of IEEE EMBS, July 2013
- In Preparation: A paper that describes the method of sealing the microchannel array
- In Preparation: A paper to describe the results of implantation of the latest SPNI design including the signal processing
- In Preparation: A paper that describes the zebrafish recording array, to be finalised once ECG has been recorded.
- In Preparation: A paper that describes the EcoG recording array, to be finalised after in vivo testing has been performed.

BIBLIOGRAPHY

[1] F Spelman. The past, present, and future of cochlear prostheses. *IEEE engineering in medicine and biology magazine*, 18(3):27–33, 1999.

[2] Gislin Dagnelie and Robert W Massof. Toward an artificial eye. *Spectrum, IEEE*, 33(5):20–29, 1996.

[3] Johan Wessberg, Christopher R Stambaugh, Jerald D Kralik, Pamela D Beck, Mark Laubach, John K Chapin, Jung Kim, S James Biggs, Mandayam A Srinivasan, and Miguel AL Nicolelis. Real-time prediction of hand trajectory by ensembles of cortical neurons in primates. *Nature*, 408(6810):361–365, 2000.

[4] Andrew B Schwartz. Cortical neural prosthetics. *Annu. Rev. Neurosci.*, 27:487–507, 2004.

[5] N Birbaumer, U Strehl, and T Hinterberger. *Brain-computer interfces for verbal communication. In: Neuroprosthetics; Theory and Practice. Horch and Dillon (Eds).* World Scientific, New Jersey, 2004.

[6] Yevgeny Perelman and Ran Ginosar. *The neuroprocessor: an integrated interface to biological neural networks*, volume 14. Springer, 2008.

[7] A Branner and R Norman. A multielectrode array for intrafascicular recording and stimulation in sciatic nerve of cats. *Brain. Res. Bull.,*, 51:293–306, 2000.

[8] Miguel AL Nicolelis. Actions from thoughts. *Nature*, 409(6818):403–407, 2001.

[9] JD Simeral, S-P Kim, MJ Black, JP Donoghue, and LR Hochberg. Neural control of cursor trajectory and click by a human with tetraplegia 1000 days after implant of an intracortical microelectrode array. *J. Neural Eng*, 8:025027, 2011.

[10] S Benmerah, S Lacour, and E Tarte. Design and fabrication of neural implants with thick microchannels based on flexible polymeric materials. *31st Annual Int IEEE EMBS Conference*, pages 6400–6403, 2009.

[11] Fitzgerald et al. Microchannels as axonal amplifiers. *IEEE Trans. on Biomed. Eng.*, 55:1136–46, 2008.

[12] T Stieglitz, H Beutel, and J Meyer. Microflex-a new assembling technique for interconnects. *J. of Int. Mat. Sys. and Struc.*, 11:417–425, 2000.

[13] J Fitzgerald, N Lago, S Benmerah, J Serra, CP Watling, RE Cameron, E Tarte, S S Lacour, S McMahon, and J Fawcett. A regenerative microchannel neural interface for recording from and stimulating peripheral nerve axons *in vivo*. *.J Neural Eng*, 9, 2012.

[14] KW Horch and G Dhillon. *Neuroprosthetics : Theory and Practice (Series on Bioengineering and Biomedical Engineering, Vol. 2)*. World Scientific, 2004.

[15] C Krebs, J Weinberg, and Akesson. *Neuroscience*. Lippinott Williams and Wilkins, 2012.

[16] Richard A Berger. *Hand surgery*. Wolters Kluwer Health, 2004.

[17] MC Dodla and RV Bellamkonda. *Principles of Regenerative Medicine; Peripheral Nerve Regeneration*, pages 500–544. Academic Press, 2007.

[18] A Frommhold. *Nanotexturisation of Gold Surfaces and its Application to Neural Implants*. PhD thesis, University of Birmingham, 2010.

[19] X Navarro, T. Krueger, N Lago, S Micera, T Stieglitz, and P Dario. A critical review of interfaces with the peripheral nervous system for the control of neuroprostheses and hybrid bionic systems. *Journal of the Peripheral Nervous System*, 10(3):229–258, 2005.

[20] Gregory TA Kovacs et al. Introduction to the theory, design, and modeling of thin-film microelectrodes for neural interfaces, 1994.

[21] A Fischer. *Electrode Dynamics*. Oxford University Press, 1996.

[22] S Metz. *Polyimide based microfabrication technologies for microelectrode and microfluidic devices in biomedical engineering*. PhD thesis, EPFL, Lausanne, 2003.

[23] MK Ghosh and KL Mittal. *Polymides: fundamentals and applications*. New York: Marcem Dekker, 1996.

[24] JD Bronzino. *Biomedical Engineering Handbook.* CRC Press and IEEE Press, 1995.

[25] LA Geddes and R Roeder. Criteria for the selection of materials for implanted electrodes. *Ann Biomed Eng.*, 7:879–90, 2003.

[26] *CRC Handbook of Chemistry and Physics;*. 93rd Edition Internet Version 2013, 2013.

[27] M Wieler, S Naaman, and RB Stein. Walkaid: An improved functional electrical stimulator for correcting foot-drop. *Proc. 1st Ann Conf IFES*, 1996.

[28] PN Taylor et al. Clinical use of odstock dropped foot stimulator: its effect on the speed and effort of walking. *Arch Phys Med Rehabil*, 80:1577–83, 1999.

[29] R Kobetic et al. Implanted functional electrical stimulation system for mobility in paraplegia: a follow-up case report. *IEEE trans Rehabil Eng*, 7:390–398, 1999.

[30] N Bhadra, KL Kilgore, and PH Peckham. Implanted stimulators for restoration of function in spinal cord injury. *Med Eng Phys*, 23:19–28, 2001.

[31] RJ Triolo, C Bieri, J Uhlir, R Kobetic, A Scheiner, and EB Marsolais. Implanted fns systems for assisted standing and transfers for individual with cervical spinal cord injuries. *Arch Phys Med Rehabil*, 77:1119–1128, 1996.

[32] Kevin L Kilgore, P Hunter Peckham, Michael W Keith, Fred W Montague, Ronald L Hart, Martha M Gazdik, Anne M Bryden, Scott A Snyder, and Thomas G Stage. Durability of implanted electrodes and leads in an upper-limb neuroprosthesis. *Journal of rehabilitation research and development*, 40(6):457–468, 2003.

[33] GE Loeb, RA Peck, WH Moore, and K Hood. Bion system for distributed neural prosthetic interfaces. *Med Eng Phys*, 23:9–18, 2001.

[34] GG Naples, JT Mortimer, and TGH Yuan. Overview of peripheral nerve electrode design and implantation. *Neural Prostheses: Fundamental studies, biophysics and bioengineering series. Agnew, WF and Mcreery DB.*, pages 107–144, 1990.

[35] Martin Schuettler, Anne Vanhoestenberghe, Nooshin Saeidi, Xiao Liu, Joe Evans, Cindy Colinge, Andreas Demosthenous, and Nick Donaldson. Realization of an active book for multichannel intrathecal root stimulation in spinal cord injuryâĂŤpreliminary results. In *Engineering in Medicine and Biology Society, EMBC, 2011 Annual International Conference of the IEEE*, pages 2965–2968. IEEE, 2011.

[36] Richard B Stein, Dean Charles, L Davis, Jack Jhamandas, A Mannard, and TR Nichols. Principles underlying new methods for chronic neural recording. *The Canadian journal of neurological sciences. Le journal canadien des sciences neurologiques*, 2(3):235–244, 1975.

[37] Mohamad Rahal, Jeff Winter, John Taylor, and Nick Donaldson. An improved configuration for the reduction of emg in electrode cuff recordings: a theoretical approach. *Biomedical Engineering, IEEE Transactions on*, 47(9):1281–1284, 2000.

[38] James D Sweeney, David A Ksienski, and J Thomas Mortimer. A nerve cuff technique for selective excitation of peripheral nerve trunk regions. *Biomedical Engineering, IEEE Transactions on*, 37(7):706–715, 1990.

[39] GE Loeb and RA Peck. Cuff electrodes for chronic stimulation and recording of peripheral nerve activity. *Journal of neuroscience methods*, 64(1):95–103, 1996.

[40] William B Marks and Gerald E Loeb. Action currents, internodal potentials, and extracellular records of myelinated mammalian nerve fibers derived from node potentials. *Biophysical journal*, 16(6):655–668, 1976.

[41] RB Stein and KG Pearson. Predicted amplitude and form of action potentials recorded from unmyelinated nerve fibres. *Journal of theoretical biology*, 32(3):539–558, 1971.

[42] A Huxley and R Stampfli. Evidence for saltatory conduction in peripheral myelinated nerve fibres. *J. Physiol.*, 108:315–339, 1949.

[43] GE Loeb and RA Peck. Cuff electrodes for chronic stimulation and recording of peripheral nerve. *J Neurosci Methods*, 64:95–103, 1996.

[44] John Clark and Robert Plonsey. A mathematical evaluation of the core conductor model. *Biophysical journal*, 6(1):95–112, 1966.

[45] Jaakko Malmivuo and Robert Plonsey. *Bioelectromagnetism: principles and applications of bioelectric and biomagnetic fields*. Oxford University Press, 1995.

[46] DR Mcneal. Analysis of a model for excitation of myelinated nerve. *IEEE Transactions in Biomedical Engineering*, 23:329–337, 1976.

[47] Peter H Veltink, Benno K Van Veen, Johannes J Struijk, Jan Holsheimer, and Herman BK Boom. A modeling study of nerve fascicle stimulation. *Biomedical Engineering, IEEE Transactions on*, 36(7):683–692, 1989.

[48] Paul Ducheyne, Kevin Healy, Dietmar E Hutmacher, David W Grainger, and C James Kirkpatrick. *Comprehensive Biomaterials: Online Version*, volume 1. Newnes, 2011.

[49] Jumana Boussey. *Microsystems technology: Fabrication, test & reliability*. Kogan Page Science, 2003.

[50] Sami Franssila. Introduction to microfabrication. 2004.

[51] Fujifilm. Durimide 7020 data sheet.

[52] Shipley. Megaposit spr-220-7 photoresist datasheet.

[53] Shipley. Microposit s1813 photoresist datasheet.

[54] Bruker Corp. Dektak surface profiler manual.

[55] Diener Group. Femto oxygen plasma etcher manual.

[56] *Laurier M9 Manual, BESI*.

[57] Stuart F Cogan. Neural stimulation and recording electrodes. *Annu. Rev. Biomed. Eng.*, 10:275–309, 2008.

[58] Agilent. Network analyser hp 9424, user manual and technical guide.

[59] S Lacour, R Atta, J Fitzgerald, and M Blamire. Polyimide micro-channel arrays for peripheral nerve regenerative implants. *Sensors and Actuators A*, 147:456–63, 2008.

[60] S Lacour, J Fitzgerald, N Lago, E Tarte, S McMahon, and J Fawcett. Long micro-channel electrode arrays; a novel type of regenerative peripheral nerve interface. *IEEE Trans on Neur. Sys and Rehab Eng*, 17:454–60, 2009.

[61] Stephen C Kolesar. Principles of corrosion. In *Reliability Physics Symposium, 1974. 12th Annual*, pages 155–167. IEEE, 1974.

[62] Thomas Stieglitz, Hansjoerg Beutel, and J. Uwe Meyer. "microflex" new assembling technique for interconnects. *Journal of Intelligent Material Systems and Structures*, 11(6):417–425, 2000.

[63] M Schuettler, C Henle, JS Ordonez, W Meier, T Guenther, and T Stieglitz. Interconnection technologies for laser-patterned electrode arrays. *30th Annual Int IEEE EMBS Conference*, pages 3212–3215, 2008.

[64] C Henle, M Raab, JG Cordeiro, S Doostkam, A Schulze-Bonhage, T Stieglitz, and J Rickert. First long term *in vivo* study on subdurally implanted micro-ecog, manufactured with a novel laser technology. *Biomed Microdevices*, 13:59–68, 2011.

[65] Dae-Hyeong et al Kim. Dissolvable films of silk fibroin for ultrathin conformal bio-integrated electronics. *Nat Mater*, 9:511–517, 2010.

[66] John W Balde. The effectiveness of silicone gels for corrosion prevention of silicon circuits: the final report of the ieee computer society computer packaging committee special task force. *Components, Hybrids, and Manufacturing Technology, IEEE Transactions on*, 14(2):352–365, 1991.

[67] Hansjoerg Beutel, Thomas Stieglitz, and Joerg-Uwe Meyer. Versatile microflex-based interconnection technique. In *5th Annual International Symposium on Smart Structures and Materials*, pages 174–182. International Society for Optics and Photonics, 1998.

[68] George G Harman et al. *Wire bonding in microelectronics: materials, processes, reliability, and yield*, volume 21. McGraw-Hill New York, 1997.

[69] T. Stieglitz, H. Beutel, R. Keller, M. Schuettler, and J.-U. Meyer. Flexible, polyimide-based neural interfaces. In *Microelectronics for Neural, Fuzzy and Bio-Inspired Systems, 1999. MicroNeuro '99. Proceedings of the Seventh International Conference on*, pages 112 –119, 1999.

[70] Martin Schuettler, Christian Henle, Juan S Ordonez, Wolfgang Meier, Thomas Guenther, and Thomas Stieglitz. Interconnection technologies for laser-patterned electrode arrays. In *Engineering in Medicine and Biology Society, 2008. EMBS 2008. 30th Annual International Conference of the IEEE*, pages 3212–3215. IEEE, 2008.

[71] Christoph Jeschke, M Schuettler, L Reindl, and T Stieglitz. A telemetry platform for implantable devices providing inductive energy supply and a bi-directional data link. In *4th European Conference of the International Federation for Medical and Biological Engineering*, pages 2447–2450. Springer, 2009.

[72] DR Allee and AN Broers. Direct nanometer scale patterning of silicon dioxide with electron beam irradiation through a sacrificial layer. *Applied physics letters*, 57(21):2271–2273, 1990.

[73] W.H. Teh, J.K. Luo, C.-T. Liang, and C.G. Smith. Crosslinked pmma as a low-dimensional dielectric sacrificial layer for mems/nems and quantum nanostructures fabrication. In CorneliusT. Leondes, editor, *MEMS/NEMS*, pages 504–552. Springer US, 2006.

[74] Robert W Johnstone, IG Foulds, and M Parameswaran. Self-sacrificial surface micromachining using poly (methyl methacrylate). *Journal of Micromechanics and Microengineering*, 18(11):115–120, 2008.

[75] Jianqiao Ye. *Structural and stress analysis: theories, tutorials and examples*. CRC Press, 2008.

[76] Z Suo, E Ma, H Gleskova, and S Wagner. Mechanics of rollable and foldable film-on-foil electronics. *Appl. Phys. Letts*, 74(8), 1999.

[77] S Lacour, S Benmerah, E Tarte, J Fitzgronzinerald, J Serra, S McMahon, J Fawcett, Z Graudejus, O ans Yu, and B Morrison III. Flexible and stretchable micro-eletrodes for *in vitro* and *in vivo* neural interfaces. *Med Biol Eng Comput*, 48:945–954, 2010.

[78] Stéphanie P Lacour, Sigurd Wagner, and Z Suo. Stretchable conductors: thin gold films on silicone elastomer. In *MATERIALS RESEARCH SOCIETY SYMPOSIUM PROCEEDINGS*, volume 795, pages 193–198. Cambridge Univ Press, 2004.

[79] Elena Koukharenko, Michael Kraft, GJ Ensell, and N Hollinshead. A comparative study of different thick photoresists for mems applications. *Journal of Materials Science: Materials in Electronics*, 16(11-12):741–747, 2005.

[80] S. Metz, A. Bertsch, and P. Renaud. Partial release and detachment of microfabricated metal and polymer structures by anodic metal dissolution. *Microelectromechanical Systems, Journal of*, 14(2):383–391, 2005.

[81] *Intermolecular and Surface Forces*. London:Academic, 1985.

[82] D Morrow, R Mckenzie and M Bilek. The time-dependent development of electric-double layers in saline solutions. *J. Phys. D: Applied Physics*, 2006.

[83] L Burke and P Nugent. The electrochemistry of gold:i the redox behaviour of the metal in aqueous media. *Gold Bulltin*, 30(2), 1997.

[84] Richard SC Cobbold and RSC Cobbold. *Transducers for biomedical measurements: principles and applications*. Wiley New York, 1974.

[85] Kensall D Wise and JB Angell. A low-capacitance multielectrode probe for use in extracellular neurophysiology. *Biomedical Engineering, IEEE Transactions on*, (3):212–219, 1975.

[86] Khalil Najafi and Kensall D Wise. An implantable multielectrode array with on-chip signal processing. *Solid-State Circuits, IEEE Journal of*, 21(6):1035–1044, 1986.

[87] T Pajkossy. Impedance spectroscopy of interfaces of metals and acqeous solutions- surface roughness, cpe and relater issues. *Solid State Ionics*, 2005.

[88] Andrew O Fung, Christos Tsiokos, Omeed Paydar, Li Han Chen, Sungho Jin, Yibin Wang, and Jack W Judy. Electrochemical properties and myocyte interaction of carbon nanotube microelectrodes. *Nano letters*, 10(11):4321–4327, 2010.

[89] Kuldip C Gupta, Ramesh Garg, Inder Jit Bahl, and Prakash Bhartia. *Microstrip lines and slotlines*, volume 2. Artech house Dedham, MA, 1979.

[90] George M Whitesides. The origins and the future of microfluidics. *Nature*, 442(7101):368–373, 2006.

[91] Yu-Ting Cheng, Liwei Lin, and Khalil Najafi. Localized silicon fusion and eutectic bonding for mems fabrication and packaging. *Microelectromechanical Systems, Journal of*, 9(1):3–8, 2000.

[92] A Berthold, L Nicola, PM Sarro, and MJ Vellekoop. Glass-to-glass anodic bonding with standard ic technology thin films as intermediate layers. *Sensors and Actuators A: Physical*, 82(1):224–228, 2000.

[93] Martin A Schmidt. Wafer-to-wafer bonding for microstructure formation. *Proceedings of the IEEE*, 86(8):1575–1585, 1998.

[94] Viorel Dragoi, Thomas Glinsner, Gerald Mittendorfer, Bernhard Wieder, and Paul Lindner. Adhesive wafer bonding for mems applications. In *Microtechnologies for the New Millennium 2003*, pages 160–167. International Society for Optics and Photonics, 2003.

[95] F Niklaus, G Stemme, J-Q Lu, and J Gutmann. Adhesive wafer bonding. *J. Appl. Phys.*, 99, 2006.

[96] Xuan Xiong Zhang and J-P Raskin. Low-temperature wafer bonding: a study of void formation and influence on bonding strength. *Microelectromechanical Systems, Journal of*, 14(2):368–382, 2005.

[97] J.M. Engel, J. Chen, Chang Liu, and David Bullen. Polyurethane rubber all-polymer artificial hair cell sensor. *Microelectromechanical Systems, Journal of*, 15(4):729–736, 2006.

[98] Jessamine Ng Lee, Cheolmin Park, and George M. Whitesides. Solvent compatibility of poly(dimethylsiloxane)-based microfluidic devices. *Analytical Chemistry*, 75(23):6544–6554, 2003.

[99] E. King, Y. Xia, X.-M. Zhao, and G. M Whitesides. Solvent-assisted microcontact molding: A convenient method for fabricating three-dimensional structures on surfaces of polymers. *Adv. Mater.*, 9:651–654, 1997.

[100] AbelL. Thangawng, RodneyS. Ruoff, MelodyA. Swartz, and MatthewR. Glucksberg. An ultra-thin pdms membrane as a bio/micro nano interface: fabrication and characterization. *Biomedical Microdevices*, 9:587–595, 2007.

[101] B-H Jo, Linda M Van Lerberghe, Kathleen M Motsegood, and David J Beebe. Three-dimensional micro-channel fabrication in polydimethylsiloxane (pdms) elastomer. *Microelectromechanical Systems, Journal of*, 9(1):76–81, 2000.

[102] Intan Technologies RHA-2216. Intan technologies rha-2216 technical guide.